UNIVERSITY OF SOUTHAMPTON

FACULTY OF ENGINEERING AND THE ENVIRONMENT

Group of Engineering Materials

Oxidation-fatigue mechanisms at moderate service temperatures in single crystal turbine blade materials

by

Angelos Evangelou

Thesis for the degree of Doctor of Philosophy

September 2017

Abstract

The shortage of fossil fuels and the emergence of renewable energy technologies have increased the demand for a more variable and efficient power output from conventional gas turbine units. Single crystal Ni-based superalloys have long been the materials of choice for high temperature, gas turbine blade, applications due to their excellent fatigue, creep and oxidation resistance. However, the increased number of start-ups and shut downs, produce complex, unpredictable, cyclic loadings even at moderate temperatures, where the fatigue - oxidation behaviour of such materials is less well understood. The gas turbine industry has significant economic incentives to optimise maintenance scheduling and determine the useful lifetime of such components and thus a substantial effort is put in the development of damage tolerant, life assessment methods. This thesis aims to elucidate the mechanisms of oxidation - fatigue damage at moderate service temperatures, in single crystal, Ni-based superalloy turbine blade materials, in order to provide the basis for a physics based lifing model accounting for fatigue oxidation interactions.

The oxidation behaviour of two commercially available single crystal nickel based superalloys (in CMSX-4 and MD-2) has been investigated at the lower operating temperature range (450-550ºC) of an industrial gas turbine blade. Isothermal oxidation was carried out for varying times up to 640h and it was found that exposure resulted in a sub-micron thick oxide. The external and internal oxide kinetics were studied via high resolution image analysis and both showed sub-parabolic growth rates. Thermogravimetric tests indicated that the overall oxidation growth obeys a near quartic power law while parabolic kinetics can describe the transient oxidation period. Characterisation of the resulting oxides was carried out using field emission gun scanning electron microscopy, energy dispersive spectroscopy and X-ray diffraction. Results from thermodynamic modelling (Thermo-Calc) of the oxide formation are also presented. Low temperature oxidation in these Ni-based superalloys begins with the formation of porous NiO protrusions over the γ matrix. As the oxygen partial pressure drops in the substrate, a transition alumina forms near the surface within the γ'. The oxygen anions that diffuse into the alloy, preferentially through the γ/γ' interface and come in contact with the internal Al-rich γ' phase. This leads to the preferential oxidation of the γ' particles internally while the γ matrix remains relatively unaffected.

The notch fatigue initiation process has been studied at 450-550ºC in CMSX-4 in both air and vacuum (low oxygen partial pressure) environments, to assess the effect of oxidation. Detailed, electron microscopy, fractography indicated that crack initiation in an oxidising environment at 450°C and 550°C, is dominated by subsurface porosity while initiation at lower temperatures and

low oxygen partial pressure environments result in crystallographic cracking promoted by surface defects. At these temperatures, oxidation acted as a retardation mechanism to surface initiation processes by plugging porosity and interfering with the resulting strain levels. Porosity not only controlled initiation but also produced significant scatter in the fatigue lives obtained thus constituting an inherent feature of service conditions and should be considered in lifing approaches.

Dwell-fatigue testing was conducted on CMSX-4 samples at 450°C and 550°C in air and vacuum (low oxygen partial pressure). The effects of frequency (dwell) on the fatigue crack growth behaviour were studied using a constant stress intensity range test and blocks of alternating frequencies. It was found that at 550°C, a dwell time of 20s or higher (<0.04Hz) promotes a mixed time/cycle dependent crack growth rate. In order to further investigate the effect of dwell on the crack tip damage, pre-cracked samples were held under sustained loads for 12h. The resulting crack tips were examined using transmission electron microscopy and the resulting oxides using high resolution energy dispersive spectroscopy. Cracks forming under long dwell fatigue conditions had a complex morphology and formed several sub-branches that resulted in rougher fracture surfaces. During dwell fatigue crack propagation at intermediate temperatures, several competing mechanisms contribute synergistically to damage. In addition, the effects of oxidation were found to be two-fold. Strain assisted oxygen diffusion at small distances ahead of the crack tip can promote fracture at the γ/γ' interface while oxide formation on the crack tip surfaces can bridge the crack tip opening and reduce the effective driving force.

Table of Contents

List of Tables

List of Figures

Declaration of authorship

I, Angelos Evangelou declare that the thesis entitled:

Oxidation-fatigue mechanisms at moderate service temperatures in single crystal turbine blade materials

and the work presented in the thesis are both my own, and have been generated by me as the result of my own original research. I confirm that:

- this work was done wholly or mainly while in candidature for a research degree at this University;
- where any part of this thesis has previously been submitted for a degree or any other qualification at this University or any other institution, this has been clearly stated;
- where I have consulted the published work of others, this is always clearly attributed;
- where I have quoted from the work of others, the source is always given. With the exception of such quotations, this thesis is entirely my own work;
- I have acknowledged all main sources of help;
- where the thesis is based on work done by myself jointly with others, I have made clear exactly what was done by others and what I have contributed myself;
- none of this work has been published before submission

Signed:……..

Date:…….

Acknowledgments

First and foremost I would like to thank my supervisor Professor Philippa Reed who not only gave me the opportunity to shape my own work but for the patience and guidance through every stage of my research career over the past four years. My gratitude also goes to my second supervisor Dr. Nong Gao, and to my industrial supervisors Dr. Katherine Soady and Professor Scott Lockyer of Uniper Technologies for offering their technical expertise and making sure that the work retained an industrial focus.

I would also like to thank Dr. Rong Jiang who was the first person that welcomed me to the University of Southampton and for teaching me how to operate (and fix) the infamous Instron 1. Having to face primarily experimental tasks a major part of this work has been conducted in the TSR Lab where Dr. Andy Robinson lives and whom I owe my gratitude for teaching me virtually everything I know about mechanical testing. In addition, the assistance of the technical staff Dave, Chris and Heather in metallography and in taming the behaviour of Instron 1 is greatly acknowledged.

I am also greatly indebted to past and present members of the research group for the valuable discussions and help with various aspects of my work. Most importantly though I am grateful for their friendship and the laughs we had together. In no particular order I would like to thank Chao (thanks for Abaqus too), Alex R., Pawee, Andreu, Mike, Mr. Somsubhro of England, Alex M., Stephen and even the noob guy Alvaro.

Special thanks go to Athina Manoli for her unconditional support and encouragement. Thank you for putting up with me during the gloomy days of writing and for always cheering me up (and even for feeding me!). Finally, to my parents and brothers, thank you for shaping me to the person I am today and for being by my side every step of the way.

Αφιερωμένο στους παππούδες μου, Βαγγέλη Ευαγγέλου και Νίκο "Πασσιά" Αντωνιάδη,

… ἐς γῆν ἐναλίαν Κύπρον, οὗ μ' ἐθέσπισεν οἰκεῖν Ἀπόλλων.

Abbreviations

APB	Anti-phase boundary
BSE	Backscattered secondary electrons
CMSX-4	Cannon Muskegon single crystal 4 (2^{nd} generation Ni-based superalloy)
CSSC	Cyclic stress-strain curve
CT	Computer tomography
CTE	Coefficient of thermal expansion
CTOD	Crack tip opening displacement
DCPD	Direct current potential drop
DS	Directional solidification
EBSD	Electron backscatter diffraction
EDM	Electrostatic discharge machining
EDS	Energy dispersive X-ray spectrometry
EPFM	Elastic-plastic fracture mechanics
ESR	Electro-slag remelting
FCC	Face centred cubic
FCGR	Fatigue crack growth rate
FCP	Fatigue crack propagation
FE	Finite element
FEG-SEM	Field emission gun scanning electron microscope
FIB	Focused ion beam
GTU	Gas turbine unit
HCF	High cycle fatigue
HP	High pressure

IR	Interdendritic region
KW	Kear-Wilsdorf (locking mechanism for dislocations)
LCF	Low-cycle fatigue
LEFM	Linear elastic fracture mechanics
NDT	Non-destructive technique
OM	Optical microscope
OP-AA	Oxide polishing acidic aluminium suspension
PDA	Primary dendritic arm
PM	Powder metallurgy
PH	Precipitation hardening
PSB	Persistent slip band
SDA	Secondary dendritic arm
SEI	Secondary electron imaging
SEM	Scanning electron microscope
SENB	Single edge notch bending
SIMS	Secondary ion mass spectrometry
SF	Stacking fault
SFE	Stacking fault energy
SSH	Solid solution hardening
STEM	Scanning transmission electron microscope
SX	Single crystal
TA	Tensile axis
TCP	Topologically closed packed
TEM	Transmission electron microscope
TGO	Thermally grown oxide
VAR	Vacuum arc remelting
VIM	Vacuum induced melting

Chapter 1 Introduction

1.1 Background

Gas turbines comprise the core of conventional power stations. Since their first application in the electricity generation sector 8 decades ago, there have been significant technological advancements that continue to expand the limits of their performance. Developments in aerodynamics, mechanics, fluid dynamics and material engineering have enabled these performance improvements. Gas turbines work on the basis of the Brayton cycle and therefore their power output, as well as their efficiency, greatly rely on high pressure ratios and combustion temperatures. Nowadays, gas turbine inlet temperatures (TIT) are reaching 1600°C [1] while components such as turbine blades are subjected to high centrifugal stresses. As such, the performance of the gas turbine unit (GTU) is directly related to the ability of these components to operate safely under these stringent conditions.

These demanding environments unavoidably degrade the performance of turbine blades typically through the mechanisms of fatigue, creep, oxidation and hot corrosion. Material science and engineering developments in turbine blades are constantly working towards preventing these types of failure whilst allowing higher TIT. Considerable research is therefore being conducted to develop alloy compositions, heat treatment techniques and advanced manufacturing processes, to optimise service performance. Single crystals of nickel based superalloys are widely used in turbine blade applications due to their excellent combination of properties such as: high strength at elevated temperature, good resistance to fatigue, creep, oxidation and corrosion. The blades are investment cast in hollow complex shapes with internal air passages and are typically coated with thermal barrier coatings (TBC). The air passages are used to cool the blades down internally while the coatings offer increased oxidation and hot corrosion resistance. In addition, the blades are typically cast in final form with the longitudinal axis along the <001> crystallographic orientation. This direction coincides with the minimum Young's modulus of the anisotropic single crystal Ni-based superalloys and thus minimises the thermal stresses associated with the thermal strains from the turbine's start-ups and shut-downs, providing higher thermal fatigue resistance [2]. However, the overall complex shape of the blade leads to complex stress states that can initiate cracks in crystallographic directions other than the <001> direction. In addition, the incorporation of cooling passages and TBCs influence the temperature gradients across the entire component and even though the majority of blade life problems are encountered in the hottest parts, the aforementioned

complex stress states and localised stress raisers combined with the large temperature gradients may lead to less predictable failures at lower temperature regions.

Oxidation and hot corrosion are two of the main mechanisms that cause degradation of the alloys' performance. Once more, these mechanisms are more severe in the hottest sections of the blade which are generally protected by TBCs. However, considering that stresses can significantly influence oxidation processes [3] and that the internal cooling passages and the fir tree root are typically left uncoated, the significance of the problem also extends to the cooler sections of the blade.

Nowadays, the demand for a more variable output, required to match the variations in the power supply levels from other sources (e.g. renewables with seasonal output which are also connected to the electricity supply network) has increased the number of part-load cycles, producing complex, detrimental, cyclic loadings even at low to moderate temperatures. It is therefore important to examine the fatigue failure mechanisms at these temperatures, investigate the effect of environment and understand the synergies between the two. To date there has been little focus on these combined failure regimes at moderate temperatures.

1.2 Industrial Motivation

The durability and life management of hot gas path components has always been of primary interest to the gas turbine industry. During start-ups and shut downs, high value components, such as the turbine blades, are subjected to cyclic mechanical and thermal stresses. To monitor the condition of these safety critical parts, non-destructive testing (NDT) is carried out routinely during maintenance inspections to identify and monitor defects. A range of refurbishment activities are then undertaken to ensure the performance and integrity of the turbine blade during the next operational cycle. A typical maintenance outage takes several weeks, and for large ~GW power stations the cost in lost generation over this period is substantial. Considering the coal-fired power plants currently operating in the UK, the majority of them have been commissioned in the 1960s and have already undergone thousands of start-ups/shut-downs. The monitoring requirements for the ageing fleet are therefore becoming even more stringent, adding to the overall operating costs. It is estimated that nearly 2/3 of the maintenance costs are attributed to the repair and replacement of hot gas path components. In addition, the UK plans to phase out coal-fired power stations by 2025 [4] which gives gas turbine operators a strong incentive to both increase the remaining life and to justify increasing the time between necessary maintenance intervals.

In order to optimise maintenance scheduling and determine the useful lifetime of such components, a substantial effort is put in the development of damage tolerant, life assessment methods. However the complexity and the synergies between the damage processes that take place during operation make this a complex problem. The development of these damage processes and characterisation of their synergistic effects defines the scope of this study. Specifically, this work focuses on the synergistic effects of fatigue and *intermediate service temperature* oxidation on the lifetime of single crystal turbine blades and represents a contribution to the development of physics based lifing models with a view to improving life cycle efficiency and reducing operator cost.

1.3 Project scope and thesis structure

This study aims to assess and understand the damage processes that take place during fatigue at intermediate service temperatures (450°C-550°C) in an attempt to contribute to the development of more comprehensive life assessment methods for gas turbine blades. The following broad objectives have been set:

i. Characterise the oxidation behaviour of typical turbine blade material under service-relevant conditions at intermediate to low service temperatures.
ii. Assess fatigue crack initiation and early propagation mechanisms in typical, single crystal nickel based superalloys at intermediate to low service temperatures.
iii. Investigate the fatigue crack propagation behaviour in an oxidising environment representative of service relevant conditions.
iv. Explain the synergies between the fatigue and oxidation at intermediate to low service temperatures, and the corresponding implications for blade lifing.

This thesis is divided into 3 main sections.

Background

The first part includes the remainder of Chapter 1 and the literature review of Chapter 2. The literature review aims to develop the overall technical and theoretical background governing the subject. In turn, Chapter 2 is divided in three sections. The first section considers fatigue and summarises the existing knowledge in the field and the second investigates high temperature oxidation of metallic components. The third section introduces Ni-based superalloys and includes sub-sections considering fatigue and oxidation damage processes specifically for these material systems. A final subsection discusses current lifing approaches that are applicable to single crystal Ni-based superalloy materials. Whilst the bulk of the literature review is covered in Chapter 2,

more specific elements that address critical gaps in current understanding are included in the introduction and discussion sections of Chapters 4-6 to support the thesis narrative.

Experimental Work

Chapters 3-6 represent the bulk of the experimental work. Chapter 3 presents the materials used in this study and characterises microstructural features and some basic mechanical properties. Chapter 4 considers the oxidation performance and addresses the effects of externally applied loads on the oxidation behaviour. In Chapter 5 the fatigue life and fatigue crack initiation mechanisms under the effect of intermediate temperature oxidation are discussed. Chapter 6 expands on the knowledge obtained from the previous chapters and investigates how intermediate temperature oxidation affects fatigue crack propagation by focusing on the mechanisms acting at the crack tip.

Conclusions and Further Work

The final part of the thesis includes Chapter 7 to Chapter 9. Chapter 7 presents a general discussion that expands on the findings of the thesis and focuses on the implications on lifing approaches. Chapter 8 summarises the main findings and Chapter 9 presents recommendations for further work based on the results of this study.

The structure of the thesis (excluding the introductory Chapters 1 and 2) is illustrated in the process flow diagram of Figure 1.1, which is divided into four sections. Starting from the left, the four experimental packages are outlined. Each experimental package links to a methodology from which the results are derived. The final section of the diagram illustrates how certain results link and contribute towards the aims of the project.

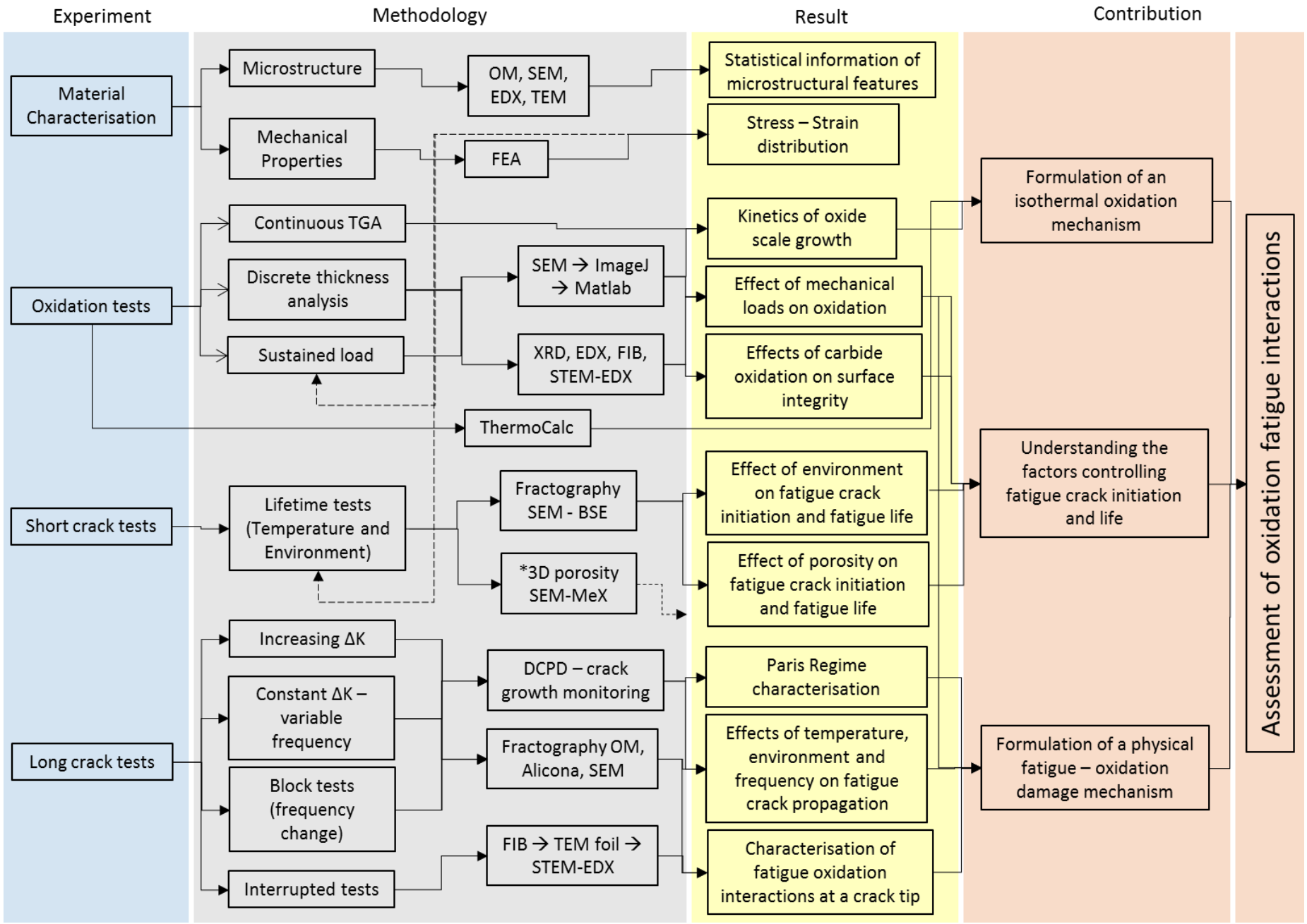

Figure 1.1: Process flow diagram of the thesis outlining the experimental work and the route followed to achieve the aims.
Boxes marked with asterisc (*) imply on going work which is described in Chapter 9 – Future work.

Chapter 2 Literature review

2.1 Fatigue of metallic materials

Fatigue, in the context of metallic components, is most commonly defined as the failure mode which occurs under the influence of cyclic loads whose peak values are lower than the yield strength of the material. Fatigue failure can be affected by various parameters and occurs in many forms. The material's microstructure and geometry, the loading conditions and the environmental conditions are some of the main factors that control fatigue failure. Cyclic loading at high temperature can lead to *creep-fatigue* or *thermo-mechanical fatigue* when the temperature fluctuates as well. Operation in a chemically aggressive environment can result in what is known as *corrosion-fatigue* failure. When sliding or rolling contact is involved with cyclic loading it can result in *sliding or contact fatigue*. Lastly, *fretting fatigue* refers to the failure that occurs as a result of pulsating stresses in conjunction with frictional sliding between surfaces. Overall, it is believed that approximately 80-90% of the failures in non-static structural components are attributed to one of the above fatigue failures.

Fatigue life is generally characterised by considering individual stages of the damage caused to the component. These stages of fatigue damage can be broadly classified into the following [5]

i. Sub-structural and microstructural changes which cause nucleation of permanent damage.
ii. The creation of microscopic flaws/cracks.
iii. The growth and coalescence of microscopic flaws to form 'dominant' cracks.
iv. Stable propagation of the dominant crack.
v. Structural instability or complete fracture.

The features of a fatigue loading cycle can be described by considering the simple case of a sinusoidal load, as shown in Figure 2.1. The parameters that are typically used in the description are the mean stress or strain and the corresponding amplitudes, ranges and ratios. These are defined in the following equations.

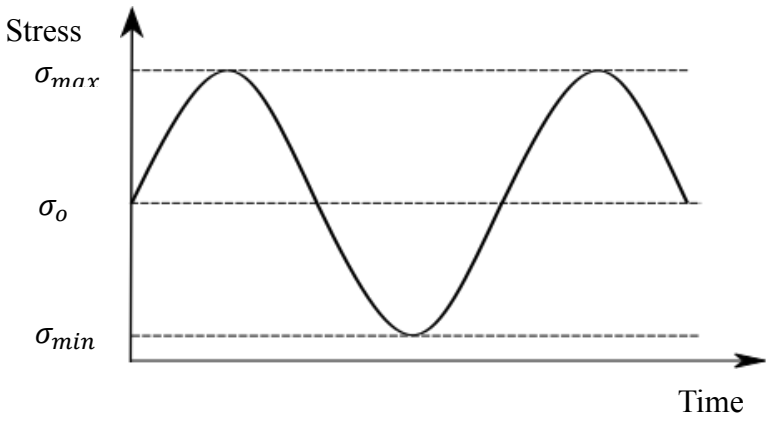

Figure 2.1: Schematic of a typical fatigue cycle under sinusoidal loading

	Stress		**Strain**	
Mean	$\sigma_o = \frac{\sigma_{max} + \sigma_{min}}{2}$	(2.1a)	$\varepsilon_o = \frac{\varepsilon_{max} + \varepsilon_{min}}{2}$	(2.1b)
Amplitude	$\sigma_{amp} = \frac{\sigma_{max} - \sigma_{min}}{2}$	(2.2a)	$\varepsilon_{amp} = \frac{\varepsilon_{max} - \varepsilon_{min}}{2}$	(2.2b)
Range	$\Delta\sigma = \sigma_{max} - \sigma_{min}$	(2.3a)	$\Delta\varepsilon = \varepsilon_{max} - \varepsilon_{min}$	(2.3b)
Ratio (load/strain)	$R_\sigma = \frac{\sigma_{min}}{\sigma_{max}}$	(2.4a)	$R_\varepsilon = \frac{\varepsilon_{min}}{\varepsilon_{max}}$	(2.4b)

The various stages of fatigue and other important concepts in the established fatigue literature that are discussed in the following sections are mainly based on the review work by Suresh [5] unless otherwise referenced.

2.1.1 Fatigue Life Approaches

One of the main challenges in the development of accurate fatigue life prediction models is associated with the quantitative definition of the different stages and especially of crack initiation. The two main approaches to fatigue are outlined in the following sections.

2.1.2 Total Life Approach

The first approaches taken to evaluate the fatigue performance of a material involved the characterisation of the total time to failure (fatigue life) in terms of the cyclic stress or strain range. This is known as the S-N curve approach. An S-N curve describes the relation between the applied cyclic stress or strain (S) with the number of cycles (N) to failure of the component (Figure 2.2). Underpinning the total life approach, both stress-life and strain-life approaches are usually

employed to characterise the total fatigue life. The stress-life is typically employed in situations where low amplitude (and typically high frequency) stresses induce primarily elastic deformation in a component; normally known as high cycle fatigue (HCF) situations. With this approach, the concept of fatigue or endurance limit was also introduced (Figure 2.2). The fatigue limit refers to a stress amplitude value below which a material (with no defects) is expected to have an infinite fatigue life. This limit however, does not exist in all materials, particularly in FCC metals where glide of dislocation is easier. In the case of alloys, if strain ageing (due to pin down of dislocations by solute atoms) is possible, a fatigue limit will exist.

In contrast, when considerable plastic deformation results from cyclic loading (typically high stress amplitudes and often low frequencies) the strain-life approach is adopted. These conditions are known as low cycle fatigue (LCF).

The linearization of the S-N curve through the application of logarithms led to the development of an expression for fatigue life based on the stress amplitude (Basquin 1910):

$$\frac{\Delta\sigma}{2} = \sigma_{\alpha} = \acute{\sigma_{\mathrm{f}}}(2\mathrm{N_f})^{\beta} \qquad (2.5)$$

where σ'_f is the fatigue strength coefficient, N_f are the cycles to failure and β is the fatigue strength exponent.

On a similar basis as the stress-life equation, Coffin and Manson linearised the strain-life S-N plot and developed an expression for the plastic strain and cycles to failure, which is known as the Coffin-Manson equation:

$$\frac{\Delta\varepsilon_{\mathrm{p}}}{2} = \varepsilon_{\alpha_p} = \acute{\varepsilon_{\mathrm{f}}}(2\mathrm{N_f})^{\mathrm{c}} \qquad (2.6)$$

where ε'_f is the fatigue ductility coefficient, and c the fatigue ductility exponent.

The total strain amplitude ($\Delta\varepsilon/2$) (in a constant strain amplitude test) can be expressed as the sum of the elastic strain amplitude ($\Delta\varepsilon_e/2$) and plastic strain amplitude ($\Delta\varepsilon_p/2$) i.e.:

$$\frac{\Delta\varepsilon}{2} = \frac{\Delta\varepsilon_{\mathrm{e}}}{2} + \frac{\Delta\varepsilon_{\mathrm{p}}}{2} \qquad (2.7)$$

By noting that the elastic strain of a component in terms of its Young's Modulus (E) is given by:

$$\frac{\Delta\varepsilon_{\mathrm{e}}}{2} = \frac{\Delta\sigma}{2\mathrm{E}} = \frac{\sigma_{\alpha}}{\mathrm{E}} \qquad (2.8)$$

and by using the Basquin and Coffin-Manson equation the total strain amplitude (elastic and plastic) can be expressed as:

$$\frac{\Delta\varepsilon}{2} = \frac{\acute{\sigma}_f(2N_f)^{\beta}}{E} + \acute{\varepsilon}_f(2N_f)^{c} \qquad (2.9)$$

This equation was later modified by Morrow (1965) to incorporate the detrimental effects of mean load (σ_o):

$$\frac{\Delta\varepsilon}{2} = \frac{(\acute{\sigma}_f - \sigma_o)(2N_f)^{\beta}}{E} + \acute{\varepsilon}_f(2N_f)^{c} \qquad (2.10)$$

The above equation comprises the basis of the strain-life approach and has found widespread application particularly in components that undergo localised plastic flow.

In general, total life approaches define the fatigue life as the total number of cycles required to induce fatigue damage and to initiate a dominant crack. Such conservative approaches are extremely useful when crack initiation is the main design concern but are unreliable when crack propagation life needs to be considered.

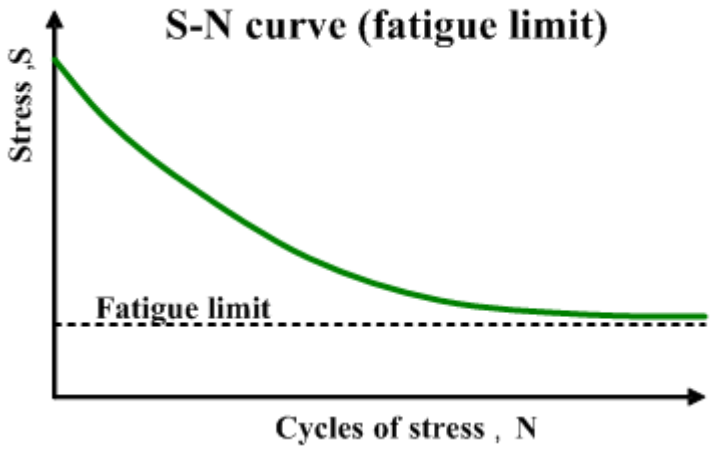

Figure 2.2: A typical S-N curve [6].

2.1.3 Damage Tolerant Approach

The principle by which this approach works is that all engineering components are likely to contain an existing defect. The size of the defect is typically determined from NDT such as visual

inspection, dye penetrant, X-ray and ultrasonic techniques. In the case where no cracks/defects are detected by NDTs the flaw size is derived from the resolution of the technique employed for the inspection. The safe fatigue life is then defined as the number of cycles taken until the initial flaw size (a_o) reaches a critical value (a_c). The calculation of the critical flaw size at any given point may be based on the fracture toughness of the material, the limit load, the allowable strain or the acceptable change in the compliance of the component. The characterisation of fatigue life on the basis of the defect tolerant approach can be successfully evaluated through fracture mechanics. In particular the theories of linear elastic fracture mechanics (LEFM) and elastic-plastic fracture mechanics (EPFM) are widely employed to describe the crack driving force.

Theories regarding fracture from the extension of cracks have been initially developed by Griffith [7] and Orowan [8] on the basis of a global energy balance approach. The critical conditions for crack growth can also be described through the theory of elastic fracture mechanics in terms of local stress distribution at the crack tip. However, before considering the variation of stress field around cracks however, one needs to consider the different modes of crack opening. As shown in Figure 2.3 there are three fundamental crack-opening modes:

- Mode I: The tensile opening mode in which the loads are applied perpendicular to the surfaces and cause them to move vertically away from the crack plane.
- Mode II: The in-plane shearing or sliding mode in which the loads are applied normal to the crack front, in opposite directions (push-pull).
- Mode III: The tearing or anti-plane shear mode, in which the loads are applied parallel to the crack front.

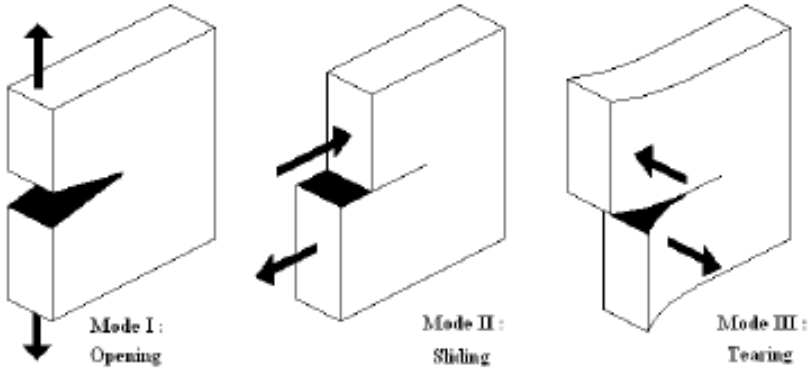

Figure 2.3: Crack opening modes [9].

The local stresses at any (r, θ) coordinates close to the crack tip in a component subjected to a mode I type of loading (Figure 2.4) can be described mathematically by the following equations:

$$\sigma_{xx} = \frac{K_I}{\sqrt{2\pi r}}[\cos\frac{\theta}{2}(1 - \sin\frac{\theta}{2}\cos\frac{3\theta}{2})] \quad (2.11a)$$

$$\sigma_{yy} = \frac{K_I}{\sqrt{2\pi r}}[\cos\frac{\theta}{2}(1 + \sin\frac{\theta}{2}\cos\frac{3\theta}{2})] \quad (2.11b)$$

$$\sigma_{zz} = \frac{K_I}{\sqrt{2\pi r}}[\cos\frac{\theta}{2}\sin\frac{\theta}{2}\cos\frac{3\theta}{2}] \quad (2.11c)$$

Where K_I is the stress intensity factor for mode I loading and is defined in terms of the applied (far-field) stress (σ) and flaw length (a) as:

$$K = \sigma\sqrt{\pi a} \cdot f(\frac{a}{W}) \quad (2.12)$$

where $f(\frac{a}{W})$ is the compliance function which accounts for differing component geometries and shapes. The stress intensity factor is a measure of the magnitude of the stress field close to the crack tip under linear elastic conditions.

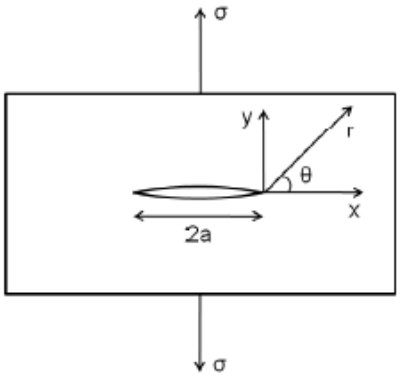

Figure 2.4: Crack in a thin elastic plate under mode I loading [9].

The near crack area at which the stress field can be satisfactorily described by K is known as the "region of K-dominance". This region is an annular zone whose outer radius is defined as the point where the asymptotic solutions of the above equations deviate significantly (an approximate value of 10% is given by Suresh S. [5]) from the solution of the fully elastic equation (T-term and other non-singular terms included). Additionally, real materials when subjected to loading exhibit plastic yielding at the crack tip to relieve and redistribute the stresses. This invalidates the basis of linear elastic fracture mechanics. Therefore, the inner radius of the K-dominance region can be defined as the point where the near tip plastic zone ceases. The plastic zone and the K-dominance region are shown schematically in Figure 2.5. Nevertheless, it is generally accepted that as long as the

plastic zone is significantly smaller than the specimen size and the crack length (typically less than $1/50^{th}$ [5]), the region of K-dominance controls the behaviour of the crack.

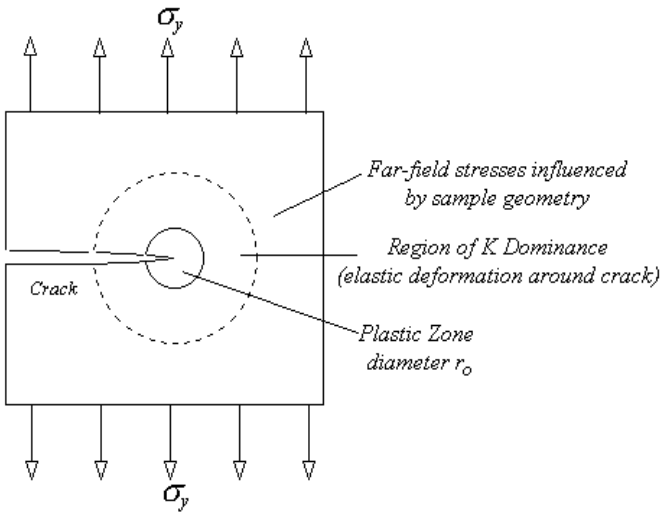

Figure 2.5: Schematic of the plastic and K-dominance zones [10].

The ability of a material containing a crack to resist fracture is characterised by a critical value of the stress intensity factor (K_c). This value is a function of the mode of loading, environment, material microstructure, strain rate, stress state (plane stress or strain) and the temperature. Under plane strain conditions K_c is known as the fracture toughness of the material at the specific environment. Depending on the mode of loading, K_c is given the analogous subscript; K_I, K_{II} or K_{III}.

In the case of fatigue loading, the crack growth behaviour is described by the stress intensity factor range ($\Delta K=K_{max}-K_{min}$) obtained from the applied stress range ($\Delta\sigma=\sigma_{max}-\sigma_{min}$). Such crack propagation data is typically obtained from test samples of the material containing a pre-existing, relatively large, defect of known dimensions. By plotting the crack growth rate (da/dN) against ΔK on a log-log plot, a sigmoidal relationship divided into three distinct regions is typically produced (Figure 2.6). Region A is characterised by low ΔK values and almost negligible crack growth rates. However, the crack growth rate is observed to increase rapidly with small changes in ΔK. A threshold value of stress intensity factor (ΔK_{th}) represents the smallest driving force to attain a detectable crack growth rate. Region B exhibits a steady crack growth rate and is governed by the Paris law:

$$\frac{da}{dN} = C\Delta K^m \qquad (2.13)$$

Where *C* and *m* are empirical constants which are functions of the material properties, loading frequency, mean stress, load ratio, environment, loading mode, stress state and temperature.

Finally, in region C the material approaches its fracture toughness (K_c) and the crack growth rate increases rapidly. This regime is heavily influenced by the microstructure and mean stress levels, but it only applies for relatively few cycles, thereby its contribution towards the overall fatigue lifetime is generally considered to be of minor importance in most service applications.

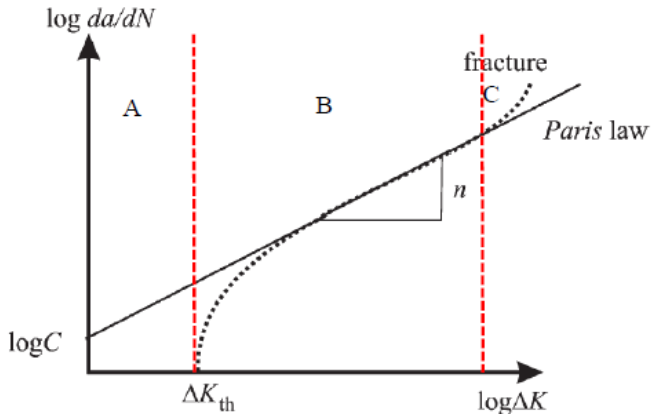

Figure 2.6: Crack growth rate (da/dN) against stress intensity factor (ΔK) diagram illustrating the three different propagation regimes [11].

2.1.4 Cyclic Deformation Behaviour

As mentioned in an earlier section, the fatigue life can be generally categorised into (i) crack initiation (ii) growth and propagation of cracks and (iii) final catastrophic failure. However, when the whole fatigue process is considered, cyclic plastic deformation prior to crack initiation should also be taken into account. Cyclic loading causes changes in the structure of a material and depending on the materials initial state, mean stress, load ratio, temperature, environment and frequency it can cause hardening, softening or stabilised behaviour. The intensity of the cyclic hardening/softening processes decreases with time (number of cycles) until a saturation point is reached where no more changes to the properties of the material are induced [12]. The reason that metallic materials harden or soften during cyclic straining is related to the nature and stability of the dislocation substructures and depends on the temperature and strain amplitude [13]. In general two conditions may apply:

1. For a soft material (e.g. after an annealing heat treatment) the initial dislocation density is low, and during cyclic plastic straining, it increases rapidly. This increase in dislocation density causes a cycle dependent strengthening termed cyclic hardening. In precipitate strengthened alloys cyclic softening is associated with extensive precipitate shearing.
2. For a hard material (e.g. cold worked), the initial dislocation density is high, and during cyclic straining the rearrangement and annihilation of dislocation substructures causes the

overall dislocation density to decrease. This decrease in dislocation density causes a cycle dependent loss of strength termed cyclic softening.

Therefore, it is typical in some materials that the first stage of the fatigue process starts with cyclic hardening followed by cyclic softening (or vice-versa). The hardening/softening deformation process of a material can be quantitatively described in terms of its stress-strain response. For either type of material, the cyclic stress or strain amplitude often saturates after a number of cycles. This stable cyclic behaviour of metals is described in terms of a stress-strain hysteresis loop, as shown in Figure 2.7a.

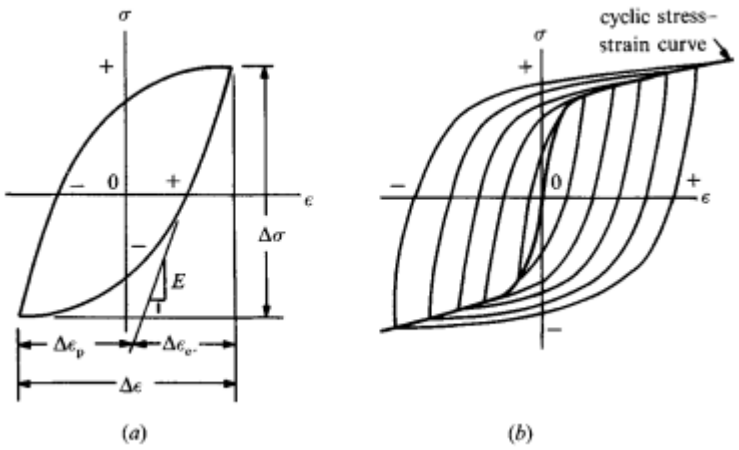

Figure 2.7: a) Schematic of typical hysteresis loop where $\Delta\varepsilon_p$, $\Delta\varepsilon_e$, $\Delta\sigma$ and E are the plastic strain range, elastic strain range, stress range and elastic modulus, b) Schematinc definition of cyclic stress strain curve [5].

For different stress or strain amplitudes different hysteresis loops can be produced. The curve connecting the peak stress or strain values of these saturated hysteresis loops is known as the cyclic stress strain curve (CSS curve) of the material [12]. The CSS curve is generally considered a very important fatigue characteristic as it describes the stress-strain relation of the loaded material for a substantial part of the overall fatigue life. There are important differences between the cyclic deformation behaviour between single crystal and polycrystalline material. These arise from the different orientations of the individual grains within the polycrystalline material. The applied resolved shear stress responsible for slip (and hence deformation) varies between grains. Since the material of this study is a face-centred cubic (FCC) single crystal, the following section will focus on the deformation mechanisms of single crystals.

2.1.4.1 Cyclic Deformation of Single Crystals

Deformation of single crystals is characterised in terms of the resolved shear stress (τ_R) and strain (γ_R) acting on a specific slip system. Consider a cylindrical single crystal specimen of cross

sectional area (*A*), subjected to uniaxial tensile load (*P*) (Figure 2.8). The angles of the slip plane vector, ***n*** and of the slip direction ***b*** with respect to the loading axis are φ_o and λ_o respectively. The corresponding initial stress resulting from the applied load is given by:

$$\tau_{R_O} = \frac{P}{A}\cos\varphi_o \sin\lambda_o = \sigma\cos\varphi_o \sin\lambda_o \qquad (2.14)$$

The condition for the onset of plastic deformation is described by the Schmid Law which states that a crystalline solid flows plastically when the resolved shear stress (τ_{Ro}) acting along the slip direction in the slip plane reaches a critical value (τ_c).

$$\tau_c = \sigma\cos\varphi_o \sin\lambda_o = M\sigma \qquad (2.15)$$

,where *M* is the Schmid factor and has a maximum value of 0.5 which corresponds to the orientation $\varphi_o = \lambda_o = 45^o$

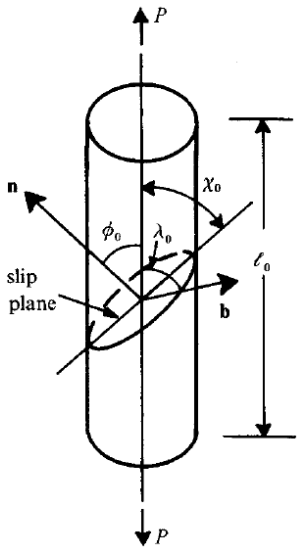

Figure 2.8 Schematic representation of a single crystal cylindrical sample under uniaxial loading [5].

2.1.5 Fatigue Crack Initiation

Crack initiation is broadly defined as the process by which microscopic cracks outside the detectable limits of conventional microscopes are formed. The main sites that fatigue cracks have been reported to initiate are at or near singularities on or just below the surfaces of metals. Such singularities may be inclusions, pores, grain boundaries, sharp scratches, pits and slip bands [14].

Crack initiation at a surface is closely related with surface roughening associated with cyclic plastic deformation. The slip irreversibility along persistent slip bands (PSB) causes protrusions and

intrusions on the surface (Figure 2.9) which, in turn cause a microscopic stress concentration effect. These local stress concentration features further promote slip and hence greater stress concentrations and eventually fatigue crack initiation.

At elevated temperatures, subsurface nucleation has been observed in metals and alloys having a strong adherent surface oxide, which retards crack initiation at the external surface [9,14]. On the other hand, the accelerated diffusion of various species in the material, promotes oxidation of grain boundaries and precipitates and in the case of alloys, the subsequent depletion of oxidising elements near the surface degrades the material's mechanical properties. In addition, the brittle cracking of oxidizing products can by itself contribute to fatigue crack initiation. Thermally grown oxide (TGO) scales may initiate cracks by penetrating the substrate and causing embrittlement.

Creep is the second key factor determining the service life of high-temperature materials. Crack initiation during creep may be caused by the formation of cavities or triple lines at grain boundaries due to the combination of grain boundary sliding and vacancy diffusion towards areas of high hydrostatic tension [11].

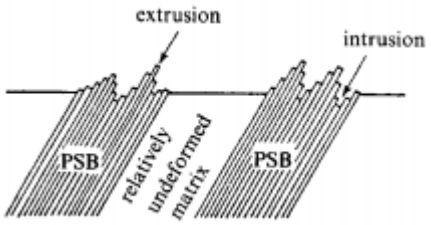

Figure 2.9: Schematic showing a rough surface caused by irreversible slip bands [5].

2.1.6 Fatigue Crack Growth

2.1.6.1 Long Crack Growth Behaviour

The process of fatigue crack growth is controlled by the localised deformation at the crack tip. The behaviour of the growth is generally influenced by the slip characteristics of the material, the characteristic microstructural dimensions, the applied stress level, the size of the plastic zone at the crack tip and the environment. There are three distinct fatigue propagation modes which can also be generally linked to the three regimes of the da/dN versus ΔK behaviour shown in Figure 2.6. These are briefly discussed below.

Stage I crack growth:

This mode of propagation is typically observed at low ΔK levels when the crack and the plastic deformation zone are within a few grain diameters (or a characteristic microstructural dimension). When this is true, the crack propagates by a single shear in the direction of the primary slip system.

This mechanism is characterised by a zig-zag path that creates faceted fracture surfaces and it is often referred to as a crystallographic growth mechanism (Figure 2.10).

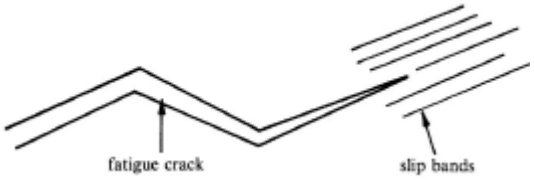

Figure 2.10: Schematic representation of the zig-zag crack path of stage I [5].

Stage II crack growth:

At higher ΔK levels the plastic zone size becomes larger than "a few grain diameters" and the crack growth mode changes to stage II. The crack in this stage alternates or follows simultaneously two slip systems and grows normal to the far field tensile axis (Figure 2.11). When the fracture surface of this stage is examined microscopic parallel ridges called "striations" may be observed to follow the crack front. In the Paris regime of crack propagation, it was found that the distance between adjacent striations can represent one fatigue cycle. Striations are not always visible and are strongly dependent on the ΔK level, stress state, environment and alloy content [5] but they have been previously found in single crystal nickel based superalloys during high temperature fatigue testing [15]. Stage II propagation is also known to be promoted during fatigue at elevated temperature in Ni-based superalloys (this will be discussed further in the relevant results section - 6.3.1)

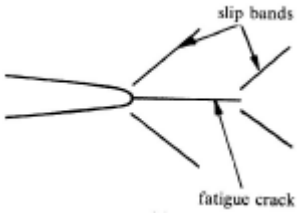

Figure 2.11: Schematic of idealised propagation under stage II mode with alternating slip bands forming ahead of the crack tip [5].

Stage III crack growth:

As the value of K_{max} approaches the fracture toughness of the material the crack propagates in an unstable manner at very high rates. The stage III behaviour is sensitive to the microstructure, the load ratio and stress state. The fracture surface is fibrous, rough and has an irregular morphology with evidence of plastic deformation often visible. Stage III crack growth corresponds to the shortest proportion of the lifetime of a component.

2.1.6.2 Short Crack Growth Behaviour

Fatigue cracks of different dimensions behave differently when subjected to similar driving forces. It is well known that the growth rates of small cracks can be significantly higher than the corresponding growth rates of long cracks. For engineering components such as turbine discs and blades whose operation is safety critical, understanding the behaviour of small flaws is vital as a large part of their useful fatigue life is spent in the short crack growth phase. Before discussing the behaviour of such cracks it is important to define them. A number of short crack definitions are clearly outlined by Suresh [5] as follows.

- *Microstructurally short cracks*, where the crack length is comparable to a characteristic microstructural dimension such as grain size in monolithic materials.
- *Mechanically short cracks*: i) for smooth specimens, when the crack length is comparable to the crack tip plastic zone, or ii) for notched specimens, cracks that are engulfed by the plastic strain field of a notch.
- *Physically short cracks*, which may be larger than any microstructural dimension or plastic zones, but small in relation to the size of the component in which they have occurred (typically <2mm).
- *Chemically short cracks*, which are nominally amenable to LEFM analyses, but exhibit apparent anomalies in the propagation rates below a certain crack size as a consequence of the dependence of environmental stress corrosion fatigue effects on crack dimensions.

As mentioned in section 2.1.3, within the K-dominance zone, there is a plastic zone region around the crack tip where the LEFM does not hold. It is evident then, that mechanically short cracks in particular cannot be characterised by ΔK. In this case elastic-plastic fracture mechanics and the use of the ΔJ parameter has been previously shown to produce valid results [16]. The reasons for the anomalous growth behaviour of small cracks was summarised by D. Taylor [17]. These include, i) influence of microstructure; grain boundaries and second phase particles act as obstacles that retard or arrest the growth of small cracks), ii) closure effects; since plasticity induced crack closure depends on the size of the plastic zone's wake behind the crack tip, for a small crack the effect is expected to be minimised, iii) K-estimation errors; difficulties related to the accurate calculation of the stress distribution of sharp small crack, iv) crack deflection; this tends to lower the effective K value and v) constraint of the crack; a small crack at the free surface is essentially within the surface plane stress field until it penetrates into the plane strain field of the material where different growth rates are induced.

2.1.7 Shielding effects and closure

Crack propagation rates can be significantly affected by shielding effects, due to premature contact between the cracked surfaces behind the crack tip, such that the minimum K applied is not experienced at the crack tip. The closure effects may arise from a variety of factors including, environmental, mechanical and microstructural. The main mechanisms that can cause contact between the surfaces of a metallic material are briefly described below [5],[18].

Plasticity induced closure

The mechanism governing plasticity induced closure depends on whether a plane strain or a plane stress condition is prevailing. Under plane stress conditions the material in the plastic zone is elongated parallel to the stress axis (and experiences a reduction in thickness). As the crack propagates through the plastic zone, the stretched volume of material in the wake comes into contact acting as a wedge. In plain strain conditions where out of plane flow of material is not possible, wedging results from plastically sheared material at the wake of the tip.

Oxide induced closure

The oxidation of metals and alloys is typically accompanied by a volume increase. Hence, oxidation of the fracture surfaces at the vicinity of the crack tip can lead to premature contact of the crack faces after unloading. This phenomenon is particularly pronounced at higher temperatures, at low R ratios and generally low crack growth rates (i.e. near threshold) where sufficient time is allowed for the development of thick oxides.

Roughness induced closure

This type of closure is dependent on the roughness profile of the fracture surfaces. In turn, the roughness profile is influenced by the material's microstructure such as the grain size and the crystallographic misorientation. Specifically in the case of single crystal alloys, roughness induced crack closure is prominent during stage I crack growth and is affected by the number of active slip systems. The highly faceted mode of propagation associated with Stage I growth combined with local mixed modality (due to microstructural anisotropy and inhomogeneity near the crack) can lead to premature contact before the sample is unloaded. In general, any mismatch in the roughened surface profile (also due to irreversible shear for example) will cause premature contact as the crack tries to propagate.

All these shielding effects cause retardation of the crack propagation at a stress intensity factor ($K_{closure}$) greater than the minimum stress intensity factor (K_{min}). Therefore, the crack tip actually experiences an effective ΔK less than the one applied/expected.

2.2 High Temperature Oxidation

Within the gas turbine industry, oxidation refers to the reaction of an alloy with oxygen in an environment free of contaminants such as sodium, sulphur and vanadium [19]. Degradation by oxidation is reported to be one of the main failure modes in the hot components of a gas turbine unit. The oxidation process of alloys is often complex as individual elements behave and interact differently. It is of vital importance therefore to understand the basic processes that occur during oxidation before discussing oxidation in Ni-based superalloys (which is covered in sections 2.4.1 of the literature review and in Chapter 3 in further discussion of the results of this thesis)

The oxidation process can be outlined as below [20,21]:

1) Starting with a clean metal surface, the very first step of the process is the adsorption (chemisorption or physical adsorption) of oxygen atoms on the alloy.
2) The reacting oxygen creates a thin initial metal oxide layer.
3) The diffusion of metal cations (positively charged ions) to the surface of the metal oxide scale increases the oxide scale thickness.
4) Oxygen diffuses into the metal through the growing oxide scale - internal oxidation
5) Microcracks are formed in the base metal and/or in the growing oxide scale due to microstructural changes causing stress concentration sites.
6) Microcracks coalesce to form visible cracks at or near the base metal and oxide interface. Changes in temperature or additional loading stresses can cause the protective oxide layer to spall, thus resulting in an unprotected area of the base metal.
7) If there are enough reactive elements (like Al and Cr in the case of Ni-based superalloys [22]) left in the alloy close to the surface, the protective oxide scale formation will restart. If these elements are depleted, other elements may preferentially oxidize creating a non-protective scale resulting in mass loss and eventual failure of the material.

To improve hot corrosion and oxidation resistance of the turbine blades there have been several evolutions of alloy compositions. The high temperature oxidation resistance, specifically, is attributed to the incorporation of Cr, Al and Hf within the nickel base, which is itself resistive to oxidation. Resistance to oxidation is achieved by the formation of a protective, adherent oxide layer on the outer surface of the exposed component. The layer should ideally be tightly adhered and non-porous, so it does not spall during thermal cycling and acts as a diffusion barrier preventing oxygen from reaching the substrate. A review study by Reed et al. [23] reported that under isothermal conditions for temperatures lower than 1000^{o}C, in nickel based single crystal superalloys, a NiO layer is formed over an internal oxidation zone composed of firstly Cr-based oxides followed by an inner Al-based oxide layer.

2.2.1 Thermodynamics of Oxidation

Thermodynamic calculations allow understanding of the oxidation driving forces in terms of i) which species tend to oxidise and ii) product stability and volatility [21] [20]. For a constant temperature and pressure the reaction between a metal and a gas (formation of an oxide) can be described by considering the 2nd law of thermodynamics and Gibbs free energy (G), which is given by the equation:

$$\Delta G = \Delta H - T\Delta S \qquad (2.16)$$

where ΔH and ΔS are the enthalpy and entropy change of the system during the reaction and T is the absolute temperature at which the reaction takes place. A positive ΔH represents the case where heat (energy) is taken from the environment (endothermic) while a negative ΔH means that heat is emitted during the reaction (exothermic). In gas turbine applications, even though the temperature at which oxidation occurs is extremely high, the reaction is commonly exothermic.

If $\Delta G < 0$, the reaction will be spontaneous (occurs naturally – no external work), if $\Delta G > 0$, the reaction will be nonspontaneous (the forward reaction requires external work), and if $\Delta G = 0$, the reaction is at equilibrium.

The chemical equation of the oxidation of a metal (M) can be represented as follows:

$$xM + \frac{y}{2}O_2 = M_xO_y \qquad (2.17)$$

,where M_xO_y is the oxidation product and "x" and "y" are the reacting moles.

Based on what is stated above; a chemical reaction will occur if the total free energy of the products is less than the total free energy of the reactants i.e.:

$$\Delta G = G_{products} - G_{reactants} < 0 \qquad (2.18)$$

Under these conditions (oxidation of a metal) the Gibbs free energy equation can be written in the following form:

$$\Delta G = \Delta G^o + RT \ln \left[\frac{\alpha_{metal\ oxide}}{{\alpha_M}^x \times {\alpha_{O_2}}^{y/2}} \right] \quad (2.19)$$

,where ΔG^o is the standard free energy, R is the universal gas constant and "x" and "y" are the reacting moles. "α" is the thermodynamic activity of the reactants or products (describes the deviation from the standard state) and it is defined as:

$$\alpha = \frac{p_i}{p_i^o} \quad (2.20)$$

,where p_i is the partial pressure of the gas and p_i^o is its partial pressure at standard state.

If the reaction reaches a point of equilibrium (ΔG=0), by replacing the oxygen activity with its partial pressure (since it will behave as an ideal gas) the above equation becomes:

$$\Delta G^o = -RT \ln \left[\frac{a_{metal\ oxide}}{{a_M}^x} \times \left(\frac{1}{p_{O_2}} \right)^{\frac{y}{2}} \right]_{equilibrium} \quad (2.21)$$

Assuming that the metal and metal oxides are pure solids it can be deduced that they have already reached their standard state. Therefore their activity is 1 and hence the above equation can be re-written as:

$$\Delta G^o = -RT \ln \left[\left(\frac{1}{p_{O_2}} \right)^{\frac{y}{2}} \right]_{equilibrium} \quad (2.22)$$

$$or \qquad \Delta G^o = -RT \ln k_p \quad (2.23)$$

For equilibrium, the term in the parenthesis can be written as equal to an equilibrium constant - k_p.

Since for oxidation to occur ΔG must be negative, the oxygen partial pressure needs to be greater than the oxygen partial pressure at equilibrium and hence ΔG^o in the above equation must be less than zero. The equilibrium partial pressure (where the driving force of the reaction becomes zero)

can be therefore calculated at a particular temperature from the value of ΔG^o by rearranging the above equation to:

$$p_{O_2 eq} = e^{\left(\frac{\Delta G^o}{RT}\right)} \qquad (2.24)$$

The more negative the standard free energy (ΔG^o) the more stable the oxide is. The standard free energy per mole of oxygen of a reaction as a function of temperature can be plotted to form an Ellingham diagram (Figure 2.12). These diagrams consist of lines of: $\Delta G^o = \Delta H^o - T\Delta S^o$ and can be mainly used to i) determine the relative stability of oxides and ii) determine the oxygen partial pressure at equilibrium (criterion for oxidation to occur)

Although, the free energy change is the driving force of the oxidation process it does not describe the rates of reaction as the most stable oxide does not always become the rate-controlling oxide. This is largely a kinetics problem and is discussed in the following section.

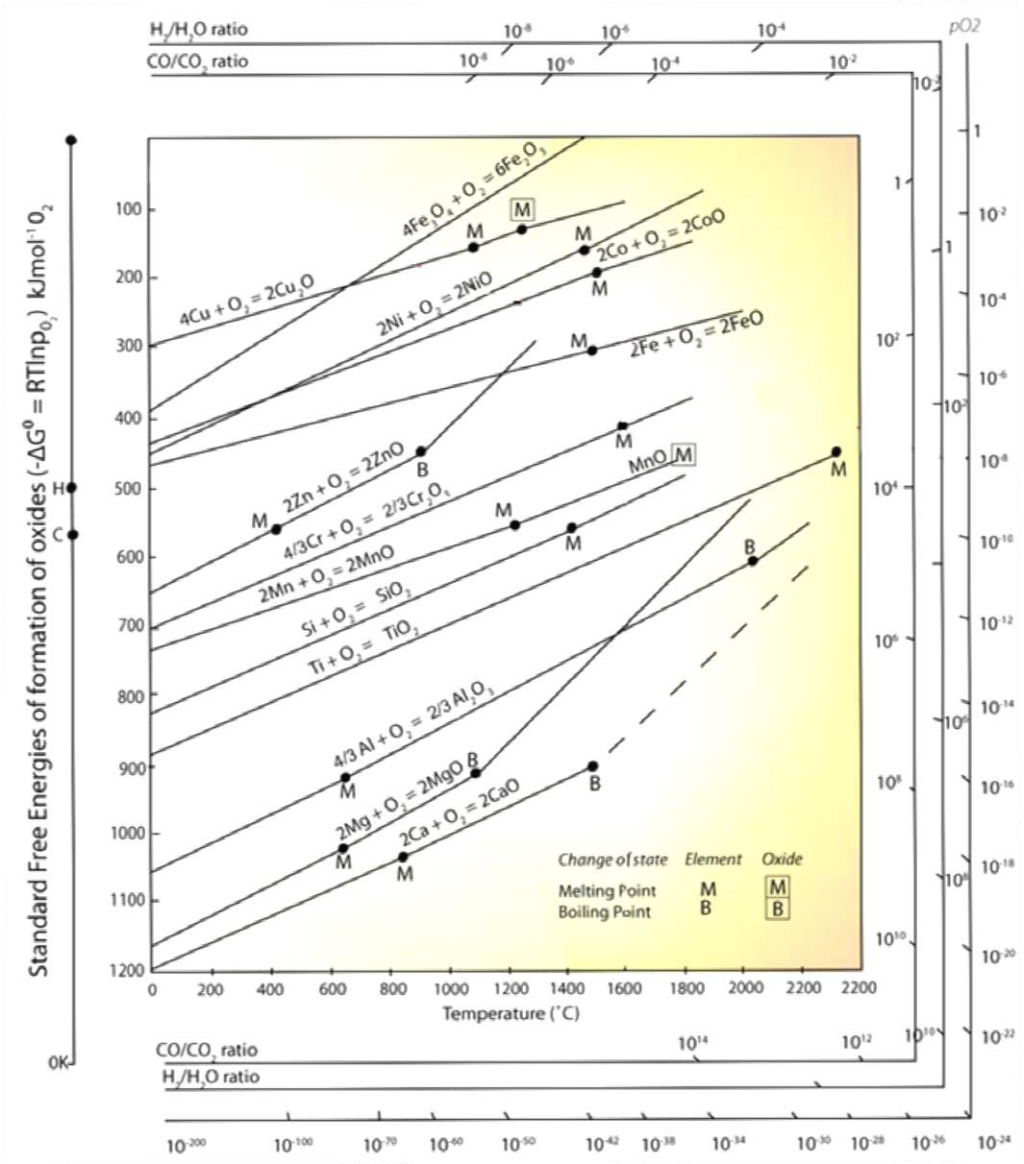

Figure 2.12: Ellingham diagram showing the formation of various oxides at different standard free energies and temperatures [24].

2.2.2 Kinetics of Oxidation

The oxidation reaction described in the previous section can be rate limited by a number of mechanisms. Usually, high temperature oxidation is reported in the literature to be a form of diffusion dependent process which has a parabolic time dependent oxide growth [21,22,25–27]. The parabolic rate equation is given below:

$$\Delta m^2 = k_p t + C \qquad (2.25)$$

where C is the integration constant, Δm the normalised mass change (mg/cm^2), t is the time in hours and k_p is the parabolic rate constant ($\frac{mg^2}{cm^4}/hour$).

The parabolic law is supported by Wagner's theory where the rate limiting mechanism is described as the diffusion of cations and anions through a compact, relatively thick and adherent scale [28]. If however the oxide scale is not defect free (porosity, grain boundaries, dislocations etc.) or has poor adhesion with the metal surface, a form of short-circuit transport contributes to the growth and the bulk parabolic law may not apply as surface diffusion paths become prevalent [29]. Knowledge of the O_2 transport paths is therefore important in understanding and interpreting the oxidation mechanism in hand. A purely parabolic law is rarely observed during actual oxidation testing, making it only applicable to a limited number of pure metals. Therefore, variations in rate laws are often reported in the literature, which include sub-parabolic, linear, logarithmic and inverse logarithmic [21]. Logarithmic and inverse logarithmic rate laws are typically only observed at lower temperatures (generally < 400^{o}C), where the reaction is initially rapid and then levels out. Linear oxidation occurs when a non-protective oxide scale develops, which does not prevent or retard further oxidation. The rate of mass gain is constant with time and it is independent of the metal or gas previously consumed in the reaction. The kinetics of linear oxidation may be described by:

$$\Delta m = k_L t \qquad (2.26)$$

Sub-parabolic oxidation rates can be described as the combination of linear and parabolic behaviours. For example, when the initial oxide that forms is non-protective, a linear trend between mass gain and oxidation time is observed, while later, the formation of a more protective and adherent oxide, shifts the relationship between mass gain and oxidation time to a near parabolic or parabolic [21]. Sub-parabolic kinetics can be described by:

$$t = C + \frac{1}{k_L}(\Delta m) + \frac{1}{k_p}(\Delta m^2) \qquad (2.27)$$

,where C is the integration constant, where if neglected the equation can be rewritten as:

$$\Delta m = k_p \frac{t}{\Delta m} - k_L \qquad (2.28)$$

And thus by plotting Δm against $\frac{t}{\Delta m}$, k_p can be obtained from the slope and k_L by the interception with the vertical axis.

2.2.3 Oxide Scale Spallation – Induced Stress Effects

High temperature oxidation resistance is attributed to the formation of a thick, chemically stable and adherent oxide scale over their surfaces. In the case of Ni-based superalloys such protection is most commonly provided by Cr_2O_3 and Al_2O_3 [23]. Rapid development of a protective oxide is desirable as it minimises further diffusion and oxidation of elements in the substrate. Retention of the protective layer is not however solely dependent on reacting elements. Failure can arise from a number of factors such as fluxing by exposure in a chemically aggressive environment, erosion by particles, fretting and spalling due to induced in plane stresses [21]. Spallation is most commonly understood as the cracking and subsequent decohesion of the scale which results in exposure of the bare alloy underneath. Qualitative and quantitative characterisation of spallation is of great importance as the alloy's useful life can be significantly reduced by the phenomenon. Spalling of the oxide layer generally arises from the generation of compressive stresses within the scale. Tensile stresses within the oxide could also initiate spallation but these are most commonly related to through scale cracking and not decohesion [3]. These can be either termed as growth stresses during isothermal oxidation or thermal stresses which arise during temperature fluctuations as a result of differential thermal expansion/contraction between the alloy and the scale. The effects of induced stresses on the ability of oxides to maintain their mechanical properties and adherence has been previously reviewed in the literature [3,28,30–33].

The mechanism by which spallation can occur, as a result of the aforementioned stresses, depends on the adherence of the compressively stressed oxide scale [3,28]. For failure to occur, the elastic strain energy stored per unit area within the scale must be greater than the fracture resistance (G_c) of the interface. This criterion is described by the equation below:

$$\frac{(1-\nu)\sigma^2 h}{E_{ox}} > G_c \qquad (2.29)$$

,where ν is the Poisson's ratio of the scale, σ is the equal biaxial residual stress in the film, h is the scale thickness and E_{ox} its elastic modulus of the scale.

The above criterion, however, is necessary but not sufficient for failure. Spallation under compression requires either a buckling instability or a wedge crack in order to occur. Failure by buckling arises for scales with poor adhesive strength, which could result from accumulation of voids or by segregation of elements that induce oxides with poor adhesion properties. Buckling of a thin film under biaxial compression to form a buckle of radius a will occur at a critical stress σ_c which is given by:

$$\sigma_c = 1.22 \frac{E}{(1-\nu)} \left(\frac{h}{a}\right)^2 \qquad (2.30)$$

Hence, when the above critical stress is reached a stable buckle will occur. If at the same time the strain energy criterion described earlier also holds, decohesion failure by delamination will take place (Figure 2.13a).

On the other hand, weak oxide scales with high adhesive strength tend to fail by wedging. During wedging, compressive shear cracking causes the initial failure of the oxide which is followed by decohesion of the scale when adjacent shear cracks propagate and meet at the interface between alloy and oxide (Figure 2.13b).

In the case where the fracture resistance is high and the alloy is relatively weak simultaneous deformation of the oxide and alloy interface can occur without spallation (Figure 2.13c).

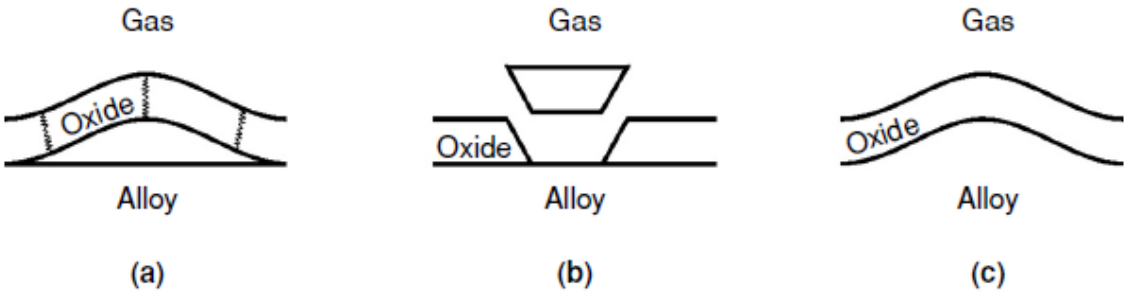

Figure 2.13: Schematic diagram showing the responses of an oxide scale loaded in compression a) Buckling and decohesion b) shear cracking and wedging c) plastic deformation of the oxide and the substrate alloy

2.3 Nickel based Superalloys for Gas Turbine Applications

The term "superalloy" was initially used shortly after World War II to describe a group of metallic alloys with exceptional high temperature mechanical properties. They were primarily developed for aircraft turbine engines that required high performance at elevated temperatures but nowadays their applications range from gas turbine units to nuclear and chemical processing plants [34]. Particularly, superalloys exhibit high strength, high toughness, good corrosion and long fatigue and creep performance at temperatures often in excess of 70% of their absolute melting point [2]. Superalloys are typically based on iron, cobalt or nickel with the latter being the most widely used.

Nickel based superalloys are the material of choice when applications involve significant creep and fatigue loading in conjunction with temperatures in excess of 800^{o}C. This is the case when gas turbine units are used in large electricity production plants. Blades in the early stages of the turbine are typically exposed to temperatures of 1200-1400^{o}C and high fluctuating stresses [2,19]. These more demanding conditions further increase the requirements governing the material selection.

2.3.1 Composition and Microstructure

Nickel is the major element of the superalloy and it typically comprises 60-70% of the total mass. Its melting point is 1455°C and is consequently the absolute temperature capability limit for all Ni-based superalloys. Nickel has a face-centre cubic (FCC) crystal structure which combines toughness and ductility. The foundation of Ni-base superalloy compositions is the binary nickel-aluminium system. By increasing the amount of aluminium added to the γ nickel phase a secondary γ' phase begins to form. However, typically up to 12 elements are combined to form the alloy, each one contributing differently to its high temperature performance. The elemental composition of some widely used nickel-based superalloys are categorised according to their processing in Figure 2.14. Significant amounts of chromium (Cr), cobalt (Co), aluminium (Al) and titanium (Ti) are typically found in most of these alloys. Tungsten (W) is also used as an alloying element in high concentrations, but less often. Amounts of boron (B), carbon (C) and zirconium are often included in smaller quantities. Most modern alloys, especially those cast as single crystals, also contain appreciable quantities of molybdenum (Mo), rhenium (Re), tungsten (W) and tantalum (Ta). The various elemental additions in Ni-base superalloys can be categorized according to the phase they partition to [2,19,35]. Generally, the phases that characterise the microstructure of typical Nickel superalloys are the following:

I. Gamma (γ): This phase forms a continuous matrix that exhibits FCC crystal structure. It is a nickel-based phase with high concentrations of solid-solution elements such as cobalt (Co), chromium (Cr), Molybdenum (Mo), tungsten (W) and rhenium (Re).

II. Gamma prime (γ'): The main elements that form this precipitate (strengthening) phase are aluminium (Al) and titanium (Ti). Other elements such as tantalum (Ta), hafnium (Hf) and niobium (Nb) also contribute to the formation and strengthening of the γ' phase. This coherent $Ni_3(Al,Ti)$ phase has an ordered $L1_2$ (FCC) intermetallic crystal structure [19,36]. The resulting γ' volume fraction is directly related to the amount of Al and Ti present and is typically ~70% for modern alloys. The formation kinetics of γ' are related to the rate at which the alloy is cooled through the solvus temperature. Different cooling rates will result in different distribution and size of the γ' precipitates. It has been previously shown that faster cooling rates result in smaller γ' precipitates with larger γ/γ' interfacial widths [37,38]. At extremely small sizes they are spherical but as their size grows their shape changes to cubes or plates depending on the value of matrix/precipitate (γ/γ') lattice mismatch (δ) [35,39]. Typically, mismatches of 0-0.2% correspond to spherical shape, 0.5-1% to cubes and above 1.25% to plates [19]. For a matrix (γ phase) with cubic lattice, the γ/γ' surface (interfacial) energy is minimised by forming the γ' as cubes. This close match in lattice parameters along with this chemical compatibility allows the γ' to precipitate coherently in the matrix and promotes long term stability.

III. Carbides and borides: Carbon is added to some nickel based superalloys at concentrations up to 0.2%. When combined with reactive and refractory elements such as titanium, tantalum, and hafnium it forms metal carbides (MC) (e.g., TiC, TaC, or HfC). Other forms of carbides such as $M_{23}C_6$ and M_6C can be formed from the decomposing of these primary carbides either during heat treatment or in service. Carbides generally have an FCC crystal structure and a coarse cubic or script morphology. They preferentially reside on the γ-grain boundaries [2,35]. Although opinions regarding carbide effects are two-edged, the general view is that in superalloys with grain boundaries, carbides (in a fine distribution) are beneficial by increasing rupture strength at high temperature [35]. Similarly, Boron (B) additions can result in chromium or molybdenum borides that cluster along the grain boundaries [2,40] .

IV. Other: Topologically closed-packed (TCP) phases (μ, σ, Laves etc.) can be found in some Ni-based superalloys as a result of poorly controlled composition [19]. These generally form during heat treatment or service, have a plate-like structure and exhibit undesirable, brittle characteristics. TCPs have a negative effect on the properties of the superalloy as they deplete strengthening elements from the microstructure and can serve as fatigue crack initiation sites [39].

Alloy	Cr	Co	Mo	W	Ta	Re	Nb	Al	Ti	Hf	C	B	Y	Zr	Other
Conventionally Cast Alloys															
Mar-M246	8.3	10.0	0.7	10.0	3.0	—	—	5.5	1.0	1.50	0.14	0.02	—	0.05	—
Rene′ 80	14.0	9.5	4.0	4.0	—	—	—	3.0	5.0	—	0.17	0.02	—	0.03	—
IN-713LC	12.0	—	4.5	—	—	—	2.0	5.9	0.6	—	0.05	0.01	—	0.10	—
C1023	15.5	10.0	8.5	—	—	—	—	4.2	3.6	—	0.16	0.01	—	—	—
Directionally Solidified Alloys															
IN792	12.6	9.0	1.9	4.3	4.3	—	—	3.4	4.0	1.00	0.09	0.02	—	0.06	—
GTD111	14.0	9.5	1.5	3.8	2.8	—	—	3.0	4.9	—	0.10	0.01	—	—	—
First-Generation Single-Crystal Alloys															
PWA 1480	10.0	5.0	—	4.0	12.0	—	—	5.0	1.5	—	—	—	—	—	—
Rene′ N4	9.8	7.5	1.5	6.0	4.8	—	0.5	4.2	3.5	0.15	0.05	0.00	—	—	—
CMSX-3	8.0	5.0	0.6	8.0	6.0	—	—	5.6	1.0	0.10	—	—	—	—	—
Second-Generation Single-Crystal Alloys															
PWA 1484	5.0	10.0	2.0	6.0	9.0	3.0	—	5.6	—	0.10	—	—	—	—	—
Rene′ N5	7.0	7.5	1.5	5.0	6.5	3.0	—	6.2	—	0.15	0.05	0.00	0.01	—	—
CMSX-4	6.5	9.0	0.6	6.0	6.5	3.0	—	5.6	1.0	0.10	—	—	—	—	—
Third-Generation Single-Crystal Alloys															
Rene′ N6	4.2	12.5	1.4	6.0	7.2	5.4	—	5.8	—	0.15	0.05	0.00	0.01	—	—
CMSX-10	2.0	3.0	0.4	5.0	8.0	6.0	0.1	5.7	0.2	0.03	—	—	—	—	—
Wrought Superalloys															
IN 718	19.0	—	3.0	—	—	—	5.1	0.5	0.9	—	—	0.02	—	—	18.5Fe
Rene′ 41	19.0	11.0	10.0	—	—	—	—	1.5	3.1	—	0.09	0.005	—	—	—
Nimonic 80A	19.5	—	—	—	—	—	—	1.4	2.4	—	0.06	0.003	—	0.06	—
Waspaloy	19.5	13.5	4.3	—	—	—	—	1.3	3.0	—	0.08	0.006	—	—	—
Udimet 720	17.9	14.7	3.0	1.3	—	—	—	2.5	5.0	—	0.03	0.03	—	0.03	—
Powder-Processed Superalloys															
Rene′ 95	13.0	8.0	3.5	3.5	—	—	3.5	3.5	2.5	—	0.065	0.013	—	0.05	—
Rene′ 88 DT	16.0	13.0	4.0	4.0	—	—	0.7	2.1	3.7	—	0.03	0.015	—	—	—
N18	11.2	15.6	6.5	—	—	—	—	4.4	4.4	0.5	0.02	0.015	—	0.03	—
IN100	12.4	18.4	3.2	—	—	—	—	4.9	4.3	—	0.07	0.02		0.07	

Figure 2.14: Composition and processing of commercially available Ni-based superalloys (wt.%, bal. Ni) [39].

2.3.2 Strengthening Mechanisms and Heat Treatment

Strengthening mechanisms are based upon methods of restricting dislocation motion and thus controlling plastic deformation and failure processes. The main processes employed to strengthen superalloys are solid solution hardening (SSH), precipitation hardening (PH) and dispersion strengthening.

2.3.2.1 Solid Solution Strengthening

Solid solution strengthening elements for Ni-based superalloys typically include Co, Cr, W and Mo (which reside in the γ matrix). The atomic diameters of these elements vary from nickel atoms from +1% for Co to +13% for W. Apart from lattice distortion (lattice strains by interstitial or substitutional atoms interact with dislocation strain fields hindering their motion), the atoms in solid solution will induce regions with different elastic modulus. This will cause further strengthening of the material as extra energy will be required for the dislocations to move through stiffer and non-compliant regions in the matrix [19]. Solid solution strengthening may also act to decrease the stacking fault energy (SFE) in the crystal lattice leading to primarily inhibition of

dislocation cross slip (the main expected deformation mechanism at high temperatures) [41]. This is due to the stabilisation of stacking faults (SF) created by the dissociation of a dislocation into partial dislocations and their subsequent motion. The lower SFE corresponds to a lowering of the force tending to pull the partial dislocations back together [42] thus cross slip (which requires re-association of the particles) is inhibited.

2.3.2.2 Precipitation Hardening

As mentioned previously, by alloying the Ni with Al and/or Ti above a certain concentration, a second, precipitating phase is created (γ' phase). The formation of these intermetallic compounds such as γ' [Ni_3(Al, Ti)] and γ'' (Ni_3Nb) is responsible for the majority of strength found in Ni-based superalloys. Precipitation hardening also offers increased creep resistance making it an essential strengthening mechanism for high temperature applications.

The most significant impact of the precipitates is that they constrain the movement of dislocations by forcing the dislocations to cut through or bypass the precipitates in order to propagate. The four main factors that control the effectiveness of PH are given below [41]:

I. Volume fraction of the precipitating particles
II. Particle size
III. Coherency strains between the matrix (γ) and the precipitate (γ', γ'')
IV. Antiphase-boundary (APB) energy in the presence of an ordered precipitate

The strengthening effect of the latter two is related to the particle size as these mechanisms require that the dislocation cuts through the precipitates [41]. The APB represents the energy required for a dislocation to cut through an ordered particle. When a dislocation passes through a particle it destroys the periodic ordered atomic arrangement in its slip plane leaving behind a distorted plane which is known as the APB. The shearing dislocations in ordered crystal structures therefore travel in pairs. The first dislocation, known as the leading dislocation, causes the APB. The trailing dislocation interacts with the distorted particle which then restores the ordered structure. This additional breaking and rearrangement of the chemical bonds of the particle leads to strengthening [43].

Because the γ' precipitates are coherently embedded into the γ matrix any difference between their lattice parameters ($a_{\gamma'}$ and a_{γ}) causes a strain field which interacts with dislocation motion. The higher the magnitude of the lattice misfit (δ), the larger the stress field is, and consequently the greater the strengthening contribution of the coherent particles. The lattice misfit and the lattice parameters are defined as:

$$\delta = \left[\frac{\alpha_{\gamma'} - \alpha_{\gamma}}{\left(\alpha_{\gamma'} + \alpha_{\gamma}\right)/2} \right] \tag{2.31}$$

$$\alpha_{\gamma'} = \alpha^{o}_{\gamma'} + \sum\nolimits_i \Gamma_i^{\gamma'} x_i^{\gamma'} \quad \text{or} \quad \alpha_{\gamma} = \alpha^{o}_{\gamma} + \sum\nolimits_i \Gamma_i^{\gamma} x_i^{\gamma} \tag{2.32}$$

Where $\Gamma_i^{\gamma'}$ & Γ_i^{γ} are known as the Vegard coefficients and $x_i^{\gamma'}$ & x_i^{γ} are the mole fractions of added solutions in the γ' and γ phases respectively. The Vegard coefficients are larger for elements with larger atomic size and therefore the lattice misfit depends greatly on elemental partitioning between the two phases. Due to different thermal expansion coefficients (α_{γ} higher than $\alpha_{\gamma'}$), the lattice parameters are affected by temperature, and hence the negative lattice mismatch increases with increasing temperature. The increased lattice mismatch between γ/γ' enhances creep strength in single crystal Ni-based superalloys by superimposing the external (positive) tensile stresses. The negatively stressed γ/γ' interfaces, essentially, act as barriers to mobile dislocations. The above are particularly important when microstructural coarsening (or rafting) is considered as coherency stresses in the γ/γ' phases and externally applied loads are the controlling factors. A more detailed discussion on the matter and tabulated lattice misfit values for CMSX-4 and other single crystal Ni-based superalloys are given in [44].

The volume fraction and the size of the γ' precipitates are also important in providing effective precipitation hardening. As the particle size increases the dislocations are forced to increase their curvature resulting in more particles meeting their path. The overall strength is hence increases as higher stresses are required to force the dislocation through multiple precipitates. However, as shown in Figure 2.15a, the increase in strength related to particle size decreases after a "critical size" even with all the other factors constant. This is because at a certain particle size dislocations can no longer cut through particles but instead will loop around them [45]. This is known as the Orowan looping mechanism and the strength varies according to the Orowan equation given below:

$$\Delta\sigma \sim \frac{Gb}{L - d} \tag{2.33}$$

,where *G* is the shear modulus, *b* is the Burgers vector, *L* is the spacing of precipitates and d their diameter.

Since precipitates must exist within the γ matrix, from the above equation one could conclude that the optimum microstructure lies within minimising the *L* parameter, i.e. the width of the γ channels. However as shown in Figure 2.15b maximum creep strength is achieved at approximately 70% γ' volume fraction. This indicates that (creep) strength in Ni-based superalloys is also enhanced by the γ/γ' interfaces and it is not solely or simply controlled by the γ' particles size and distribution.

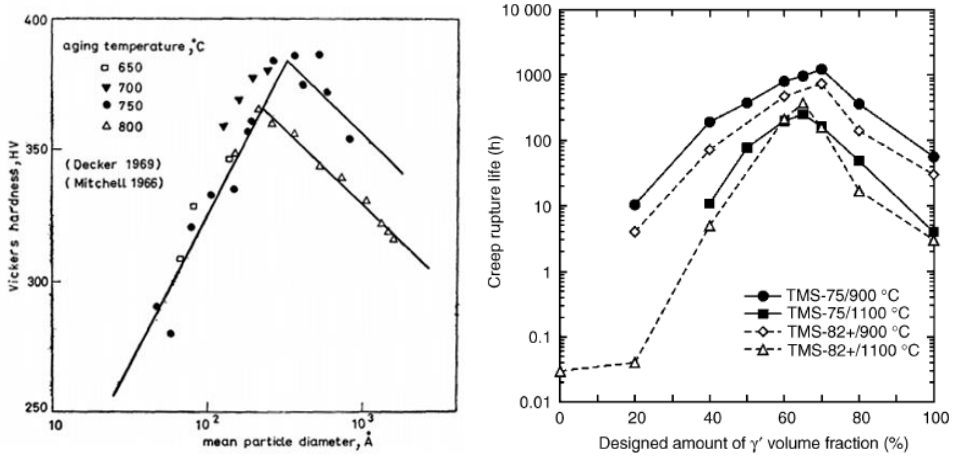

Figure 2.15: Effect of a) particle size on hardness of Ni-Cr-Al-Ti alloys [46] and b) γ' volume fraction on creep strength [47].

The flow stress of the γ' has been found to increase as the temperature rises up to approximately 800°C [2]. Figure 2.16 shows the yield stress variation for some typical Ni-based superalloys. This anomalous temperature dependence on the flow stress, which is typical of the $L1_2$ alloys, was related to the Kear-Wilsdorf (KW) locking mechanism initially by Takeuchi and Kuramoto [48]. Their model which was based on the single crystal intermetallic compound Ni_3Ga was later on revised by Paidar et al. [49] for Ni_3Al compounds. Briefly, the KW mechanism can be explained as follows. During cyclic deformation, the anisotropic properties of the material promote the cross slip of the γ' superpartial dislocation from the (111) slip planes to the (001) slip planes. The cross slipped segments were observed to act as microstructural locks (KW locks), as they resist deformation. Since cross-slip is a thermally activated process, as the temperature increases cross slip behaviour is enhanced and hence the formation of the KW locks is promoted, leading to an increase in strength with increasing temperature [2].

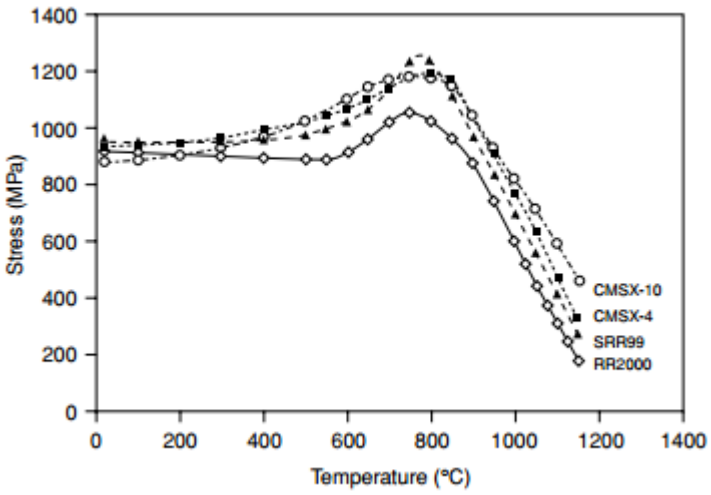

Figure 2.16: Variation of the yield stress for several single crystal Ni-base superalloys with temperature [2].

2.3.3 Heat Treatment

It is well known that the mechanical properties of superalloys are controlled to a great degree by their microstructure. The application of heat for a period of time together with composition control, is an effective way of manipulating the microstructure of superalloys. A heat treatment is most typically applied to achieve one of the following: i) stress relief, ii) redistribution of alloy elements, iii) promote grain growth, iv) recrystallization, v) dissolve phases and vi) produce new phases. The most common heat treatment techniques applied for Ni-based superalloys are the solution heat treatment (annealing) and the aging heat treatment (in one or more steps). Solution treatment followed by precipitation treatment is a typical sequence for precipitation hardened superalloys [50].

Solution treating or homogenising is generally the first part of the operation and it is designed to homogenise the microstructure and reduce elemental segregation which is known to promote γ' coarsening and thereby creep failure [51,52]. This is particularly important in cast microstructures such as turbine blades. At this stage, the superalloy is held at a temperature between its solidus and solvus temperature (heat treatment or solutioning window) for a sufficient amount of time to achieve a homogeneous solution of all phases present [53]. The choice of heat treatment window is particularly important because it should allow for total solution of the γ' phase without incurring a high scrap rate due to incipient melting [54]. The solvus temperature of the γ' phase for a selection of Ni-base superalloys is shown in Table 2.1.

Cast Ni-based superalloys exhibit high elemental segregation and heterogeneous structures in the as-cast condition therefore longer exposure times are required compared to Wrought or PM

processed alloys [51], [53], [55]. In order to capture the achieved structure, the solid solution obtained is rapidly cooled to room temperature typically by water quenching or air cooling. At this stage, the phases in the alloy that have a low degree of solubility at room temperature are not in equilibrium and the alloy is unstable. Precipitation or secondary phase particles is a function of time and temperature and the process is known as precipitation or aging treatment. The purpose of the aging treatment is therefore to produce a high volume fraction of γ' precipitates in a favourable morphology, which may give for example an optimum stress rupture property, although other properties are also important. The close control of the precipitation process is usually achieved by applying multiple steps at various temperatures and times. However, over-aging should be avoided as it can result in the production of undesirable phases that affect the strength of the alloy [41].

Alloy	Process	γ' solvus (^{o}C)
Rene 95	Wrought	1120-1160
Udimet 500	Wrought	1050-1100
MAR-M 200	Wrought	1180-1200
Rene 80	Cast	1150
Udimet 700	Cast	1140
Inconel 713LC	Cast	1180-1200
Inconel 792	Cast	1100-1150
CMSX-4	Cast	1305
CMSX-10	Cast	1345

Table 2.1: Approximate γ' solvus temperature for various commercially available Ni-based superalloys [41].

2.3.4 Processing for Turbine Blade Applications

The manufacturing process of alloys is related to the alloy system, the shape and form of the product, the condition of the end product and the required properties for the specific application. In general, superalloys can be produced and processed by: a) casting, where liquid material and molds are used to shape the components, b) wrought processes through ingot metallurgy and hot working (forging), or (c) powder metallurgy (PM) by sintering powdered material [56]. PM came later than the first two methods and is primarily used to manufacture nickel based superalloy turbine disks. Although this is a widely adopted process, turbine disks are not within the focus of this work and therefore PM is not discussed further.

In the early stages of the GTU technology, turbine blades were produced only in the wrought condition. However, with the advancements in superalloy composition and turbine blade design, casting began to emerge as the most beneficial route both in terms of achieved properties and cost. Possibly the greatest breakthrough in the development of Ni-based superalloys came with the introduction of vacuum induction melting (VIM) in the 1950s [34,56]. Vacuum melting benefited both wrought and casting processes as it allowed for greater purity superalloys to be made. Detrimental elements and impurities that compromised the effects of Al and Ti and posed the risk of reacting to form oxide inclusions could be avoided. As implied by the name, the process consists of melting the alloying elements under high vacuum and pouring them into an ingot mold (Figure 2.17a).

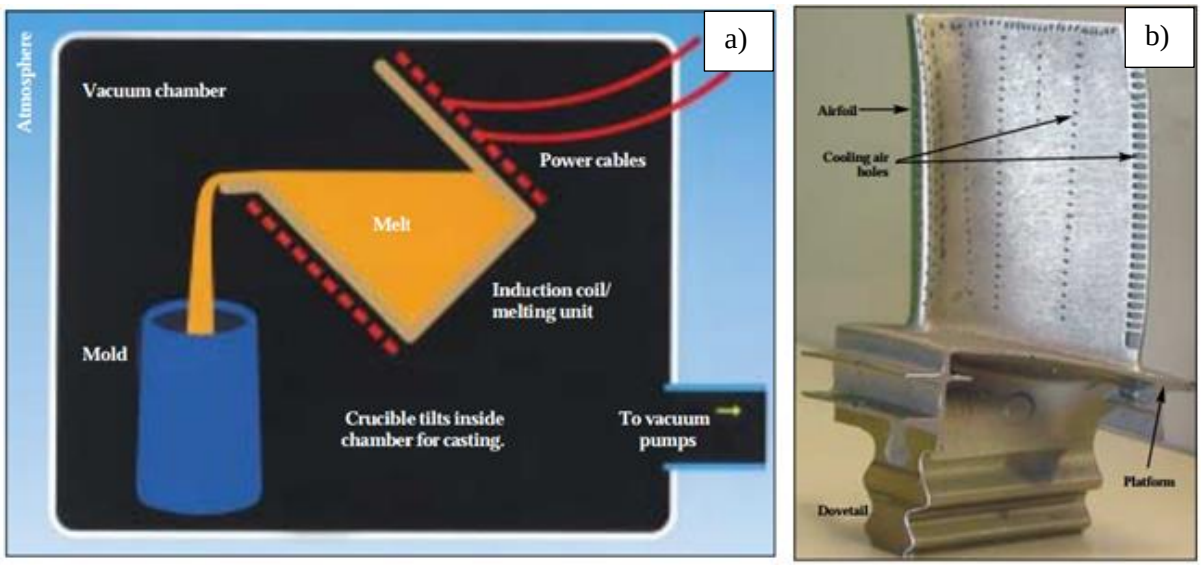

Figure 2.17: a) The Vacuum Induction Melting process, b) A nickel base superalloy high pressure turbine blade investment casted from a VIM ingot [57].

In high value applications, such as the nickel based turbine blades a secondary melting process known as Vacuum Arc Remelting (VAR) is employed after VIM. This additional processing step is used to further increase the quality of the final product. The ingot cylinder produced by the VIM, typically referred to as the electrode, is closed into a water cooled copper crucible and brought up to a high vacuum. A high current is then passed through the electrode and the baseplate of the copper mold. This creates a direct-current arc which melts the lower tip of the electrode forming a new ingot as the alloy cools at the bottom of the crucible. After an adequate purity and the correct chemistry are achieved by VIM the desired microstructure is established via the greater control of solidification rate offered by the VAR.

Electroslag Remelting (ESR) is an alternative method of secondary melting. One of the main differences of this process to VAR is that remelting is achieved by Joule (ohmic) heating (heat

released by current passing through a conductor). An AC current passes between the electrode and the forming ingot through a resistive slag. The molten metal solidifies then on the slag skin and not on the crucible baseplate. Both methods are widely used to meet the requirements of the alloy and more recently their combined advantages are exploited. This hybrid secondary melting process typically begins with ESR which produces a higher integrity ingot but may contain freckles (microstructural defects) due to segregation. Thus the ESR ingot is then remelted using the VAR method which is the most effective method in controlling segregation [56], [58].

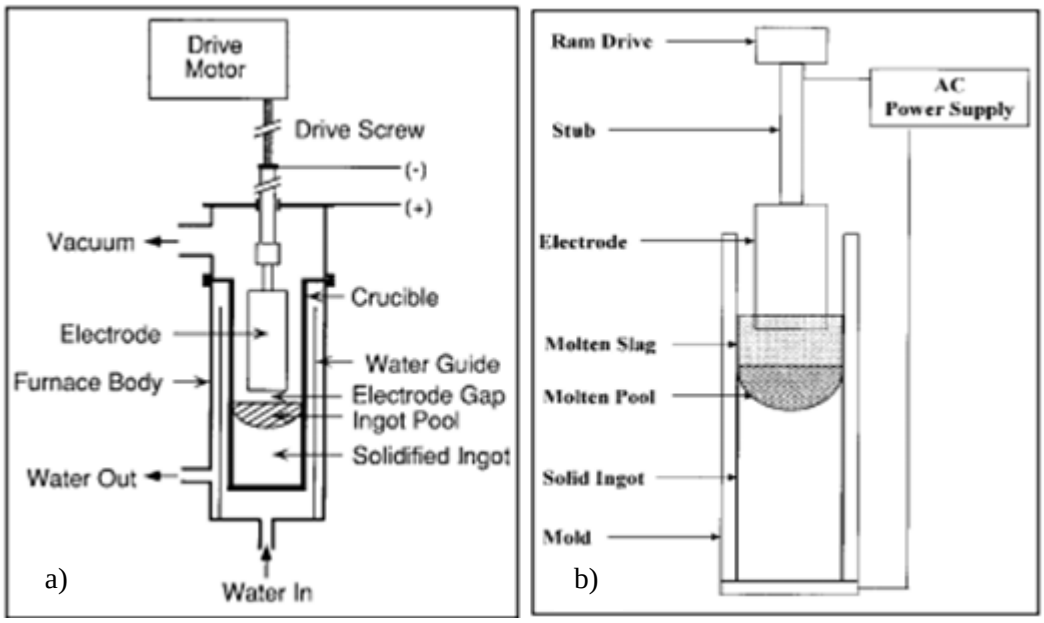

Figure 2.18: Schematic of the re-melting processes a) VAR, b) ESR [59].

At the same time, the casting methods continued to improve as they became more favourable than wrought processing. In the 1960s, the introduction of directional solidification (DS) enabled the production of turbine blades with columnar microstructure. At the time, it was already established that grain boundaries are detrimental towards the creep fracture performance behaviour of superalloy components. In early studies, the most untoward events during creep testing in polycrystalline materials were associated with grain boundary sliding, intergranular cavitation and void nucleation. Particularly, it was noted that the main detrimental events (excessive precipitation, cavitation and void formation) all occur on the grain boundaries orientated normal to the stress axis [60]. Therefore the main aim of metallurgists in the early 70s was to eliminate these boundaries from the material's structure. The columnar structure was achieved by withdrawing the investment mold, containing the liquid metal, at a controlled rate from a furnace. To do this, the mold is pulled from a high temperature region at very slow rates (typically 5-40cm/hr) allowing for a stable, unidirectional thermal gradient. This causes the liquid metal to solidify from the base of the casting and its grains to form as large columns parallel to the withdrawal direction [2,39].

Approximately a decade after the development of the DS processing method, a spin-off of the technology allowed the production of monocrystalline (single crystal) superalloys. Essentially the DS method was equipped with grain selection instruments that allowed a single grain to grow and encompass the entire part. By eliminating the grain boundaries completely, grain-boundary strengthening elements such as C, B, Si and Zr could be avoided. This resulted in an increase in the melting temperature of the alloy and consequently allowed for better heat treatments. A higher heat-treatment temperature allows for a more uniform solution of γ' and dissolution of the coarser γ' and thereby increases the overall high temperature performance of the superalloy [2,35]. The historic development of the turbine blade processes among with a schematic representation of the grain structures described above is shown in Figure 2.19. Single crystals and their turbine blade applications will be discussed in more detail in the following sections.

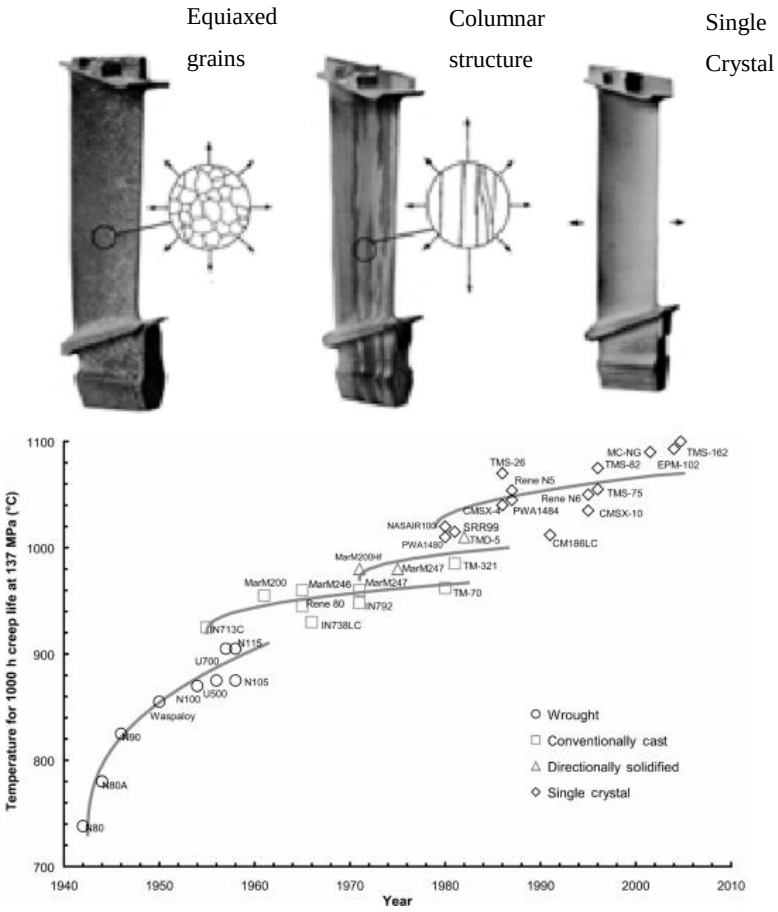

Figure 2.19: Development of turbine blade processing and material [61].

2.3.5 Single crystal turbine blades

The increased fatigue and creep resistance of single crystal (SX) Ni-based superalloys have made their use in high pressure (HP) turbine blades common practice. This section introduces the processing routes followed to manufacture single crystal Ni-based turbine blades and discusses how their chemistry evolved to serve today's needs. Single crystals are divided, mainly based on their composition, into generations.

Turbine blades nowadays are characterised by complex hollow aerofoil structures, encompassing internal cooling passages that allow air to flow through them and reduce their operating temperature. The casting process that has been utilised for fabricating such components is the investment casting or "lost-wax" process. The process begins with a metallic "master mold" which is used to create a wax replica of the turbine blade. The internal cooling passage structure is constructed by inserting ceramic cores into the wax while solidifying. The replicas are arranged in interconnected clusters that allows the manufacturing of multiple blades at once. Next, a ceramic investment shell containing Al, Si and/or Zr is progressively built up around the wax replica. A number of thermal cycles are then applied to the ceramic mold to remove the wax by melting and strengthen the mold. After the strengthening and degassing procedure is finished, the remelted superalloy is poured into the mold under vacuum at a temperature of ~1550^{o}C. Similarly to the DS method, the castings are slowly withdrawn from the hot zone of the furnace at a controlled rate. To achieve complete removal of grain boundaries two methods are available. Most typically, a constriction known as a grain selector is used at the bottom of the mold. The grain selection has most commonly a form of a pig tail and a cross section not much larger than a typical DS grain size. Therefore only one grain orientation is allowed to grow and fill the casting as it is being withdrawn from the hot zone. Figure 2.20 shows a HP turbine blade manufactured by investment casting in a single crystal form through a pig-tail grain selector. Alternatively, the single crystal can be grown from a seed located at the bottom of the casting. The seed is a small piece of single crystal from the superalloy that is used as a guide for the liquid metal to solidify in the same orientation.

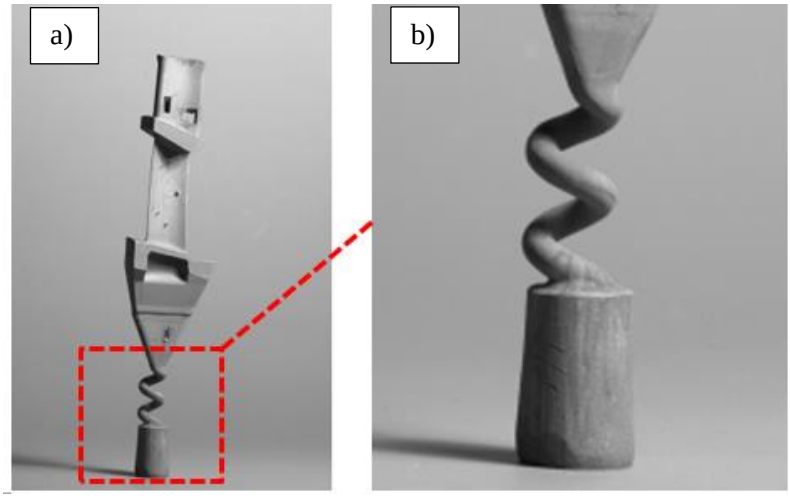

Figure 2.20: a) HP turbine blade after removal from investment cast with "pig-tail" grain selector still attached b) magnification of the grain selector section [2].

2.3.5.1 Evolution of the chemistry

The performance of gas turbine engines has significantly increased over the past decades mainly because of the increase in the capability of turbine blades to withstand higher pressures and temperatures. This improvement is partially attributed to the development of the processing methods but it has been also achieved through improved alloy compositions.

The first generation of single crystal superalloys comprises those that became commercially available with the development of single crystal processing techniques. Their main alloying elements are Cr, Co, Mo, W, Al, Ti, and Ta. Less often, small additions of Nb, V or Hf are also included [62]. Examples of alloys from the first generation are shown in Figure 2.21.

Alloy	Cr	Co	Mo	W	Al	Ti	Ta	Nb	V	Hf
Nasair 100	9	–	1	10.5	5.75	1.2	3.3	–	–	–
CMSX-2	8	4.6	0.6	8	5.6	1	6	–	–	–
CMSX-3	8	4.6	0.6	8	5.6	1	6	–		0.1
CMSX-6	9.8	5	3	–	4.8	4.7	2	–		0.1
PWA 1480	10	5	–	4	5	1.5	12	–	–	–
SRR 99	8	5	–	10	5.5	2.2	3	–	–	–
RR 2000	10	15	3	–	5.5	4	–	–	1	–
René N4	9	8	2	6	3.7	4.2	4	0.5	–	–
AM1	7.8	6.5	2	5.7	5.2	1.1	7.9	–	–	–
AM3	8	5.5	2.25	5	6	2	3.5	–	–	–

Figure 2.21: Composition of commercially available 1st generation Ni-based superalloy SX [62].

During the late 1980s studies showed that the addition of small quantities of Re has positive effects on the creep strength of Ni-based superalloys [63],[64]. Specifically, it was found that Re atoms cluster within the γ matrix retarding the coarsening of γ' and promoting large γ/γ' misfits. A Re content of approximately 3wt.% is characteristic of this generation. Other γ-former elements such as Mo, W and Cr have been reduced from the composition at the expense of the Re additions. The wt.% of γ-forming element needs to be carefully controlled in order to achieve an optimum mechanical/environmental property balance and avoid supersaturation of the solid solution and as a result, precipitation of Re-rich TCP particles [62]. Single crystal Ni-based superalloys from this generation are nowadays widely used since their behaviour is relatively well understood. Typical examples of such alloys are shown in Figure 2.22. CMSX-4 is a primary focus of this thesis as it is currently wide-spread in service in the gas turbine power generation industry and improved lifing predictions are needed.

Alloy	Cr	Co	Mo	Re	W	Al	Ti	Ta	Nb	Hf
CMSX-4	6.5	9	0.6	3	6	5.6	1	6.5	–	0.1
PWA 1484	5	10	2	3	6	5.6	–	8.7	–	0.1
René N5	7	8	2	3	5	6.2	–	7	–	0.2
SC180	5	10	2	3	5	5.2	1	8.5	–	0.1
SMP14	4.8	8.1	1	3.9	7.6	5.4	–	7.2	1.4	–
MC2	8	5	2	–	8	5	1.5	6	–	–

Figure 2.22: Composition of commercially available 2nd generation Ni-based superalloy SX [62].

The third generation of alloys were developed to increase the temperature capability and creep resistance further. By increasing the amount of Re to approximately 6 wt.% it was found that the creep-rupture resistance improved by about 30°C [65]. The inclusion of small amounts of Hf (up to ~0.2wt.%) promotes the adherence of oxide scales and reduces the diffusion of Al [66]. Alloys representative of this generation are shown in Figure 2.23. Due to the higher content of refractory elements, 3rd generation alloys can withstand even higher temperatures than their predecessors. However, for the same reason, they typically have higher densities and thereby add more weight to the engines. Depending on the application the weight penalty of these materials is an acceptable compromise for their very high operating temperature [41]. The biggest concern, regarding 3rd generation superalloys, is the precipitation of TCP phases which are known to reduce high temperature strength [67]. With the higher additions of solid-solution strengthening elements, mainly of Re, TCP phases are of greater concern than in 2nd generation Ni-based superalloys.

Alloy	Cr	Co	Mo	Re	W	Al	Ti	Ta	Nb	Hf	Others
CMSX-10	2	3	0.4	6	5	5.7	0.2	8	0.1	0.03	–
René N6	4.2	12.5	1.4	5.4	6	5.75	–	7.2	–	0.15	0.05C 0.004B 0.01Y
Alloy 5A	4.5	12.5	–	6.25	5.75	6.25	–	7	–	0.15	0.05C 0.004B 0.01Y
TMS-75	3	12	2	5	6	6	–	6	–	0.1	–
TMS-80	2.9	11.6	1.9	4.9	5.8	5.8	–	5.8	–	0.1	3 Ir

Figure 2.23: Composition of commercially available 3rd generation Ni-based superalloy SX [62].

The formation of the detrimental TCP phases led to the development of the fourth generation Ni-based superalloys which contain about 2wt% Ruthenium (Ru). Ru was reported to promote the stability of the microstructure and add approximately another 30°C to the creep strength compared to the 3rd generation [41], [26]. However, these alloys not only exhibit much higher weights than 2nd generation superalloys but also seem to have lower oxidation resistance due to the lower levels of oxidation-resistive elements [26].

The first two fifth generation Ni-based superalloys (TMS-162 and TMS-173) that have superior high temperature creep resistant compared to all previous SX Ni-based superalloys were developed in 2004 in Japan [68]. The advanced properties of these alloys are attributed to the additions of platinum group metals (such as Ru) which permit higher additions of refractory elements (such as Re and Mo) without compromising the microstructural stability (segregation and TCP formation) [69]

Currently, efforts are ade to push the boundaries of TIT even further by developing single crystal Ni-based superalloy of the 6th generation [70,71]. However, the continuous development of advanced alloys increases the need for rare earth elements which in turn raises issues concerning sustainability. World production of elements such as Re, Ru and Ta would not be able to meet the demand following current trends, with Re is already exhibiting a gap between supply and demand; to accommodate this ~27% of the demand is covered by recycled material [72–74]. Quantitative methods that evaluate the supply risks have recently been developed and are discussed elsewhere [73].

2.3.5.2 Heat treatment and microstructure

Directionally solidified superalloys exhibit a dendritic microstructure. The microstructure can be then divided into the dendritic and interdendritic (IR) regions. Each dendrite consists of the main or primary arm (PDAs) and the branches or secondary dendritic arms (SDAs). Figure 2.24 shows the dendritic structure in the as-cast condition of CMSX-4. During solidification, some elements such as Co, Re, W, Cr and Mo partition to the dendritic regions while others (Ti, Ta, Al) concentrate in the IR regions or solidify as eutectic regions [75] [76]. In the as-cast condition the microstructure of CMSX-4 is characterised by the γ matrix, the γ' precipitates and the γ/γ' eutectic regions. Elemental segregation and γ/γ' eutectic regions are both known to be detrimental to the high temperature properties of Ni-based superalloys [51,77,78]. The dendritic pattern and the γ/γ' eutectics are seen throughout the microstructure of the as-cast material (Figure 2.25a). The γ' particles are also evident in the as cast condition and exhibit a relatively fine morphology which seems to coarsen in the vicinity of eutectic regions (Figure 2.25b).

The microstructure of the as-cast CMSX-4 superalloy can be homogenised to produce the lowest possible level of residual micro-segregation through heat treatment. To eliminate this elemental segregation the material is heated at temperatures above the γ′-solvus (~1305^{o}C) and below the solidus temperatures (~1325^{o}C) (solution heat treatment). Because of the higher refractory element content of this alloy the heat treat periods are longer than previous generations of SX Ni-based superalloys and range from six to eight hours. However, the heat treatment window of approximately 19°C, ensures complete solutioning of the γ' without risk of incipient melting [54]. Following the solution heat treatment and the dissolution of the γ/γ' eutectics, the microstructure of CMSX-4 becomes uniform and fine γ' particles form throughout the material (Figure 2.26a). A certain number of precipitation treatment cycles are then undertaken to slightly coarsen the γ' to 0.5μm in size and form the desired cuboidal structure (Figure 2.26b) [79].

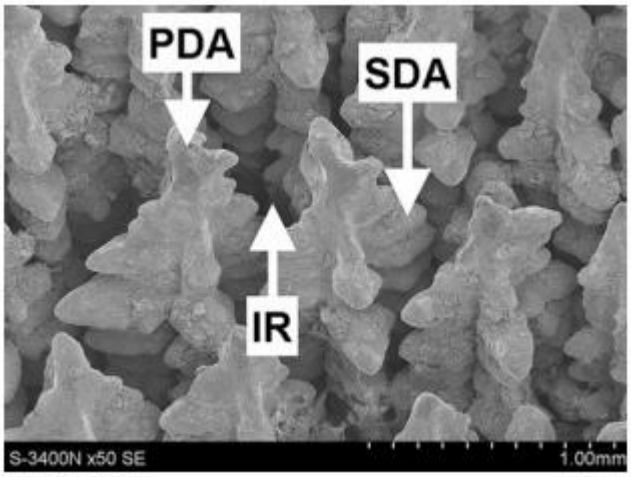

Figure 2.24: The dendritic structure of CMSX-4 [55].

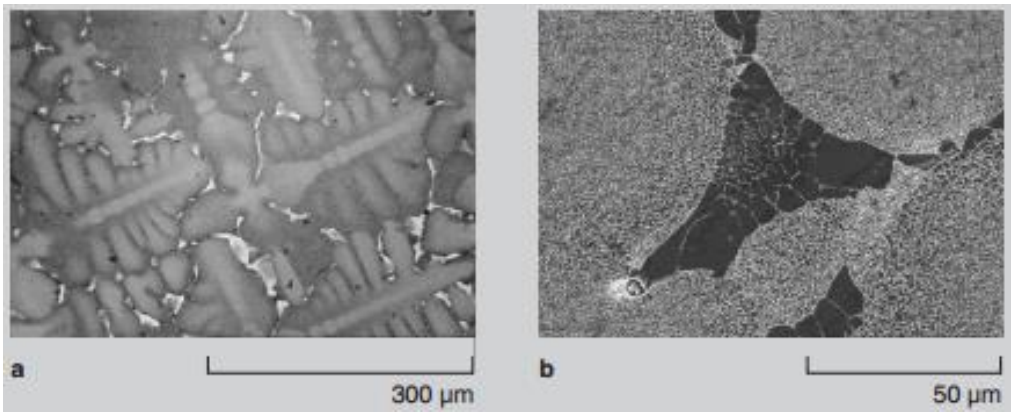

Figure 2.25: As-cast CMSX-4: a) Optical micrograph of dendrites with γ/γ' eutectic areas between, b) SEM image of a γ/γ' eutectic region [79].

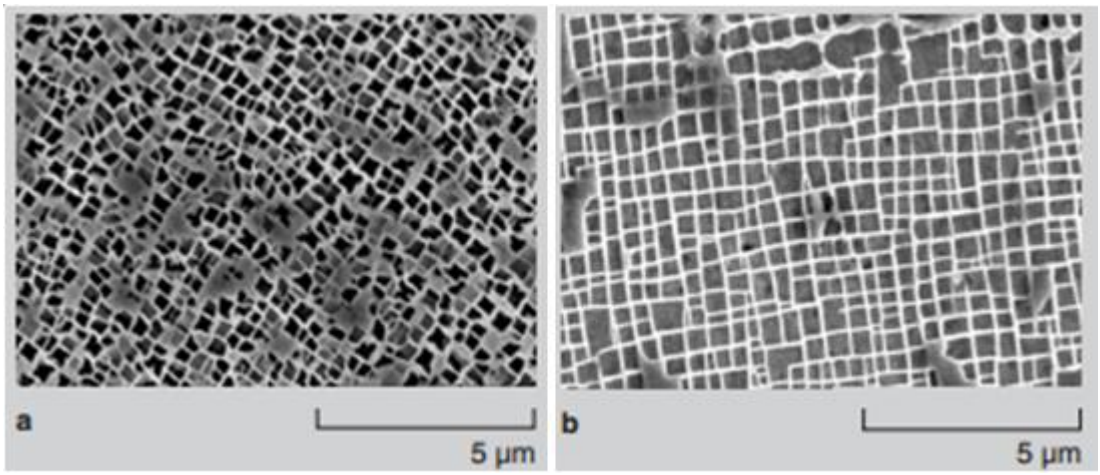

Figure 2.26: SEM images of the microstructure of CMSX-4 a) after solution heat treatment and b) after subsequent aging [79].

2.4 High temperature damage mechanisms in SX Ni-based superalloys

2.4.1 Oxidation Behaviour

The oxidation performance of 2nd generation SX Ni-based superalloys is well documented for temperatures above 650°C [22,23,27,80–86]. Even though the oxidation behaviour of these materials at lower temperatures is not reported extensively and the following section aims to provide the ground

J. E. Croll and G. R. Wallwork [86] reported that the oxidation resistance of Ni-based alloys increases with increasing chromium content. This is due to the formation of the Cr_2O_3 oxide which is non-porous and strongly adheres to the surface. However, the same work has shown that significant oxidation resistance is only observed in alloys with Cr concentrations of more than 20%. This is particularly important in the case of most 2nd generation SX Ni-based superalloys, where chromium levels have been lowered to allow increased aluminium and titanium levels, which contribute towards the formation and strengthening of the γ' phase $Ni_3(Al,Ti)$. In addition, it was shown that at temperatures higher than 1000°C, the oxidation resistance of Cr forming alloys is compromised as the protective Cr_2O_3 transforms into volatile CrO_3. At higher temperatures oxidation protection is offered by the formation of Al_2O_3 scales as a result of the aluminium content of the material [22]. Another element within the composition of CMSX-4, which is beneficial to oxidation resistance, is Hafnium (Hf). Hafnium has been shown to increase the spallation resistance of the formed oxide scales. This is due to the formation of more stable oxide HfO_2, which increases the adhesion strength between substrate and oxide layer [87].

M.H. Li et al. [83] have investigated the oxidation behaviour of a "typical" single crystal Ni-based superalloy in air at 800°C and 900°C. The composition of the material tested is given as 6.3%Al, 6%Cr, some Co, Ti, Mo, Ta and W and balance of Ni. The samples were disk specimens of Ø15mm x 5mm and the oxidation kinetics were studied using discontinuous gravimetric analysis for exposure times up to 1925h. Figure 2.27 shows an SEM image of the surface morphology of the alloy after 5h exposure at 800°C. The oxide formed over the dendritic region had a coarse, porous and blocky morphology while on the other hand the oxide formed over the interdendritic region had a finer grain structure resulting in a smoother surface. The different oxidation behaviour between the two regions indicated that dendritic segregation can influence the resulting products significantly. In addition, it was found that for the lower temperature tests (800°C) oxidation rate was higher and that the total thickness of the oxide layer varied significantly, from 3 to 18μm. The faster oxide growth rates observed during the lower temperature tests were attributed to the formation of an α-Al_2O_3 inner protective layer during the higher temperature tests. The α-Al_2O_3 is a continuous, stable and adherent oxide layer which obstructs the diffusion of reactive species and

therefore inhibits scale growth. The oxide structure at 800°C has been shown to comprise an Al-rich inner layer, a complex [$CrTaO_4$, $NiCr_2O_4$, $(Ni,Co)Al_2O_4$, etc.] middle layer and an outer NiO scale (see Figure 2.28) . The NiO scale displays nodular growth with high porosity in some areas. Even though this is in a higher temperature regime than the one to be investigated in this project, it provides an indication of the different oxide scales likely to form as the temperature decreases. Also, the less protective oxides and the less uniform scale morphologies observed for the lower temperature indicate that subsequent alloy performance (e.g. crack initiation) can be affected.

The isothermal oxidation behaviour of several SX Ni-based superalloys was investigated by M. Gobel et al. at 800°C, on mechanically abraded disks of about 3mm thick for times up to 1000h [27]. The oxidation kinetics were assessed by means of discontinuous weight measurements. The specimens were removed from the furnace and weighed at given time intervals of 30h, 100h, 300h and 1000h, with any loose oxide scale collected and examined under X-Ray diffraction (XRD). For the post experimental investigations the specimens were plated with protective nickel, sectioned and mounted for examination under the SEM. This study made similar observations to M.H. Li et al. [83] as both reported that Ni-based superalloys generally show good scale adherence and resistance to oxidation following an initial rapid weight gain.

A service related approach to the investigation of oxidation kinetics of CMSX-4 was undertaken by M. Gobel et al. [80] who experimented on the cyclic oxidation behaviour of the material. The test rig used for thermal cycling included a tube furnace where its position was automatically adjusted as well as stainless steel transmitters connected to acoustic emission transducers to monitor the spalling and cracking processes. The experimental procedure was carried out for two different oxidation (peak) temperatures, 1000°C and 1150°C. After an isothermal period of 1h the specimens were cooled down for 30min reaching temperatures of 52°C and 75°C respectively. The temperature profile for the 1150°C cycle is shown in Figure 2.29. After 200-300 cycles CMSX-4 tested under cycling loading (1000°C) began to exhibit some weight loss with a large number of nodules on the surface. Cracking and spalling of the oxide was also observed and the oxide formed in subsequent cycles became more enriched in NiO and Cr_2O_3 as aluminium and titanium depleted zones developed in the alloy. As discussed by Evans and Taylor [88] oxide spalling is greatly affected by creep stress relaxation. The mechanical stability of the oxide layer was found to be controlled by the compressive stresses induced both during the oxide scale growth and the development of thermal strains in the cooling process of the cycle as the thermal expansion coefficient of the oxides is less than the thermal expansion coefficient of the metal substrate.

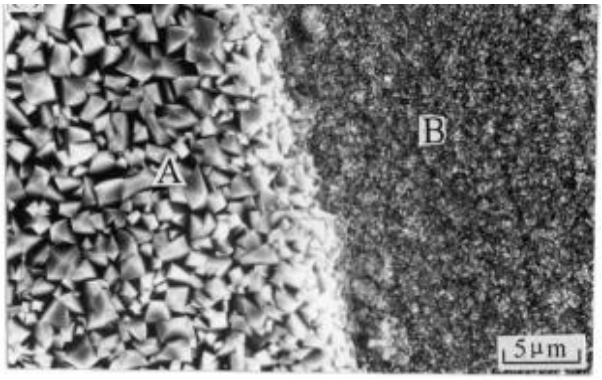

Figure 2.27: SEM image of dendritic (A) and interdendritic (B) surface morphologies of a Ni-based superalloy exposed for 5h at 800°C [83].

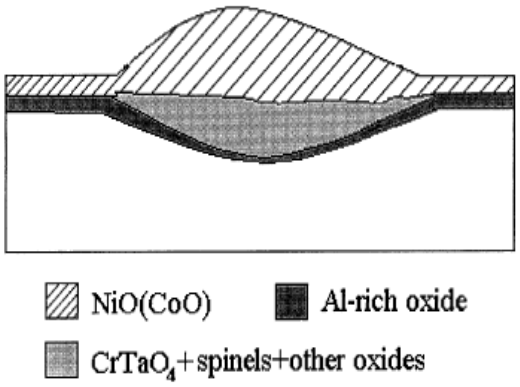

Figure 2.28: Schematic model of the oxide scales formed on the surface of a Ni-based superalloy at 800°C [83].

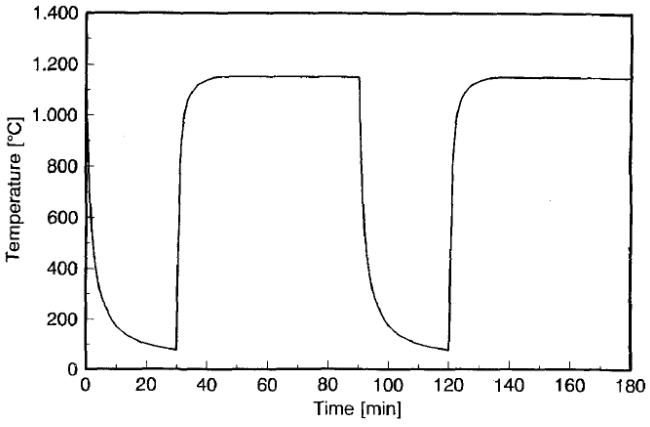

Figure 2.29: Temperature profile against exposure time of cyclic oxidation tests [80].

2.4.2 Fatigue Behaviour

Since single crystal Ni-based superalloys are generally used in turbine blade applications, much of the work in the open literature is concerned with high temperature creep performance. Less work on fatigue performance (especially high cycle fatigue) is published and it is generally concerned with the higher spectrum of in-service operating temperatures (>650°C). Before considering fatigue, this section will briefly review the cyclic deformation behaviour in Ni based single crystal superalloys.

Compared with pure metals, cyclic deformation behaviour in Ni-based superalloys exhibits enhanced slip planarity caused by the addition of various alloying elements such as Co, Cr and W that can effectively lower the SFE as well as the ordered nature of the strengthening phases γ' and γ'' [89]. The cyclic deformation of a nickel based superalloy (CMSX-4) was studied in terms of its low cycle fatigue (LCF) by MacLachlan and Knowles [90]. They conducted tests at a single stress level at 750, 850 and 950°C at a load ratio $R = 0$. At the lower temperatures or high frequencies, crystallographic crack growth occurs rapidly along persistent slip bands (PSBs) formed on {111} planes. As temperature is increased or frequency reduced they found that deformation becomes more homogeneous with a network of dislocations spread in the γ matrix resulting in failure by stage II crack growth. A similar study was carried out by K.Obrtlik et al. [91] who investigated the cyclic behaviour of CMSX-4 at temperatures of 700, 850 and 950°C. SEM observations revealed the presence of PSB along the {111} planes only on the surface of the lower temperature (700°C) samples when tested at high strain amplitudes ($R_\varepsilon = 0.05$). The absence of PSB at temperatures higher than 750°C was also observed by other authors on similar single crystal superalloys [92,93].

Whan and Rae [94] investigated the microstructural deformation processes in CMSX-4 under LCF with $R = 0$ and at loads both above and below the yield stress. They observed that cyclic loading at stresses above the yield stress at 750°C caused extensive cutting of the γ' particles by dislocation dipoles and by partial dislocations trailing SFs. High dislocation density within the γ matrix was also reported. The above dislocation dipoles were studied by Charles et al. [95] and were identified as dislocation loops in the γ' trailing either the APB or the SFs. The deformation mechanisms of CMSX-4 under a strain-controlled approach have been characterised in the work of Hong et al. [96] through LCF tests with $R = 0$ at temperatures of 750, 850 and 950°C. In contrast with the above studies, their results at 750 and 850°C showed no evidence of extensive γ'shearing by slip. Instead, partial dislocations were only sporadically seen to shear the γ' leaving SFs behind. At 850°C, the dislocation movement was observed to be slightly more activated by cross slip compared to 750°C. At the highest temperature, dislocation movement by thermally activated processes such as cross slip and climb homogenised the deformation.

Due to their unique microstructure and complex composition, single crystal Ni-based superalloys exhibit complex deformation mechanisms which depend on temperature and loading conditions. Therefore, understanding of the deformation mechanisms at the particular conditions of interest becomes essential part of the safe design and life prediction against fatigue damage.

Fatigue crack initiation and the effects of environment were studied by M.Miller et al. [97] on CMSX-4. The experiments were conducted on a servo-hydraulic machine on U-notched bend bar samples. All fatigue testing was carried out under pure mode 1 loading in 3-point bending with a load ratio of 0.1. A trapezoidal 1s-1s-1s-1s waveform was employed, giving a frequency of 0.25 Hz. The samples were oriented so that their tensile axis was along the <001> direction. Two different notch orientations (secondary orientations) were investigated; <110> (orientation A) and <100> (orientation B). The effect of environment was assessed by carrying out fatigue tests at 650°C and 725°C in both air and vacuum. Despite the fact that heavy oxidation obscured the detail of the notch root surfaces, several initiation points were identified at both temperatures tested. Crack initiation in air was not observed to occur from surface features. Despite the fact that surface cracks were seen to form on the oxide scale of the U-notch they were not found to penetrate into the substrate and all fatigue crack initiation in air was associated with subsurface interdendritic pores. It was proposed that during cyclic loading, repeated cracking and re-oxidisation of the surface pores builds up an oxide plug which reduces the stress concentration in the area and shifts initiation to subsurface pores. In contrast, under vacuum conditions fatigue crack initiation from surface or close-to-surface pores was typically observed, while evidence of planar slip processes at the crack tip was also clear.

In agreement with the work of M.Miller et al. [9,97], D.J. Duquette and M.Gell [85] also observed that high temperature oxidation can alter the fatigue crack initiation mechanism by acting as plugs to micro-defects cracks but can also form oxidisation pits on the free surface. The experimental procedure involved axial fatigue testing of un-notched, cylindrical, Mar-M200 specimens at temperatures between RT and 927°C in air and vacuum. The results showed that between 423°C and 760°C crack initiation occurred subsurface for the air tests and on surface for the vacuum tests. This behaviour was assumed to be linked to surface oxidation. To evaluate the effects of oxidation a preoxidised specimen (for 24h at 760°C) was fatigue tested in air at room temperature. The observation made was that, similarly to the non-preoxidised room temperature specimens, failure was surface-initiated. A second specimen was also preoxidised (for 24h at 423°C) and it was observed to form a relatively thin oxide layer. This specimen was then fatigued at 423°C in vacuum and also showed surface initiated failure. Based on these experiments it was concluded that static oxides do not restrain surface-initiated failure and thus the role of oxidation is a dynamic one. This

indicates that for temperatures between 423°C and 750°C the dynamic oxidation of newly emerging slip steps (from cyclic loading) acts as a "restrainer", thus preventing surface crack initiation.

Using similar set up and loading conditions as [97], M.R.Joyce et al. [98] investigated the effects of environment and crystallographic orientation on the fatigue crack propagation behaviour of the CMSX-4. The effects of environment were assessed by testing at 650ºC in air and vacuum while using samples with either <110> or <100> secondary orientations (with the same <001> tensile axis). Crack length monitoring was performed with the four point direct current potential drop (DCPD) method. The results indicated that fatigue behaviour was dependent on both secondary orientation and environment. Generally, fatigue crack propagation (FCP) rates were found to be faster in vacuum than in air. This was linked to the effects of oxidation which induced closure and increased slip homogenisation (suppressing faster Stage I crack growth). Preferential oxidation of the γ matrix was also observed but it was not linked to the FCP behaviour. Oxidation of the matrix is believed to have occurred after crack growth due to the increased time of high temperature exposure of the fracture surfaces. Macroscopically, crack growth was observed to occur along the {100} plane for both orientations. Microscopically, at low-mid ΔK levels, propagation occurred with cooperative slip along alternating {111} slip-planes whilst at higher ΔK levels a transition to a far coarser extended slip band cracking along the {111} planes was observed. Differences in the FCP rate between the two secondary orientations were attributed to the following reasons: (1) alignment and amount of interdendritic porosity causing local crack path perturbations and increasing shielding; (2) promotion of Stage I crack growth when the secondary orientation was along the <110> direction (closure/shielding due to facet formation); (3) <110> is a stiffer crack growth direction than <010>, which may have implications for shear band decohesion crack propagation mechanisms.

Similar effects of oxidation on the FCP rate of CMSX-4 were made by Schubert et al, [99] who carried out fatigue tests on single edge notch specimens at 750°C and 1000°C in both air and vacuum. The samples were manufactured from <001> castings with small corner or edge cracks to simulate small cracks in turbine blades and tests were carried out at a load ratio of 0.1 and a frequency of 5Hz. At low to mid ΔK levels, fatigue cracks in air at 750°C, were seen to propagate along the γ channels or the γ/γ' interface with occasional shearing of the γ' particles (alternating between the {111} and {100} planes). At higher ΔK levels, the crack growth mechanism changed to propagation by slipping along the {111} planes with extensive cutting of the γ' particles. In contrast, γ' cutting was not observed at 1000°C and propagation, constrained to the γ channels, took place by cross sliding at {100} planes. The effect of environment (testing in vacuum) on fatigue crack growth rates was evident at low ΔK levels (<20 MPa√m). For both temperatures, testing in vacuum produced higher FCP rates. This difference in the propagation behaviour was

linked to closure mechanisms promoted by additional oxide formation during the air tests, which imparted a greater influence on the crack growth rate at low ΔK levels due to smaller crack opening displacements.

Sengputa et al. [100] have studied the fatigue behaviour of CMSX-4 at 650°C. Testing was carried out on compact tension (CT) samples with <001> tensile axis and <001> secondary orientation in air. Loading was applied with a constant amplitude sinusoidal waveform of 10Hz and R ratios of 0.1, 0.3 and 0.5. A non-crystallographic growth mechanism was observed at low ΔK levels for all three R ratios. As the ΔK level increases a transition from stage II to stage I crack growth is observed at a microscopic level. This behaviour was linked to the slip characteristics of the material. According to G.R. Leverant and M. Gell [101], single crystal Ni-base superalloys exhibit a wavy homogeneous slip (stage II FCP) at low strain and high temperatures, whereas low temperatures and/or high strains result in a planar heterogeneous slip along the {111} planes (stage I FCP). From experimental observations it was deduced that thermally activated deformation processes must be involved in the determination of the fracture mechanism. Planar slip of dislocations is generated at stress concentrations at the crack tip but are unstable with respect to thermally activated recovery processes such as dislocation climb or cross slip [101]. Suppressing the formation of these planar slip bands, the promotion of stage I is inhibited and stage II crack growth is promoted.

The influence of load ratio, temperature, orientation and hold time on fatigue crack growth of CMSX-4 was also investigated by Muller et al. [102]. CT specimens were machined from <001> ingots, having their tensile axis in the <001> and <011> directions. The crack growth direction was along <010> for both samples. Tests were performed at two temperatures (550°C and 950°C) for R-ratios of 0.1 and 0.7. Some tests were carried out at a fixed frequency of 5Hz, whilst in others the frequency ranged from 5Hz at high ΔK to 50Hz at low ΔK within one test. In order to investigate the effect of hold time, a test at 950°C (R=0.7, f=5Hz) was performed where a hold time of 300s was introduced after every 1000 cycles. Although specimens were tested in two orientations no apparent difference in the fatigue behaviour was noted between the secondary orientations. Pre-cracking at room temperature led to the formation of facets due to crystallographic crack growth along the {111} planes which are known to be the glide planes of highest shear stress when the material is loaded in the <001> direction. In addition, the fatigue threshold obtained by the variable frequency tests was considerably lower than that found in tests performed at constant frequency. This was attributed to enhanced oxidation occurring from the increased exposure time (for the low frequency tests) and the associated closure effects. Fractographic investigation of the 950°C samples revealed that fracture surfaces were smooth and apparently independent of stress intensity. This was attributed to the plastic deformation along the {100} planes, which is constrained to the γ

channels. The oxide film on the fracture surfaces (speculated to be Al_2O_3) was measured visually and was found to be dependent only on the exposure time at 950°C. The fatigue thresholds at 550°C were found to be lower than at 950°C and this was explained in terms of decreased oxide induced closure at the lower testing temperature. Although different thresholds were measured, the FCP rates in the Paris regime were comparable at both R-ratios at 550°C. Fractography showed macroscopically smooth fracture surfaces (similar to the 950°C test) and an oxide scale at low and medium ΔK levels. At higher ΔK levels, due to the easier shearing of the γ' particles, the fracture surface seems to deviate from stage II controlled propagation especially at the sample edges where propagation seems to occur along the {111} planes.

In agreement with other work on another Ni-based superalloy [103], the FCP rate in [102] generally increased with increasing load ratio since the magnitude of the mean tensile stress acting on the crack also increases. However, Sengputa et al [100], who also found that the FCP rate increases significantly with increasing load ratio, attributed the effect to the interaction of the crack with the environment. They proposed that oxygen diffusion at the crack tip moves along dislocations pins them down and causes oxidation embrittlement of the surface. The embrittlement effect is strongly dependent on the maximum load applied and therefore, a higher load ratio will increase the FCP rates. Testing conducted on CMSX-4 at room temperature [104] showed that the load ratio effects on the FCP rate are dramatically reduced (since oxidation embrittlement is almost eliminated), enhancing the speculation that increased load ratio effects are due to environmental interactions.

2.4.3 Creep Behaviour

The yield stress of a number of <001>-oriented single crystal superalloys, including CMSX-4, is shown with respect to the surrounding temperature in Figure 2.16. The yield stress seems to remain rather constant (~900MPa) up to a temperature of approximately 700°C and it falls rapidly if the temperature is increased beyond 850°C. However, in reality, the possibility of a time-dependent plastic deformation is of great importance at stresses considerably lower than the yield stress. This process is known as creep deformation. Creep behaviour of 2nd generation SX Ni-based superalloys is well documented in the literature [91,105–110]. Tests are normally conducted at higher temperatures (750°C to 1000°C) as the time and stresses required to cause creep rupture at lower temperatures are significantly high. For example, Penkalla and Schubert [110] have found that creep failure, in CMSX-4 at 700°C and stress of 700MPa, occurs after 120h. Similarly, Matan et al. [107] have reported a minimum creep life of ~220h at 750°C and 750MPa for a number of samples that had their primary crystallographic orientations at various small angles away from the [001]

tensile axis. However, these stresses are well above the average stress levels that are normally seen in service and failure under these conditions is unlikely to occur. In addition, as seen in Figure 2.30, for temperatures below 500°C inelastic creep deformation is insignificant in CMSX-4, while for temperatures up to 600°C plastic deformation only occurs for stress levels above ~85% of the yield stress. Therefore creep failure is generally considered in the literature for temperatures in excess of 700°C.

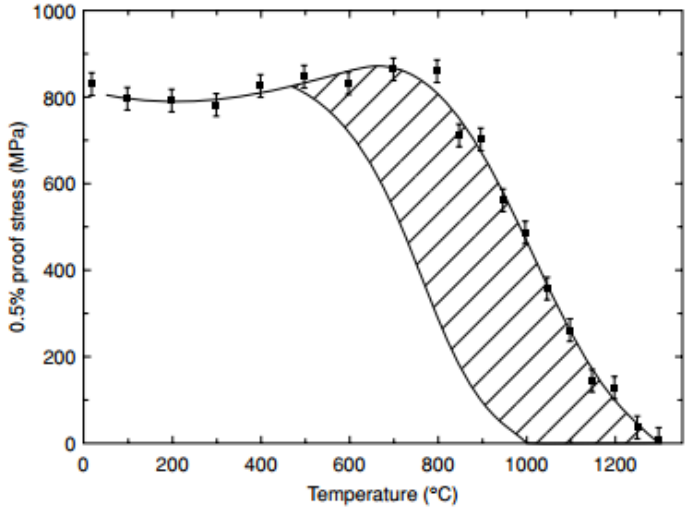

Figure 2.30: Yield stress variation of <001> orientated CMSX-4. Hatched regions shows the conditions under which plastic creep deformation is observed [2].

2.4.4 Review of oxidation-fatigue damage mechanisms with emphasis on modelling approaches

The interaction between oxidation and fatigue is two-way and is both frequency and temperature dependent. In many early attempts [111–114], the problem was approached by simply considering a linear summation of two independent damage mechanisms: oxide induced (time dependent) crack propagation and fatigue (cycle dependent) crack propagation i.e. $\frac{da}{dN}_{total} = \frac{da}{dN}_{fatigue} + \frac{da}{dN}_{oxidation}$. This approach however, fails to capture the synergistic phenomena that simultaneously take place ahead of a propagating crack. This issue can be exacerbated at intermediate temperatures where neither of the two mechanisms (cycle or time dependent) dominates. Such interactions have already been proved experimentally and include the following:

- Oxidation induced crack closure due to the formation of thick oxides on the crack tip surfaces during dwell fatigue. Wedging of the crack tip and crack wake reduces the effective stress intensity factor [98].

- Acceleration of the oxidation kinetics and diffusion of oxygen due to the mechanical cycling loading and strains at the crack tip. This can lead to embrittlement and general degradation of the mechanical properties in a micro-volume ahead of the crack tip [115,116]. Direct evidence of such an embrittled zone have been previously shown in CMSX-4, when the FCP rates of pre-oxidised and non-oxidised specimens have been compared [117] (e.g. Figure 2.31).
- Oxygen adsorbing on freshly emerging slip steps during fatigue inhibits the reversed slip mechanism and effectively results in larger, net slip irreversibility [85,118,119].

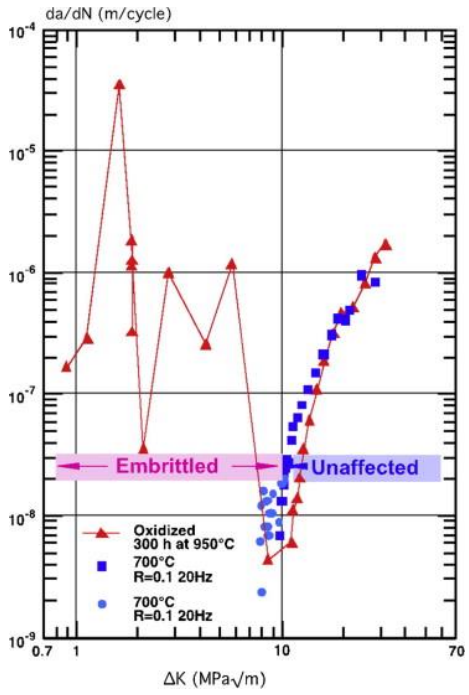

Figure 2.31: Comparison of the fatigue crack growth rates of a preoxidised and a virgin CMSX-4 samples tested at 700°C [117].

Even though it is recognised that the synergistic effects between oxidation and mechanical fatigue should be accounted for in any life or damage prediction models, the physical mechanisms underpinning the process are still not well understood. In order to gain a better understanding of the current interpretations of the synergy mechanism, the relevant models available in the literature are presented here. As expected, there are a large number of models considering high temperature fatigue in the literature but this review will focus on models that meet the following criteria:

I. Oxidation damage is the main environmental degradation mechanism and its detrimental effects are considered on the basis of an embrittlement mechanism.
II. The model is applied, or has the capability of being applied to single crystal superalloys.
III. Crack propagation is explicitly and comprehensively considered in the model.

A model considering an oxidation-embrittlement damage mechanism has been developed by Remy et al. [120] for the polycrystalline cobalt-based superalloy MAR-M509. The oxidation-assisted fatigue damage was attributed to a decrease in the critical stress for monotonic fracture ahead of the crack tip, due to oxygen diffusion. The crack growth is then treated as a dynamic crack nucleation event based on the total life ($N(\lambda)$) of an oxidised microstructural volume element (λ) ahead of the crack tip. The variation of the critical stress with distance from the crack tip is correlated through an empirical equation to the variation of oxygen concentration ahead of the crack tip. Oxidation of the interdendritic regions is assumed to be the controlling oxygen related damage and thus oxygen concentration head of the crack tip was related to the depth of an interdendritic oxide. The applicability of the model to single crystals is brought into question since none of the damage mechanisms considered (mechanical and environmental) prevail during high temperature fatigue of such systems. Heterogeneities in the two-phase single crystal Ni-base superalloys primarily exist at the microscopic level from the presence of γ' precipitates and at the mesoscopic level from the presence of casting defects, such as porosity. In addition the depth of oxygen diffusion could be larger than the depth of oxide (which is also known to be affected by stress/strains [121]). The propagation of a fatigue crack in a single crystal alloy and the effects of oxidation would therefore be expected to firstly interact with the aforementioned heterogeneities.

A more recent study by Remy et al. [117], seems to be addressing some of these issues by employing a crystallographic constitutive model [122]. In contrast to the model described above, the constitutive equations here were written at the micro-scale and deformation is linked to slip irreversibility at the crack tip. The interaction between oxidation and fatigue is introduced in a similar manner to the previous model, by assuming that localised oxidation reduces a critical strength value which corresponds to a volume ahead of the crack tip. The kinetics of oxidation are considered by taking into account the influence of plastic deformation. Even though the model seems to be short crack based the physics of micro-crack growth proposed can be used for the growth of long cracks. A limitation of this model lies in that fact that, despite damage along crystallographic slip and the concept of slip irreversibility being considered, the effects of oxidation on the slip behaviour [85,118,119] have not been taken into account.

The brittle fracture of oxides at the crack tip and the contribution of this towards fatigue crack propagation was later investigated and an analytical model was proposed by Martinez-Ensaola et al. [123]. The fatigue term is modelled in terms of crack tip plastic blunting and the fatigue crack growth rate is obtained through a modified Paris type equation. The effect of oxidation is assumed to be twofold. Brittle failure of the oxide scales forming at the crack tip enhance crack growth rates during crack opening (added as a separate $\frac{da}{dN}_{oxidation}$ term) while at the same time, the oxide scales in the wake of the tip wedge the crack and reduce the driving force (ΔK_{eff}) via a closure

mechanism (interaction effect that influences the $\frac{da}{dN}_{fatigue}$ term). The authors also conducted fatigue experiments on CMSX-6 and SRR99 samples at 500°C and found that the da/dN vs ΔK plots had a two way slope that transitioned from the first to the second at a certain ΔK level. It was therefore deduced that two different crack propagation modes exists. The modes were characterised by propagation either through the γ channels or along the crystallographic {111} planes. Based on these findings, it was proposed that in order to capture this change in slope, the Paris law describing the fatigue term of the damage equation should transition accordingly. This transition was presumed to be dependent on temperature and ΔK and should reflect the mode of propagation. At this stage, the authors seem to assume that oxidation would not affect the propagation mode whilst in reality this is unlikely to be the case. Any form of embrittlement at the γ/γ' interface (region of relatively high strain) would cause the crack to propagate within the γ channels. Although to the knowledge of the author, such damage mechanisms have not been explicitly described, there are numerous studies [124–127] that indicate preferential segregation of oxygen at the γ/γ' interface.

The proposed oxide induced closure effect was recently adopted by Kiyak et al. [128] who simulated the oxide scale growth using FE with their results essentially confirming the validity of the mechanism. The failure of brittle oxides at the crack tip and the accelerated growth rates is based on the assumption that the oxides formed contain a major defect whose size is proportional to the scale thickness. Failure of this oxidised zone will occur when the stress intensity factor of the defect (K_{local}) reaches the oxide scale fracture toughness (K_{Ic}^{ox}).

It is however difficult to obtain accurate fracture toughness values for the oxide scales and relevant literature data are rare. Acoustic emission combined with quantitative metallography is most commonly employed to monitor failure in stressed oxides from which strains to failure and fracture toughness values are derived [129–131]. A simpler, less commonly used, method to determine the fracture toughness, of brittle materials, is the use of Vickers hardness indentations [132,133]. However, this method relies on empirical formulae and the idea that measurable cracks are formed from the edges of the indent (high brittleness). A detailed review on the matter is given by [134].

Operating on the same oxidation mechanism assumptions (twofold effect of oxidation) as [123], Bouvard et al. [135] developed a phenomenological model to predict the crack growth rates of the AM1 single crystal superalloy at high temperatures. The model follows the framework of classical linear elastic fracture mechanics and the time effects are captured by considering both creep-fatigue and oxidation-fatigue interactions. As mentioned earlier, the oxidation's twofold effects consist of: i) the thickening of the oxides at the crack tip which increases the opening threshold and ii) oxygen penetration at the crack tip which decreases the local material toughness. The fracture toughness of

the oxide (K_{Ic}^{ox}) is defined through an Arrhenius type equation and was deduced experimentally through fatigue testing conducted on pre-oxidised specimens as described in [115]. The oxide depth is defined as a function of time and temperature and it is also described by an Arrhenius law derived from isothermal oxidation kinetic experiments. The effects of stress on the oxidation kinetics are also considered through the use of an empirical weight function. The beneficial effect on crack growth caused by the thickening oxide layer was modelled considering an analytical solution to define the crack opening and compare it with the oxide scale thickness at a distance (δ) from the tip. A stress intensity factor for crack opening was then defined using the stress calculated from the aforementioned analytical solution in the case where the scale thickness equals the crack opening. This approach seems to extend the model first proposed by Remy et al. [117] and described above, with the added advantage of using *K* rather than stress or other more localised parameters to the crack tip which are difficult to determine.

2.5 Summary of literature review

In this Chapter the various stages of fatigue damage have been firstly presented and then discussed with particular focus on turbine blade Ni-based superalloy materials. By eliminating grain boundaries, single crystal superalloys have significantly improved the life of turbine blades by reducing thermally induced stresses (oriented in the low modulus [001] direction) and by eliminating sliding (creep) and defects associated with grain boundaries. Their unique microstructure which consists of ordered intermetallic γ' precipitates coherently embedded in an FCC γ matrix, offers excellent temperature depended mechanical properties. Although nowadays 6th generation single crystals are being developed, 2nd generation alloys are still being extensively used in the power generation industry. While materials and manufacturing procedures have greatly improved turbine blade performance, their associated costs are very high and there is great industrial interest in optimising maintenance intervals and further extending component life.

During loading in single crystal Ni-based superalloys, the crystal orientation and the shear stress acting in the slip direction on the slip plane (resolved shear stress) will dictate whether plastic deformation will occur. Plastic deformation is then localised in slip bands with most of the dislocation activity restricted within those planes. These so called persistent slip bands result from this stress localisation and are generally encountered at temperatures lower than 700°C and at relatively high stresses. Such bands can form intrusions and extrusions on the surface that can be precursors to fatigue damage. Fatigue damage however, can take place at nominally elastic stresses as plastic deformation can be very localised, typically near sites of stress concentration such as pores.

Fatigue crack initiation during high temperature exposure has been linked to oxide induced surface pits or oxide spallation/cracking. At the same time, depending on the test frequency, at intermediate temperatures, oxidation was shown to interact with surface porosity and promote internal cracking. It is therefore necessary to carefully analyse the interaction of such defects with oxidation and elucidate the damage mechanisms that prevail and the factors that shift the behaviour between them.

The mode of crack propagation depends on the temperature, stress state, frequency and crystallographic orientation. Generally, at lower temperatures and higher stresses, planar slip promotes stage I propagation. At higher temperatures or when stresses are low, dislocation activity is restricted within the γ channels and slip becomes more homogenous, thus promoting stage II crack growth. Oxidation also becomes important as temperature increases as it can hinder slip irreversibility, promote embrittlement and closure effects. Microscopic failure ahead of the crack tip by an embrittlement type mechanism has been mainly examined in polycrystalline Ni-based superalloys, but more recent studies and modelling works have adopted this to explain FCP behaviours in SX superalloys as well. The exact mechanism however is still not well understood, especially at the intermediate service temperatures (400-600°C) of a gas turbine blade.

Although the detrimental effects of oxidation and cyclic loading are generally well investigated individually, the interaction between environment and mechanical loading is less well understood. This issue becomes more important at intermediate temperatures where neither environmental nor mechanical effects dominate. At such temperatures, despite the fact that oxidation reactions are slower (and hence oxide damage is generally expected to be less), the formation of protective oxides such as α-Al_2O_3 and Cr_2O_3 is compromised and the resulting oxidation products have not been yet investigated in detail. Such oxidation processes, by acting synergistically with mechanical loads, can lead to less predictable failures, since they can either enhance or hinder each other.

A number of modelling approaches have been developed aiming to capture the interaction effects but in many cases the lack of robust physical evidence brings them into question. The development of a comprehensive life assessment model requires proper understanding of the damage mechanism that control FCP and the following chapters aim to address this.

Chapter 3 Material Characterisation

3.1 Introduction

The materials used in this study are the single crystalline Ni-based superalloys CMSX-4 and MD-2. CMSX-4 is a 2nd generation superalloy developed by the Cannon Muskegon Corporation in the early 1980s for utilisation in the hot sections of gas turbine units, such as blades and vanes [136]. Particular focus has been given to this alloy throughout this study as it is of most immediate interest to the industrial partners. MD-2 has been recently developed by GE Power (formerly Alstom) with the aim of improving upon the lifetime of their current blade materials and offers an insight into potential future maintenance requirements.

All materials were supplied by GE Power and Uniper Technologies in the form of <001> cylindrical cast bars in lengths of 140 to 160mm. The CMSX-4 batch had undergone a seven stage stepped solution heat treatment with rapid gas fan quench in argon. This was followed by two stages of ageing (air-cooled), to optimise the γ' distribution. The heat treatment followed to produce the MD-2 bars consists of a four step solution treating in argon followed by two steps of precipitation hardening (rapid fan quench in argon followed by air cooling). The specific details of the solution heat treatment and precipitation hardening processes are commercially proprietary to GE Power.

The compositions (at. %) of CMSX-4 and of MD-2 are shown in Table 3.1. CMSX-4 was developed based on the hafnium-containing single crystal CMSX-3 with the aim of achieving higher temperature/stress creep resistance. To realize this, ~3wt% Re and increased amounts of refractory elements (Mo, Ta and W) were added. The main purpose of the Re addition is to retard coarsening of the γ' phase, increase the γ/γ' misfit and as a result to improve the creep strength of the alloy [63]. To allow for the increase in refractory elements the Cr levels have been reduced from previous alloy generations (CMSX-2 and CMSX-3). Even though Cr contributes significantly to the environmental resistance properties of the alloy this reduction was considered acceptable in view of the major gains regarding the high temperature strength. The increased levels of Al and Ti contribute to the formation and strengthening of the γ' phase which further increases high temperature strength. As seen in Table 3.1 MD-2 has a similar composition to CMSX-4. The main differences are seen in the increased Cr levels and in the additions of small amounts of C and B. This was achieved mainly at the expense of Re which is found at levels of less than 0.05% in the MD-2. Carbon was previously shown to decrease the frequency of solidification defects (e.g.

freckle type) [39] and reduce the formation of the as-cast metallic surface scale [137] when used in single crystal nickel-base superalloys. The effects of boron addition and its interaction with carbides in single crystals are much less understood but are generally associated with improved mechanical properties [138].

Alloy	Cr	Co	Al	Ti	W	Mo	Ta	Hf	Si	C	B	Re	Ru	Ni
CMSX-4	7.53	9.71	12.31	1.24	2.07	0.37	2.13	0.32	-	-	-	0.96	-	63.37
MD-2	9.39	5.22	11.32	1.65	2.62	1.29	2.00	0.04	0.02	0.25	0.12	0.04	0.06	65.98

Table 3.1: Chemical composition of the SX Ni-based superalloys CMSX-4 and MD-2 (at.%).

3.2 Experimental Procedures

3.2.1 Microstructural Characterisation

Material cut-offs from cylindrical cast bars were used to produce suitable samples to characterise the microstructure of the alloys. Rectangular samples were sliced from the excess material left from machining the cast bars using a Mechatome T210 linear precision saw with an 11-4207 abrasive wheel (Figure 2.33a). The samples were then mounted in conductive phenolic resin (bakelite) for microscopy examination. For each alloy, samples of the (001), (010) and (100) planes were prepared as shown in Figure 2.33b. Subsequently, the samples were ground and polished on an automatic polisher through the following procedure:

i. 120 grit paper at 250 rpm contra rotating, 10N down-force, 3 minutes
ii. 800 grit paper at 250 rpm contra rotating, 10N down-force, 3 minutes
iii. 1200 grit paper at 250 rpm contra rotating, 10N down-force, 4 minutes
iv. 9μm Diamond suspension on a magnetic “one step” fine grinding disk at 250rpm same rotation direction, 10N down-force, 4-6 minutes.
v. 3μm Diamond suspension on a magnetic nap cloth at 200rpm same rotation direction, 10N down-force, 4-6 minutes.
vi. 0.02μm OP-AA solution on a nap cloth, 150 rpm same rotation direction, 10N down-force, 4-6 minutes

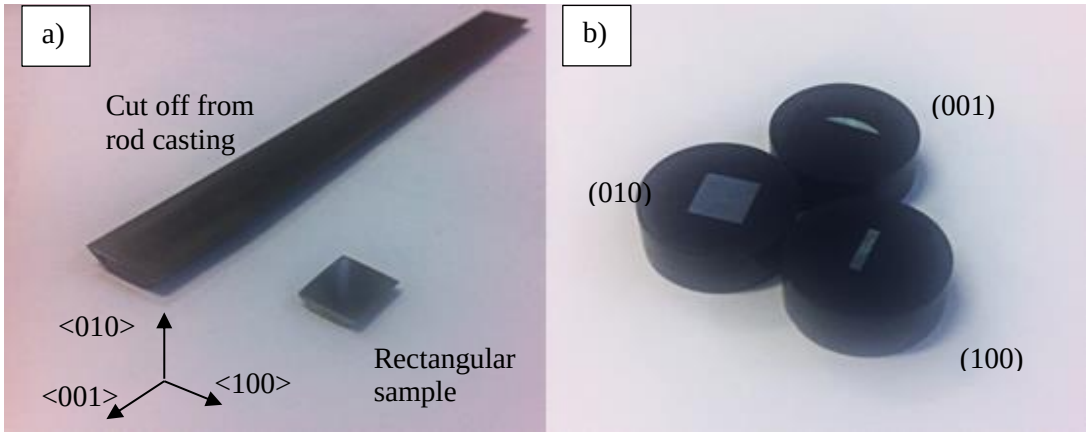

Figure 3.1: Samples used for material characterisation: a) cut-offs from cylindrical bars used to produce rectangular specimens, b) rectangular specimens mounted to conductive Bakelite showing different crystallographic planes for examination.

In order to reveal the microstructure of the material, Marble's Reagent (10g Copper (II) Sulphate, 50ml hydrochloric acid, 50ml water) was used to selectively corrode/etch individual features and phases. Following preparation, the samples were examined under a Wild M420 macroscope, an Olympus BH2 optical microscope (OM) and a JSM 6500F field emission gun (FEG) scanning electron microscope (SEM). Examination of the samples under the SEM was performed in both the secondary electron imaging (SEI) and backscatter electron imaging (BSE) modes. Images were typically taken using acceleration voltages of 10-15kV at a working distance of 10mm.

The primary (PDA) and secondary (SDA) dendritic arm spacing were obtained by analysing SEM BSE and OM images of etched surfaces. To obtain the PDA spacing, the (x, y) coordinates of the (001) dendrite centroids (shown as red dots in Figure 3.2a) were obtained using ImageJ (Fiji). By then using the Nearest Neighbour Distances plugin the average distance between two PDA centres was calculated. The SDA was calculated by averaging 20 measurements taken from a (010) etched sample. The schematics of Figure 3.2 define the PDA and SDA spacing as measured in this study.

Statistical and morphological information for the γ and γ'phases was obtained by analysing high magnification SEM images in ImageJ. Data for the γ' precipitates were obtained from dendritic and interdendritic regions separately while information for the γ matrix was derived from an arbitrary area. The method followed for the analysis is shown in the process flow diagram of Figure 3.3. In addition, element partitioning between the γ and γ' phases was examined using a FEI Talos scanning transmission electron microscopy (STEM) equipped with 4 silicon drift detectors (SDD) for energy dispersive spectroscopy (EDS). The analysis was carried out on a thin foil CMSX-4

sample extracted by focused ion beam (FIB) milling in a FEI Versa 3D dual beam system consisting of a focused gallium ion beam and a FEG SEM.

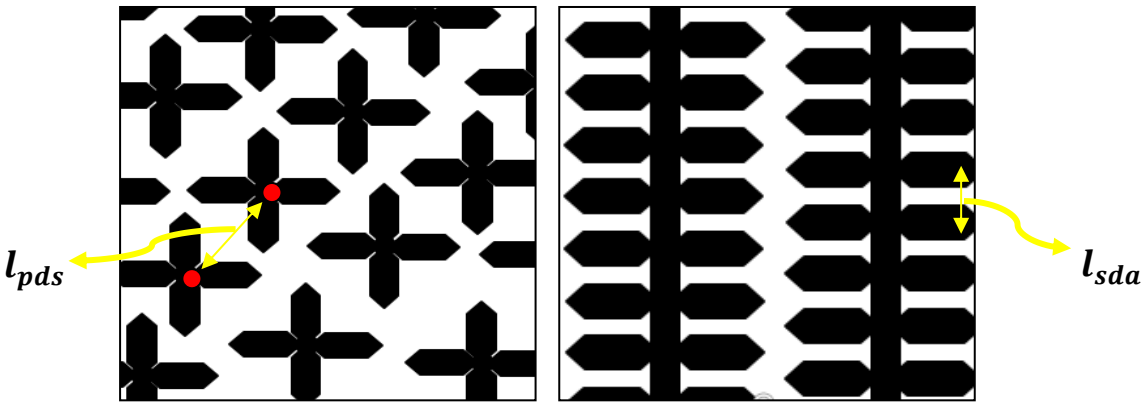

Figure 3.2: Schematic representation of the dendrites on the a) (001) plane and b) (010) plane - illustrating the measurement of primary (l_{sda}) and secondary (l_{sda}) dendritic spacing.

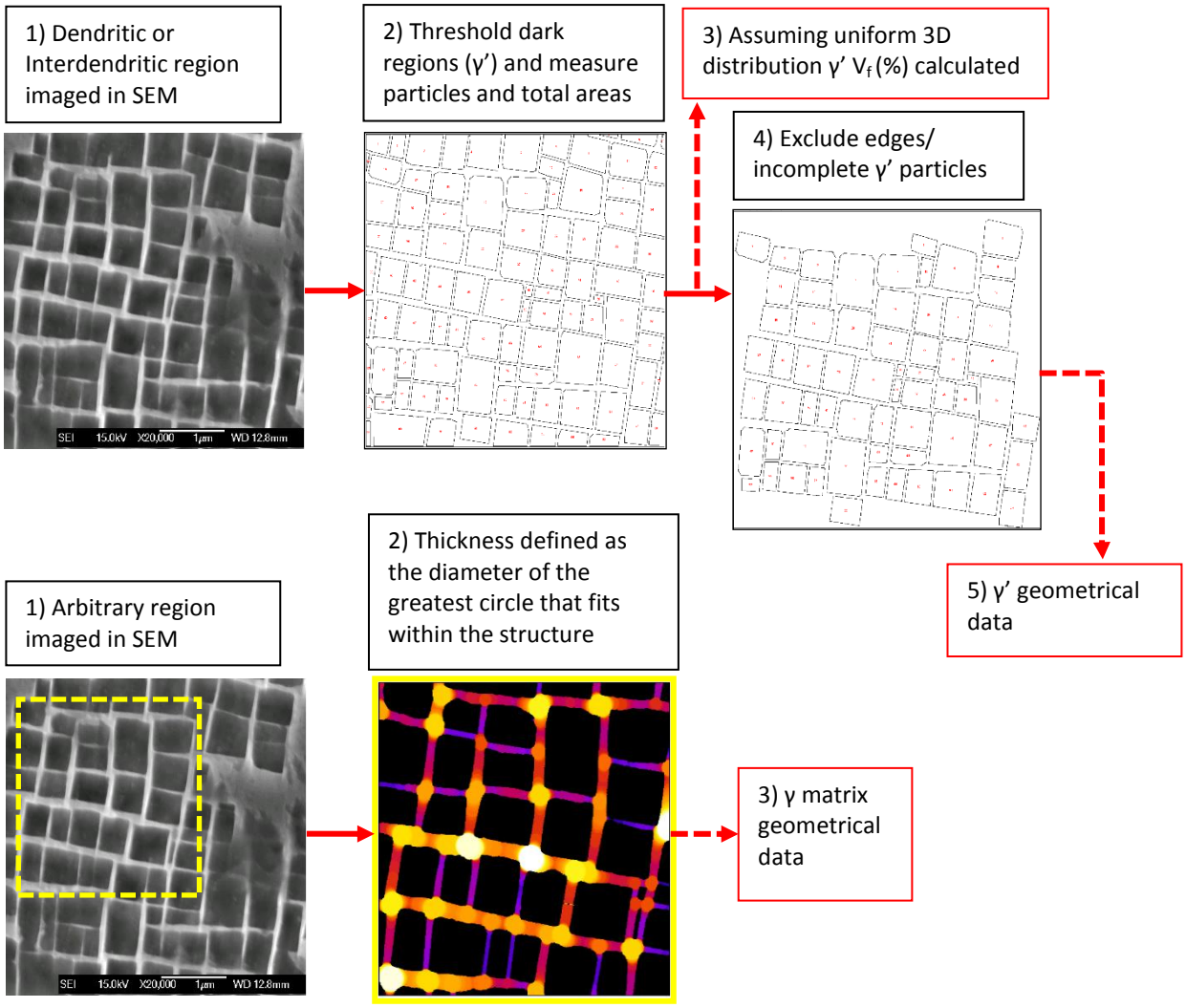

Figure 3.3: Illustration of the steps followed in ImageJ to obtain statistical information on the γ' precipitates and γ matrix of CMSX-4 and MD-2.

3.2.2 Characterisation of porosity and carbides

X-ray computed tomography (CT) was used to study the internal microstructure of CMSX-4 and MD-2. Characterisation of the MD-2 was conducted at the SPring-8 Synchrotron X-ray facility in Japan as part of a separate EPSRC project. The samples used were dog-bone shaped and are schematically shown in Figure 3.4. Characterisation of CMSX-4 was conducted on an in-house XRadia Versa CT scanner using matchstick samples of approximately 0.9mm in diameter. Because porosity is concentrated in the interdendritic areas, volume fraction results can be influenced by the extraction location of the scanned sample. In addition, the field of view of the in-house scanner was limited to 0.7x0.7x0.7mm (compared to 1x1x1mm of the Spring8 facility) which compromised the statistical representation of the results. In order to avoid this, scanning was conducted on two CMSX-4 samples, extracted from random locations from a <001> cast bar and the results were averaged. To quantify porosity and carbide information, segmented data was processed using the

ImageJ. The scanning set up parameters used for each case (Spring 8 and in-house XRadia Versa) are shown in Table 3.2.

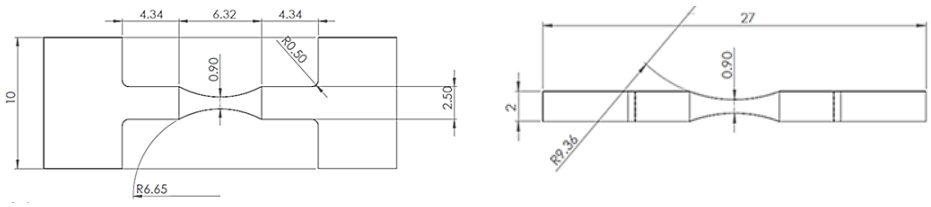

Figure 3.4: MD-2 samples used for X-Ray characterisation at the SPring-8 facilities.

Parameter	**SPring-8 Synchrotron CT**	**In-house (XRadia Versa) CT**
Energy	53 kV	160 peak kV, 10W
Voxel resolution	0.5 µm	0.755 µm
Scan time	1.2 hours	~9 hours
Number of projections	1800 (180° rotation)	1501 (360° rotation)
Exposure time	2 s	27 s
Detector binning	x1	x2

Table 3.2: Scanning parameters used for X-Ray characterisation of MD-2 and CMSX-4 samples at the Spring-8 facilities and in house.

3.2.3 Tensile testing

High temperature tensile tests were carried out on dog bone shaped samples (Figure 3.5). All tests were completed at Uniper Technologies Ltd. (formerly E.ON) with the support of technical staff working there. The tensile tests were performed on an Instron 5500R 100kN test machine in air with an initial strain rate of 0.00025mm/mm/s up to yield followed by a strain rate of 0.002mm/mm/s until failure. Heating was applied with a split furnace and the temperature was measured using three K-type thermocouples equidistantly placed along the gauge length. The temperature gradient over the gage length did not exceed ±2 °C. Strain variations were monitored with a high resolution Instron extensometer while the applied load was continuously recorded directly on a computer. A total of 3 tensile tests were run to rupture the details of which are given in Table 3.3.

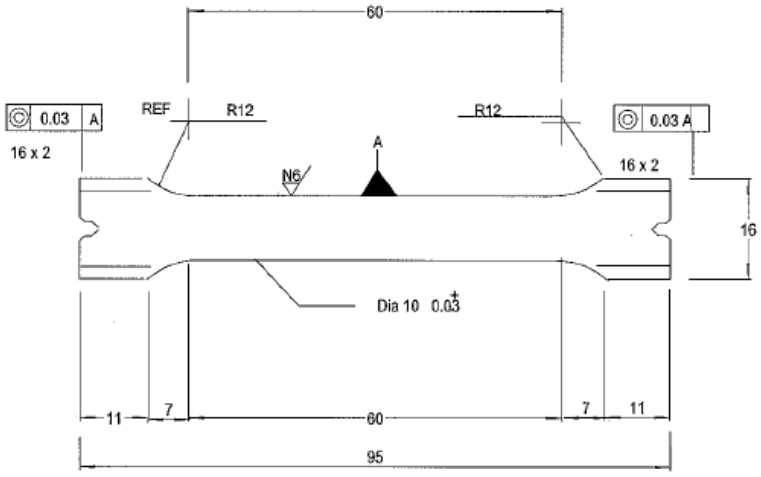

Figure 3.5: Sample dimensions used for high temperature tensile testing.

Material	Temperature (◦C)	Tensile axis	Θ (deg.◦)
CMSX-4	550	<001>	3-8
MD-2	550	<001>	2-7
MD-2	450	<001>	2-7

Table 3.3: List of high temperature tensile tests conducted to obtain constitutive materials data for the FE model.

3.3 Results

3.3.1 Microstructure

Figure 3.6 shows OM images of the dendritic structures of CMSX-4 and MD-2 on the (010) and (001) planes. Dendrite orientation was later used to determine the notch direction of the fatigue test specimens. The secondary dendritic arms are known to grow along the <100> directions [139] and with the longitudinal cast direction known, the samples could be orientated accordingly. The PDA and SDA spacing are presented in Table 3.4 , where CMSX-4 is shown to have wider spacing between its dendrites. The dendritic structures, imaged in SEM using the BSE mode, are shown in Figure 3.7 for CMSX-4 and Figure 3.8 for MD-2. Segregation of elements with higher atomic numbers (such as Re and W which tend to partition during solidification [9,140]) into the dendritic regions (lighter colour) provides the contrast in the images. Porosity is clearly visible on the surface of the CMSX-4 sample and appears to be mainly interdendritic in nature (Figure 3.7b). The inclusion of carbon in the composition of the MD-2 alloy has resulted in the formation of metallic carbides (MC) within the interdendritic regions (Figure 3.8b and c). Energy dispersive X-ray spectroscopy (EDX) revealed that these mainly consist of Ta and/or W (Figure 3.8d).

The microstructure of the materials was examined by observing polished and etched surfaces under the SEM. Both alloys exhibit the typical, cuboidal γ/γ' microstructure which is shown in Figure 3.9 for CMSX-4. Figure 3.9(b) was taken from [9] which studied the same batch of CMSX-4 and shows the crystal lattice as projected from the (111) plane under the BEI mode for both the etched and plain polished conditions. As seen in Table 3.5, both alloys exhibit similar high γ' volume fraction (>70%) and sizes (~200μm² area). The size and volume fraction of the γ' particles were found to be smaller in the interdendritic areas of both alloys. This is in contrast with expectations as γ' forming elements (such as Al, Ni, Ti) tend to segregate within the interdendritic regions [55,141]. This unexpected difference in the results might be attributed to the methodology followed for the analysis. Variations in etching (dissolution of the γ matrix), the surface preparation and 3D/volume effects (only 2D sections investigated) can all contribute to deviations in the results. In addition, it is also important to mention that secondary precipitates that are present in both alloys, have not been taken into account during the analysis since they are extremely small in size but could have also contributed towards this variation in the results.

The STEM-EDS composition maps presented in Figure 3.10 show the partitioning of the main alloying elements between the γ and γ' phases in a CMSX-4 sample. As expected, the γ' phase shows increased concentrations of Al and Ni and also contains Ti, W and Ta. The γ matrix, which also contains Ni (albeit at lower levels) mainly contains Cr, Co and Re.

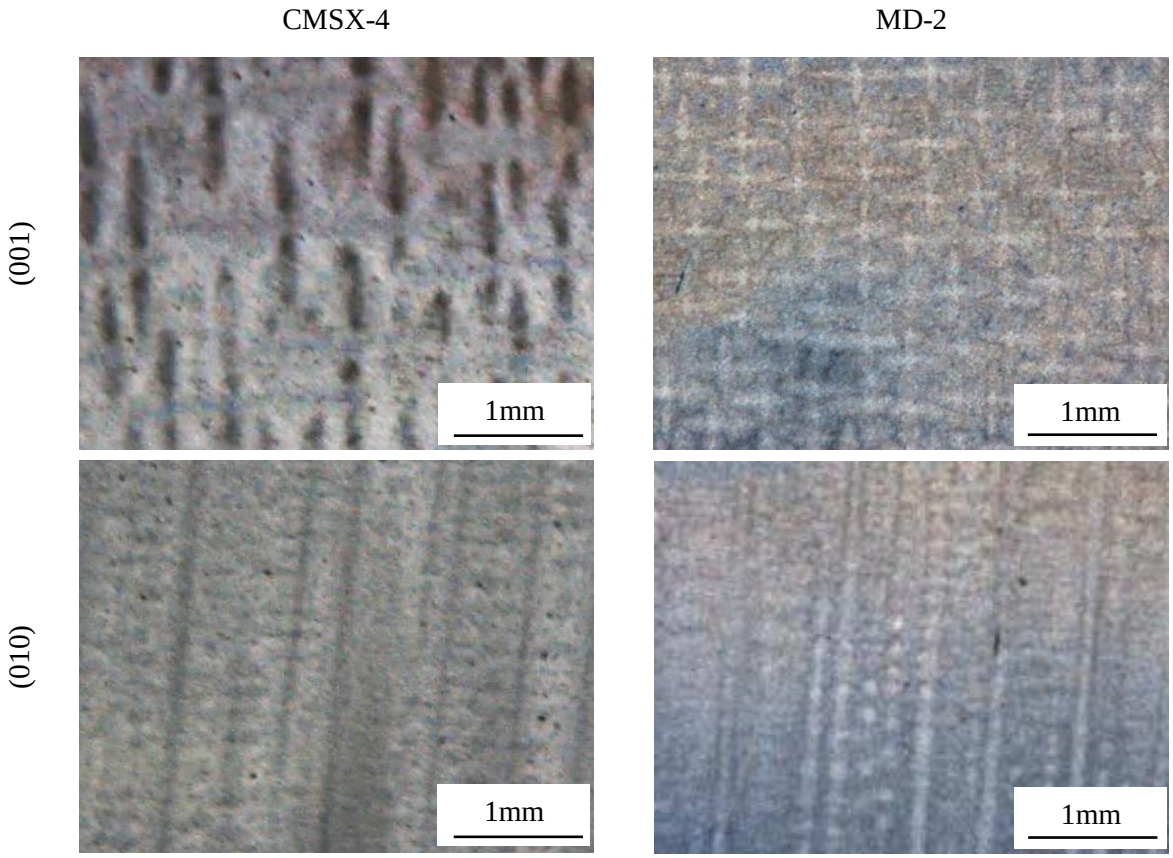

Figure 3.6: Optical macroscope images of polished and etched surfaces showing the dendritic structure on the (001) and (010) planes CMSX-4 and MD-2 .

Alloy	PDA spacing (μm)	SDA spacing (μm)
CMSX-4	552 ± 117	259 ± 38.0
MD-2	445 ± 44.4	164 ± 59.8

Table 3.4: Dendritic arm spacing for CMSX-4 and MD-2 (± 2 x standard deviations).

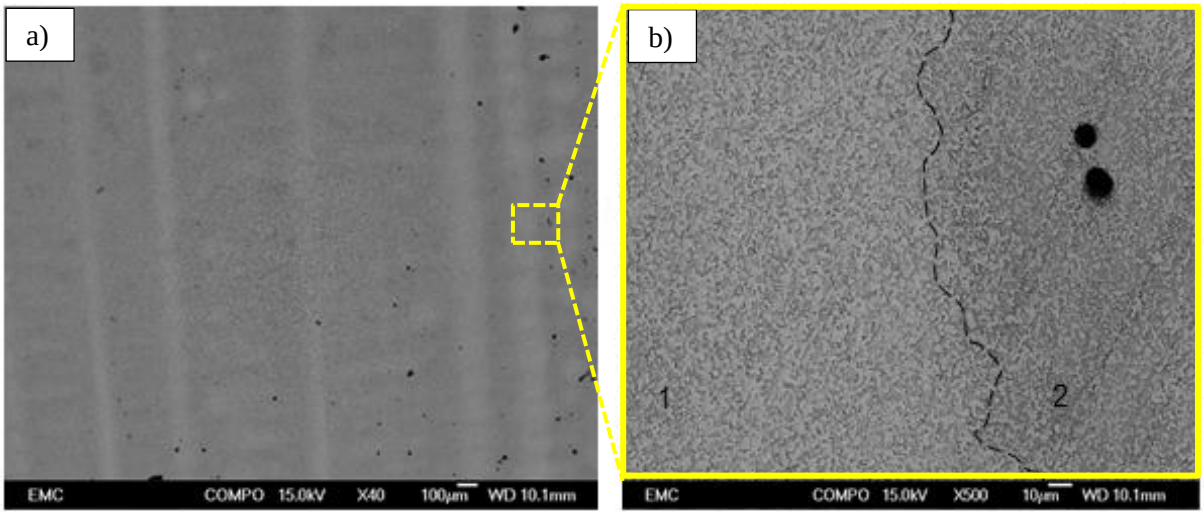

Figure 3.7: BSE images of polished and etched CMSX-4 surface: a) low magnification view of (010) plane, b) segregation of elements between dendritic (1) interdendritic (2) regions.

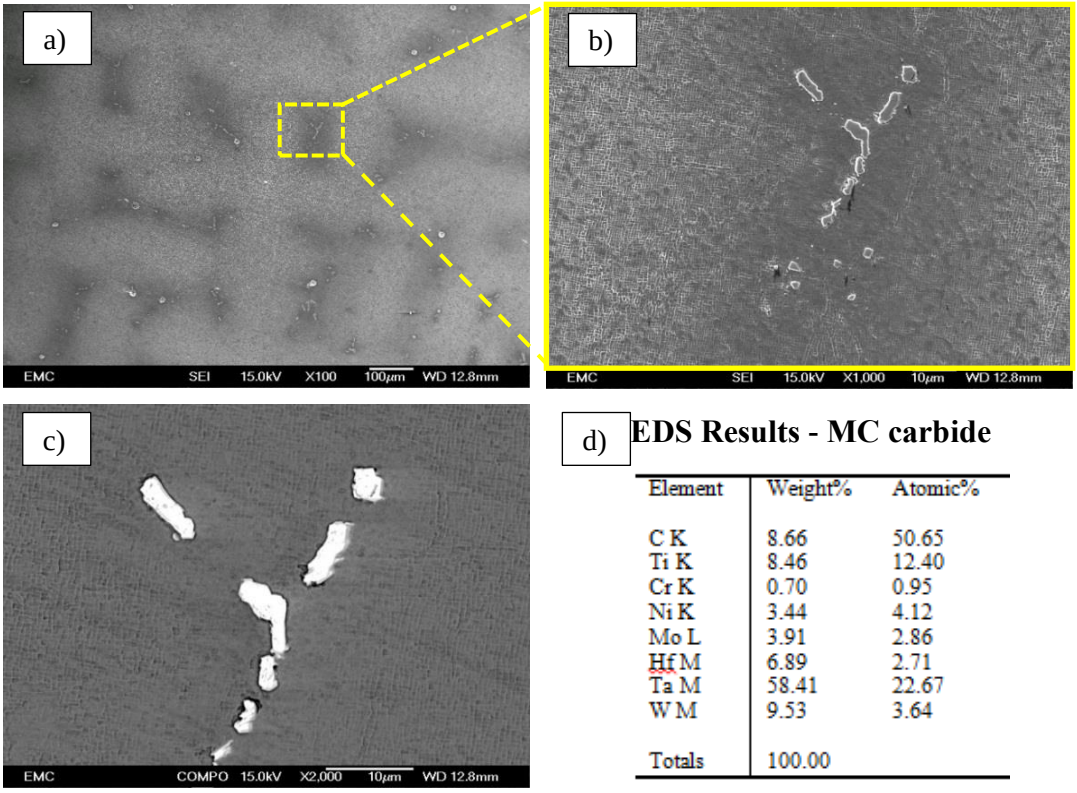

d) **EDS Results - MC carbide**

Element	Weight%	Atomic%
C K	8.66	50.65
Ti K	8.46	12.40
Cr K	0.70	0.95
Ni K	3.44	4.12
Mo L	3.91	2.86
Hf M	6.89	2.71
Ta M	58.41	22.67
W M	9.53	3.64
Totals	100.00	

Figure 3.8: BSE images of polished and etched the (001) surface of an MD-2 sample revealing: a) its dendritic structure, b) and c) the MC carbide formation within the interdendritic regions in the SE and BSE modes respectively and d) EDS point analysis reuslts from the centre of the carbide.

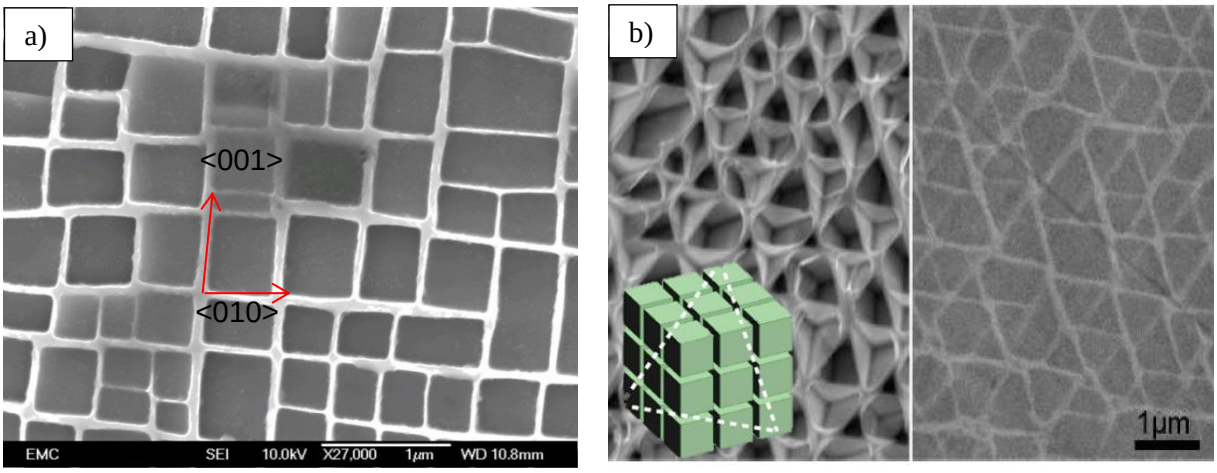

Figure 3.9: 3D cuboidal array and SEM images showing the microstructure of CMSX4: a) SEI mode etched condition b) BSE mode showing the (111) plane in etched and plain polished conditions respectively

Phase	**γ' size (μm^2)**		**^1V_f of γ' (%)**		**γ channels thickness (μm)**
Region	Dendritic	Interdendritic	Dendritic	Interdendritic	
CMSX-4	0.214 (±0.06)	0.205 (±0.08)	71.9 (±2.01)	70.5 (±2.75)	0.141 (±0.05)
MD-2	0.221 (±0.09)	0.203 (±0.08)	79.2 (±3.23)	73.1 (±2.88)	0.125 (±0.05)

Table 3.5: Size and volume fraction data of the γ and γ' phases of CMSX-4 and MD-2

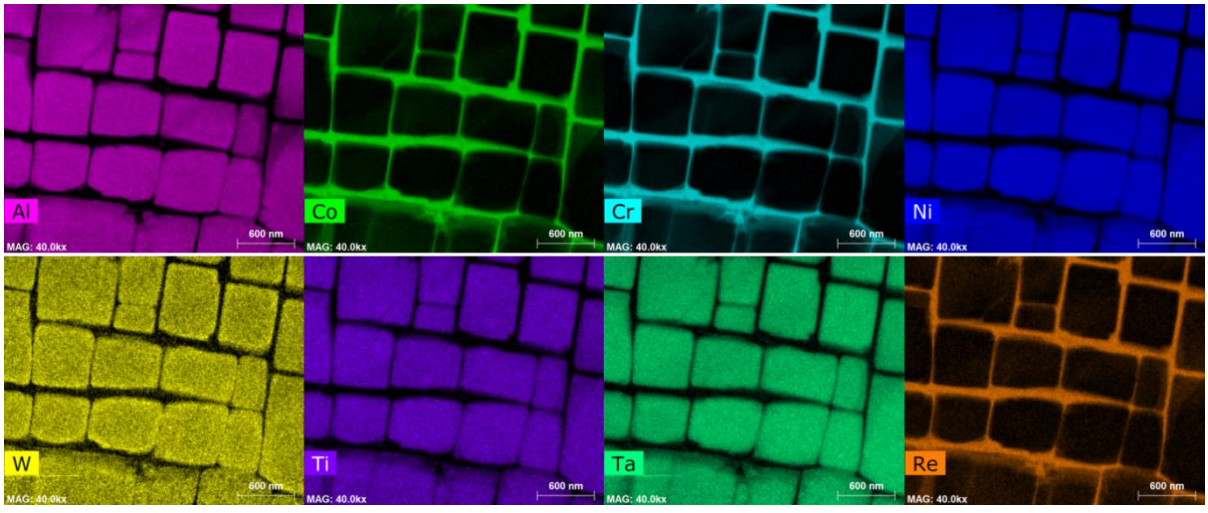

Figure 3.10: STEM-EDS composition maps of the γ and γ' phases of a CMSX-4 sample

[1] The values presented in the volume fraction columns have been derived from 2D measurments.

3.3.2 Porosity and carbide distribution

The 3D renderings of Figure 3.11 show the porosity distribution of one of the CMSX-4 scans. Similarly, Figure 3.12 shows the porosity and carbide distribution of MD-2. The porosity volume fraction of CMSX-4 was calculated as 0.3% for the first scan and 0.11% for the second scan, giving an average of 0.205% (Figure 3.11 shows the sample with 0.11% porosity volume fraction). The large variation between the two values is indicative of porosity clustering within the interdendritic regions. Since the samples were extracted from random locations of a cast bar, the amount of dendritic or interdendritic region include within the scanned volume is expected to affect the results. This can also be confirmed by the plot of Figure 3.11b, which shows the porosity distribution along the (100) plane, normal to the solidification direction of the alloy.

Similar observations were made from the MD-2, where both porosity and carbides were seen to congregate within the interdendritic regions. In essence, the occurrence of a pore is likely to be in close proximity to carbides, with locally dense and sparse distributions of these features. The porosity and carbide volume fractions of MD-2 were 0.12% and 0.20% respectively. Even though porosity is highly dependent on sample location and would also vary between different cast batches the reduced amount observed in MD-2 was expected as it was previously shown that the physical presence of interdendritic carbides reduces the amount of casting defects [142].

CMSX-4 Porosity volume fraction: 0.205%

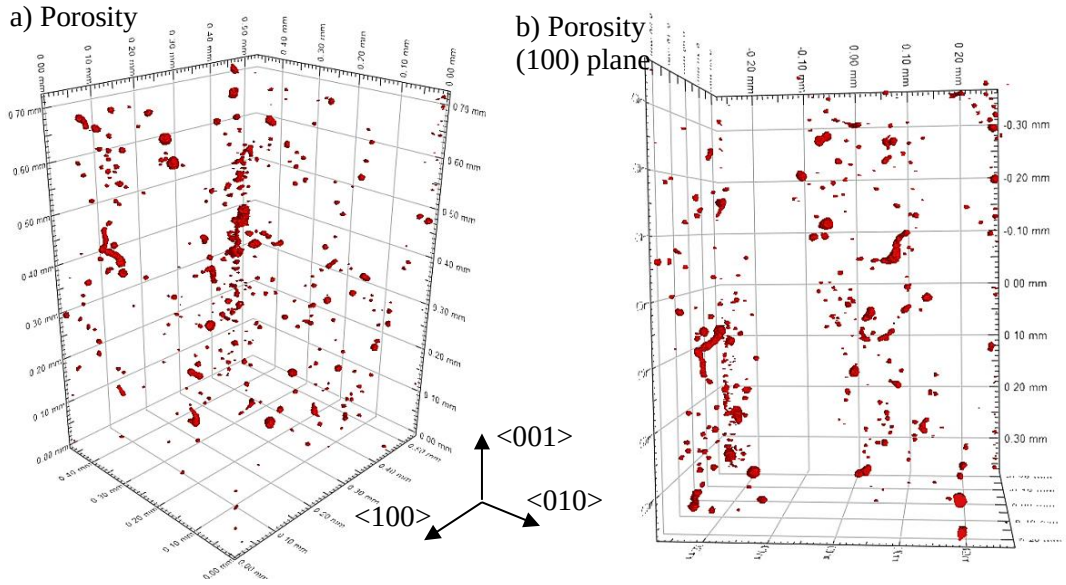

Figure 3.11: X-ray CT of CMSX-4 showing the porosity distribution.

MD-2 Porosity volume fraction: 0.12% Carbide volume fraction 0.20%

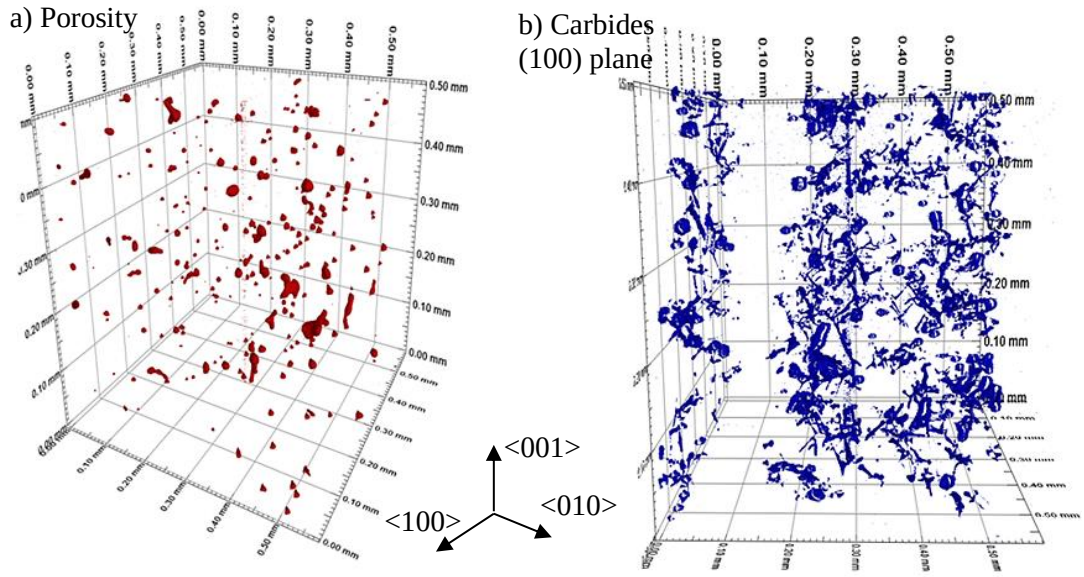

Figure 3.12: X-ray CT of MD-2 showing: a) the porosity and b) carbide distributions.

3.3.3 Tensile properties

Figure 3.13 presents the tensile properties of MD-2 and CMSX-4 at the temperatures of interest. Due to shortage of material only the 550°C test was completed for CMSX-4 but 650°C data, from previous work at Southampton [9], are included for comparison. There is no apparent strain hardening after yielding for either material at all temperatures. In the case of MD-2 it was found that the yield stress decreases as the temperature increases from 450°C to 550°C. On the contrary, in the case of CMSX-4, the higher temperature test (650°C) resulted in a higher yield stress as well. Although this appears an inconsistency in the results it can be explained by considering the expected variation in mechanical properties of single crystal Ni-based superalloys with temperature. As explained in section 2.3.2.2, the flow stress of the γ' in $L1_2$ alloys peaks at a temperature of approximately 800°C. Figure 3.14 shows the variation of yield stress with temperature for CMSX-4. It appears that initially the yield stress decreases to a minimum around 300°C at which point it starts to increase up to approximately 800°C before it exponentially decreases again. The temperatures of 450, 550 and 650°C considered here seem to fall very close to the transition from decreasing to increasing yield stress hence the results obtained seem reasonable.

A summary of the tensile properties for the two alloys is shown in Table 3.6 along with comparative values from the literature. Young's modulus values were in line with those obtained from the literature for both CMSX-4 and MD-2. Larger discrepancies are observed when the values of yield strength and UTS are compared with the ones from the literature. A number of reasons could have caused these discrepancies with the degree of crystallographic misalignment being the most notable. Unfortunately the material available for this study was inherited from a previous project and individual misalignment angles were not available. In addition, Ref. [143] which shows the largest differences in all three parameters compared to the current tests does not provide any misalignment information making direct comparison of the values difficult. Strain rates are also known to affect the high temperature mechanical properties of Ni-based superalloys [144,145] . A <001> single crystal Ni-base superalloy tested at 800°C and 1000°C under various strain rates has shown a positive trend between the applied strain rate and the yield strength [145]. Differences observed in yield strength and UTS could have also been enhanced by the higher strain rate (0.00083mm/mm/s compared to 0.00025mm/mm/s) used in [143].

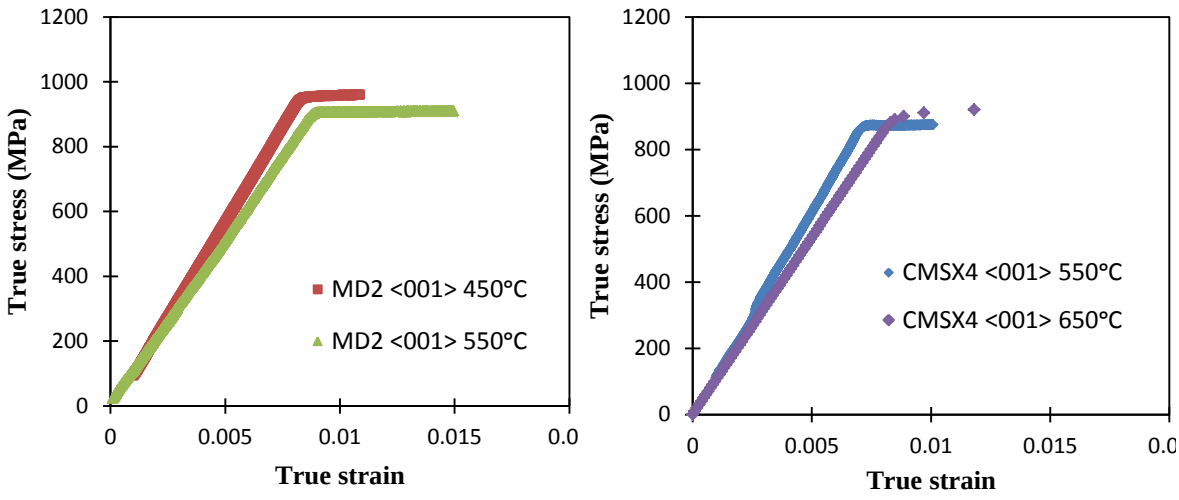

Figure 3.13: Stress strain curves of a) MD-2 at 450°C and 550°C and b) CMSX-4 at 550°C and 650°C

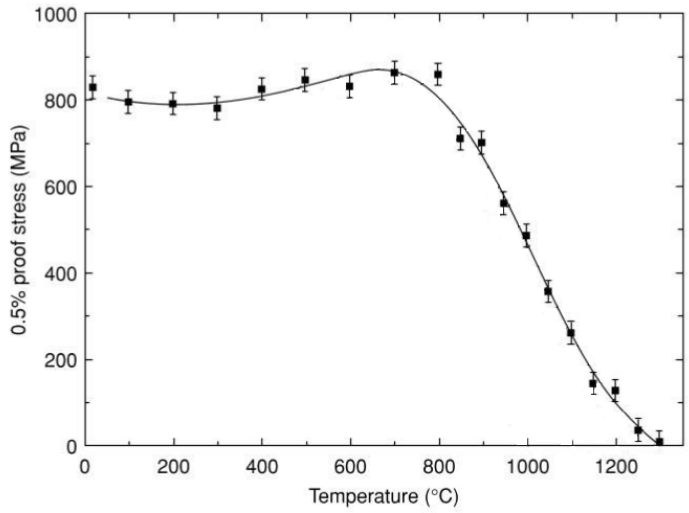

Figure 3.14: Variation of the uniaxial 0.5% yield stress of <001> CMSX-4 with temperature (adapted from [2]).

Material	Temperature (°C)	0.2 proof stress (MPa)	Modulus (GPa)	UTS (MPa)	Elongation (%)
CMSX4 (this study)	550	873	121	875	13.3
	650	943	107		8.8
CMSX-4 [143]	538	929	105	1049	12
CMSX-4 [146]	400	-	119	-	-
CMSX-4 [147]	550	-	118	-	-
CMSX-4 [148]	550	995	-	995	-
MD2 (this study)	450	936	126	957	4.2
	550	905	120	913	2.2
MD-2 [149]	500	880	115	-	-

Table 3.6: Tensile properties of CMSX-4 and MD-2 compared with available literature.

Chapter 4 Oxidation behaviour at 450 & 550°C

4.1 Introduction

Their demanding operating environments unavoidably degrade the performance of turbine blades, with oxidation being one of the main damage mechanisms [150,151]. The chemical composition of single crystal Ni-based superalloys is continuously being improved to resist oxidation as TIT continue to rise. However, these alloys alone are still not capable of withstanding temperatures in excess of ~1200°C without suffering incipient melting [39]. Thermal barrier coating (TBC) technology development [152] along with advances in the internal cooling of the blades enables the base materials to withstand temperatures above their melting point. Similarly to the blade material, TBCs are also subjected to the harsh gas turbine operating environment and are prone to similar failure mechanisms [153]. In the case of spallation or cracking of the TBC the base superalloy would be exposed to high temperature gases where its oxidation resistance would dictate the safe operation of the turbine blade. In addition, parts of the blades (e.g. fir tree root, cooling passages) are usually left uncoated and even though they operate at much lower temperatures (typically <650°C) they are directly exposed to oxidation damage. The complex geometry of these components also results in areas of stress concentration and it is known that mechanical stresses can further influence oxidation in Ni-based superalloys. In the limited amount of work available in the literature, two opposing scenarios are generally found. Firstly, the applied stresses may cause scale failure, greater depletion zones and ultimately weaken the near surface material resulting in greater damage [3]. Subsurface pit formation, deeper penetration depths and oxide cracking, which may lead to fatigue crack initiation and faster propagation, could also result from externally applied loads [3,154–156]. On the other hand, the second scenario is that externally applied stresses may reduce the amount of oxide formation [3,157]. This is mainly attributed to the modification of diffusion properties that decrease the less protective transient oxidation period.

The high temperature oxidation resistance of Ni-based superalloys is attributed to the rapid formation of a coherent, chemically stable and adherent oxide scale over their surfaces. Such protection is mostly provided by Cr_2O_3 and the α-phase of Al_2O_3 [23]. Whilst there is an extensive body of research [22,23,27,82,83] on oxidation behaviour at the highest range of the gas turbine operating temperatures (>700°C), there seems to be little or no previous work on the intermediate to lower temperature oxidation processes of single crystal Ni-based superalloys. At lower temperatures, the thermodynamic driving force for oxidation is inherently reduced. However, at the

same time the formation of protective scales is greatly compromised and the resulting oxidation products have not been yet investigated in detail. Although oxidation damage alone at low temperatures might not be the predominant damage mode, in many cases it has been described as the precursor to fatigue damage [97,158–160]. Understanding the extent of such oxidation damage is particularly important when gas turbine components such as discs and blades are considered. The synergistic effects between environment and mechanical load can be catastrophic and their systematic characterisation is of critical importance in order to accurately inform lifing approaches. Oxidation also plays an important role as a contributor to enhanced fatigue crack growth and it has been the subject of investigation by many researchers [161–163] mostly centring on the mechanisms within the crack-tip oxygen induced damage zone and the role of dynamic embrittlement. Generally, these phenomena are considered when temperature and strain rate (frequency/dwell time) allow significant amounts of oxygen to diffuse to the crack tip. However, the severity of this damage mechanism (embrittlement) can be high even at intermediate/low temperatures where the formation of compact and adherent oxides (such as Cr_2O_3 or α-Al_2O_3) is restricted.

The aim of this chapter is therefore to capture the physical phenomena that characterise isothermal oxidation at 450°C and 550°C and provide an initial assessment on the effects of externally applied loads on the oxidation behaviour of CMSX-4 and MD-2.

4.2 Experimental procedure

The oxidation performance of the two alloys was investigated under isothermal conditions, at 450°C and 550°C in static, laboratory air. Oxidation kinetics were assessed through oxide scale thickness measurements and mass change measurements. Table 4.1 summarises the tests conducted. Although a complete kinetic record was obtained using a single specimen from the continuous thermogravimetric measurements, by examining cross sections of oxidised samples exposed for different times, growth rates for internal and external oxides were also obtained. As an additional test, the effects of externally applied loads were investigated on a CMSX-4 sample at 550°C.

Temperature (°C)	CMSX-4		MD-2	
	TGA	Thickness	TGA	Thickness
450	✓	-	✓	-
550	✓	✓	✓	✓

Table 4.1: Test matrix showing oxidation temperature and approach taken to assess growth kinetics.

4.2.1 Thermogravimetric analysis (TGA)

Sample preparation

The samples used for TGA were produced from heat treated <001> rod castings in the form of 1.5mm thick and 10mm in diameter (tolerances of +/- 0.005mm) discs, which were sliced perpendicular to the solidification direction of the rod. A hole with diameter 1mm was machined 2.5mm from the edge of the discs to allow suspension of the samples in the furnace. Figure 4.1 shows a schematic of the disc sample geometry and its orientation. Standard metallographic procedures were followed to polish these samples which resulted in an average surface roughness (R_a) of 0.04μm, measured using the Form Talysurf profilometer. To ensure there was no contamination on the surface, a cleaning process consisting of a 15 minute immersion in a degreaser (Volasil) and a further 15 immersion in isopropyl alcohol was carried out prior to testing.

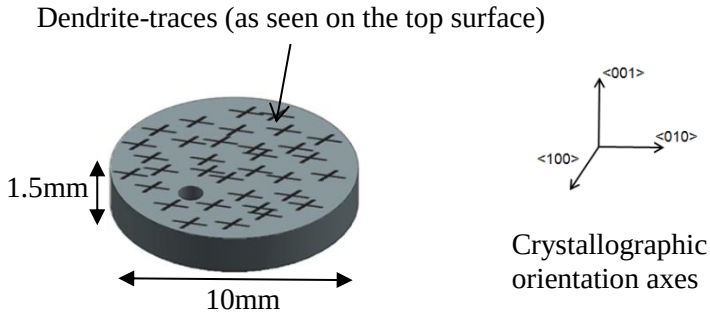

Figure 4.1: Schematic illustration of TGA specimen geometry and orientation with respect the crystallographic directions.

Testing procedure

All TGA experiments were conducted by Dr. Adriana E. Oropesa at Cranfield University utilising a Setaram 'Setsys Evaluation' TGA system. This is a very sensitive system (resolution of 10μg) that allows a single sample of < 1g to be exposed at a temperature of up to 2400°C in a controlled atmosphere environment. During exposure, the weight of the sample and the temperature of the exposure zone were monitored at 50s intervals and automatically recorded on the computerised control system. Testing was conducted in dry air (bottle supplied) for periods of 200 hours. The TGA system and the sample set up are shown in Figure 4.2.

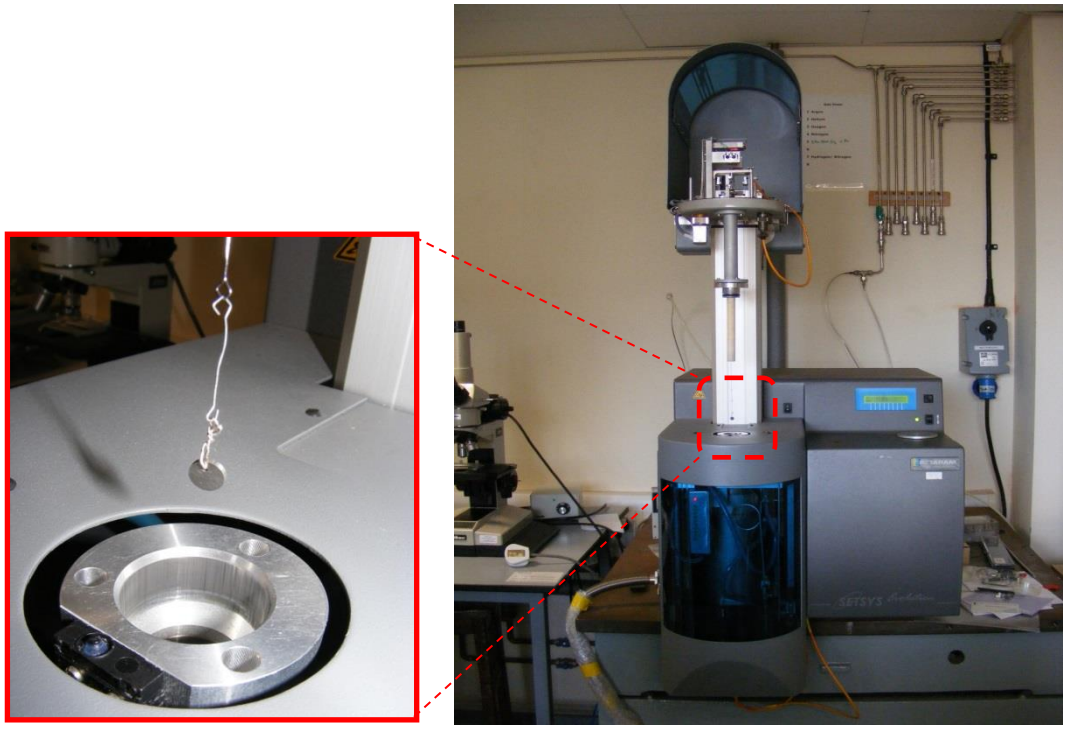

Figure 4.2: The Setaram 'Setsys Evaluation' TGA system at Cranfield University showing how the sample is loaded into the furnace.

4.2.2 Oxide thickness analysis

Sample preparation

To supplement the TGA analysis an additional set of 20 coupon samples (10x10x3mm) 10 for each alloy, was used for oxide thickness measurements. The samples were produced from cut-offs remaining after machining <001> cast bars. A cutting diagram and the sample dimensions are illustrated in the schematic of Figure 4.3. Prior to oxidation the samples were ground down to a 4000 grit SiC paper following a series of 2 min grinding steps (120, 800, 1200 and 4000 SiC grit papers). A 3μm diamond suspension and a 0.02μm active oxide polishing (acidic alumina - OPAA) suspension were then used to polish the samples. A time period for each polishing step of 3 to 4 minutes was adequate to achieve a mirror like finish. Finally, the samples were ultrasonically cleaned in methanol for 10 minutes.

After the completion of the oxidation tests and an initial examination of the oxidised surface additional preparation steps were taken prior to the SEM investigation of the oxide scale profile. Firstly, the oxidised surface was coated with Nickel to preserve its integrity. A Watt's solution (500ml H_2O, 150g Nickel Sulphate, 20g Nickel Chloride, 20g Boric Acid) was used as the plating bath. A 99.9% Nickel rod was used as an anode whereas the specimens were acting as the cathode. The temperature of the solution was controlled between 50-60^{o}C with a hot plate

and the process was accelerated by a magnetic stirrer. A potential of 3V with a current of 1.5A was applied across the system for approximately 45min to ensure the entire surface was sufficiently coated. The apparatus set up for the nickel plating is shown schematically in Figure 4.4.

Once plated, the samples were sectioned along their width (perpendicular to the growth direction of the dendrites) on a Mechatome T210 automatic cutting machine with diamond abrasive wheel. The samples were then mounted in conductive bakelite leaving their cross sections exposed (Figure 4.5). The grinding and polishing sequence shown in Table 4.2 was followed to remove the effects of the cutting saw and reveal the oxide. An automated polishing machine that allows for duration, rotation speed and pressure control was used for all steps. It is important to note that great care was taken as oxide scales are very fragile and have differing hardness from the substrate alloy. Oxide scales are damaged to a greater depth than the metal and porosity/cracking may be induced on their surfaces if this is not accounted for [28]. To avoid this, more steps were included in the sequence, and grinding and polishing times were increased with each step.

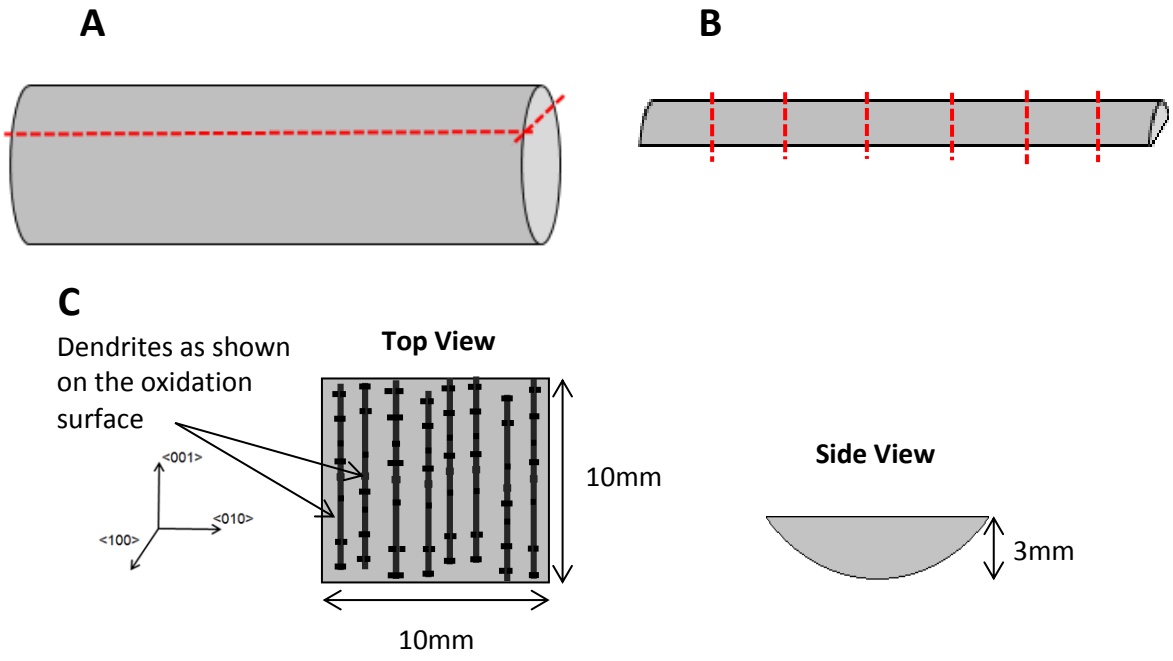

Figure 4.3: Schematic illustration of the CMSX-4 isothermal oxidation samples used for oxide scale thickness measurements. The letters A-C represent the cutting sequence for the production of the samples. The crystallographic orientation and the oxidised surface are also shown.

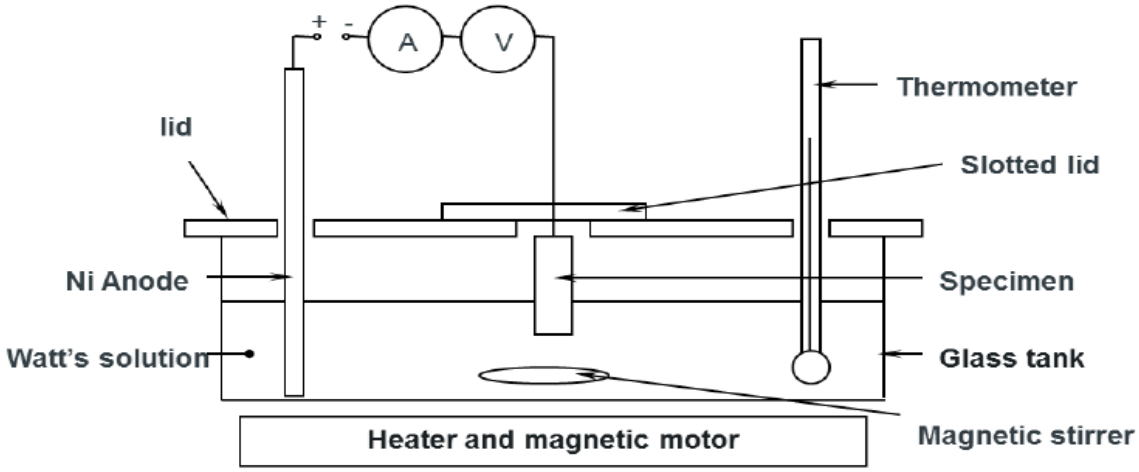

Figure 4.4: Schematic illustration of the nickel plating apparatus used to coat the oxidised samples prior to sectioning.

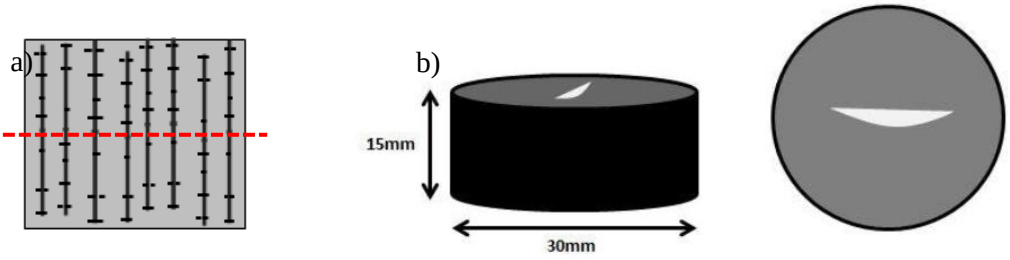

Figure 4.5: a) Shows the orientation of the section with respect to the dendrites on the surface of the sample and b) shows the exposed cross section of the sample after being mounted in bakelite.

No.	Paper/Cloth	Lubricant	Duration (min)	Force (N)	Speed (rpm)
1	120grit SCi	Water	1-2min	10N	225
2	800grit SCi	Water	2-3min	10N	225
3	1200grit SCi	Water	3-4min	10N	225
4	Satin woven acetate magnetic cloth	Water based 9µm diamond suspension	4-5min	10N	200
5	Satin woven acetate magnetic cloth	Water based 3µm diamond suspension	4-5min	10N	150
6	Porous Neoprene magnetic cloth	Water diluted active oxide polishing (0.02µm acidic Al) suspension	10-12min	10N	150

Table 4.2: Grinding and polishing sequence followed for sectioned oxidised specimens prior to SEM examination.

Testing and Characterisation Procedures

Ten samples of each alloy were oxidised, in a pre-calibrated (+/-2ºC) electric furnace, for 1h, 5h, 10h, 20h, 40h, 80h, 160h, 320h, 640h and 1000h respectively. The experiments were conducted in an RHF 1600 furnace fitted with a Eurotherm 3200 temperature controller. The prepared samples were placed on ceramic boats and the furnace was left to stabilise at the desired temperature for 1h prior to exposure. After testing, each sample was allowed to cool in laboratory air for 10-15min before being stored in a desiccator.

Following completion of the oxidation test the surface of each sample was investigated under an Alicona Infinite Focus microscope (IFM G4) and in a JEOL 6500F Field Emission Gun Scanning Electric Microscope (FEG-SEM). The Alicona microscope was used to produce surface maps that were later utilised to pinpoint locations of interest for SEM examination. Such points included spallation sites, areas of variable oxide morphology (such as dendritic and interdendritic regions) and surface cracks. The surface maps were created with the built in 3D Image-Field feature of the Alicona software package by recording an array of images aligned in a rectangular pattern and merging them into a single image. More detailed investigation of the surface morphology and composition was undertaken with the SEM using EDS analysis and BSE imaging mode. Surface maps were once more produced by capturing a series of BSE images and stitching them in the ImageJ (Fiji) image analysis software. BSE mode images provided better contrast between areas of spallation, cracking and generally of variable compositions.

A quantitative analysis of spallation on CMSX-4 with increasing temperature was possible by examining the BSE maps. Examination of the oxidised surface of MD-2 samples revealed that spallation was sparse and very small in size, hence similar analysis was deemed redundant. For each surface map a region of interest (ROI) at the centre of the samples was analysed using ImageJ. The ROIs were selected at the centre of the samples (by excluding a strip of approximately 1-2mm around the edge) to avoid possible shape and edge induced effects on the oxidation behaviour.

Characterisation of the oxides on the sectioned samples was carried out in a FEG-SEM and EDS was used to identify their composition. The images were taken in the BSE mode with an acceleration voltage of 15-20kV. A length of approximately 0.5mm at the centre of each sample was imaged to ensure a good statistical representation of the oxide scale formed as this covered the average distance between a set of primary dendritic arms (see section 3.3.1). The BSE images were then stitched together and the external and internal scales manually selected using a graphics pen, allowing the relevant oxide profiles to be extracted and binarised for further analysis (Figure 4.6). A MatLab script[2] was used to systematically process the binary images and to measure the number

[2] The code was written with help of Dr Daniel Bull and can be seen in Appendix A

of black pixels per pixel column which were then scaled to physically representative measurements. Oxide scale thickness measurements however, were not possible for the samples oxidised at 450°C due to the very low scale thickness. For this reason, characterisation of the oxide thicknesses was predominantly focused on the samples exposed at 550°C only.

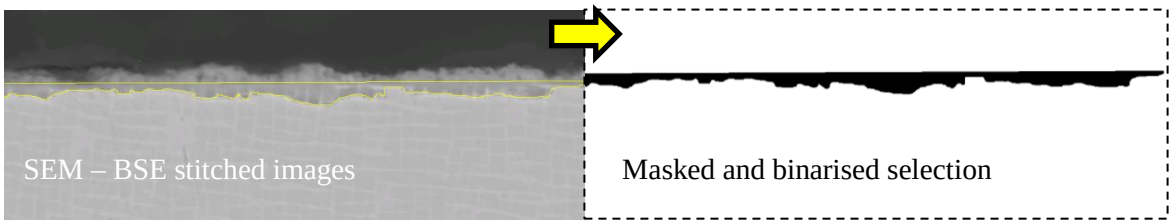

Figure 4.6: Procedure followed to measure the oxide scale thickness for each sample, a) manually selected penetrative oxide profile and b) example of the extracted and binarised selection.

4.2.3 Sustained Load Oxidation of CMSX-4

Sample Preparation

The sustained load oxidation experiments were conducted on 4 x 4 x 60mm plain bend bar samples. The samples were produced via EDM from cylindrical rods. Their orientation was selected to have their tensile axis along the <001> direction when subjected to bending. A schematic illustrating the sample dimensions and orientation is shown in Figure 4.7. A grinding and polishing procedure same to the one described in section 4.2.2 was followed to remove the residual surface effects from the EDM process.

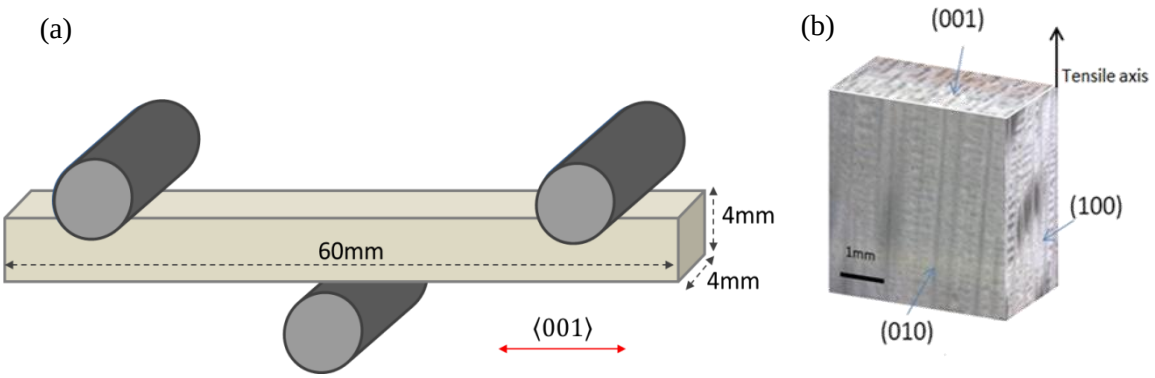

Figure 4.7: Sustained load oxidation samples: a) Dimensions and loading direction and b) dendritic structure and crystallographic orientations with respect to the loading direction

Testing and Characterisation Procedures

The samples were loaded in three-point bending in an Instron 8501 servo-hydraulic machine retrofitted with an ESH Ltd. high temperature vacuum chamber. The chamber utilises four high intensity quartz lamps to heat to the testing temperature which is monitored by a spot welded thermocouple attached to the sample and connected to a Eurotherm 815 thermo controller. The experimental set up and the specimen orientation is shown in Figure 4.8.

Prior to testing, an elasto-plastic finite element (FE) model was constructed in Abaqus CAE software to examine the stress/strain distribution on the bar under various loads. This allowed identification of an appropriate testing load and for the correlation of the stress/strain state with the observed oxidation behaviour across the length of the bar. Since at the load levels required to initiate fatigue damage the material is likely to deform plastically, the load selected for this test was chosen to be sufficient to induce some plastic strain. A load of 1.2kN, which induced a nominal, top surface, tensile stress of 900MPa (from simple bend theory) and a maximum plastic strain of 0.7%, was selected.

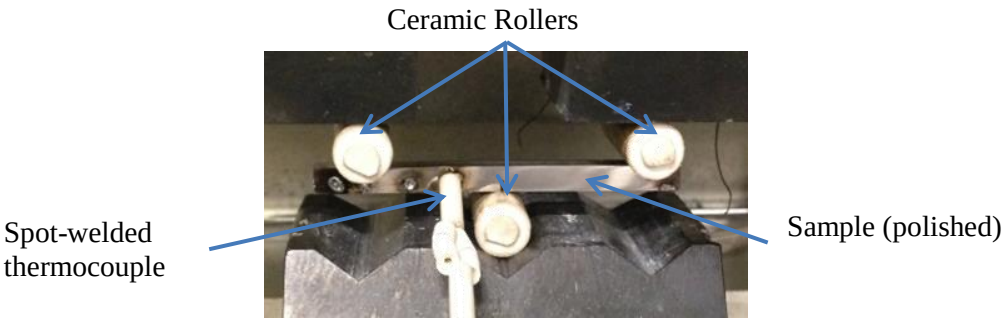

Figure 4.8: Sustained load oxidation set up under a 3-point bending.

4.3 Results

4.3.1 Isothermal Oxidation Kinetics

Reaction rates for the two superalloys at 550°C were assessed via both scale thickness and weight change measurements. The experimental curves of scale thickness as a function of time for both additive (external) and penetrative (internal) oxidation are shown in Figure 4.9. The variance in the data (standard deviation indicated by the error bars on Figure 4.9) was accounted for, in the fitting process, by assigning weights to each data point according to $weight = \frac{1}{\sigma^2}$. The overall "intermediate" temperature reaction was a good fit to the generic form of the power law which is given by:

$$x^n = k_n t + C \quad (4.1)$$

, where x is the oxide scale thickness, k_n is the reaction constant, t the reaction time and n and C are constants.

If the scale reaction does obey classic parabolic kinetics then fitting should yield a value of n close to 2. The values of the fitting parameters for the two alloys, for both the external and internal oxides, are compared in Table 4.3. It is important to note that the fit was applied to data obtained after 5h exposure meaning that very early stages of oxidation behaviour are not accounted for. It is clear from Figure 4.9 that the oxide formed on CMSX-4 is much thicker (both external and internal) than on MD2 (which has the higher Cr content).

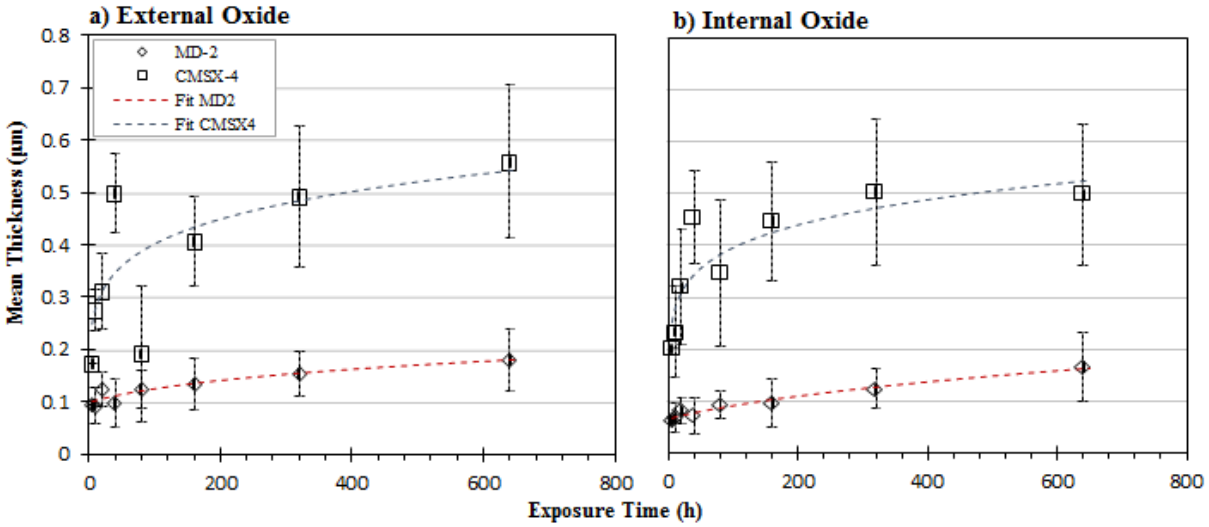

Figure 4.9: Oxidation kinetics of CMSX-4 and MD-2 at 550°C as a function of scale thickness a) External oxide and b) Internal oxide.

Oxidation	Alloy	k_n $(\mu m^n/h)$	n	C
External	CMSX4	3.44×10^{-5}	6.2	6.21×10^{-11}
	MD2	1.45×10^{-6}	4.0	9.11×10^{-5}
Internal	CMSX4	2.15×10^{-5}	6.6	9.72×10^{-14}
	MD2	1.80×10^{-5}	2.4	1.56×10^{-3}

Table 4.3: Oxidation rate constants for the external and internal scales formed on CMSX-4 and MD-2 when oxidised isothermally at 550°C.

Oxidation kinetics were also evaluated by monitoring weight changes in a second set of samples via TGA. Continuous gravimetric measurements can yield more averaged, and hence to some extent, more representative reaction kinetics as data are generated and averaged from the entire

exposed surface area in the same sample. The sensitivity of the technique allowed examination of the overall oxide growth rate from the early stages while data for the lower temperature of interest (450°C) were also possible to obtain for both alloys. The TGA results are shown in Figure 4.10 where a good fit was obtained when the general power law time dependence equation was used:

$$\Delta m^n = k_{n_{TGA}} t + C \quad (4.2)$$

, where Δm is the specific mass gain, $k_{n_{TGA}}$ is the reaction constant and *n* and *C* are constants.

The values of these parameters are summarised in Table 4.4. In both alloys the amount of oxide seems to double from 450°C to 550°C when the exposure time reaches 200h. As also seen in the oxide scale thickness results, CMSX-4 is much more susceptible to oxidation than MD-2 with much faster reaction kinetics.

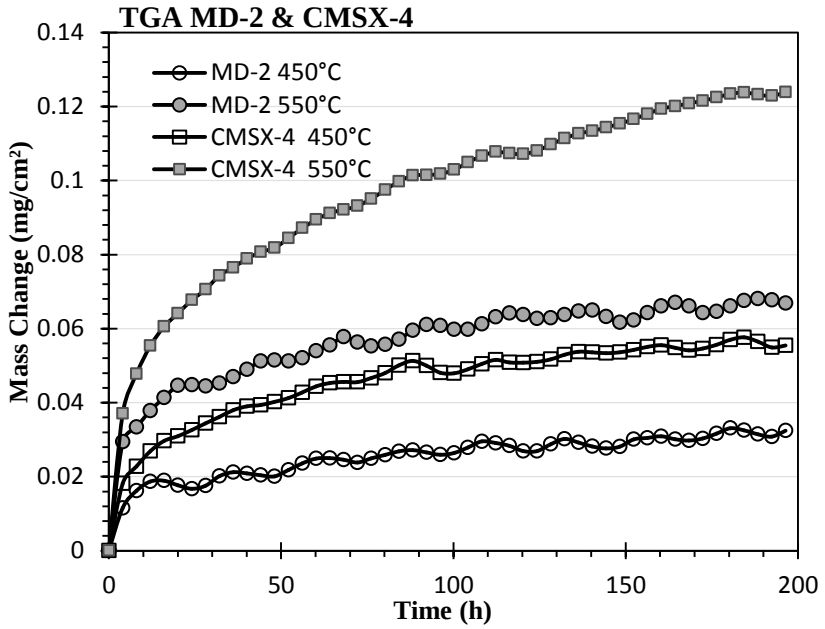

Figure 4.10: Oxidation kinetics of CMSX-4 and MD-2 at 450°C and 550°C as a function of normalised weight change measurements obtain via TGA.

Alloy	Temperature	k_n $((mg/cm^2)^n/h)$	n	C
CMSX-4	550°C	4.71×10^{-6}	3.3	2.34×10^{-11}
	450°C	1.07×10^{-7}	3.8	2.34×10^{-14}
MD-2	550°C	2.00×10^{-8}	4.7	4.7×10^{-11}
	450°C	4.71×10^{-6}	3.4	2.34×10^{-14}

Table 4.4: Values of the oxidation growth rate constants calculated by fitting a power type law to the TGA results of CMSX-4 and MD-2 at 450°C and 550°C. NB the units of $\boldsymbol{k_n}$ depend on the value of *n*.

4.3.2 Oxide scale morphology

4.3.3 Oxidation effects on surface morphology

Oxidation of CMSX-4 was not completely uniform for any test duration. Macroscopically, small, circular, blemishes/spallation sites and areas of lighter and heavier oxidation were observed (Figure 4.11a). The blemishes/spallation sites observed are examined separately in the next section. Under SEM BSE observations, dendrites appear lighter than interdendritic regions indicating that the compositional differences between them result in varying degrees of oxidation. The difference in oxidation behaviour between the two regions is evident from the high magnification images of Figure 4.11c and d. Interdendritic regions (which have higher contents of Al) appear to oxidise significantly less than the dendrites.

On the other hand, oxidation of MD-2 appears more uniform. There is no apparent difference between the oxide forming on the substrate of dendritic and interdendritic regions. In addition, none of the samples tested had similar blemishes/spallation to the CMSX-4 samples. However, the carbides which are embedded in the interdendritic regions of the alloy (Figure 4.12a) become more pronounced and appeared to be readily attacked by oxidation (Figure 4.12b). The oxidation mechanism is significantly different from that of the alloy matrix. The surface carbides appear to be selectively oxidised and form characteristic, protruding, eruptions that caused decohesion of the oxide around them (Figure 4.12c and d).

The evolution of the oxide scale morphology under isothermal conditions at 550˚C is shown in Figure 4.13 for both alloys. In the case of CMSX-4, it can be seen that oxidation is well advanced after only 1h of exposure and that the alloy's microstructure is reflected in the morphology of the oxides produced. Generally at short exposure times, there is a clear distinction between the oxides forming over the γ'-Ni_3Al precipitates and over the γ channels. The lighter colour oxide, corresponding to the γ channels, appears interconnected and raised while the regions of darker contrast which have similar dimensions to the γ' seem to be forming a thinner oxide. For exposure times higher than 40h the entire surface appears heavily oxidised making the underlying microstructure indistinguishable. Similar morphological observations have been reported elsewhere [164] following the isothermal oxidation of the RR3000 single crystal nickel based superalloy at 750˚C.

In contrast with CMSX-4, the oxide forming on the surface of the MD-2 samples appears much finer with the microstructure being less pronounced. Instead, oxide islands, which seem to initiate as early as after 1h exposure, connect and expand as the exposure time increases. The nodular/island oxide formation mechanism is more evident at the longer exposure times where

parts of the surface had still to develop a thick and uniform oxide. At the same time, preferential oxidation of the γ channels becomes apparent.

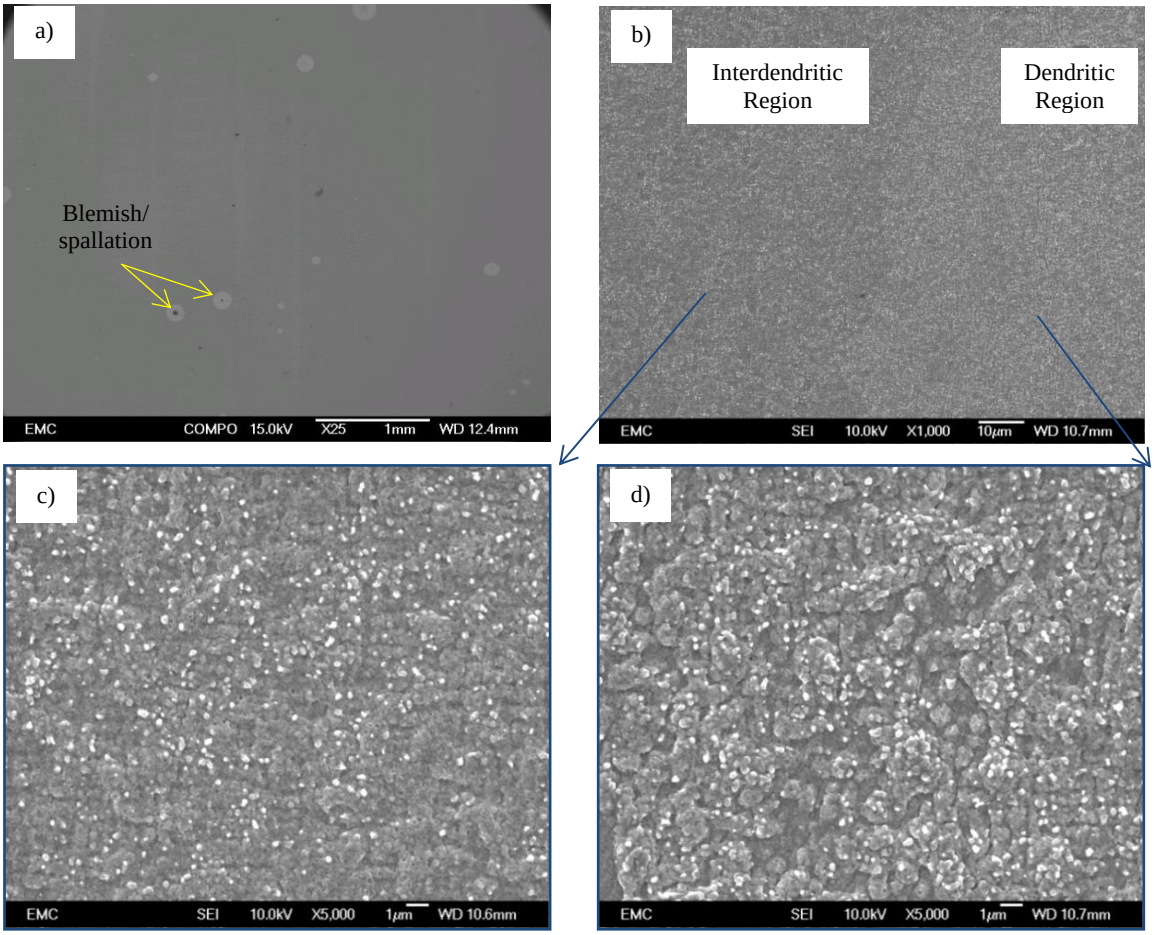

Figure 4.11: SEM images of the surface of a CMSX-4 sample oxidised for 160h at 550°C showing a) overview of sample surface, b) dendritic and Interdendritic regions, c) high magnification image of the interdendritic region and d) high magnification image of the dendritic region.

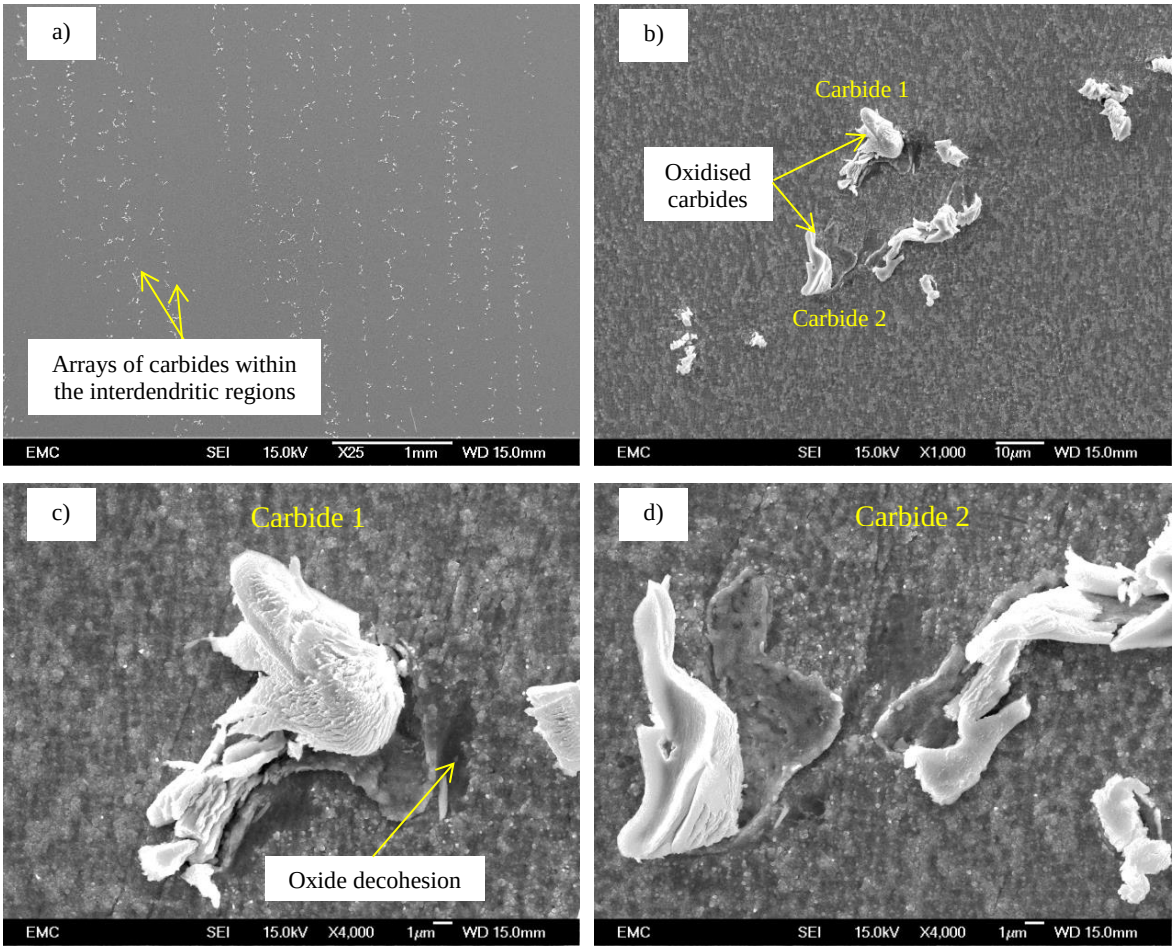

Figure 4.12: SEM images of the surface of an MD-2 sample oxidised for 160h at 550°C, showing a) overview of sample surface, b) high magnification image of an interdendritic region containing carbides and c) & d) high magnification images of the oxidised carbides shown in b).

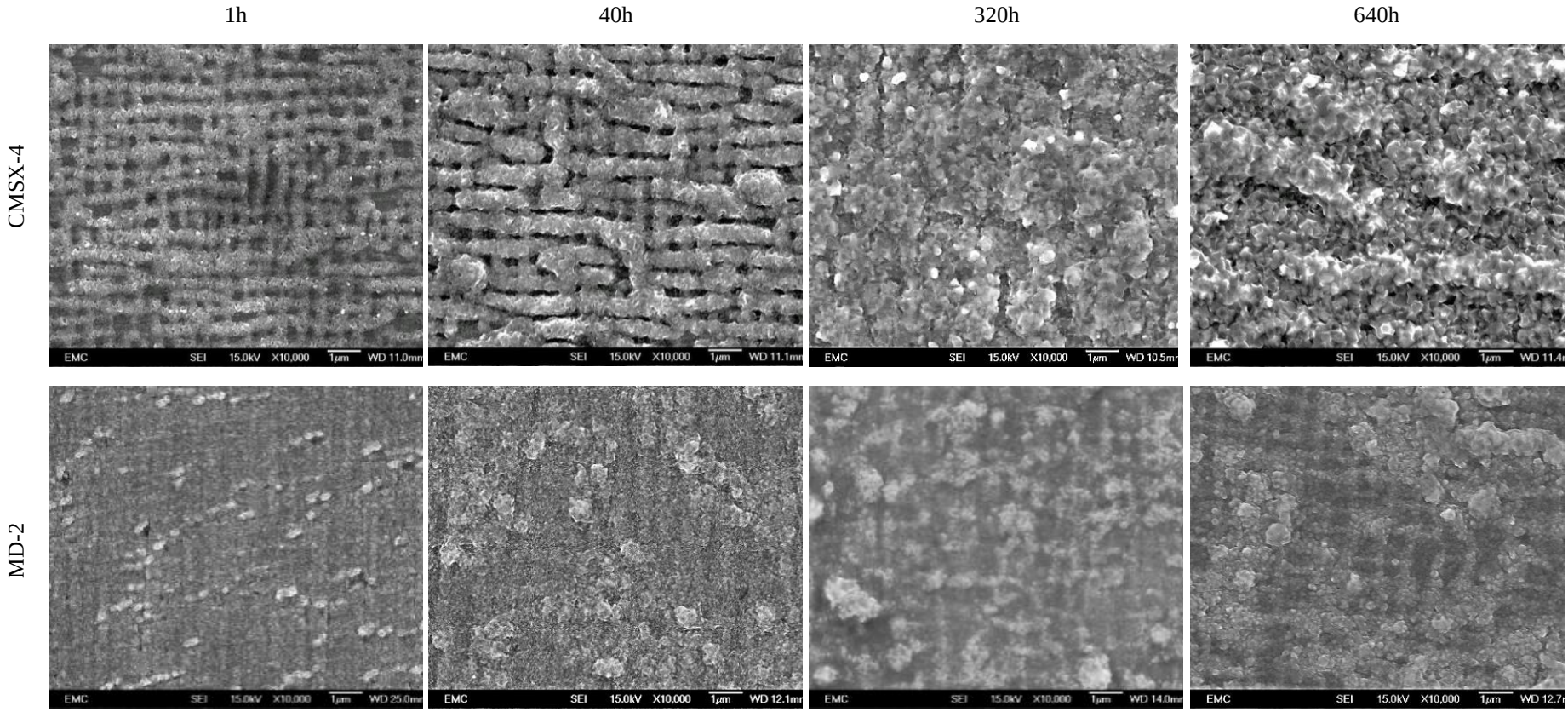

Figure 4.13: Oxide scale evolution on the surface of isothermally oxidised CMSX-4 and MD-2 samples at 550ºC.

4.3.4 Spallation in CMSX-4

Figure 4.14 shows the stitched overviews of the oxidised surfaces obtained from the Alicona microscope and the SEM. The SEM images (right) have been taken under the BSE mode and represent the regions of interest that were further analysed in ImageJ. As seen from Figure 4.15 the spallation sites formed were generally circular in shape and exhibited a certain type of morphology. Exceptions to this include sites of elongated circular shapes and short strips of spalling. Figure 4.16 shows the typical profile of a spallation as measured using Alicona. It can be generically described as a pit with engorged edges and a bulge at the centre of its bed. Figure 4.17a shows a SEI mode image of a spallation site which appears dark with a brighter circumference. SE images reveal the topology of the surface features as more electrons can leave protruded edges (edge effects) causing them to appear brighter. This confirms the shape of the profiles obtained by the Alicona microscope. Figure 4.17b shows the same spallation site as seen in the BSE mode. The spallation area in this case appears brighter than the surrounding oxide scale. This due to the high contrast caused by the difference in the average atomic number between the spalled and unspalled regions. As expected, since the oxide scale is less dense than the substrate material, it backscatters less electrons thus appearing darker than the spalled areas.

Careful examination of the BSE maps obtained revealed that oxide spalling mainly occurs within the interdendritic regions. From a total of 168 distinguishable spallation sites, across all samples, 54% initiated within interdendritic regions, 21% initiated within the dendritic regions while the remaining 25% straddled both regions and the exact point of initiation could not be identified. Figure 4.18 shows the amount of spallation measured on the surfaces of the samples with increasing exposure time. Interestingly, the 80h sample that exhibited the highest number of spallation sites also corresponded to the smallest average spallation size. Area fraction measurements indicate an overall increase in the amount of oxide scale spallation up to 20h followed by a sudden decrease between 20-80h. Overall, spallation increases again on the surface of the 160h sample after which it becomes almost negligible for the 320h and 640h samples. This behaviour could possibly be explained by considering the stresses induced in the oxide during growth and during cooling following exposure. Cyclic oxidation studies in similar alloy systems have reported that oxide spallation takes place during the cooling cycle where compressive stresses are generated as a result of the differential in thermal contraction coefficients [23,80,165]. There are a number of studies in the literature that by using spectroscopy [166,167], XRD [168] or numerically [30], have attempted to quantify the stress evolution in the oxides during growth and/or cooling. This is however beyond the scope of this PhD project but could provide an avenue of further assessment for future work on the subject.

Microscope maps (Alicona) BSE maps of ROIs (FEG-SEM)

1h

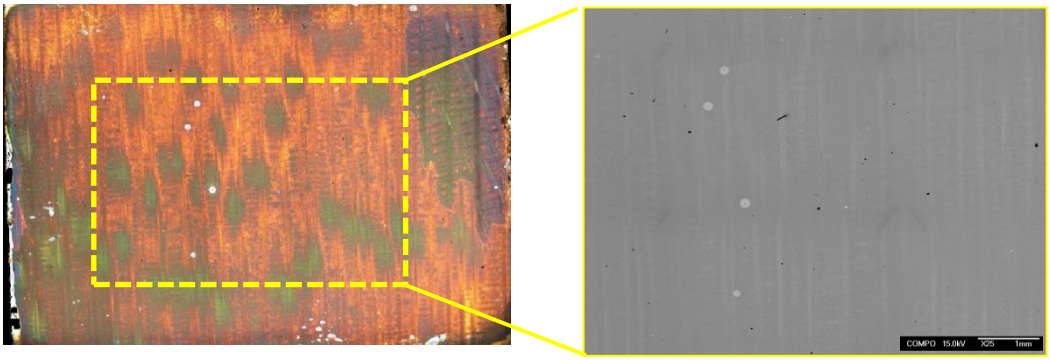

5h

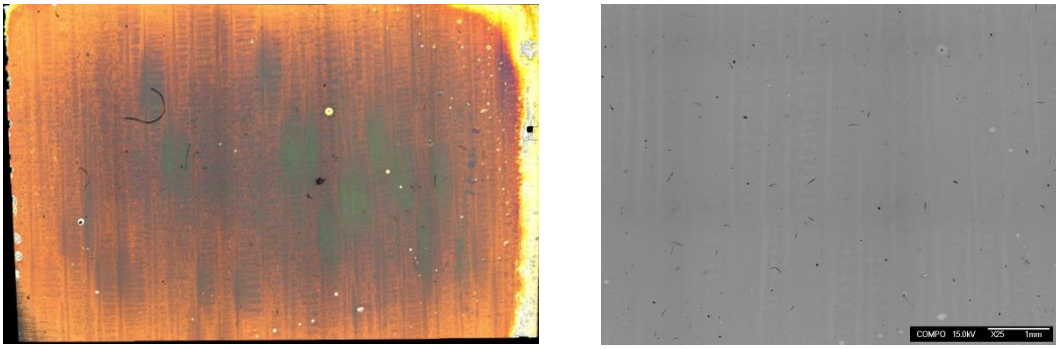

10h

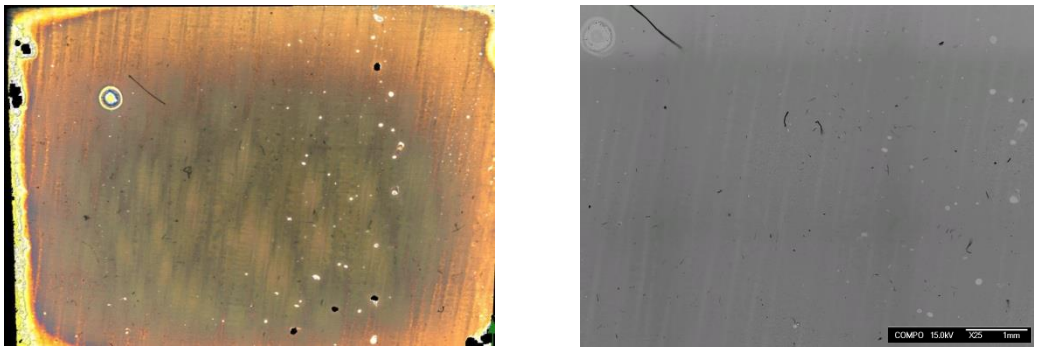

20h

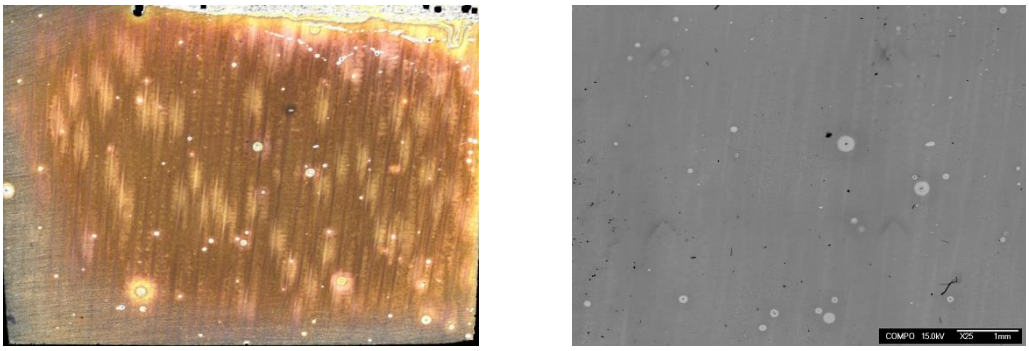

40h

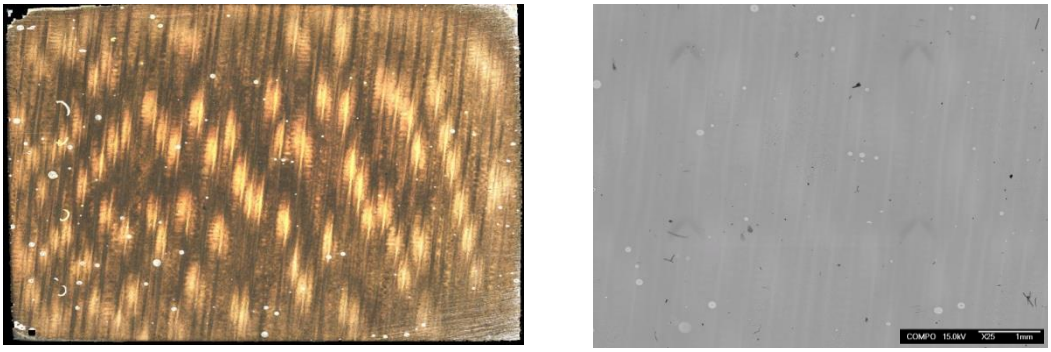

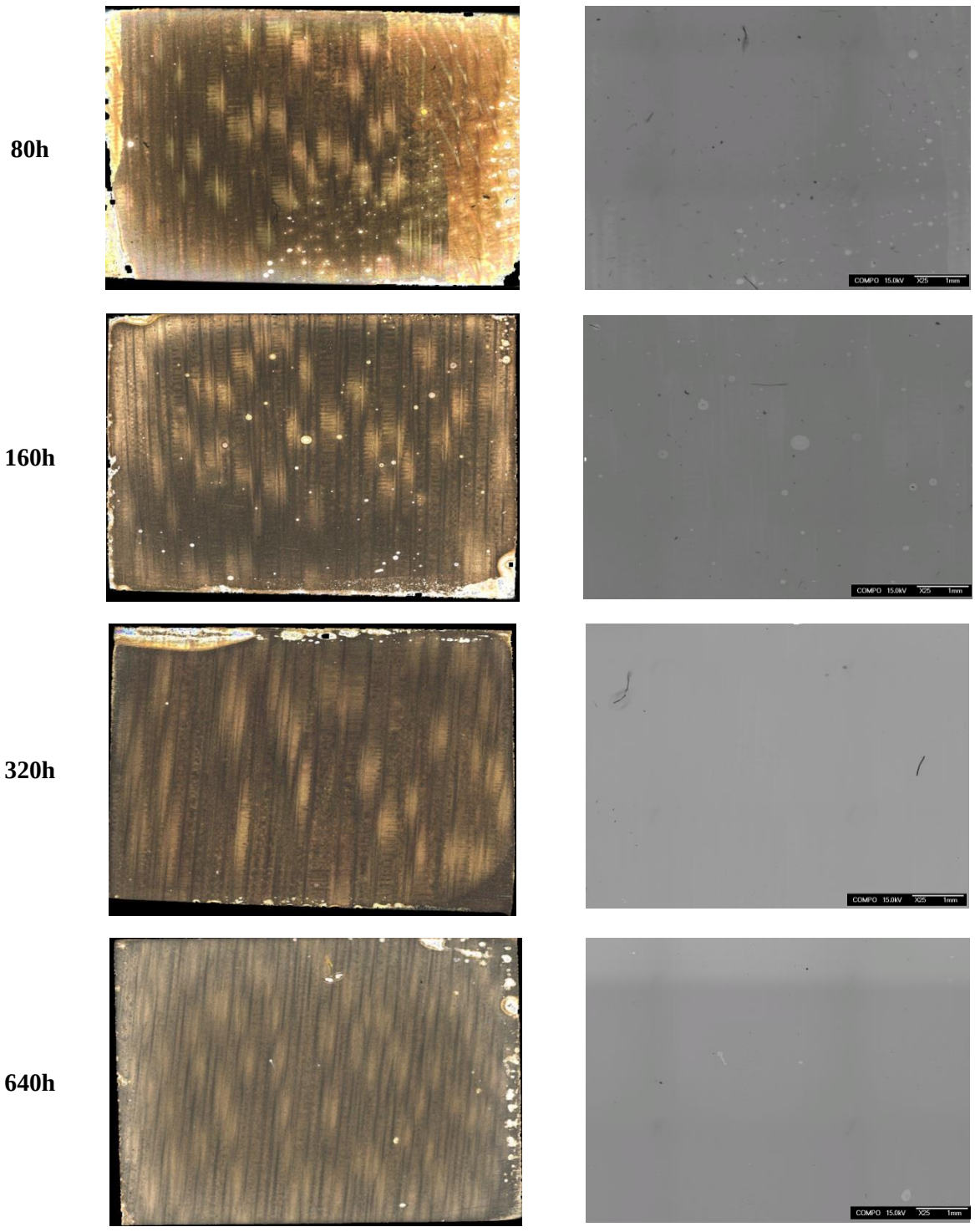

Figure 4.14: Optical Microscope and SEM BSE mode images showing the oxidation surfaces of CMSX-4 samples ((001) planes) exposed isothermally for various times at 550˚C .

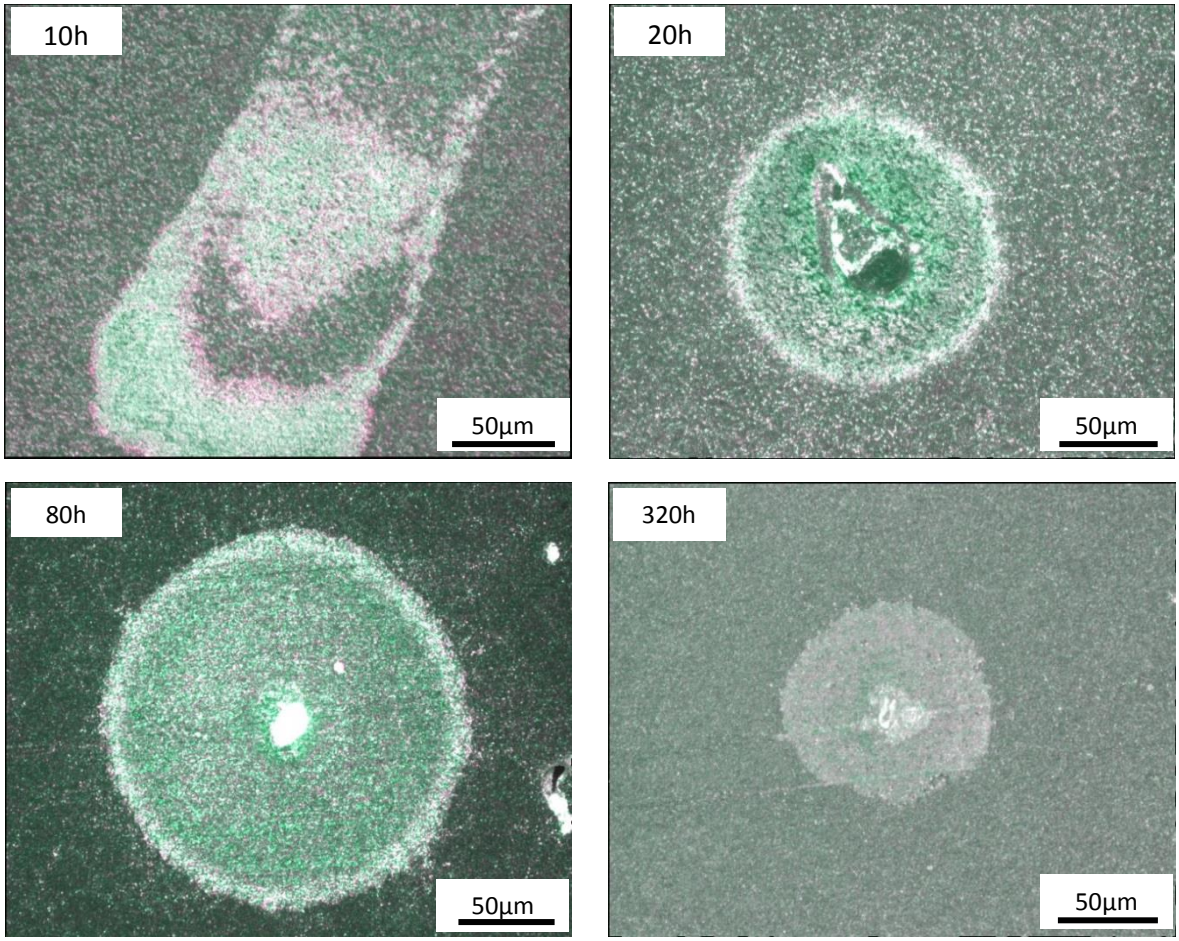

Figure 4.15: Various spallation sites on the surface of the CMSX-4 isothermally exposed samples (550^{o}C) as seen from the Alicona microscope.

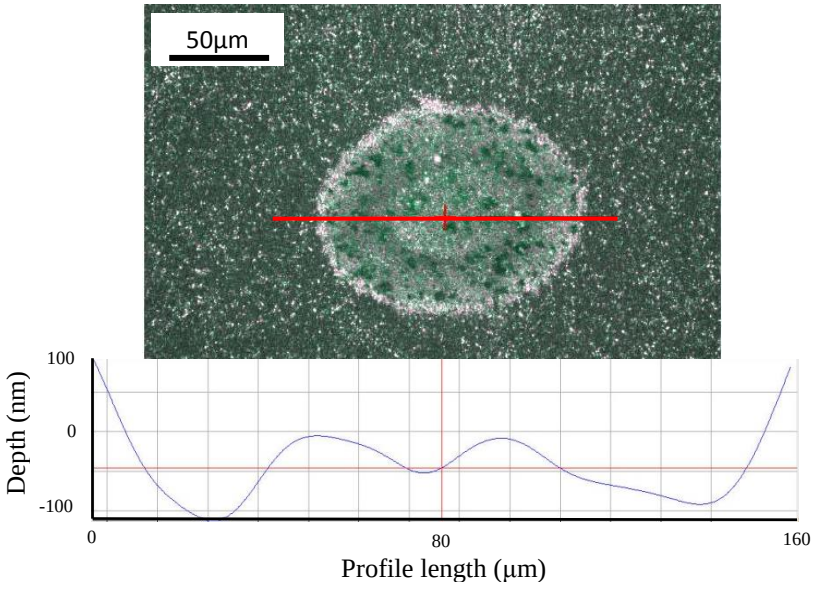

Figure 4.16: Typical profile of most spallation sites observed in this study on the oxidised surfaces of the samples.

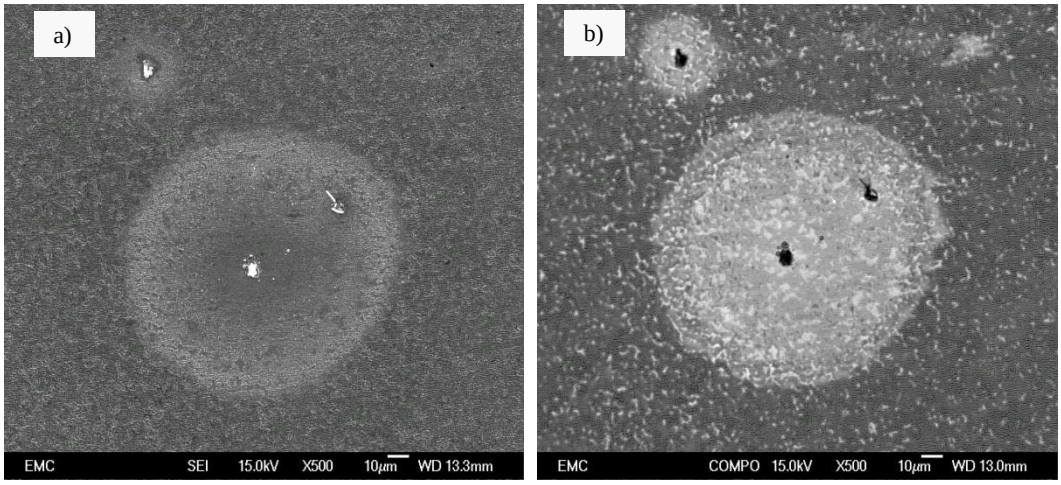

Figure 4.17: Spallation sites on the surface of the CMSX-4 sample oxidised isothermally for 40h in a) SEI mode and b) BSE mode.

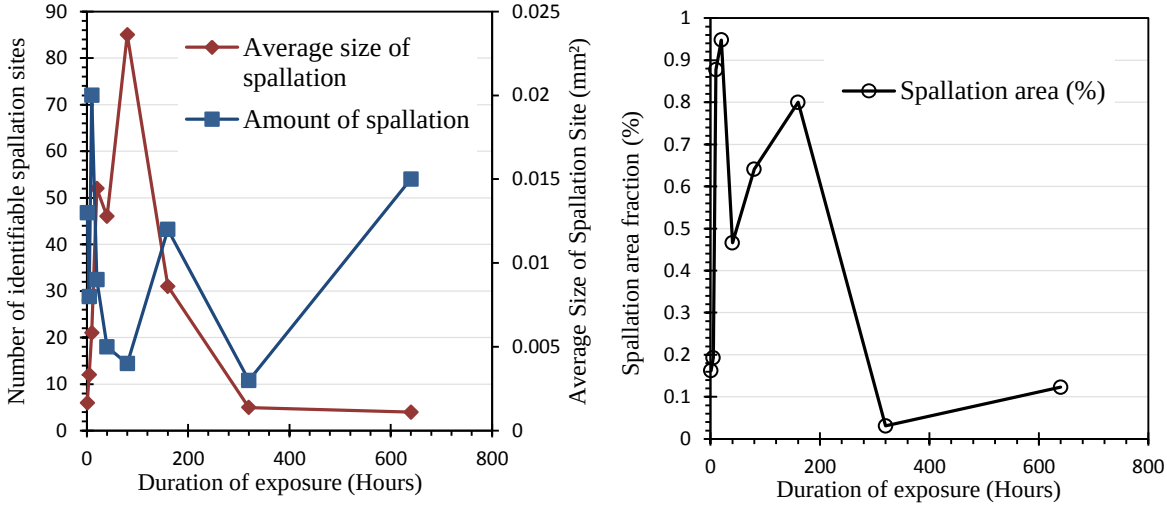

Figure 4.18: Quantification of surface spallation on CMSX-4 (001) samples at 550°C: a) Plot of spallation size and amount against exposure time, b) Plot of spallation area fraction against exposure time.

4.3.5 Oxide characterisation – XRD and EDS

XRD analysis was carried out on a CMSX-4 sample oxidised for 1000h at 550°C as this produced thicker oxides compared to MD-2, and hence was more likely to generate detectable signals. To ensure that the analysis would yield meaningful results, the depth from which at least 90% of the diffracted beam signal is generated was estimated using the AbsorbDX software (DIFFRACplus evaluation package) for different incident angles. Calculations were carried out assuming that the entire scale is NiO with a linear attenuation coefficient equal to 6.85g/cm^3. Using the power law

derived for the oxide scale thickness growth rate the estimated thickness for 1000h oxidation at 550°C was calculated to be 1.1μm. By varying the X-Ray incident angle in the calculations the penetration depth for 0.75° was found to be between 1.05 and 1.13μm for diffraction angles (2θ) between 10° and 90°. The results from the phase analysis using XRD are shown in Figure 4.19. As expected, there is a very strong indication of the formation of NiO. At the same time the spinel ternary phases Al_2NiO and $NiWO_4$ were also detected. Surprisingly, there was no indication of any Cr-rich oxide forming despite this being shown to form either as spinel or as the corundum phase in similar alloys [22]. Interestingly though, a less common transition alumina (η-Al_2O_3) was found to be present.

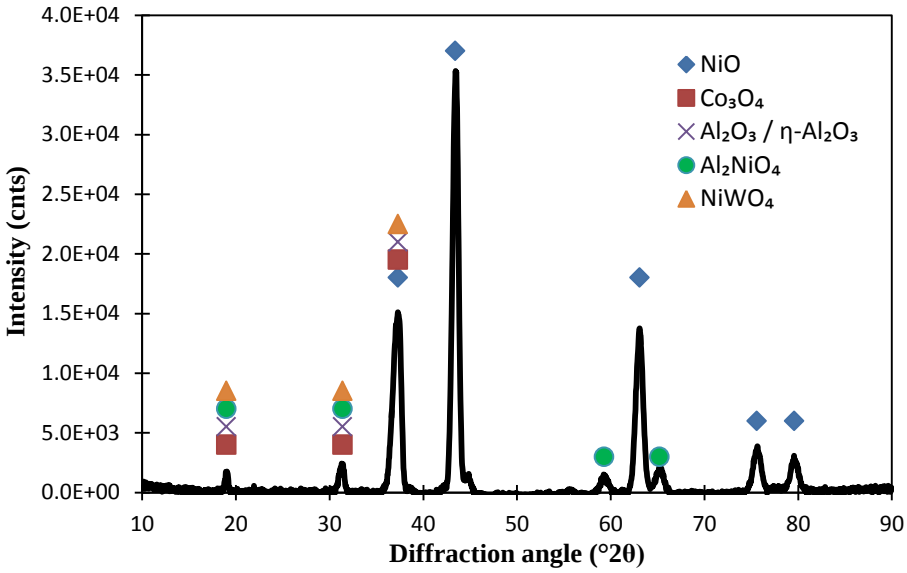

Figure 4.19: XRD diffraction pattern of a CMSX-4 sample oxidised for 1000h at 550°C.

Investigation of the oxidation mechanism was continued by examining the cross section of the scales as illustrated in Figure 4.20 and Figure 4.21. During the initial stages of oxidation the scale appeared to be discontinuous and preferentially formed over the γ matrix resulting in a wavy profile morphology (Figure 4.20a). This is in agreement with the surface observations of Figure 4.13. As the reaction process progresses, it is evident that the external oxide thickens approximately at the same rate as the internal oxide. Areas with un-oxidised γ channels spanning the entire length of the oxidation affected zone as well as areas of complete oxidation of both γ' and γ phases were observed at longer exposure times (Figure 4.21). These effects are much more pronounced in the CMSX-4 samples even though similar behaviour can be distinguished for MD-2. EDS line scans were taken across the scale formed after 640h of exposure, as shown by the red dotted lines on Figure 4.21. The results shown in Figure 4.22 indicate that the external scale is predominantly formed by Ni. A small increase in Al content

was observed to coexist with O at the point where the Ni amount decreases. At the same time, in both alloys an increased amount of W was detected within the Al & O -rich region.

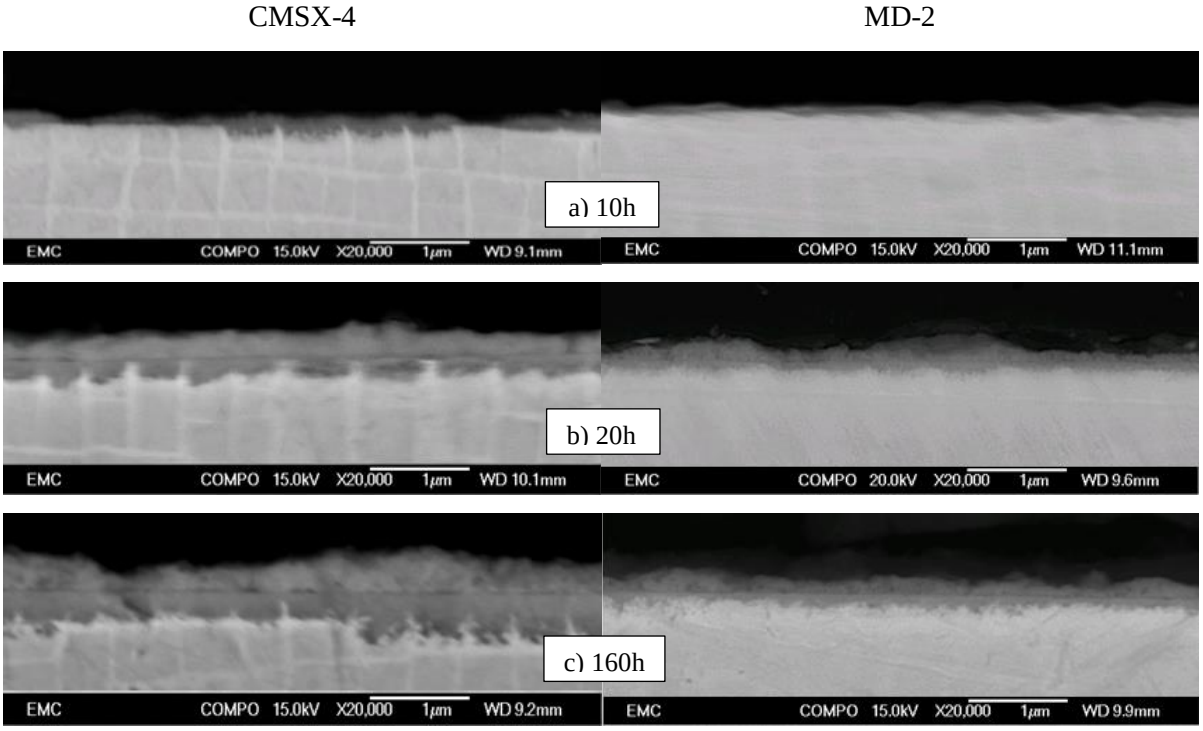

Figure 4.20: Backscattered electron images of the oxide profile development on the surface of CMSX-4 and MD-2 when oxidised at 550°C.

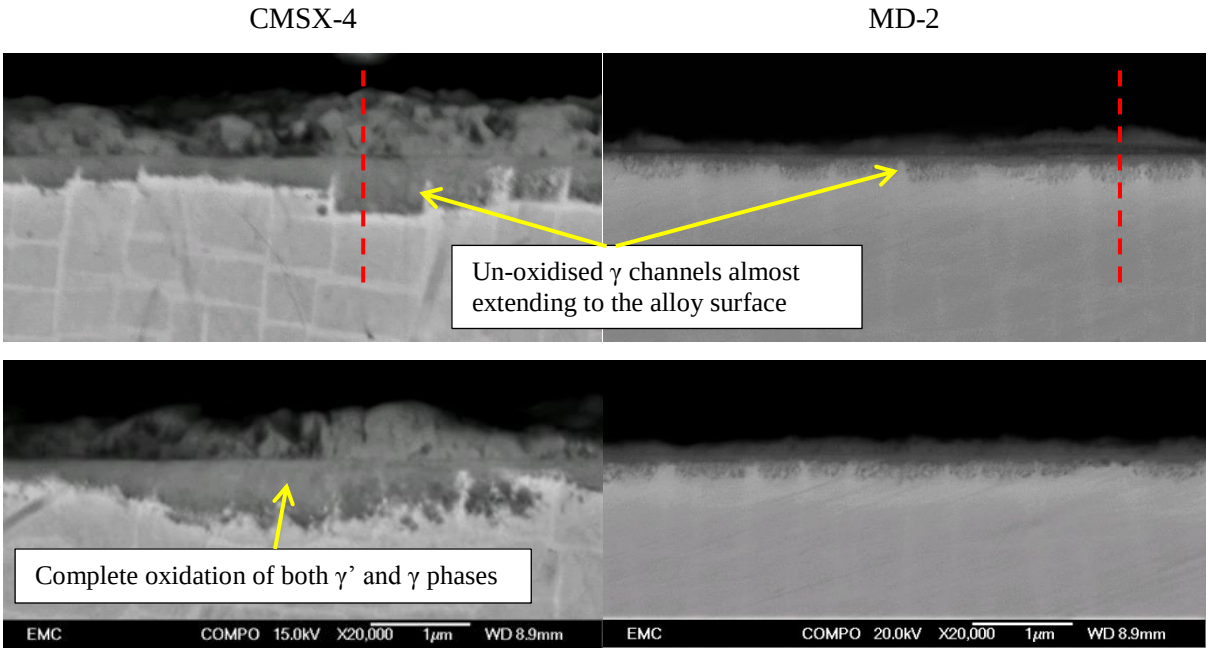

Figure 4.21: Backscattered electron images showing examples of the morphology of the oxide formed on the surfaces of CMSX-4 and MD-2 when oxidised for 640h at 550°C. The red dotted lines indicate the position of the EDX lines scans shown in Figure 4.22.

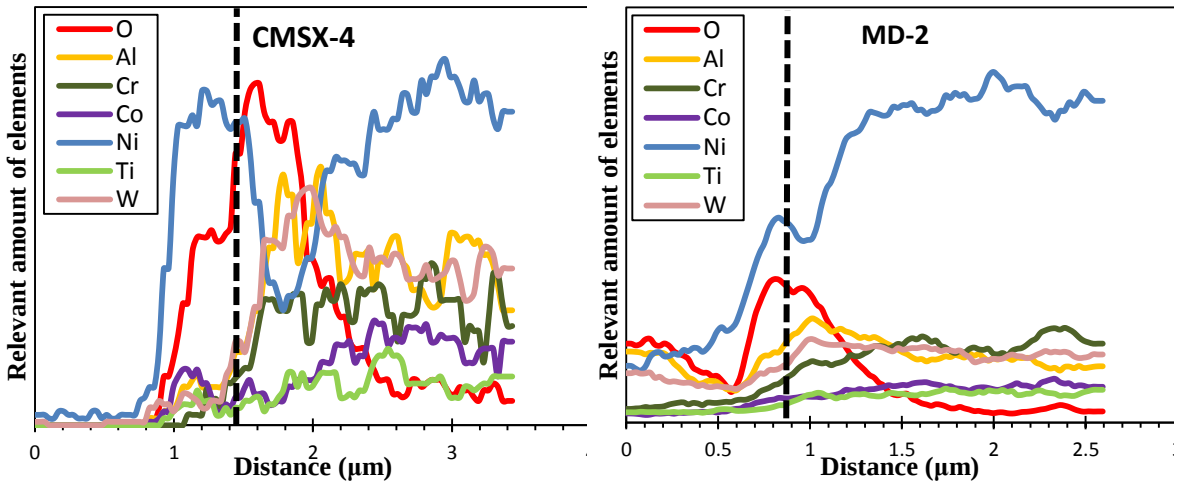

Figure 4.22: EDX line scans taken across the oxide scale of CMSX-4 and MD-2 samples oxidised for 640h at 550°C. The locations of the scans are shown in Figure 4.21 and the approximate location of the initial sample surface (separates internal and external oxides) is shown by the black dotted lines.

4.3.6 Effect of external loads on isothermal oxidation behaviour

Figure 4.23 shows the evolution of the oxide scale morphology with stress/strain on the surface of CMSX-4 following 70h of isothermal exposure at 550°C. The plot at the bottom of Figure 4.23 shows the modelled stress and plastic strain distribution on the surface of the sample and the relative locations of the SEM images shown at the top. Figure 4.23a – d show the oxides that formed within the plastically deformed area near the centre of the sample, while Figure 4.23e – h show the oxides that formed within the elastically deformed material. Oxides that formed over plastically deformed regions had a bulging morphology and protruded into the substrate while, in most instances, a γ' free/depleted zone formed adjacent to the surface. The extent of the depletion zone can be distinguished from the SEM-BSE images of Figure 4.24 - Figure 4.26, obtained after etching the surfaces. The protrusions, or pits, had a variable morphology and were found to penetrate up to approximately 1.5µm into the alloy (by various measurements on 2D sections). The morphology observed here is clearly different to the one seen in Figure 4.20 and Figure 4.21 where the samples shown had been oxidised without any loads acting on them, indicating that plastic strains can modify the oxidation behaviour.

On the contrary, oxides that formed over elastically strained regions appeared relatively uniform with minimal internal oxidation. In order to investigate whether stress or elastic strains also affect oxidation, an estimation of the average oxide thickness within the elastic region of the sample was calculated. Following the procedure described in section 4.2.2, measurements at five locations

(4.5mm, 4.91mm, 5.6mm, 8mm and 15.35mm from the centre of the sample) were made from high magnification SEM-BSE images, such as the ones shown in Figure 4.23. By averaging these measurements the external and internal oxide thicknesses were estimated. Using Equation 4.1 with the constants of Table 4.3 and *t* (exposure time) = 70h, external and internal oxide thickness values were predicted for the unloaded case. The two sets of values are compared in Table 4.5. It is apparent that the oxides formed under elastic load and under no load are quite comparable in thickness.

Oxide thickness	External	Internal
Measured (elastic deformation) (μm)	0.359±0.176	0.363±0.156
Predicted from Eq. 4.1 for unloaded case (μm)	0.378	0.374
Variation (%)	5.1	2.8

Table 4.5: Comparison of external and internal oxide thicknesses between elastically deformed (measured) and unloaded CMSX-4 (predicted) samples exposed for 70h at 550°C.

EDX was conducted on a number of oxide protrusions, examples of which are shown in Figure 4.24 - Figure 4.26. The analysis showed that these protrusions mainly consist of an external Ni, Co -rich oxide and an internal Al-rich oxide. The outward diffusion of Ni and Co cations formed a depletion zone below the oxide-substrate interface. Notably, Co oxide was not found to form during isothermal exposure in the absence of load (Figure 4.22). Similar to the unloaded state no apparent Cr oxide was observed to form.

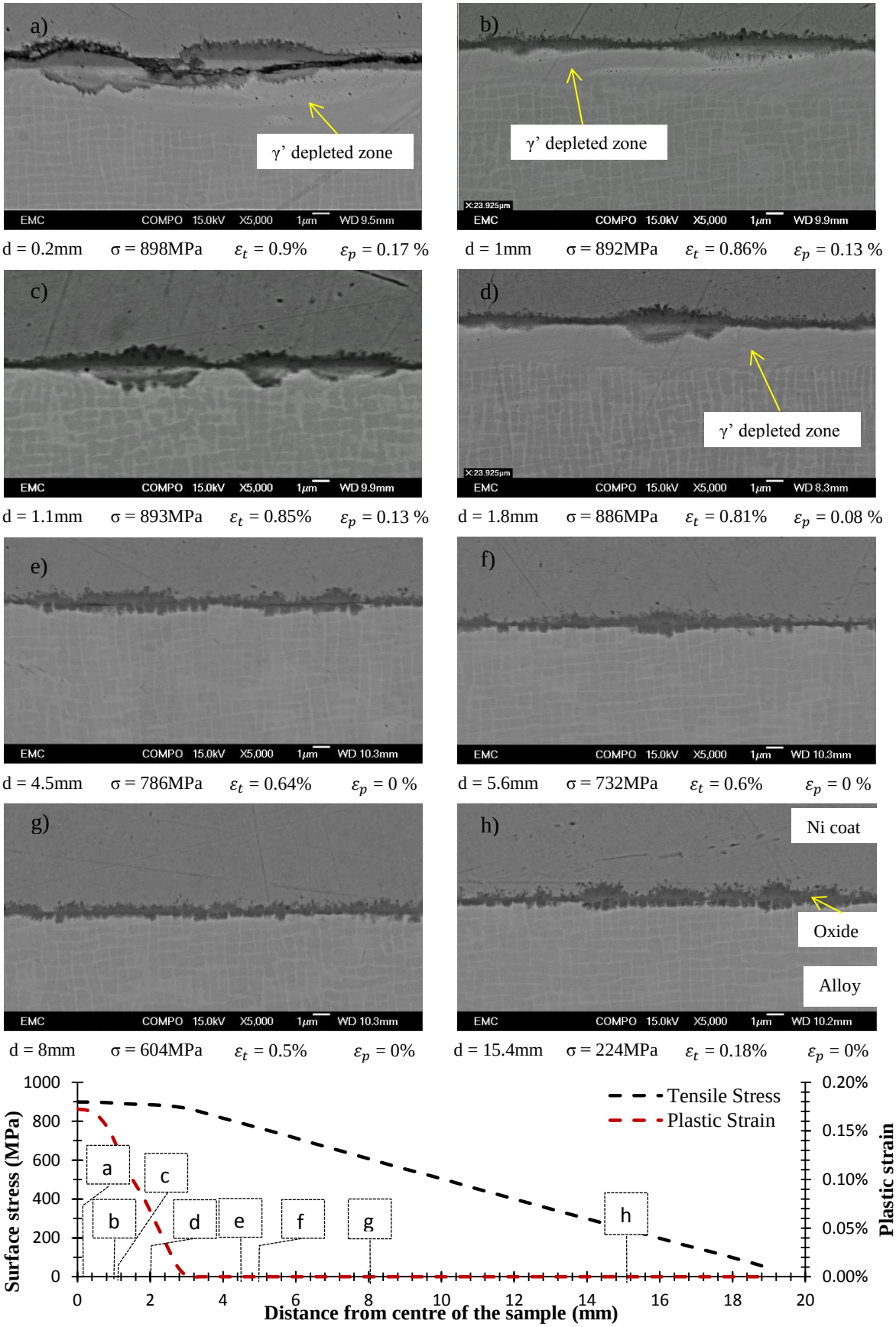

Figure 4.23: SEM BSE images of the oxide morphology formed at various stress/strain levels on a CMSX-4 sample oxidised at 550C for 70h under static load.

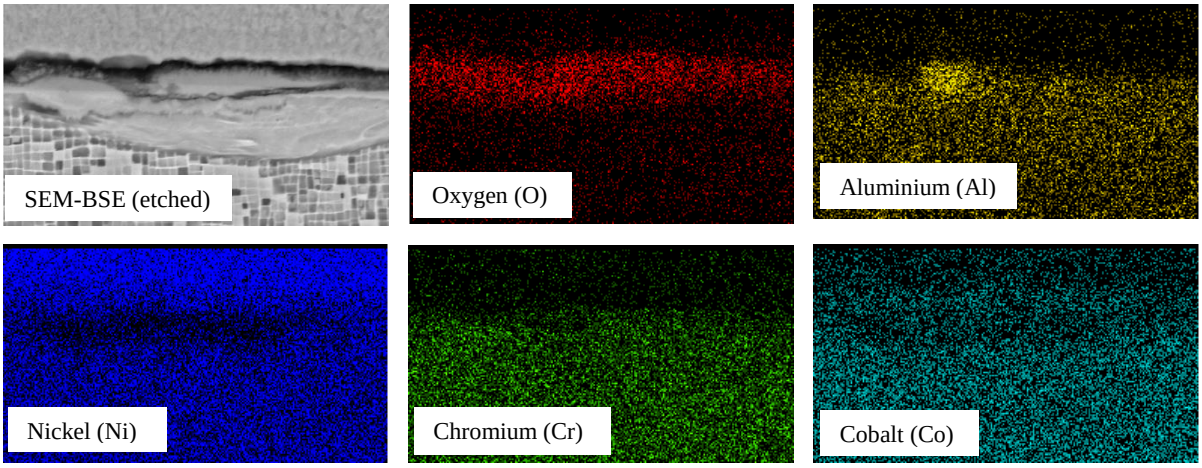

Figure 4.24: Etched SEM BSE image and EDX maps of the surface shown in Figure 4.23a.

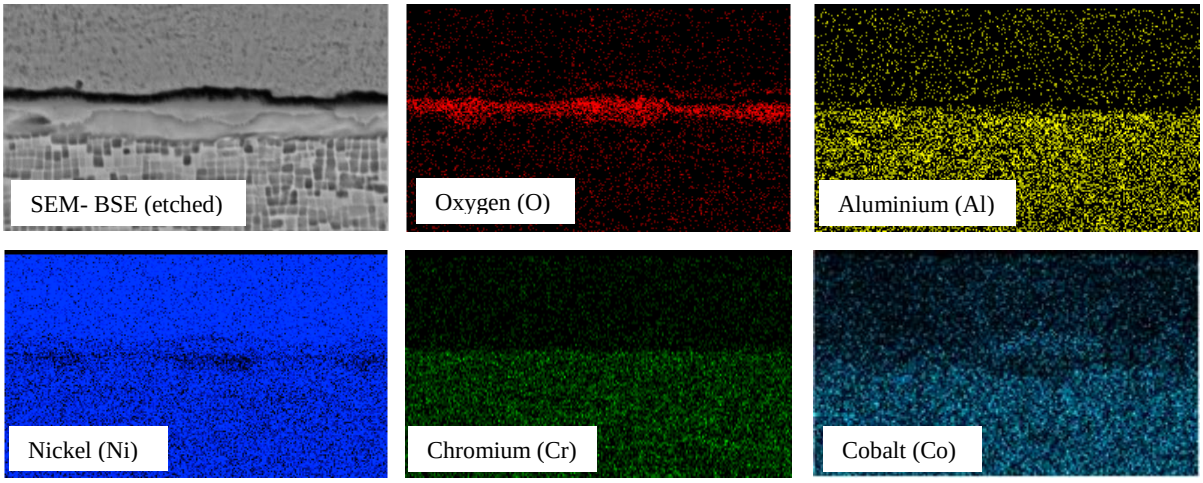

Figure 4.25: Etched SEM BSE image and EDX maps of the surface shown in Figure 4.23b.

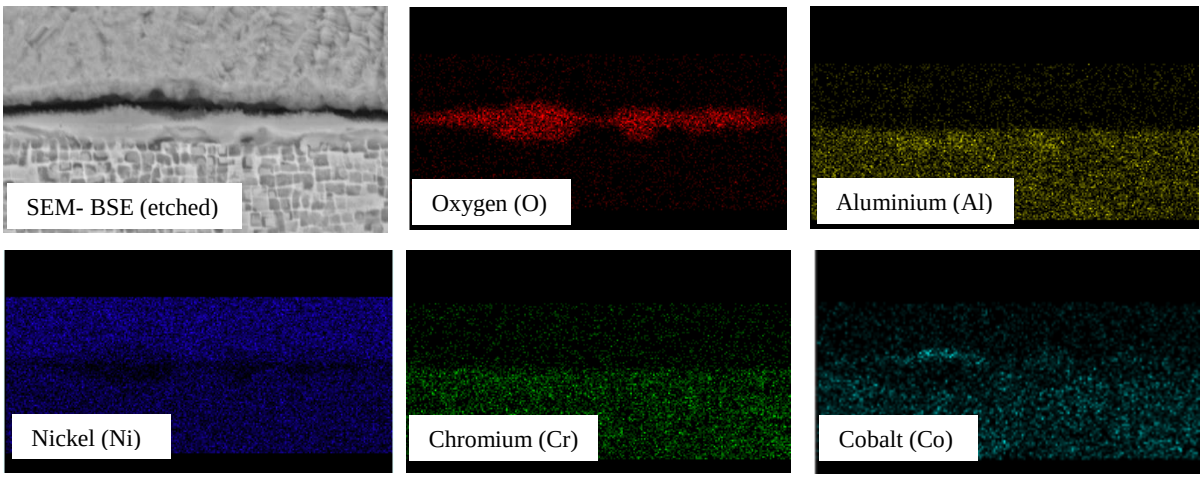

Figure 4.26: Etched SEM BSE image and EDX maps of the surface shown in Figure 4.23c.

4.4 Discussion

4.4.1 Oxide scale kinetics

It is well known that in the case of Ni-based superalloys the isothermal oxidation growth rate can be described by a parabolic law [22,27,82,83,169,170] which indicates that the process is controlled by the diffusion of species through the scale (Wagner's mechanism). Although mostly empirically derived, logarithmic type laws have also been used to describe oxidation rates for superalloys at lower temperatures and during the initial stages of oxidation [171]. The physical interpretation of this type of law was initially described by Mott [172] on the basis of electric field induced transport of ions through thin films and diffusion along low resistance paths (e.g. pores) [21]. As such, both a complete parabola ($t = A + Bx + Cx^2$) and a logarithmic ($x = \log(t + t_o) + A$) fit were attempted for the results of Figure 4.9 however, neither gave a good fit. As was seen in this case, lack of fit to these two "standardised" laws have been encountered before in both pure metals and alloys [173–175] with growth rates exhibiting sub-parabolic behaviour. Studies in similar alloys, conducted at higher temperatures [176,177], indicate more severe internal oxidation/γ' depletion. In comparison, the results of this study show that the development rate of the external and internal oxides is similar. Overall, it can be appreciated from Figure 4.9 that the oxide thickness, especially for the case of MD-2, was relatively small and the accuracy of the derived parameters may be somewhat questionable. Nevertheless, the thickness analysis provides an insight into the potential anionic and cationic diffusion processes and could be extended to inform models that consider oxide induced closure effects around cracks or damage affected zone sizes ahead of fatigue crack tips.

Although the power law derived from the TGA results can describe the full kinetic curves and could be useful for modelling approaches, it does not necessarily provide detailed information on the full scale oxidation mechanism. In addition, with the above approach, the units of k_n depend on the growth exponent *n* and would then be different between alloys exhibiting dissimilar oxidation behaviour. In the case of highly alloyed materials, such as the Ni-based superalloys examined here, oxidation becomes a very complex process. Identifying growth rates which have been linked to the growth of certain oxide phases can often provide an insight. Based on the Wagner theory, the oxidation kinetics of high temperature alloys have generally been described using the parabolic law, which has shown that such kinetics result from the diffusion of oxygen cations or metallic anions through a stable and adherent scale. In the case of Ni-based superalloys, such rates are generally attributed to the formation of the protective α-Al_2O_3 phase. Parabolic growth rates have also been linked to the formation of TiO [178] and NiO at [179], while sub-parabolic rates have been reported for the kinetics of chromium oxides [180].

A common phenomenon encountered during the oxidation of alumina forming alloys (or alloys that form protective scales that conform to Wagner's theory) is the transient oxidation period. Transient oxidation processes are observed during the initial stages of reaction where less stable oxides tend to form. This is either because of faster kinetics and an abundance of certain elements, or because the more stable oxide phase requires a longer time to form, depending on the temperature. This period is usually defined up to the point in time where the most thermodynamically stable oxide possible has formed and kinetics thereafter depend on diffusion processes through it. Although this regime is typically short in time and thus often disregarded by many researchers, characterising it is crucial, as in reality surfaces such as the tip of a fatigue crack are only exposed to oxidation for a limited time between cycles. To examine this, logarithmic values of the TGA data were plotted as shown in Figure 4.27 according to Equation 4.3 which is the logarithmic translation of the power law used earlier (see Equation 4.2).

$$\log(\Delta m) = \left(\frac{1}{n}\right)\log t + C' \qquad (4.3)$$

, where *C*' is the new constant that also contains k_n. From the plots of Figure 4.27 it was immediately clear that the measured oxide growth rates follow a two-part law with the values of *n* obtainable from the gradients of the fitted lines. The transient period was found to be less than an hour except in the case of MD-2 at 450°C. The time period of the transient growth was also found to halve when both alloys oxidise at 550°C in comparison to 450°C. These results are summarised in Table 4.6. It can be appreciated that the values of *n* in the transient regime are sufficiently close to 2 that parabolic kinetics can be assumed. To the best knowledge of the author, parabolic transient kinetics have not been previously reported in Ni-based superalloys at temperatures below 650°C. At longer exposures, the reactions approximate a cubic law for CMSX-4 and a quartic law in the case of MD-2. Understanding and explaining this behaviour requires investigation of the oxidation morphology and composition and comprises the next section of the report.

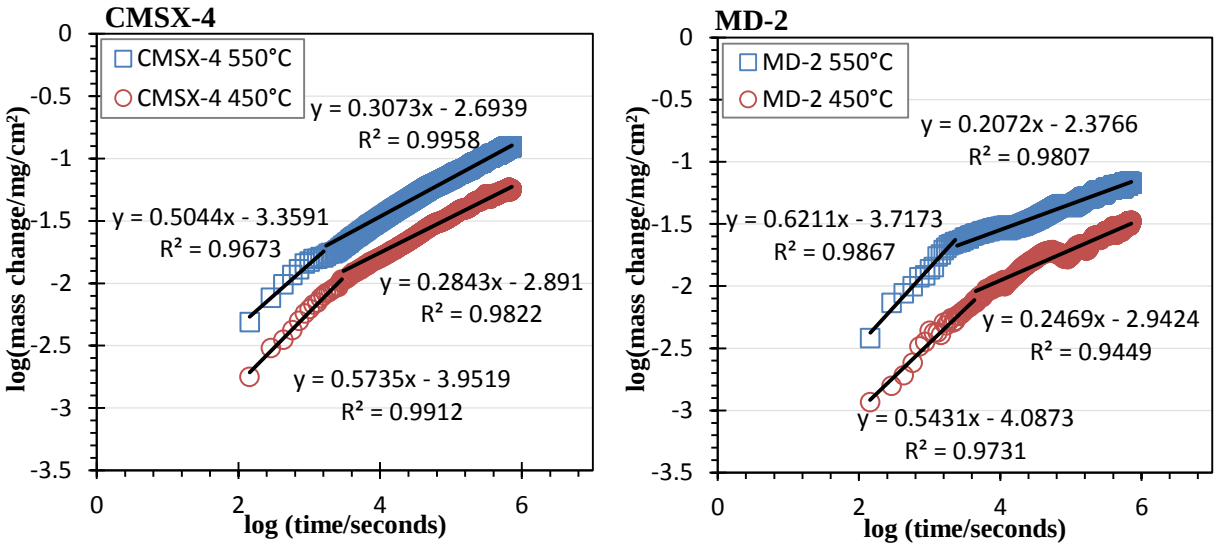

Figure 4.27: Oxidation kinetics of CMSX-4 and MD-2 at 450°C and 550°C as a function of normalised weight change measurements obtained via TGA. The data are plotted according to Equation 4.3 and reveal the transient and stable growth regimes with separate linear fits.

Alloy	Temp.	Transient Oxidation		Stable Oxidation
		Duration (h)	n	n
CMSX-4	450°C	0.80	1.7	3.5
	550°C	0.44	2.0	3.3
MD-2	450°C	1.18	1.8	4.1
	550°C	0.64	1.6	4.8

Table 4.6: Transient oxidation duration and exponent values of the power law describing the isothermal oxide growth rate of CMSX-4 and MD-2 at 550°C and 450°C.

4.4.2 Oxide scale morphology

The differences in the chemical composition between dendritic and interdendritic areas led to macroscopically visible differences in the scale morphology of CMSX-4 (Figure 4.11). It has been previously shown that even after multistep heat treatments some degree of chemical segregation exists in CMSX-4 and other single crystal Ni-based superalloys [39,55,77,181]. Re, W, Co and, to a lower degree, Cr seem to preferentially reside at the dendritic cores and arms while Al, Ta and Ti segregate to the interdendritic regions. It is therefore expected that the two regions would have some degree of variation in their oxidation performance. The higher Al content of the interdendritic regions appears to be responsible for the thinner oxides observed. Since it is thermodynamically favourable for Al to oxidise first, it can be postulated that the compact Al-rich oxide reduces the growth rate of the scale in the region.

On the contrary, the surface of the carbon containing MD-2, oxidised much more uniformly with no distinct differences between dendritic and interdendritic regions. However, the surface eruptions associated with the oxidation of interdendritic carbides appear to cause significant scale damage in their vicinity. Assuming pure TaC carbides (see Figure 3.8 of section 3.3.1), which are known to oxidise to form Ta_2O_5 [182], the likely reaction during oxidation can be represented as:

$$9O_2 + 2TaC \rightarrow 2Ta_2O_5 + 4CO_2 \qquad (4.4)$$

Using available molecular weight and density data [183,184], the molar volume expansion of TaC to Ta_2O_5 are calculated as 13.3 and 53.9 cm^3/mol. Therefore, a volume expansion of approximately 4 can be estimated for the transformation of TaC to Ta_2O_5 . It is anticipated that a volume expansion of this magnitude would induce significant stresses capable of plastic deformation of the scale and the surrounding matrix, resulting in spalling and decohesion such as the observations shown in Figure 4.12. The tower like oxide eruptions are possibly the result of a lamellar oxidation process. The exposed carbide surface oxidises and expands causing partial decohesion with the matrix. Separation of the carbide-alloy interface exposes more of the carbide and the substrate and further oxidation takes place. The process will repeat itself with additional layers of oxide forming distorting the surrounding material and forming the protruding structures observed. Similar behaviour was previously reported in Inconel 718 for NbC [160].

To further investigate the extent of damage, an additional MD-2 sample was oxidised for 1000h at 550°C. Following oxidation, FIB sections were taken normal to the carbides and the subsurface was imaged using a FEG-SEM. Evidence of oxygen diffusion through the alloy/carbide interface is shown in Figure 4.28. The formation of an oxide scale, similar to the one seen on the surface of the alloy, around the carbide and the subsequent oxide build up would have caused the outgrowth of the carbide. The large stresses resulting from this process were observed to cause repeated cracking of the embrittled particle subsurface and decohesion and spalling of the Ni-rich external oxide scale, evidence of which are shown in Figure 4.29. Figure 4.29a and c, show the erupted morphology of the oxides formed on top of surface carbides, while Figure 4.29b and d show the cross sections taken as indicated by the yellow dotted lines. Therefore it is suggested that the outward eruption of carbide oxides and internal cracking is caused by the following processes: i) large volume expansion due to different thermal expansion coefficients between carbide and alloy, ii) difference in the oxide growth rates between the alloy and the carbide and iii) the oxide scale build up beneath the carbide and at the carbide – alloy interface. An additional factor that might affect decohesion of the interface is the formation of CO_2 shown in Equation 4.4. Poor carbide performance was recently attributed to the formation of CO_2 at the interface of between a tungsten (W) carbide and its oxide, inducing porosity and scale cracking [185].

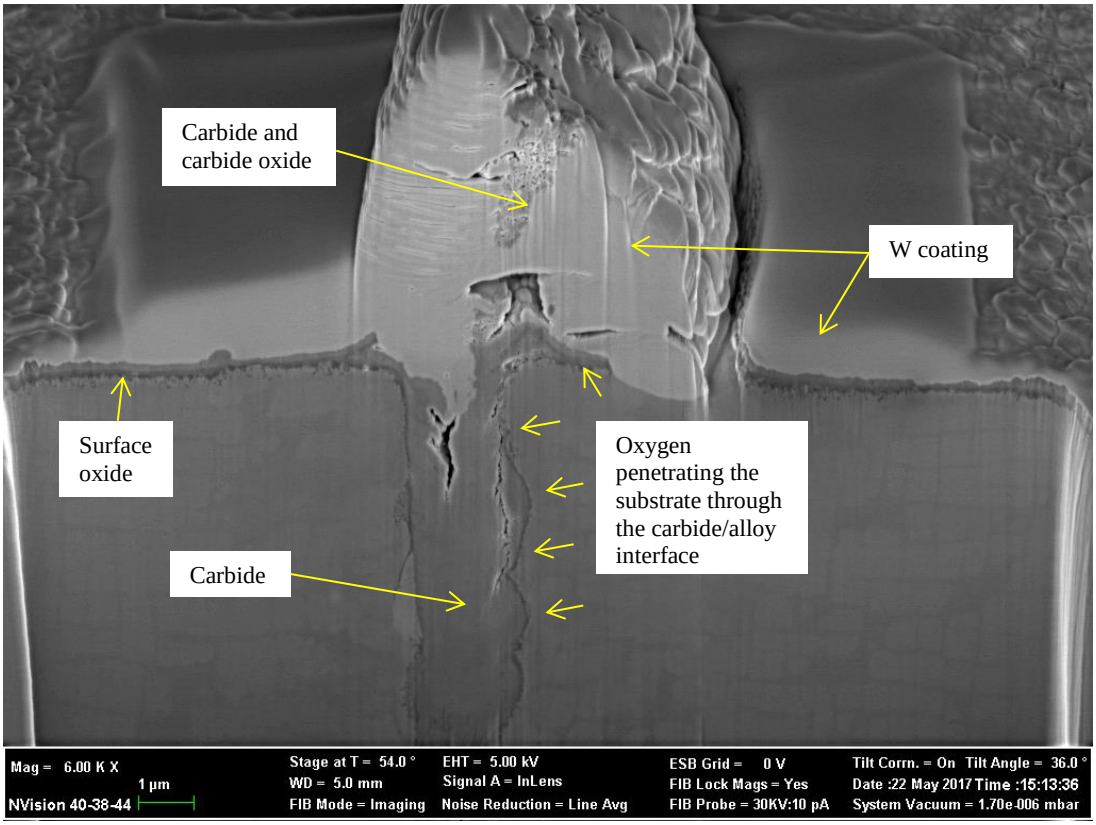

Figure 4.28: FIB cross section of an oxidised carbide in an MD-2 sample oxidised for 1000h at 550C. The oxide is shown to encapsulate the carbide particle.

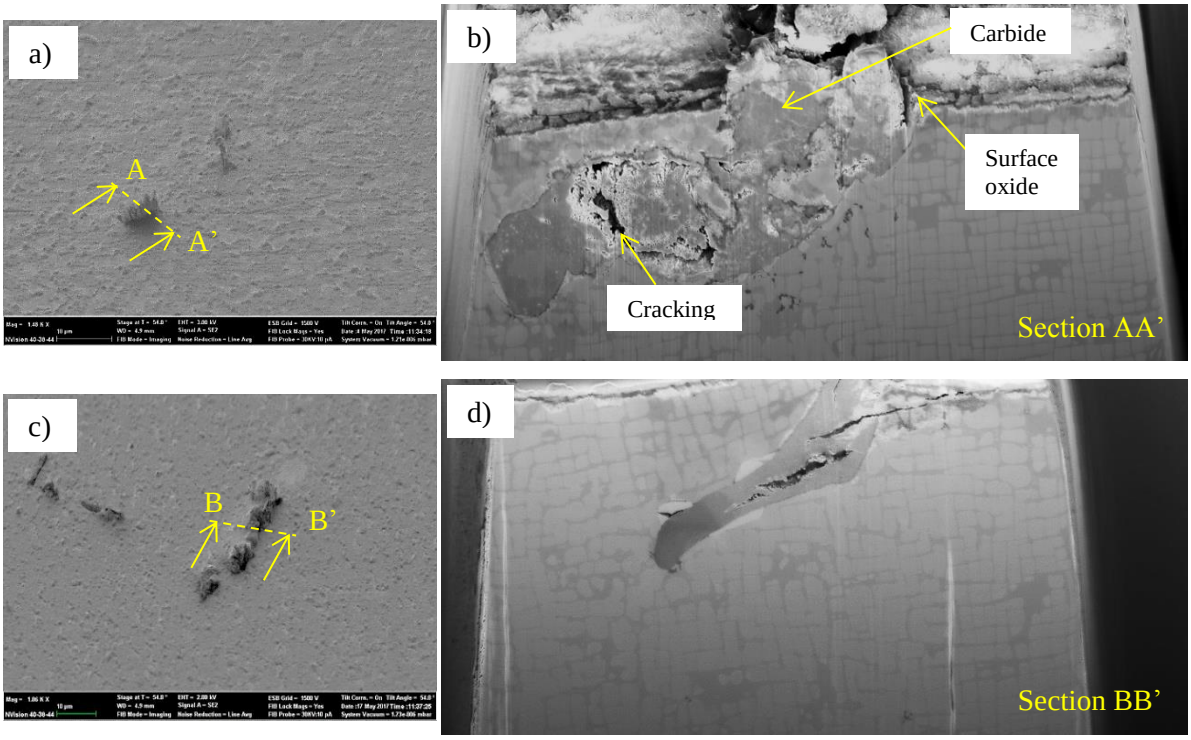

Figure 4.29: SEM-BSE images of the surface and FIB sections of the carbides forming on MD-2 at 550°C following 1000h of exposure.

4.4.3 Thermodynamic considerations

In order to understand the nature of the oxides as well as the formation sequence, it is important to consider the thermodynamics of the metal oxide systems. Whether or not an oxide is formed can be determined by considering the equilibrium partial pressure of oxygen (also known as the dissociation pressure of the oxide). A metal oxide will start to form when the oxygen partial pressure is greater than this dissociation pressure. In this study, the oxide layer sequence was simulated using the ThermoCalc software with the TCNI8 database which uses the CALPHAD approach [186]. The simulations were conducted by Dr. Shan Jin from Thermo-Calc Software.

Figure 4.30a & b show the stable oxide phases, predicted by the ThermoCalc simulations, to form on CMSX-4 and MD-2 at 550°C as a function of oxygen partial pressure. It can be seen that the higher number of alloying elements in MD-2 results in a much more complex array of oxide phases. However, at the same time, the most dominant phases are calculated to be similar in both alloys and generally are in good agreement with the experimental observations. Thermodynamic modelling indicated that at high oxygen partial pressures, i.e. closer to the outer surface of the forming scale and on top of the substrate, halite is the dominant oxide phase. Spinel and other secondary phases are also predicted to exist externally in both alloys but to a much lower degree. The halite phase, which seems to have a clear cut off point right at the interface where the FCC $L1_2$ phase (alloy substrate) begins (Figure 4.30a – consistent with the EDX scan of Figure 4.22), consists almost entirely of NiO (Figure 4.30c). The composition of the external spinel phase is shown in Figure 4.31a for CMSX-4 and Figure 4.31b for MD-2. Al is the main constituent of this external spinel phase in both alloys, but smaller amounts of Ni, Cr and Co are also predicted. According to the XRD results of Figure 4.19, the spinel oxides in CMSX-4 are Al_2NiO_4 and the Co_3O_4 and it is expected that at least the former one would exist in the MD-2 as well. The different amount of Cr and Co calculated within the spinel phases of the two alloys reflects the difference in their composition which is shown in Table 3.1.

When the oxygen partial pressure drops below approximately 1×10^{-21}Pa (just below the surface of the alloy), spinel and the ternary $NiWO_4$ phases are more thermodynamically stable. A Ti-rich rutile phase and a Ta rich oxide are also found in increased amounts within the substrate. As the oxygen partial pressure further decreases inside the alloy (>1×10^{-22}Pa), a corundum phase was calculated to form at the expense of spinel. Comparing the two alloys, it is evident that the composition of MD-2 allows for a much higher concentration of corundum at the same pressure/oxygen activity levels and according to the results of Figure 4.31 this mainly consists of a Cr rich oxide. However, EDX analysis on the cross section of a number of MD-2 samples did not indicate formation of Cr-rich oxides (see for example Figure 4.22b). On the other hand, the corundum phase in CMSX-4 is calculated to be rich in Al. This can be understood by considering

the interactions between the alloying elements in the two alloys. Assuming simple oxides, in the case of Ni-based superalloys the most commonly met ones that have the corundum structure are the α-Al_2O_3, Cr_2O_3 and Ti_2O_3. It is unlikely however that the corundum phase seen here is the α-Al_2O_3 since this is generally formed when the reaction temperatures exceed 800°C. In addition, the absence of Cr in the EDX results of the MD-2 samples, make the formation of corundum during the experimental part of this study questionable.

Even though thermodynamic calculations are a powerful tool for understanding the oxidation mechanisms under a range of conditions there are still limitations that need to be taken into account. The results are heavily dependent on the database used which is informed by experimental results obtained to date. In addition, the simulations obtained through the software represent the equilibrium conditions, which may require much longer times to achieve experimentally. As evidenced by the transient oxidation observations (Section 4.4.1), equilibrium phases might not always be achieved during service conditions (such as in the case of fatigue-oxidation damage) as the time available for oxidation would not be sufficient for phase transformations to stabilise.

Although not all of the thermodynamically predicted phases were detected, the XRD analysis seems to agree in general with the predictions. In Ni-based superalloys, the α-Al_2O_3 phase is the desired TGO for its slow-growth rate and low anion diffusivity but it has been previously shown that for temperatures lower than 800ºC transition aluminas form first [187]. Although the results here indicate the formation of the η-Al_2O_3 it is important to note that other transition aluminas such as the γ-Al_2O_3, δ-Al_2O_3, θ-Al_2O_3 produce similar peaks at the same diffraction angles [188]. Studies that investigated the transient oxides in a Ni-Al system at 600°C [189] and 1000ºC [190] reported that after the formation of an external NiO, a $NiAl_2O_4$ spinel followed the formation of an inner healing layer of γ-Al_2O_3 . Similar observations were made in the case of a Ni-9Cr-6Al alloy during the initial stages of oxidation at 900ºC, where small amounts of γ-Al_2O_3 coexisted internally with oxide spinels and regularly shaped Cr_2O_3 [170]. The formation of the $NiAl_2O_4$ open spinel detected here by XRD (found by previous workers to contain equiaxed grains, intergranular and intergranular porosity, precipitates and large voids [191]), allows for rapid cation diffusion which causes increased oxidation rates [192]. This Al/Al_2O_3 – NiO interaction behaviour could explain the sub-parabolic kinetics observed within the stable oxide growth regime as described above.

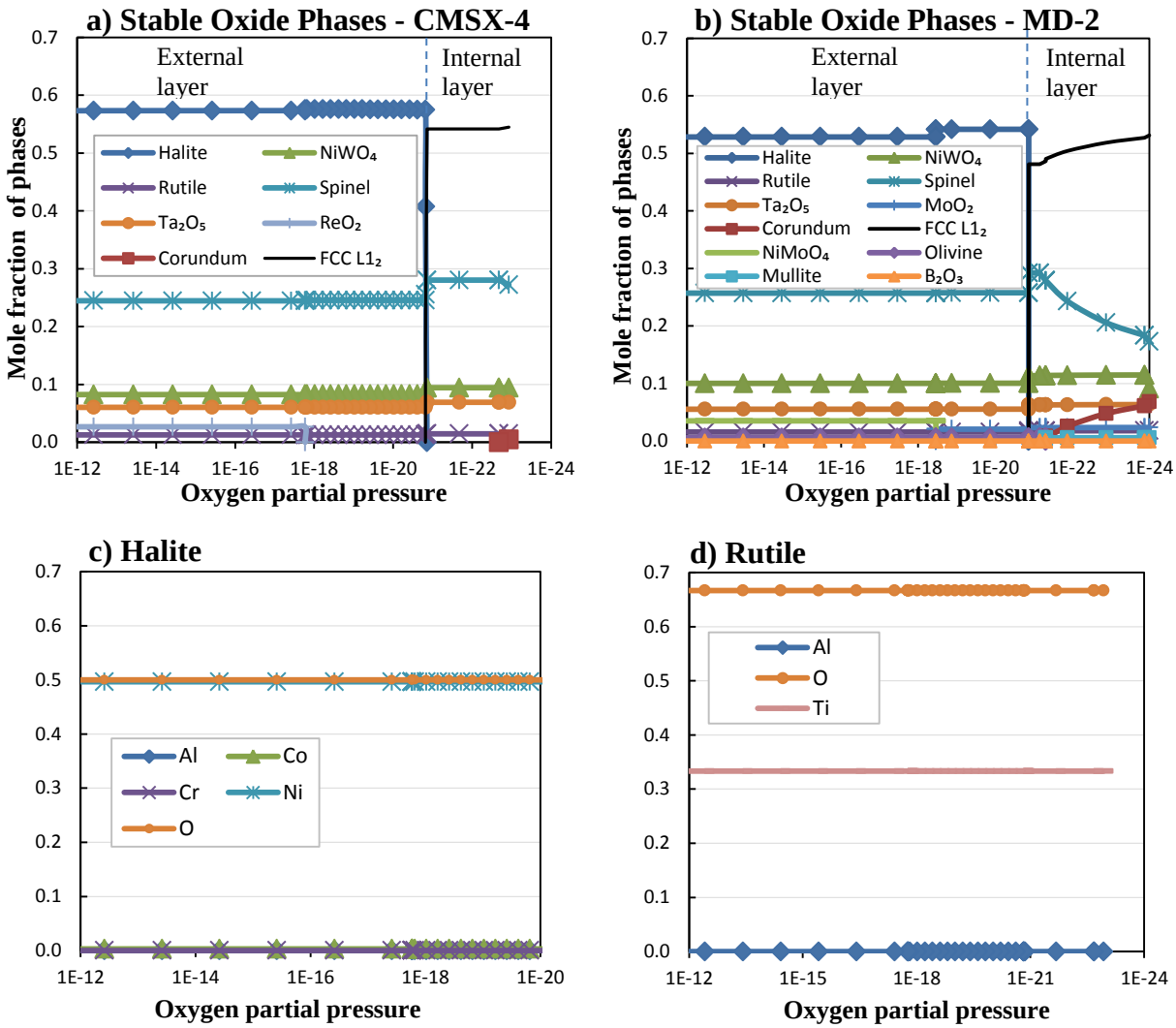

Figure 4.30: a) & b) Simulation of the stable oxides formed on CMSX-4 and MD-2 at 550°C and c), d) Elemental composition of the Halite and Rutile oxide phases found in the two alloys.

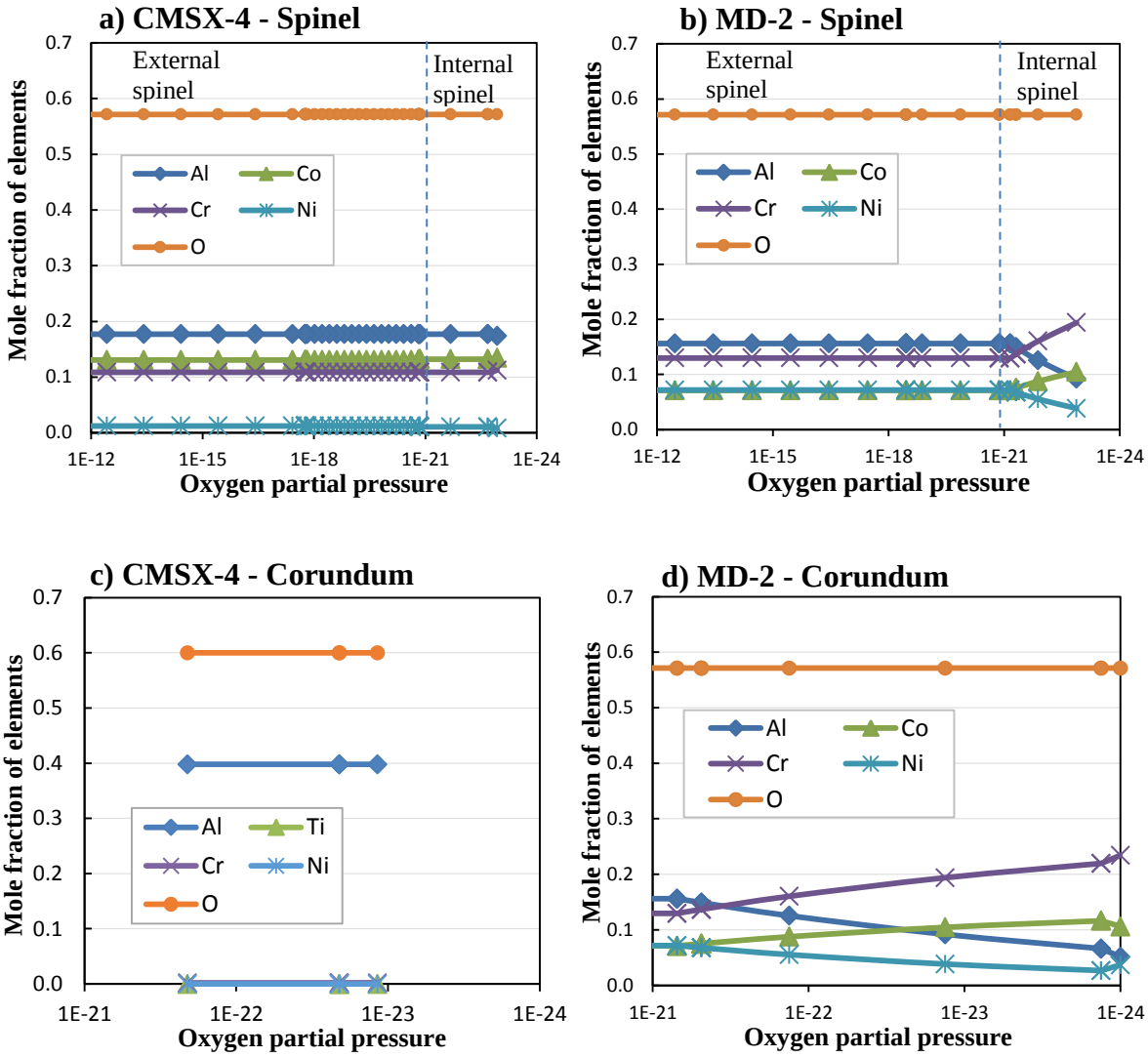

Figure 4.31: Calculated composition of the spinel and corundum phases in a) & c) CMSX-4 and b) & d) MD-2.

4.4.4 Postulated mechanism of oxidation at intermediate temperatures

Based on the observations and simulations to date, the following oxidation mechanism is therefore proposed: Assuming a perfectly flat surface the oxidation process begins by outward diffusion of Ni cations which form bulges of NiO over the γ channels. At the same time, a thin Al-rich oxide begins to form in discrete places (depending on its concentration in the area) over the γ' particles. Thus, if a simple binary phase composition (Ni_3Al) is assumed, the likely reaction can be represented as:

$$3O_2 + 4Ni_3Al \rightarrow 12Ni + 2Al_2O_3 \qquad (4.5)$$

From a kinetics perspective, the transient oxidation growth was shown to obey a near parabolic law. Previous research, showed that nickel oxidation follows parabolic kinetics at temperatures below 600°C indicating that nickel is the rate controlling element at the early stages [179]. The outward diffusion of Ni forms a narrow depletion zone adjacent to the surface of the alloy. During this transient period, oxidation is not protective and growth rates are still high as the cellular and porous morphology of NiO, forming at these temperatures [193], provides an easy path for further oxygen transportation into the substrate material. This oxygen flux was previously reported to penetrate the alloy surface through the γ channels until an Al-containing γ' particle is encountered [127]. However, the microstructures of CMSX-4 and MD-2 are characterised by the ordered alignment of γ' precipitates which results in long unblocked γ channels and for the temperature and exposure times used in this study, oxygen was not found to penetrate the alloy to a sufficient depth in order to be blocked by a γ' particle (e.g. see Figure 4.21). A recent study [194] conducted detailed investigations of the oxygen diffusion path (ODP), at 850˚C, in a nickel based single crystal superalloy using in-situ TEM observations. Based on electron energy loss spectroscopy (EELS) mapping, their results indicated that the ODP is more inclined to be the interface boundary between the two phases (γ/γ') rather than the γ channels themselves. Their results could be explained by considering the stress state of the interface. Even though the samples tested here were not subjected to any loads, single crystal nickel base superalloys have small differences in the lattice parameters of the γ and γ' phase, which represent a source of additional strain in the microstructure. The magnitude of this strain can be substantially increased in the case of exposure to high temperatures, because of the difference in thermal expansion coefficients between the two phases, resulting in increased dislocation densities at the γ/γ' interface [195]. This provides a better explanation of the initial oxidation mechanism observed here. Oxygen traveling down the interface comes into contact with both the matrix and the precipitate phases. Internally the oxygen partial pressure and the local concentration of elements (with Ni cations migrating to the surface) seem to favour the formation of ternary spinel oxides such as $NiWO_4$. As the oxides thicken, further decreasing oxygen pressure levels, the activity of O becomes insufficient to oxidise the γ phase which mainly consists of Ni, Cr and Co. On the other hand, O readily reacts with the thermodynamically favourable Al of the γ' phase.

Following the initial stages of oxidation, a continuous, thin alumina scale has started to form below the spinel oxide but within the nickel depleted zone (Figure 4.22). According to the XRD results (Figure 4.19) this is a transition type of Al_2O_3. The oxidation mechanism at this stage becomes an extension of the mechanism seen at the earlier stages. The occasional internal protrusion zones where both the γ/γ' phases oxidise could be linked to aluminium diffusion into the defect rich, transient alumina scale. This is expected to gradually deplete the γ' phase under the

alumina layer transforming it into a single disordered γ phase. The oxidation mechanism is shown schematically, for the transient and stable growth regimes, in Figure 4.32.

In agreement with the XRD analysis, no chromium oxide was detected from the EDX scans at any exposure time for both CMSX-4 and MD-2. Studies conducted on superalloys at temperatures between 750-1100ºC reported the formation of chromium oxide either in its pure-chromia form [25,83,169,180] or as a spinel with Ni and Al [23,83]. However, those temperatures are still much higher than the ones considered here and can therefore significantly affect the thermodynamic and kinetic driving forces.

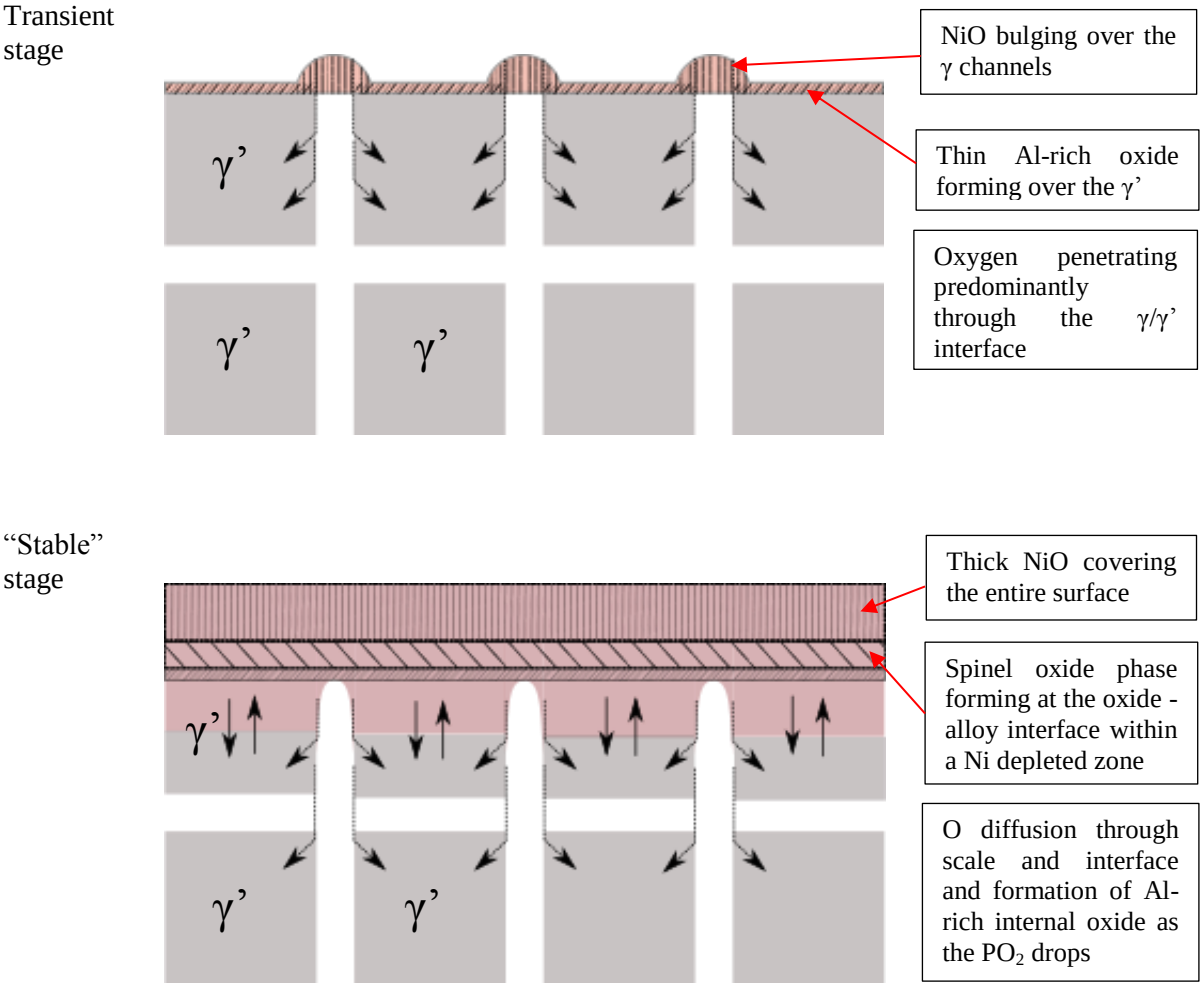

Figure 4.32: Schematic showing the isothermal oxidation mechanism of CMSX-4 at 550°C.

4.4.5 Effect of stress/strain on isothermal oxidation

Externally applied tensile loads were found to mainly affect the morphology and to a lesser degree the composition of the oxides forming. However, tensile loads insufficient to induce plastic deformation did not affect the oxidation behaviour of the CMSX-4 sample and the resulting oxide was comparable in thickness to the unloaded samples. The phenomenon can be therefore assumed to be controlled by strain and not stress. The mechanism of pit formation should be explained by first considering the effects of tensile load and creep deformation in single crystals. Defects resulting from the induced plastic deformation can provide open routes for enhanced oxygen diffusion into the substrate. Cracking, increased dislocation densities near the surface and slip band formation may have enhanced both the outward diffusion of species and ingress of oxygen. The oxidation behaviour of thin strips of a Ni–20Cr alloy was investigated under creep conditions at 500ºC and 600ºC by Calvarin-Amiri et al. [196]. From TEM and SEM-EDS observations they found that mechanical loads induce accelerated anionic diffusion (increased depth of internal oxidation/pit formation) and at a lower scale, increased cationic diffusion. On the other hand, the nature of the oxides formed remained the same. Tensile loads were reported to increase the porosity and to induce microcracks within the grains of the external NiO. These observations were then linked to the accelerated oxidation rates observed, as defects and grain interfaces act as very fast-diffusion paths. Foss et al. [154] investigated the effects of both compressive and tensile loads by conducting static bending tests on another polycrystalline Ni-based superalloy (RR1000). Bulging oxides intruding into the substrate were observed in both loading conditions with compressive stresses generating deeper pits. O^{18} was used as a tracer for diffusion and secondary ion mass spectrometry (SIMS) analysis indicated that applied stresses have little influence on the inward oxygen diffusion. It was suggested that mechanical stresses influence the diffusivity of the oxidized solute species in the substrate alloy and this is proposed to result from defects induced from creep deformation. Another recent experimental study [177] conducted on a Ni-based superalloy indicated that external tensile loads result in thicker scales even in the absence of cracking or spalling. Their conclusions were supported by the theoretical model developed by Evans et al. [3]. The model suggests that the vacancy concentration, which controls the solid-state diffusion process, is altered by external tensile stresses. The theory was later extended by Limarga and Wilkinson [197,198] who proposed a model that describes the interaction between mechanical stress and the scale growth in a multilayer system.

In light of the above it is important to note that this mechanism might not be valid for higher temperatures and/or other alloy compositions as the thermodynamics and kinetics of oxidation differ. Contrary to the findings of this study, previous studies have argued that application of load under oxidising conditions has a beneficial effect in the mass change values by reducing the transient oxidation period. An example of which is the study by Barnard et al. [157] who conducted

tensile tests on two polycrystalline Ni-bases superalloys with high Cr content (>20wt%). The high Cr levels in the examined alloy seemed to act beneficially on the oxidation resistance under load. Samples oxidised under load exhibited thinner scales with higher Cr/Ni ratios. This indicates that the applied stresses induced outward cation diffusion of Cr-atoms which formed a protective Cr_2O_3 scale externally inhibiting further oxidation. Moulin et al. [199], investigated the effects of various mechanical loadings (including creep and creep-fatigue) on oxygen diffusion in a polycrystalline nickel, in an attempt to provide additional information on the oxidation mechanism observed. Testing was conducted at 550ºC and X-ray photoelectron spectroscopy (XPS) and SIMS techniques were employed to analyse the samples. The oxide layer and the substrate material were investigated separately; it was found that oxygen mobility through the scale is restricted. Grain boundary alteration in the NiO was once more reported but oxygen was found to act as a healing agent for cracks and spallation sites. Internally, oxygen was found to reach greater depths but this was attributed to alteration of the grain interfaces in the substrate rather than the oxide scale. Subsequent experimental studies seem to agree that applied stresses influence diffusivities and increase defect and dislocation densities. Alloy composition seems to be the controlling parameter in this case.

4.5 Summary

The purpose of this chapter was to investigate the effects of oxidation on surface degradation in a single crystal Ni-based superalloy and establish an oxidation mechanism, based on physical observations, at 450ºC and 550ºC. From the experimental results and discussion the following conclusions can be drawn:

1. The isothermal oxidation behaviour in CMSX-4 and MD-2 at 450ºC and 550ºC obeys a sub-parabolic law. The external and internal oxide scales, grow with similar, sub-parabolic, rates.
2. The oxidation kinetics can also be described by a two stage law: a transient near-parabolic regime and a stable sub-parabolic regime.
3. Thermodynamic calculations showed the complexity of the oxides forming at these temperatures. The protective Cr_2O_3 did not form and instead transient and ternary spinel phases comprised the inner layers of the oxide structure.
4. The oxidation mechanism can be outlined as follows. First, the clean alloy surface comes into contact with oxygen and oxide clusters begin to form. Due to the high concentration of Ni, the γ matrix begins to form porous NiO surface protrusions. At the same time, a transition alumina forms over the γ’ phase and internally within a Ni depleted zone. Since the scale is not yet protective, oxygen anions continue to diffuse into the alloy preferentially through the γ/γ’

interface. Then, oxygen comes in contact with the γ' phase which contains higher levels of Al (which is thermodynamically favourable to oxidise first). This leads to the preferential oxidation of the γ' particles internally while the γ matrix remains relatively unaffected.

5. Isothermal oxidation of (Ta, W) Carbides occurs readily in MD-2 at 550°C and from surface eruptions causing oxide decohesion. As a result of volume expansion due to high temperatures and in conjunction with the different thermal expansion coefficient of the substrate significant plastic deformation and cracking takes place subsurface in the vicinity of the carbide.
6. External tensile loads (at 550°C) result in thicker oxide scales (bulging morphology) with deeper oxidation affected zones when the associated strains cause plastic deformation. This is likely to be the result of increased dislocation densities near the surface and slip band formation that provided additional routes for oxygen penetration and diffusion of species.

Chapter 5 Fatigue Crack Initiation and Short Crack Behaviour

5.1 Introduction

Understanding fatigue crack initiation and early propagation is vital as they control a substantial part of the fatigue life of many engineering components. Although these processes are less commonly applied in lifing procedures, where damage tolerant mechanisms are considered, lifing approaches could be adapted to include the effects of initiation.

The initiation process itself is controlled by localised plastic deformation and it is therefore more severe in turbine blade features such as notches and holes of the interior cooling system. Most of the available literature agrees that fatigue cracks initiate at intrinsic, microstructural singularities located on or near the surface of the material. Externally applied service conditions such as strain levels, loading waveform and temperature also play an important role. In the case of single crystal turbine blade superalloys it has been shown that initiation can occur at defects such as casting pores [97,200], carbides [200,201], oxide spikes [90,202] and eutectics [203] or by persistent slip bands [90,204] that form during plastic deformation, mostly at higher frequencies and/or lower temperatures. The micro mechanisms controlling crack initiation can vary substantially, depending on the service conditions and particularly on temperature.

Previous work on CMSX-4 notch fatigue behaviour, has shown that initiation at 650ºC is dominated by <001> aligned interdendritic porosity, which is directly affected by the secondary orientation of the sample [97]. Even at 650ºC, oxidation appeared to play an important role. Initiation in vacuum was found to occur predominantly from pores at the notch surface while initiation in air was shifted to subsurface pores. The postulated mechanism for this shift was that oxidation deactivates surface pores by essentially building up an oxide plug. Even though substantial oxidation was observed at the notch root no observations of oxide induced cracking were made. Casting micropores were again reported to initiate LCF cracks early in the life of MARM200 and CMSX-2 single crystals at 650ºC [200]. Both surface and subsurface initiation sites were found leading to two discrete fatigue failure mechanisms. Failure in CMSX-2 was controlled by the growth of a dominant, porosity-induced crack while in MAR-M200 porosity initiated multiple cracks that coalesced to final failure. Gabb et al. [205] conducted fatigue tests on single crystal Ni superalloys at a range of temperatures and reported a change of the initiation

mechanism with increasing temperature. At temperatures below 760ºC initiation was controlled by a single near surface pore or surface defects that then propagated by flat, stage II - like short cracks before shifting to a predominately crystallographic, stage I - like long crack. At higher temperatures (980ºC) fatigue initiation was initiated by the interaction of porosity and oxidation, followed by the formation of oxide spikes. Similar observations were also made in a DS Ni-based superalloy [202]. Prior to fatigue testing, their samples were exposed to hot air (982ºC) for 100h both in a loaded and unloaded state. Pre-exposure, in both cases, resulted in a reduction in fatigue life and multiple crack initiation from oxide spikes emanating from the surface.

Although there is a substantial body of literature investigating these mechanisms, the majority is concerned with either high temperatures (>700°C) or room temperatures where time and cycle dependent effects generally act independently. In the intermediate temperature regime (450-650ºC) time and cycle dependent processes will start to interact more, although the extent of oxidation is likely to be much more limited, and is less well understood. This chapter therefore considers crack initiation and subsequent short crack propagation behaviour in CMSX-4 at 450 ºC and 550ºC with particular focus on the effects of oxidation.

5.2 Experimental Procedure

5.2.1 Sample preparation

U-notch bend specimens were machined using EDM having their tensile axis along the <001> direction and the notch oriented along the <010> direction. A specimen size of 9mm x 4mm x 60mm was selected in order to make best use of the available material. A 2mm radius notch was machined half way along the specimen bar with the centre point of the radius set 0.5mm above the surface of the bar resulting in a notch depth of 1.5mm (Figure 5.1). The notch geometry was selected such as to provide a stress concentration factor of ~2, which is representative of various turbine blade notch features.

The EDM process left behind a highly oxidized surface layer that required grinding and polishing before testing could take place. Grinding of the U-notch was achieved by using a slotted dental felt pin with a SiC paper wound around it. The pin was then attached to a hand drill that rotated the pin while in contact with the notch surface and ground away the oxide layer. In a similar manner, polishing was completed in two stages using cone shaped dental pins soaked with 9μm and 3μm diamond suspensions.

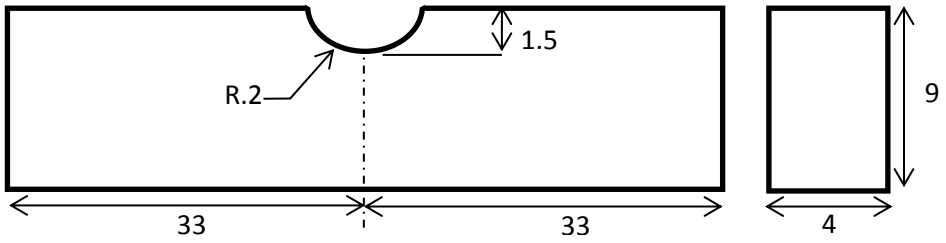

Figure 5.1: Notched sample geometry (in mm) used for short crack testing.

5.2.2 Finite element model

Prior to crack initiation, it is expected that the material in the vicinity of the initiation site will deform plastically. In order to evaluate the stress/strain distribution at the notch root and to identify appropriate loads for the test an elasto-plastic finite element analysis (FEA) was undertaken in Abaqus. Based on experimental results from previous work on CMSX-4 [9], a strain range of $\Delta\varepsilon = 1.3\%$ was chosen as the target value to give an acceptable lifetime (<50000 cycles) for the tests. The constitutive material model for this analysis was obtained from the high temperature tensile tests described in section 3.2.3 and the stress strain values were included as tabulated data in the input file. The material model was implemented by assuming isotropic monotonic data. To save computational cost half the sample was modelled using a symmetry boundary condition at the centre. The supporting (top surface) rollers were simulated as analytically rigid bodies while a pressure force was applied to simulate the loading roller (bottom surface). The width of the contact area between the rollers and the sample was calculated using the equation of contact between two cylinders and assuming that the top surface of the sample can be simulated with a cylinder of infinite radius.

$$width = 2 \times \sqrt{\frac{4F\left[\frac{1-{v_{sample}}^2}{E_{sample}} + \frac{1-{v_{sample}}^2}{E_{roller}}\right]}{\pi L\left[\frac{1}{R_{sample}} + \frac{1}{R_{roller}}\right]}} \qquad (5.1)$$

In Equation 5.1, $E_{sample} = 120MPa$ and $E_{roller} = Infinite$ are the moduli of elasticity for the sample and the (rigid) roller and v_{sample} and v_{roller} are the respective Poisson's ratios. L is the length of contact and F is the downward force applied.

To ensure good approximation of the root stress/strain fields, a dense, structured mesh was employed at the vicinity of the notch. A sensitivity analysis was conducted initially to identify a threshold size for the mesh. Figure 5.2 shows the overall mesh and the mesh detail around the

notch. Loading was applied monotonically up to an arbitrary load of 2000N. Abaqus applies the load incrementally and at each increment the magnitude of the stress and strain at the central node were recorded and the results are shown in Figure 5.3. Using these results, a load of 1780N (for the half model, hence 3560N for the test) was found to produce a maximum strain of $\varepsilon_{max} = 1.42\%$ and was selected for testing. The corresponding maximum stress was $\sigma_{max} = 979MPa$ and for a load ratio $R = 0.1$ the strain range was $\Delta\varepsilon = 1.31\%$. The stress and plastic strain distribution resulting from these loads are shown in the contour maps of Figure 5.4.

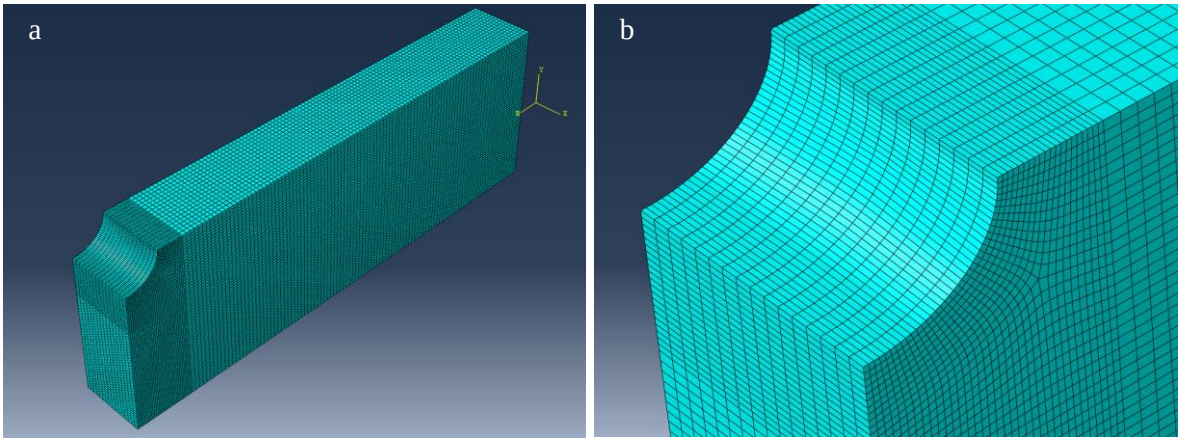

Figure 5.2: Notched fatigue sample a) model geometry and b) meshing details around the notch.

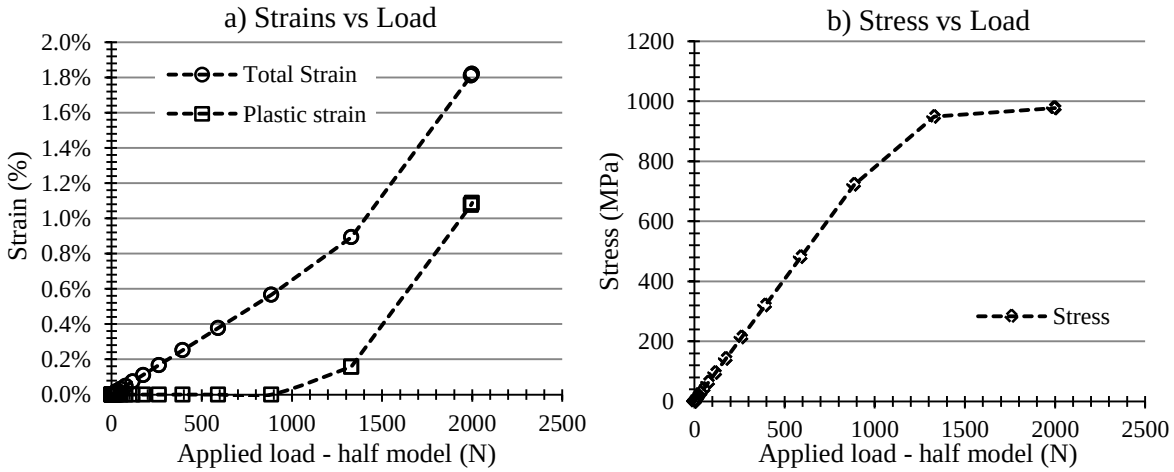

Figure 5.3: Predictions of a) total and plastic strain and b) stress at the notch root in CMSX-4 at 550°C.

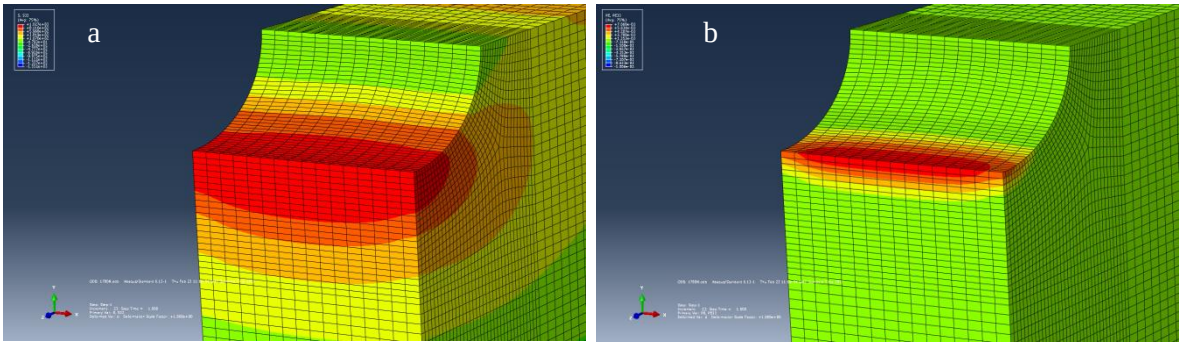

Figure 5.4: Abaqus FEA model of CMSX-4 loaded in three point bend with a 1780N load (half model) showing the S33 (Z-direction) a) stress and b) plastic strain distribution around the notch.

5.2.3 Testing procedure

Notch fatigue experiments on CMSX-4 were conducted on an Instron 8501 servo hydraulic testing machine equipped with an ESH Ltd high temperature vacuum chamber. Set-up of the fatigue tests, heating of the specimens and the temperature control were the same as detailed for the sustained load oxidation test described in section 4.2.3. During all tests the load ratio (*R*) was kept constant at 0.1. The samples were loaded in 3-point bend and fatigued to failure using a 1-1-1-1 trapezoidal waveform. This waveform is often adopted by industry as the baseline frequency for high temperature testing as it allows for some time dependent processes to occur and has also been utilised for associated comparison research at the University of Southampton [9,206]. The waveform is shown schematically in Figure 5.5 along with the sample set up.

Testing was conducted in both air and reduced oxygen partial pressure environments, at 450ºC and 550ºC, to assess the effects of oxidation. The oxygen partial pressure in the chamber was reduced by purging with nitrogen (N_2) to displace the oxygen. To achieve this, the procedure outlined below was followed.

1. The chamber was sealed and a rotary pump reduced the pressure to approximately 50mbar.
2. Once pressure stabilised, the valve connecting the pump to the chamber was closed and the pump switched off (chamber isolated).
3. N_2 was allowed to flow into the chamber by opening the valve on the supply tube.
4. The chamber was filled to 1.05mbar and isolated again.
5. Steps 1-4 were repeated 3 times to further dilute oxygen mixed with the N_2.
6. The N_2 flow was adjusted to maintain the chamber pressure at 1.05mbar to mitigate any leakage.
7. Over-pressurised chamber maintained at 1.05mbar for 10h.
8. Heating was turned on and temperature was allowed to stabilise for 30minutes.

At the end of the third cycle the oxygen partial pressure in the chamber was calculated to be $1.25 \times 10^{-3} mbar$. The experimental apparatus associated with this process is shown in Figure 5.6 and the oxygen partial pressure calculation method is presented in Appendix C.

In view of the results of section 4.4.5, (oxide intrusions forming under the effect of plastic strain), testing on samples that have been previously oxidised under sustained tensile loads was also conducted at each temperature. Following heating, these samples were loaded using the same 3-point bend set up. A 3.56kN load, corresponding to a maximum notch stress of 979MPa and plastic strain of 0.8%, was applied. The load was maintained for 70h before the 1-1-1-1 cyclic load was applied.

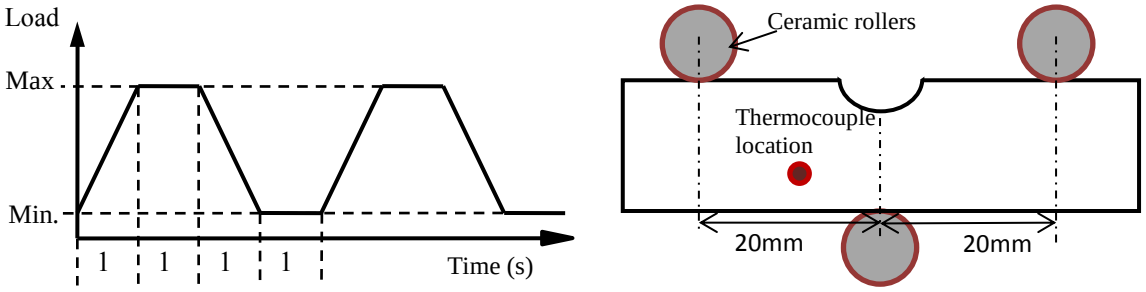

Figure 5.5: Short crack fatigue testing a) loading waveform and b) schematic of sample set-up in Instron.

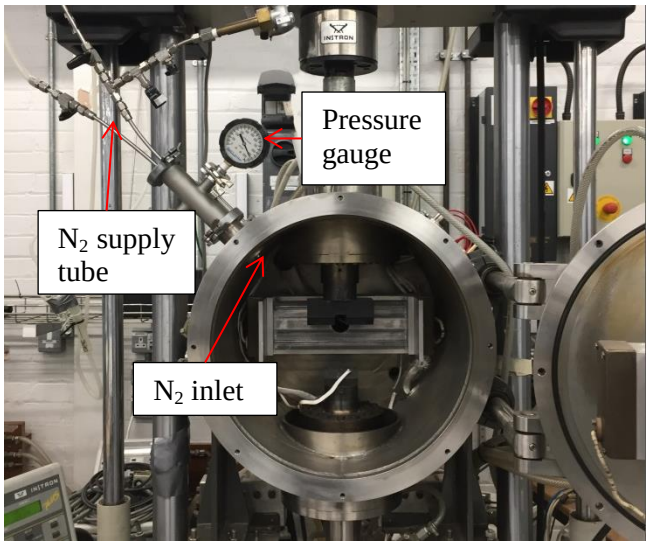

Figure 5.6: Instron machine with nitrogen gas inlet used for short crack testing.

5.2.4 Fractography

Interpretation of the results was mainly based on detailed, systematic assessment of each fracture surface. Initially, the fractured samples were examined with a Wild macroscope to assess gross macroscopic features and identify the nature of failure. A JEOL FEG-SEM was later used to examine the fracture surfaces in more detail and help pinpoint initiation sites and notch surface fracture features. High magnification images were taken from all initiation areas and crack propagation features in the SEI and BSE modes to obtain both topographical and compositional information. EDS point and map composition analysis (using the Oxford Inca 300 software) was conducted on sites of particular interest to identify oxidation products.

5.3 Results

5.3.1 Fatigue life of CMSX-4

The fatigue life data for a total of nine tests are shown in Table 5.1. The 550°C N_2 test was conducted twice to consider potential scatter. In addition, two room temperature (RT) tests were included in the test matrix in order to examine possible effects of N_2 on lifetime at low temperatures.

Even at this intermediate range of temperatures, there is an observable decrease in fatigue lifetime as the temperature increases from RT to 550°C. In both air and N_2 environments, the longest lifetimes were achieved by the RT tests while the shortest were observed for the 550°C tests. However, since one of the 550°C N_2 test had a significantly longer lifetime, not only compared to the other 550°C N_2 test but also compared to the 450°C N_2 test, the results are not conclusive. The same general observations applied to the pre-oxidised samples with the 550°C test resulting in a reduced lifetime compared to the pre-oxidised 450°C test. Interestingly though, pre-oxidation of samples resulted in significantly longer lifetimes compared to the baseline air tests (without pre-exposure). Whilst this is an insufficient number of tests to comprehensively assess the scatter in lifetimes under these conditions, it should be noted that this work primarily has a micromechanistic evaluation motivation.

Test Conditions	RT	450°C	550°C	
Air	31450	22260	9369	
Air (pre-oxidised)	-	41221	37823	
Nitrogen	22887	11665	19383	8237

Table 5.1: Fatigue life of U-notched CMSX-4 samples.

5.3.2 Fracture surface overviews

Figure 5.7 - Figure 5.9 shows low magnification fracture surface overviews of the U-notched samples fatigued to failure. All the specimens showed large and smooth side facets at approximately 45° to the tensile axis. The rough, fibrous final failure region is also easily distinguishable in all fracture surfaces.

The fracture surfaces of both room temperature tests (Figure 5.7a and b) exhibit large facets both on the sides and at the centre of the samples near the notch. Facets seem to have formed along the {111} planes during initiation at the centre while the larger side facets contributed to the overall growth.

The highest temperature (550°C) samples had the least amount of facet formation and this was generally confined to the sides (Figure 5.9). Although the side facets formed during these tests are comparable in size to the RT and 450°C tests, a characteristic stage II region is distinguishable near the notch surface at the centre of the specimens. Comparing the 550°C air (Figure 5.9a and c) and N_2 (Figure 5.9b and d) tests, the fracture surface of the samples fatigued in air appear less crystallographic particularly near the notch. This is evident in Figure 5.9c, where the flat surface extends half way down the sample with no evidence of faceting other than the sides. In addition, at 550°C, major initiation points can be identified even on these low magnification overviews (Figure 5.9a and c).

The fracture surfaces at 450°C in air look similar to those tested in N_2 (Figure 5.8). Side faceting on these tests begins earlier compared to the 550C test. Similarly to the 550°C test, flat areas are distinguishable near the notch surface indicating fatigue crack initiation. On the contrary though, near these flat regions, finer facets and crystallographic cracking cover a significant portion of the near notch surface.

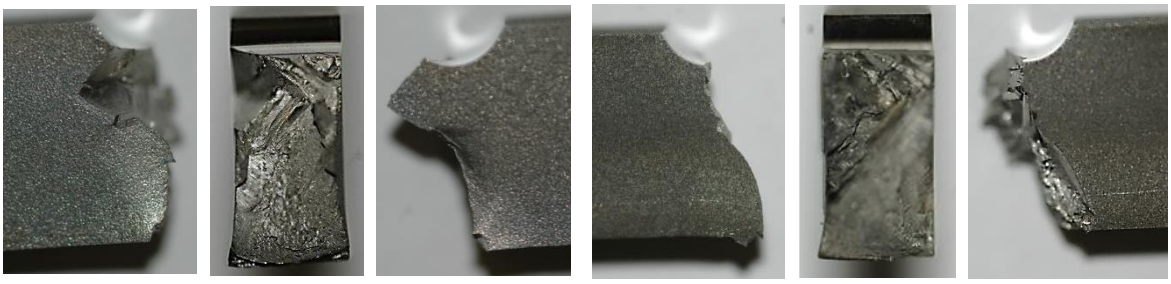

a) RT in Air (31450 cycles) b) RT in N_2 (22887 cycles)

Figure 5.7: Fracture surface overviews and lifetimes of CMSX-4 U-notch samples fatigued at RT .

a) 450°C in Air pre-oxidised sample (41221 cycles)

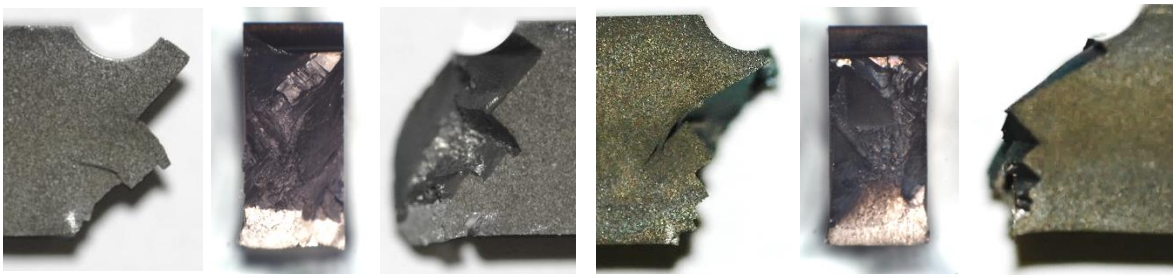

b) 450°C in Air (22260 cycles) c) 450°C in N_2 (11665)

Figure 5.8: Fracture surface overviews and lifetimes of CMSX-4 U-notch samples fatigued at 450°C

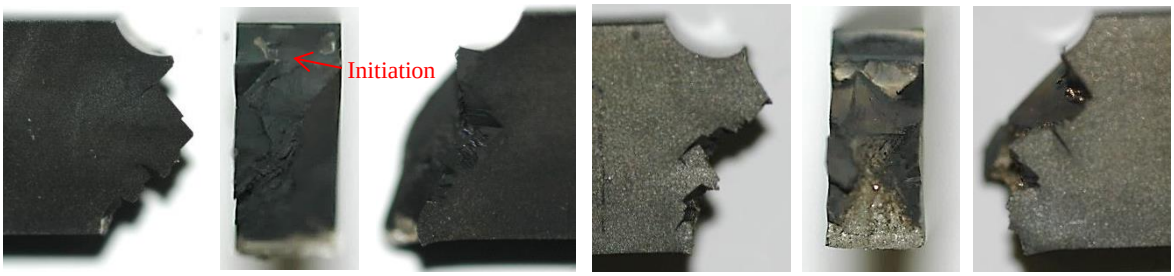

a) 550°C Air pre-oxidised sample (37823 cycles) b) 550°C in N_{2a} (19383 cycles)

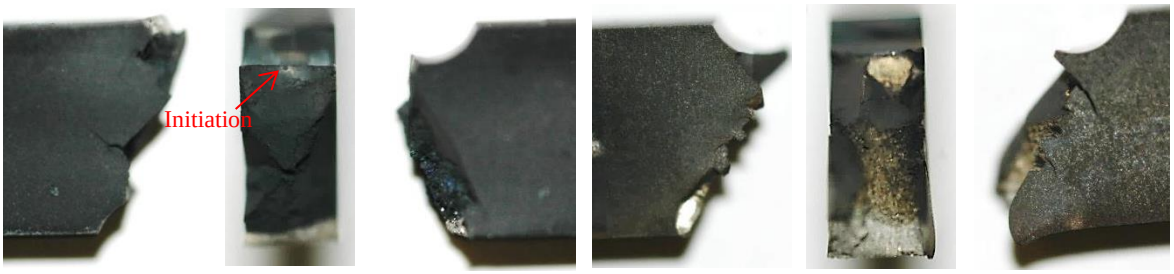

c) 550°C in Air (9369 cycles) d) 550°C in N_{2b} (8237 cycles)

Figure 5.9: Fracture surface overviews and lifetimes of CMSX-4 U-notch samples fatigued at 550°C.

5.3.3 Detailed fractography

5.3.3.1 Tests in Air

At 550°C (Figure 5.10 and Figure 5.11), even though the fracture surface is obscured by oxidation, there are salient microstructural features that reveal the nature of the crack initiation and early propagation. The fracture surface of the sample fatigued at 550°C (without pre-oxidation) was initially smooth and flat with river lines pointing back towards major and minor initiation points (Figure 5.10). The main initiation site (Figure 5.10a) was located at the centre of the sample with the crack emanating from a subsurface pore encircled by a halo. The halo is circular in shape with its uppermost boundary tangential to the notch surface. The texture of the fracture surface within the halo appears less rough and less oxidised than the surrounding area; this is particularly evident from Figure 5.10c. A secondary crack appears to have initiated, at the right of the main initiation point, also from a subsurface pore (Figure 5.10b). Even though the same distinct halo feature is not observed, the fracture surface appears to be less oxidised at close proximity to the pore. The two cracks coalesce approximately 350μm below the surface and form a semi-elliptical crack front. No {111} slip band cracking was observed and early propagation was Stage II dominant. A number of secondary cracks that did not appear to have propagated extensively were identified within 200μm from the fracture surface. Figure 5.10d shows an example of such a crack that seems to have initiated from a surface pore. Cracks were also found to initiate naturally or from surface pores on areas of spallation (Figure 5.10e). Figure 5.10f shows a high magnification image of such a region where the effects of oxidation are clearly visible on the substrate. The γ/γ' microstructure is highlighted as the γ channels were preferentially oxidised. This confirms the observations made in section 4.5 during isothermal exposure of CMSX-4 samples.

Similar observations were made for the pre-oxidised sample shown in Figure 5.11. Once more, the major crack initiated from a sub-surface pore and formed the characteristic halo around the pore. Three more initiation sites were observed on the fracture surface and these are shown in Figure 5.11a, c and e. Two of these, initiated cracks from sub surface pores (Figure 5.11a and e) while for the third one (Figure 5.11c) the initiating pore was exposed at the surface. It is notable however, that the pore that initiated the surface crack, lies within a region of spallation even though this might have taken place after fracture. The pore that initiated the main crack (Figure 5.11b) and the pore of Figure 5.11a, which appears to have initiated the second largest crack have similar, irregular shapes. Early propagation seems to have been affected by these two pores (located at the right side of the fracture surface) and formed a smooth, Stage II, fracture surface at their vicinity. On the contrary, near the left hand side of the fracture surface, where the smaller initiating pores are located on the fracture surface is more crystallographic with larger facets. Similar to the sample in Figure 5.10 a number of secondary cracks that did not cause failure were identified at the notch

surface close to fracture. Oxide filled porosity and areas of spallation were also observed across the notch surface (Figure 5.11d and f)

At the lower temperature of investigation (450°C), oxidation was less prominent on the fracture surfaces with the cuboidal microstructure still visible in some cases (Figure 5.12b). Compared with the 550°C tests, the initiation sites are not immediately evident. For both the standard (Figure 5.12) and the pre-oxidised (Figure 5.13) tests, early propagation appears faceted and crystallographic in nature. Especially in the case of the standard test (Figure 5.12) a large 45° facet spans almost the entire notch surface. In addition, evidence of alternating slip band cracking along the {111} planes was observed at the root of the notch surface (Figure 5.12d). At the same time, surface porosity was not affected by oxidation to the same extent as with the 550°C tests (Figure 5.12e). Near surface porosity caused the early crack to switch from one slip band to another (Figure 5.12b). At this location, the crack seems to follow the γ channels (or the γ/γ' interface), forming staircase like features. At the left hand side of the fracture surface, a network of near surface pores (Figure 5.12a) interacted with the crack front forming a region of Stage II - like propagation.

Predominantly crystallographic initiation was also observed in the case of the 450°C pre-oxidised sample (Figure 5.13). Subsurface porosity of similar, irregular shape, to the initiating pores of the 550°C tests, were observed at the centre of the fracture surface (Figure 5.13 a). However, they did not appear to have been the cause of failure. Similar to the sample shown in Figure 5.12, they control crack propagation in their vicinity by causing the crack to switch between planes. While the initiated crack was propagating along the {111} planes, upon encountering these pores, propagation became perpendicular to the loading axis (Figure 5.13 a). The oxide layer formed over the notch surface of this sample was thicker compared to the standard test at 450°C (Figure 5.13d). Secondary cracks emanating from oxidised surface pores were observed across the notch root which is similar to the observation made for the 550°C tests (Figure 5.13e).

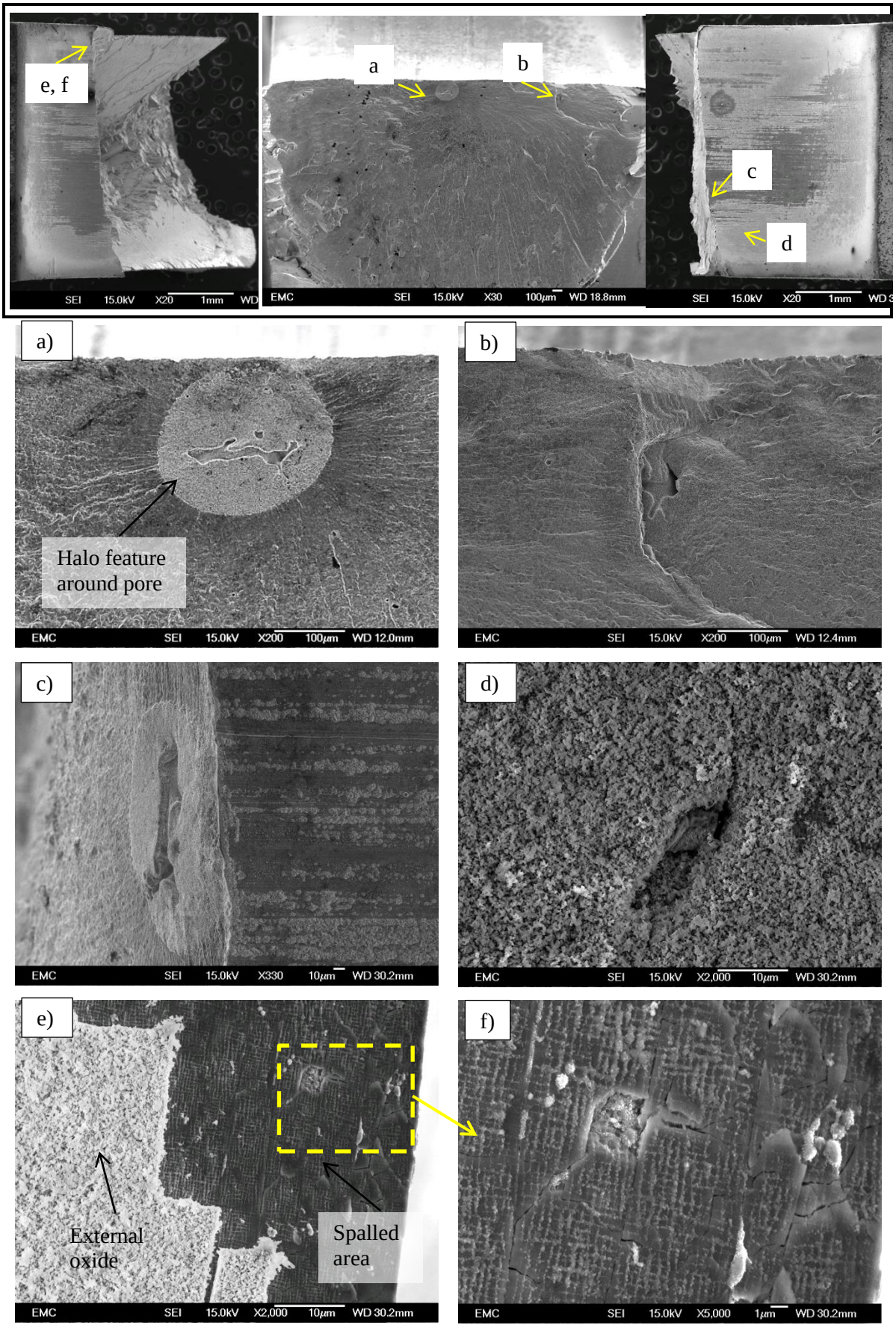

Figure 5.10: SEM fractography of a CMSX-4 sample fatigued at 550°C (life: 9369 cycles).

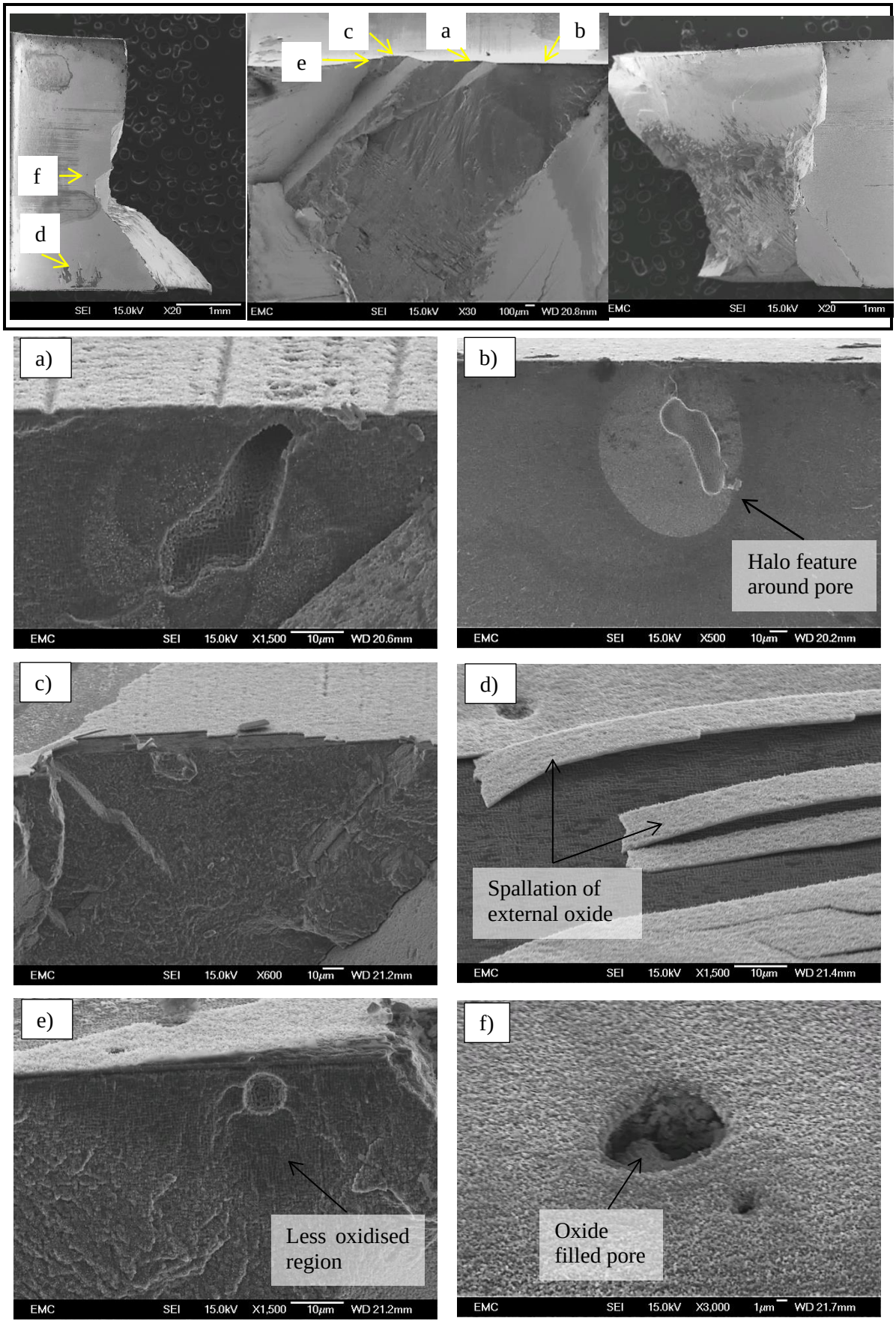

Figure 5.11: SEM fractography of the pre-oxidised (70h at 550°C under load) CMSX-4 sample fatigued at 550°C (life: 37823 cycles).

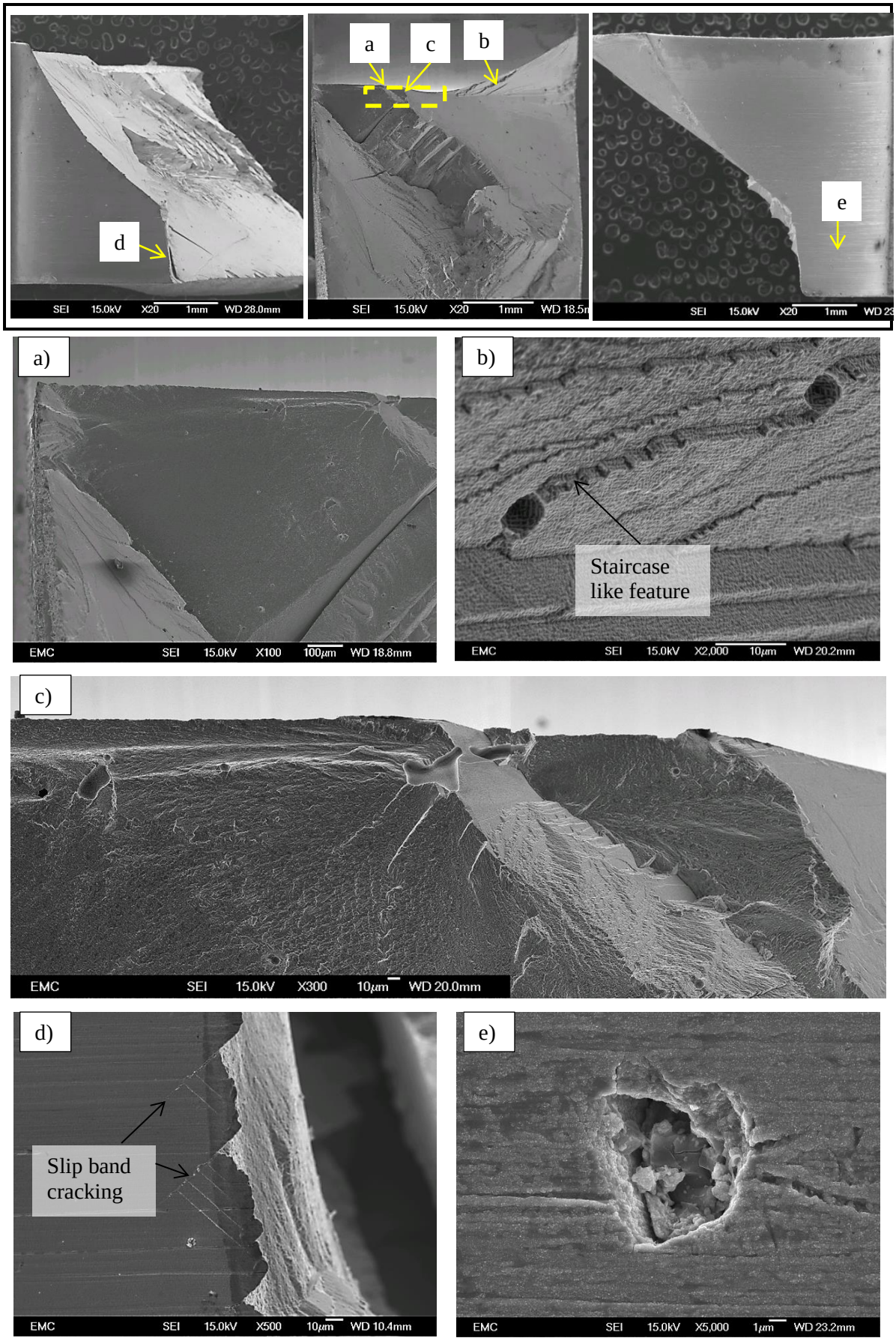

Figure 5.12: SEM fractography of CMSX-4 sample fatigued at 450°C (life: 22260 cycles).

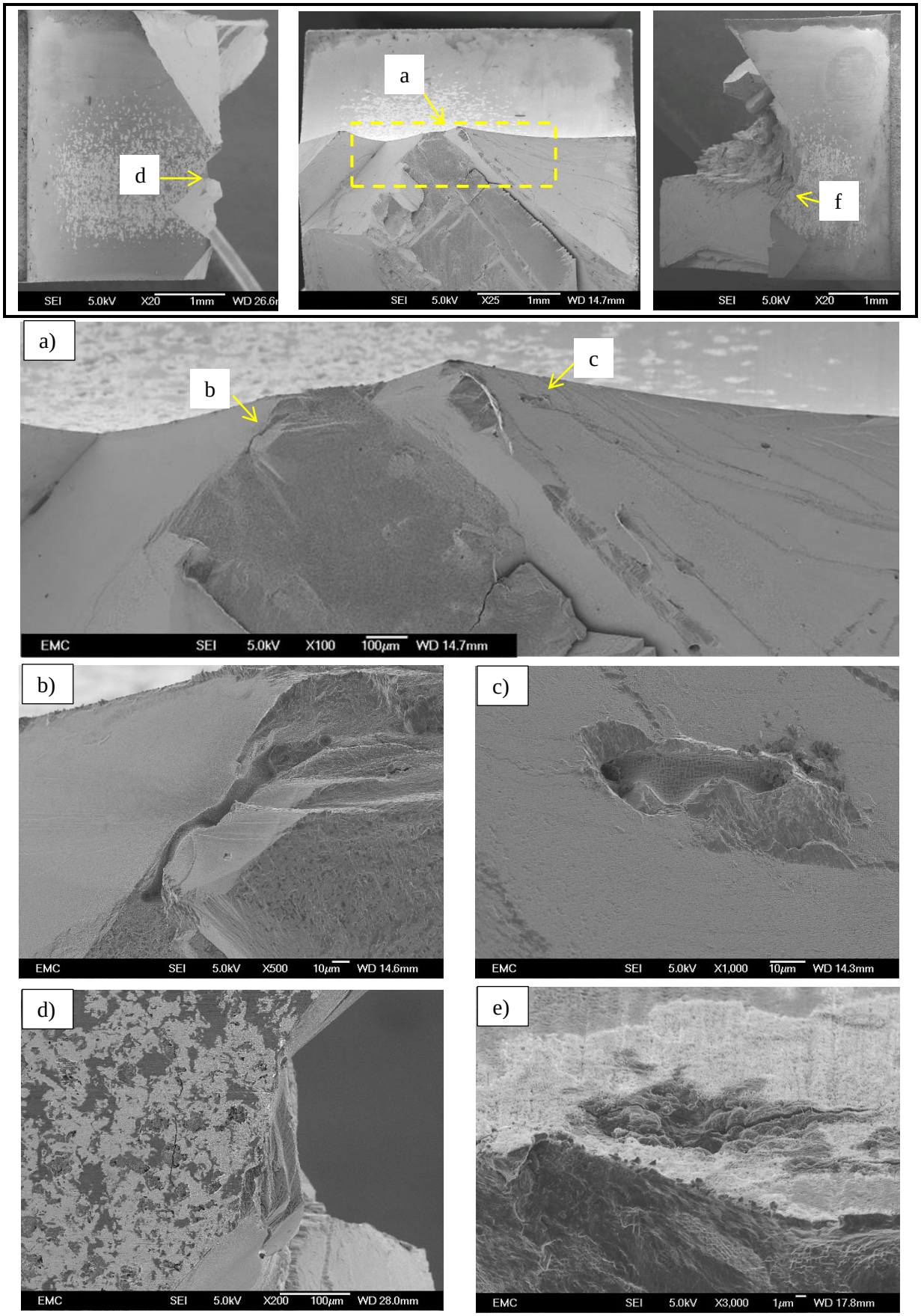

Figure 5.13: SEM fractography of the pre-oxidised (70h at 450°C under load) CMSX-4 sample fatigued at 450°C (life: 41221 cycles).

5.3.3.2 Tests in N_2

Three tests were conducted on CMSX-4 samples in N_2. An initial examination of all fracture surfaces revealed that some degree of oxidation has taken place. This is understandable, although tests were conducted in an inert gas environment at low estimated oxygen partial pressure, the formation of oxides can take place at very low oxygen partial pressure at elevated temperatures. Considering the Ellingham diagram, NiO at 550°C can form at oxygen partial pressures as low as 10^{-22}bar (compared to 10^{-6}bar that it is estimated to be achieved). Nevertheless, the reduced amounts of oxygen would have significantly reduced the kinetics of oxide formation.

For both 550°C tests crack initiation occurred at surface porosity. The absence of the characteristic halo feature, observed in the air tests, made the identification of subsurface initiation much harder. This is particularly evident on Figure 5.14, where the near surface ratchet marks indicated multiple starting cracks but there are no distinct initiation features. Evidence of surface porosity causing initiation can however be seen in Figure 5.14c and d. On the contrary, the second 550°C test which had the shorter life, had a large number of surface defects that initiated fatigue cracks (Figure 5.15a, b and c). Early, short crack propagation also seems to be affected by the presence of porosity. Figure 5.15d shows the interaction of a large slip band with a subsurface pore, as it propagates along a large side facet (Figure 5.15d).

A detailed overview of the fatigue crack initiation region of the 450°C N_2 test is shown in Figure 5.16a. Three major initiation sites (Figure 5.16b, c and d) were identified and all indicate that failure occurred from surface porosity. The morphology of the initiating pores was similar to all previous tests with the area around them appearing flat and relatively smooth. Comparing with the 550°C tests, the short crack behaviour appeared more crystallographic with some large cracks running along the notch root surface (Figure 5.16e).

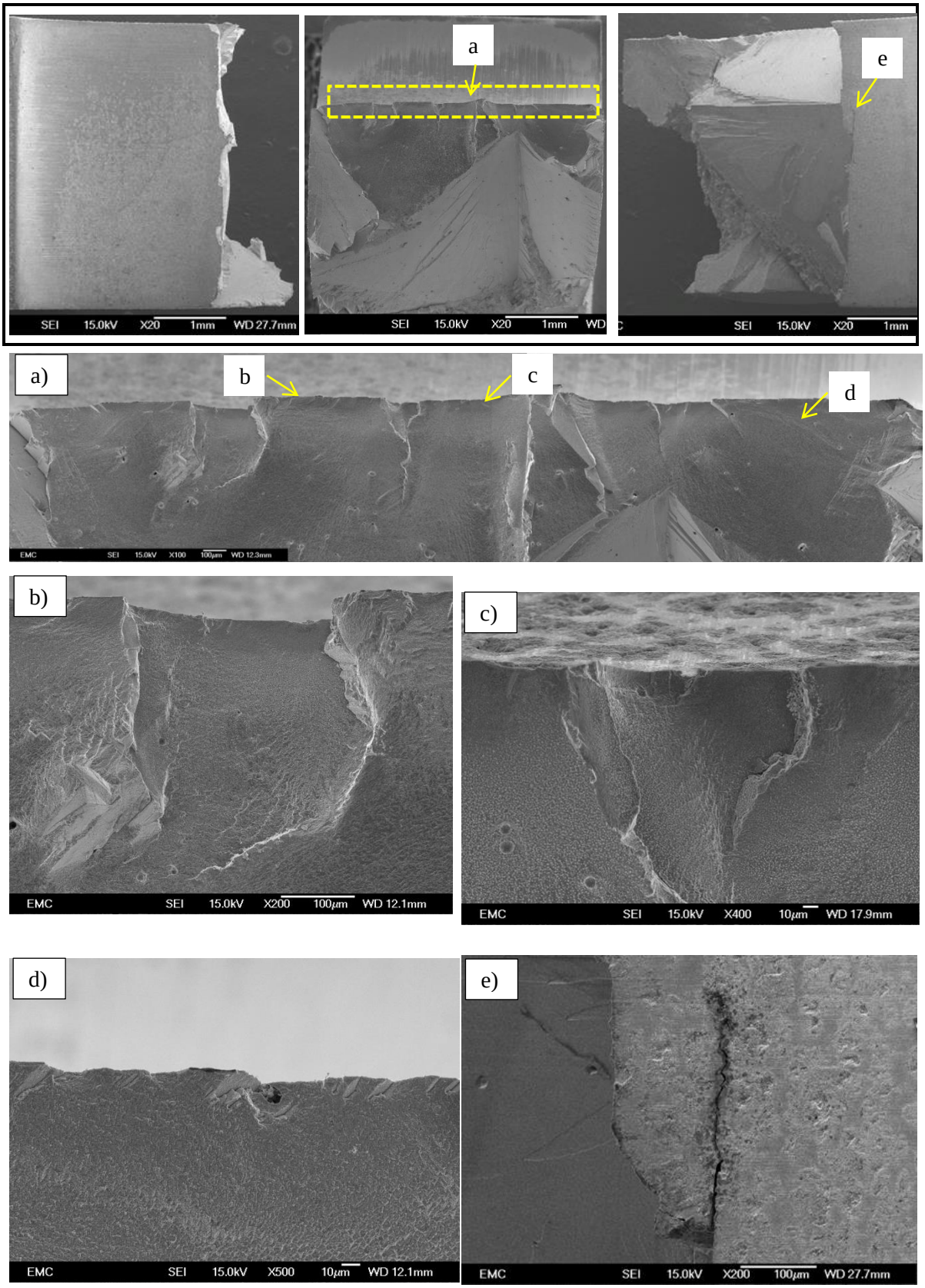

Figure 5.14: SEM fractography of CMSX-4 sample fatigued at 550°C in N_2 (life: 19383cycles).

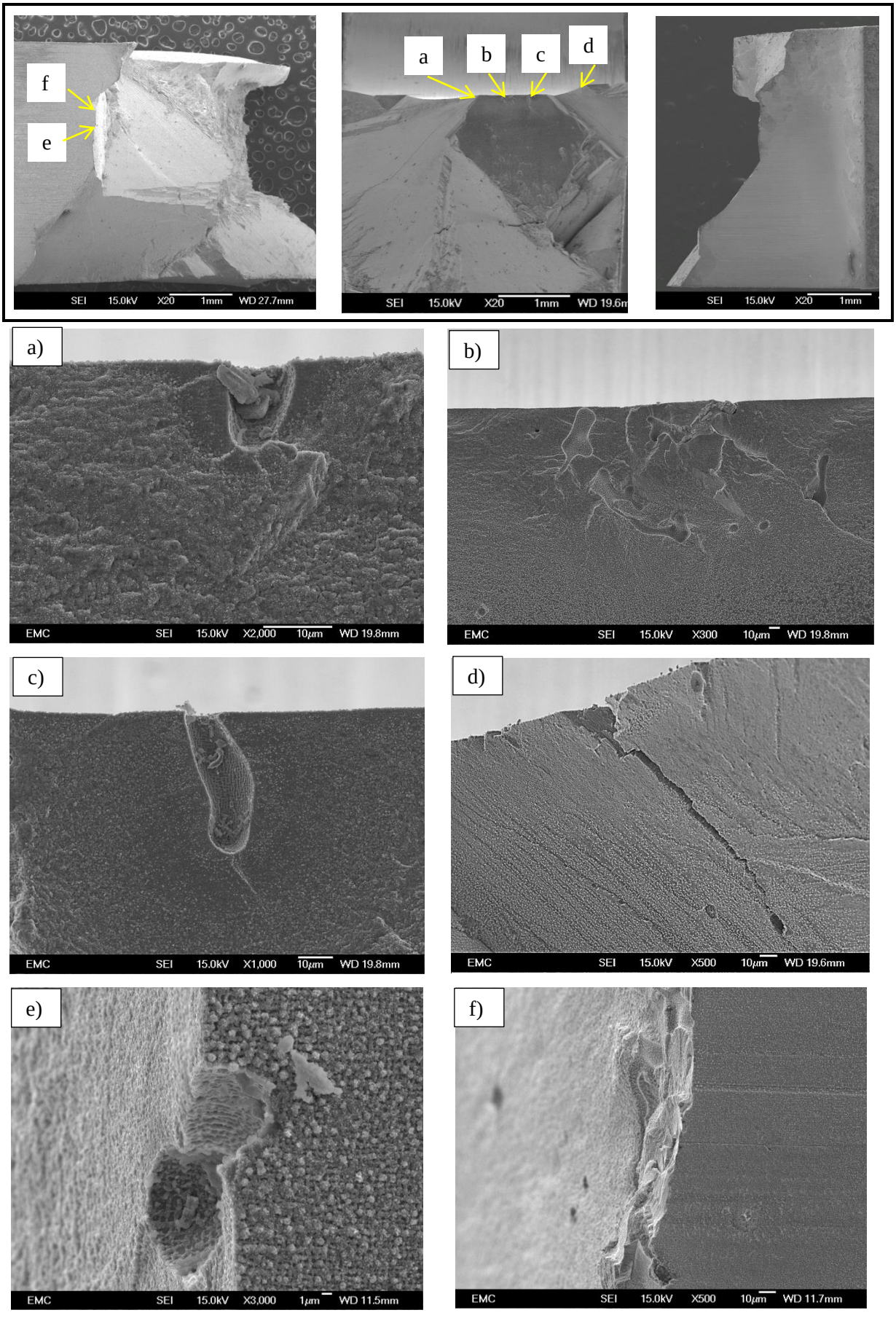

Figure 5.15: SEM fractography of CMSX-4 sample fatigued at 550°C in N_2 (life: 8237 cycles).

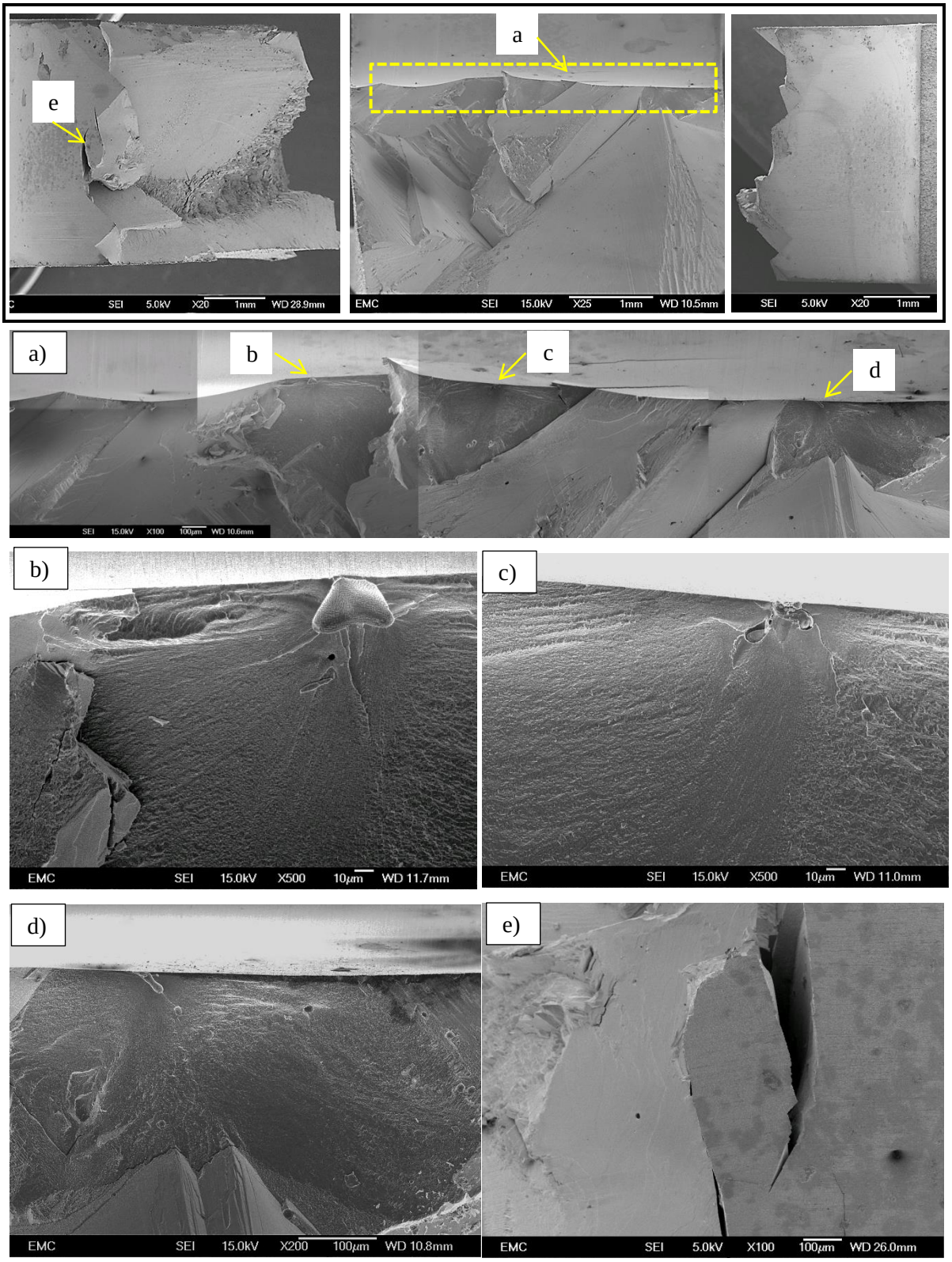

Figure 5.16: SEM fractography of CMSX-4 sample fatigued at 450°C in N_2 (life: 11665 cycles).

5.4 Discussion

5.4.1 Effect of environment on fatigue life and fatigue crack initiation

The decrease in the fatigue lifetime in air with increasing temperature (from RT to 550°C) can be partly attributed to the dependence of yield stress on temperature [5]. It is well known SX Ni-based superalloys generally increase their yield strength with temperature up to approximately 800°C [2,143]. However, as discussed earlier in 3.3.3, the variation of yield stress with temperature for CMSX-4 follows a near sigmoidal shape from room temperature to approximately 800°C (see Figure 2.30), with a minimum value at approximately 350°C and a maximum value at 800°C. In addition, due to the anisotropic properties of such materials any sample to sample variation in the misorientation angle (angle between loading axis and the nominal <001> orientation) would have induced further uncertainty and scatter to the results masking the actual effects of environment on lifetime.

More importantly though, the low cycle fatigue lifetime in single crystal Ni-based superalloys has been shown to be driven by intrinsic material defects, such as porosity [97,200]. The key role of porosity in initiating fatigue is clear from this study. The variation of lifetime with temperature during the N_2 (low oxygen partial pressure environment) tests showed a similar trend to the air tests, although the values are much closer to each other. Furthermore, one of the 550°C tests had a lifetime similar to the RT test, indicating that the variation in material properties with temperature is not necessarily the dominant initiation controlling factor. From the fractographic analysis, it was clear that in the case of the two 550°C N_2 tests, the large number of surface defects present in the sample shown in Figure 5.15, reduced the crack initiation time and subsequently the overall fatigue life. The random distribution and occurrence of such defects has also been reported previously to cause large variations in the fatigue lifetime of CMSX-2 samples at 650°C [200] at similar strain levels. The size and location of pores relative to the surface of the sample produced significant differences to fatigue lives obtained at given stress ranges. Much of this scatter could be rationalised by considering the predicted effects of pore size and distance below the notch surface, in terms of expected lifetime predicted by a crack growth approach. Furthermore, notch geometry variation can add to this scatter and significantly change the initiation mode by providing additional localised strains. This not only affects the oxidation process via an enhanced strain assisted mechanism, but it also enhances scatter since the effect of defect variation and related sampling effects becomes even more pronounced by the small, highly strained volume at the notch root (i.e. the likelihood of a detrimental geometry defect being located within the notch-strained substrate).

The results indicate that there is a transition of fatigue initiation mode from surface defects or crystallographic slip bands at low temperatures or low oxygen partial pressure environments to

subsurface porosity at higher temperatures in air. The vast majority of all initiating pores were identifiably shrinkage porosity formed during the solidification process. Their complex morphology and large aspect ratios promote high localised stresses and act as preferential fatigue crack initiation sites. In the absence of oxidation, crystallographic cracking is promoted near the sites of surface defects (Figure 5.14 and Figure 5.15), or by PSBs that shear the notch surface (Figure 5.12d). Oxidation and subsurface initiation were associated with the longer lifetimes in general. This was particularly evident from the noticeably increased lifetimes of the pre-oxidised samples with the 550°C tests showing the greatest effect of this.

Since crack initiation in low oxygen partial pressure environments was found to be controlled by slip band cracking and near surface defects, it is implied that in order for the fatigue lifetime to increase in the oxidising environment, at least one of the two mechanisms must be inhibited. Deactivation of porosity related surface stress concentrations, is the most obvious scenario. Evidence of pores filled with oxides has been observed on the fracture surface of both pre-oxidised samples (Figure 5.11 and Figure 5.13). A study contacted on IN-100 at 1000°C has shown that cyclic loading strongly enhances the oxide thickness of the matrix phase due to plastic strain effects. This was attributed to an accelerated diffusion of chemical species by a hydrostatic pressure effect or by diffusion along dislocations. The higher plastic strains induced within surface pores are potentially promoting higher oxidation rates that fill their volume with oxide over a relatively short amount of time. Considering the results of sustained load oxidation testing discussed in 4.4.5, this mechanism is also possible at the temperatures investigated in this study. Further evidence of this can be seen in Figure 5.17. The SEM image shows a section taken through a sample oxidised under a sustained load for 160h at 550°C (the same experimental procedure as in 4.2.3 was followed). From the EDS maps at the bottom of Figure 5.14, oxide products are seen to completely plug the pore, almost levelling the surface. Equivalent observations were made by Miller et al. [97] who investigated the fatigue behaviour of CMSX-4 under similar loading conditions at 650°C. Fractographic analysis revealed subsurface initiation and oxide filled porosity during testing in air at 650°C. It was argued that the strain mismatch between metal substrate and oxide, continuously breaks off the brittle oxide of the notch root during load cycling. The greater local plasticity around the pore would enhance a process of repeated cracking and re-oxidation, building up an oxide plug and essentially reducing the stress concertation at the surface.

However, this mechanism of subsurface initiation does not necessarily hold at higher temperatures. At higher temperatures (> 850°C) initiation was reported to take place from surface cracks formed at the oxide scale or from penetrating oxide spikes [90,207]. Ohtani et al. observed similar results for CMSX-10 samples tested at 1000°C [208]. In the study of Gordon et al. [202] sustained load high temperature exposure of a DS Ni-based superalloy resulted in reduced lifetimes compared to

samples fatigued without pre-exposure. This is in contrast to the results of this study at more moderate temperatures where pre-oxidation resulted in higher lifetimes. This behaviour can be explained by considering the higher testing temperature (871°C) which resulted in a degraded microstructure with much greater oxide penetration and deeper depletion zone. Duquette and Gell [85], reported a reduction in fatigue life in vacuum compared to air. Testing was conducted on cylindrical samples of the SX MarM200 at 923°C with a relatively low stress range. Crack initiation took place internally during their tests in air, suggesting that oxidation inhibited surface initiation and resulted in prolonged lifetimes; a similar finding to the mechanism observed here with the pre-oxidised specimens. It is therefore suggested that given sufficient time and low enough strain ranges (to prevent crystallographic cracking from prevailing) oxidation can effectively deactivate surface defects and prolong fatigue life by shifting initiation internally. Competing fatigue damage mechanisms are a common phenomenon in Ni-based superalloys with strain rate and temperature most often dictating the prevalent mechanism.

It therefore appears that over the range of operating temperatures of turbine blade materials, the initiation fracture mode can vary significantly according to strain rate/frequency, strain range, temperature and time for oxidation to occur. The varying regimes in initiation processes can be generalised schematically as shown in Figure 5.18.

A life prediction model which includes a fatigue initiation term, should take into account both defect distributions and their interaction with the combined effects of strain and oxidation. Systematic characterisation and quantification of such defects and determination of relevant distance/size/shape probability distributions in the material can provide a means of calculating the distribution in the fatigue life by a model that can predict both initiation and subsequent growth behaviour for such defects. Maintenance of fatigue critical components relies, in many cases, on minimum life design methods which can greatly benefit by a more accurate prediction of the scatter in fatigue life.

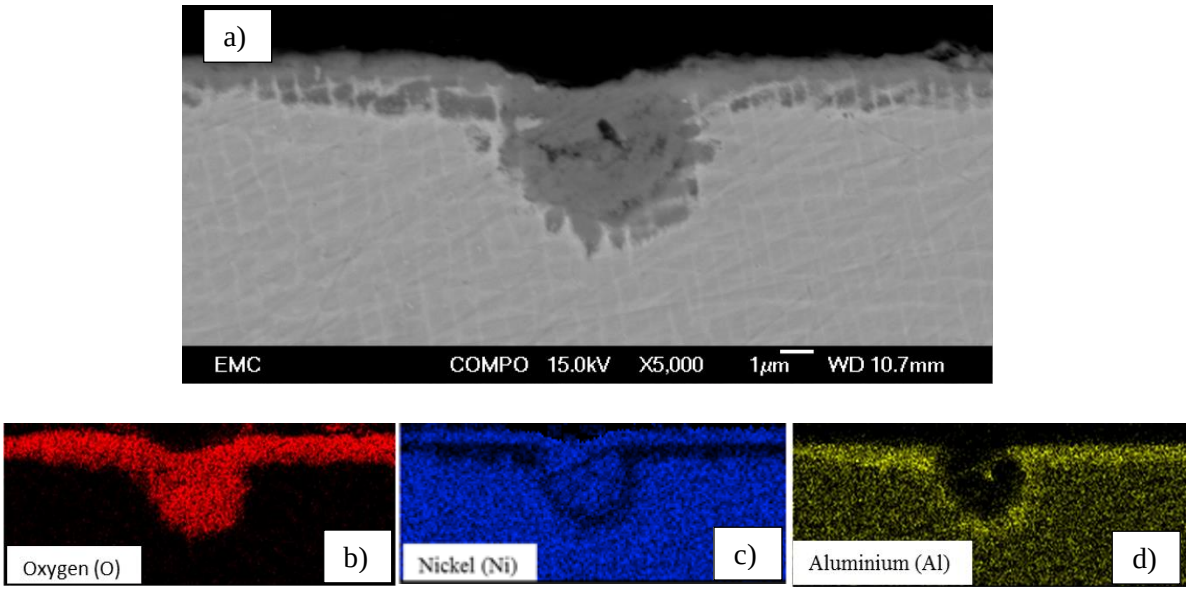

Figure 5.17: a) SEM image showing an oxidised surface pore on a CMSX-4 sample exposed to 550C for 160h while under a sustained load. b) – d) EDX compositional maps of the imaged region.

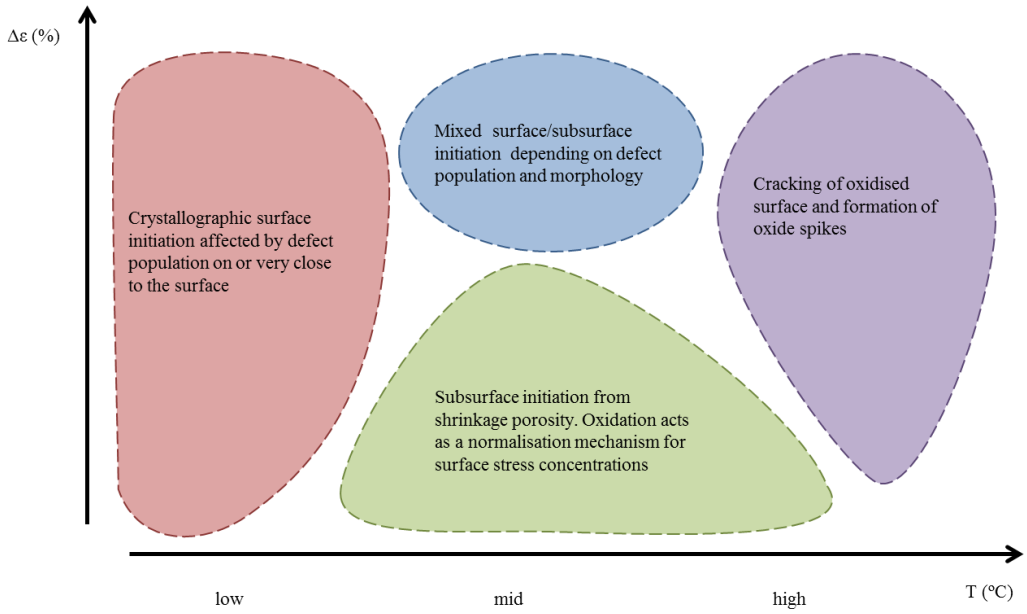

Figure 5.18: Schematic illustration showing the variation of fatigue crack initiation mechanisms of CMSX-4 with Δε and temperature in a mixed cycle/time dependent frequency regime.

5.4.2 Effect of environment on early fatigue crack propagation

Since early propagation considers the advancement of physically/microstructurally small cracks, the short crack behaviour is highly affected by the surrounding microstructure. Sub-surface initiating pores created a characteristic halo feature which formed over a macroscopically smooth

fracture surface. While the crack is confined within the material, propagation takes place at very low oxygen partial pressures and a smooth fracture forms (similar to a vacuum environment). As soon as the top of the circular crack breaks through the notch surface, oxygen penetrates the gap resulting in numerous initiation sites, fracture steps and radial river lines (Figure 5.10a).

In the FCC SX Ni-based superalloys, deformation and subsequently short crack growth are known to occur as a result of cyclic slip localisation along the {111} shear planes [5,209]. In the absence of significant oxidation, slip band formation depends on the strain levels and intrinsic slip character and extended slip band deformation at the notch surface can lead to crystallographic crack propagation. This planar slip behaviour is a result of the low SFE and high APB energy of SX Ni-based superalloys which leads to repeated cutting of the coherent γ′ along the same intense bands. Dislocations tend to be dissociated into partials (due to the low SFE) and also to travel in pairs (sometimes termed superdislocations) to restore the ordered nature of the γ′ (to reduce APB energy). These factors combine to produce very localised, planar slip bands (at low temperatures where thermally activated processes are inhibited) along the same {111} <101> slip systems to form PSB and crystallographic cracking [2]. The more homogenous fracture mode observed in the notch fatigue tests at somewhat higher temperatures and higher oxygen partial pressures are attributed to the thermally activated cross-slip of the dissociated dislocations and propagation through the γ channels [210]. The dislocation movements in Ni-based superalloys at various temperatures have been extensively discussed in review studies elsewhere [211,212]. Due to the Kear-Wilsdorf locking mechanism which leads to complex (sessile) SFs forming in the superdislocations at higher temperatures, the strengthened γ’ particles can force the dislocations to bow and prevent shearing. Oxidation itself also plays an important role in homogenising crack tip deformation processes. Duquette and Gell measured and compared the height of slip steps forming on a single crystal Ni-based superalloy during fatigue in air and vacuum [85]. Larger slip steps were formed under vacuum as the adsorption of oxygen on the slipped surfaces during the air tests effectively work hardened the slip bands preventing further step extrusion.

For the intermediate temperatures of this study both mechanisms are likely to be active, with some dislocation systems evidencing cross slip and some still preferentially cutting through the γ′ phase. This is particularly evident from the complex fracture surface of the 450˚C test. Although near the initiation sites where the higher (and more complex) strain fields promote oxidation and homogenisation of slip, at other locations near the notch root crystallographic cracking prevailed.

5.5 Summary

The fatigue crack initiation and early crack propagation behaviour of CMSX-4 at 450°C and 550°C were assessed with particular focus on the effects of oxidation. Testing was conducted under three-point bend loading and characterisation was conducted with OM, SEM and EDS. Based on the aforementioned results and discussion, the following conclusions can be made:

1. Increasing the temperature from RT to 550°C reduces the low cycle fatigue life of CMSX-4. This is true for both air and N_2 (low oxygen partial pressure) environments.

2. The fatigue lives of notched CMSX-4 components at 450°C and 550°C are greater in air than in vacuum. At these temperatures oxidation does not degrade the surface of the material enough to cause initiation, rather it acts as a retardation mechanism to surface initiation processes by plugging porosity and interfering with the resulting strain levels. Pre-oxidised samples exhibit even longer fatigue lives due to the aforementioned mechanism. However, these processes are only confined within a range of intermediate temperatures and are particularly influential at the lower strain ranges.

3. Crack initiation in an oxidising environment at 450°C and 550°C is dominated by subsurface shrinkage porosity while initiation at lower temperatures and low oxygen partial pressure environments result in crystallographic cracking promoted by surface defects.

4. The size and location of pores relative to the surface of the sample produced significant scatter in the fatigue lives obtained. This scatter is more evident in the case of notch geometries as the smaller strained volume increases the effect of localised sampling of the defect population (i.e. the likelihood of a defect of detrimental geometry being located within a small strained volume is lower, hence more samples should be tested to establish the worst case scenario) The notch stress concentration also substantially affects oxidation rates (which is also a controlling factor for subsurface initiation). This increased scatter is therefore an inherent feature of the service condition and needs to be considered in lifing approaches.

5. Porosity distribution is a key parameter as these inherent defects have been shown to control fatigue crack initiation and should be included in life prediction models. Model development requires more realistic modelling of defect distributions, crack growth laws, allowing for crack coalescence, and more extensive validation testing.

Chapter 6 Fatigue crack propagation mechanisms

6.1 Introduction

Gas turbine blades are high value components in the power generation industry and there are significant economic incentives to optimise the life management procedures currently in place. There is a particular interest in the development of approaches that comply with the "retirement for cause" concept, where the lifetime of a turbine blade is assessed on the basis of detectable flaws (retirement based on critical size) rather than on the basis of predetermined life approaches. However, in order to achieve this, the detrimental (synergistic) effects of environment and cyclic loading need to be captured. The main difficulty in doing so arises from the lack of a physical description of the interacting processes that take place at a crack tip during high temperature dwell fatigue. In addition, considering the complex shape of turbine blades and the significant temperature gradients resulting from the incorporation of internal cooling passages and thermal barrier coatings, unpredictable failures can occur even at intermediate service temperatures which are often neglected by the literature.

This Chapter aims to examine the mechanisms acting at a crack tip, during dwell fatigue, in a single crystal Ni-based superalloy at intermediate service temperatures and provide a physical interpretation of the damage process. Carefully designed mechanical tests have therefore been carried out at different frequencies, hold times and environments to obtain an understanding of the parameters influencing crack propagation. Scanning electron microscopy was used to identify the fracture mode while scanning transmission electron microscopy (STEM) equipped with energy dispersive spectroscopy detectors were used to analyse crack tip regions.

6.2 Experimental procedure

6.2.1 Sample preparation

Single edge notched bend (SENB) specimens with a cross section of 9mm x 9mm were tested in three point bending with a loading span of 40mm. To comply with the British Standards [213], a through thickness starting notch of 2.25mm ($1/4^{th}$ of breadth) was machined at the centre of each sample by EDM. The samples were machined with their tensile axis parallel to the <001> direction and the notch along the <010> direction. A schematic of the sample dimensions and orientation is

shown in Figure 6.1. The crystallographic misorientations of all samples tested were within 7° of the <001> direction.

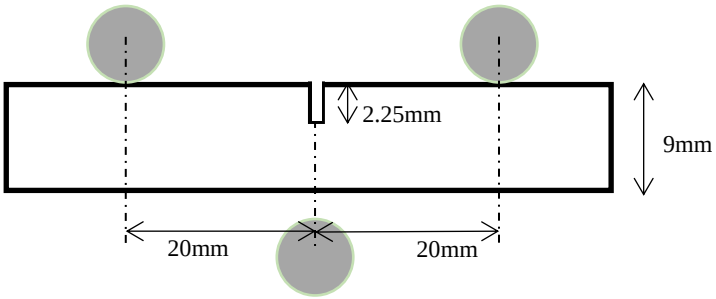

Figure 6.1: (a) Schematic diagram of the SENB samples used for long crack fatigue testing.

6.2.2 Mechanical testing

Fatigue testing was conducted on a 50kN Instron 8501 servo-hydraulic machine retrofitted with an ESH Ltd. high temperature vacuum chamber which utilises four high intensity quartz lamps. Tests were conducted either at 450°C or 550°C. The sample temperature was controlled to ±1°C by an R-type (platinum + 13% rhodium/platinum) thermocouple spot welded on the side surface and connected to a Eurotherm 815 controller.

Cyclic loading was applied in load control using a load ratio of R=0.1 and a trapezoidal waveform of the type 1s – Xs – 1s – 1s. The 1s segments corresponding to the load ramping periods and the dwell at min load while hold time at maximum load ("X") was varied between tests. The fatigue crack growth (FCG) was monitored continuously using the DCPD method. A set of PD probes were spot welded across the notch, while a second set was attached away from the propagating crack to provide a far field reading for normalisation against temperature and current variations. An experimentally obtained calibration function was used to relate the crack length (a), sample width (W) ratio (a/W) to the normalised PD. To ensure accurate values, the derived crack lengths were checked and re-calibrated, post-test, against beach marks formed on the fracture surface. The FCG rates were derived from the curve of the variation in the electrical potential with time by the secant method. The approach followed to derive the da/dN vs ΔK, including the noise reduction methods considered when plotting the data, are discussed further in Appendix B. Prior to testing, the specimen was pre-cracked at the testing temperature using a load shedding method with a 2.5Hz sine waveform, stress ratio of 0.1 and an initial stress intensity range factor ΔK = 20MPa√m. The ΔK was stepped down in 10% increments, each 10% drop was only applied after the crack had grown through four (plane stress) monotonic plastic zone sizes at the previous ΔK level. This load-shedding approach was followed until a final ΔK=15MPa√m was achieved.

In the case of a vacuum test (low oxidation environment), prior to pre-cracking the ESH chamber was evacuated down to a pressure equal or less than 5×10^{-4}mbar. The process usually required pumping for approximately 24h. Heating was then applied and the sample was allowed to stabilise at the testing temperature. The rise in temperature would cause outgassing and a slight increase in pressure so an additional 1h was allowed for the vacuum level to recover.

The experimental work included three different types of tests as outlined below:

i. **Fatigue crack propagation tests (constant load, increasing ΔK)** were conducted to obtain the characteristic crack growth rate ($^{da}/_{dN}$) vs. stress intensity factor range (ΔK) graph and the Paris law coefficients (C and m) for CMSX-4 in air and in vacuum, in order to assess the effect of oxidation. Testing was conducted using a "baseline" trapezoidal waveform of 1s – 1s – 1s – 1s starting from ΔK = 15MPa√m and run to failure.

ii. **Frequency scan tests (constant ΔK = 20MPa√m, K_{max} = 22MPa√m)** were employed to examine the effects of frequency/dwell on the FCG rate at a fixed $\Delta K/K_{max}$. The ΔK value was selected to be within the low-mid end of the Paris regime with a FCG rate low enough for significant oxidation processes to take place at the crack tip and to allow accurate control of the ΔK via load shedding. During the test 8 different loading frequencies were used ranging from 0.005Hz to 5Hz. For frequencies up to 0.25Hz the trapezoidal waveform of the type 1-x-1-1 was used whereas for higher frequencies a sinusoidal waveform was employed to allow a more accurate servo-hydraulic response. The frequency test sequence was arranged such that a high frequency testing period was followed by a low frequency one. This caused distinct changes in the fracture surface which were later used to calibrate the measured crack length to the monitored PD. At each frequency the crack was allowed to grow approximately 0.4-0.5mm corresponding to 4-4.5 monotonic plane stress plastic zone sizes.

iii. **Alternating dwell / Block tests** were conducted to assess the effect of oxidation ahead of a crack tip. Such tests (termed "block tests") were previously employed by [214] to identify the extent of oxidation induced damage ahead of a crack tip in a polycrystalline Ni-based superalloy. By switching between regimes of low and high frequency and examining the transitions in crack growth behaviour, the extent of the crack tip damage formed under particular conditions (i.e. the interaction between strain rate and oxidation) can be examined. These tests were run to failure with increasing ΔK by alternating between short and long dwell waveforms for crack increments of at least 4 plane stress plastic zone sizes. Figure 6.2 shows a schematic of the loading applied. Based on the frequency scan test results, representative dwell times were selected to induce different propagation mechanisms; 1s was selected as the baseline (short) dwell while 90s, 180s and 300s were used as the long dwells in different samples. Two of these tests were interrupted at $\alpha_1 = 6.1$mm and $\alpha_2 = 6.4$mm and held under sustained load

(corresponding to K values of $K_1 = 34\text{MPa}\sqrt{\text{m}}$ and $K_2 = 28.5\text{MPa}\sqrt{\text{m}}$) for 12h. During the hold period any crack growth was monitored with the DCPD method. Subsequent baseline fatigue crack growth rates were then monitored to assess the effect of these hold times.

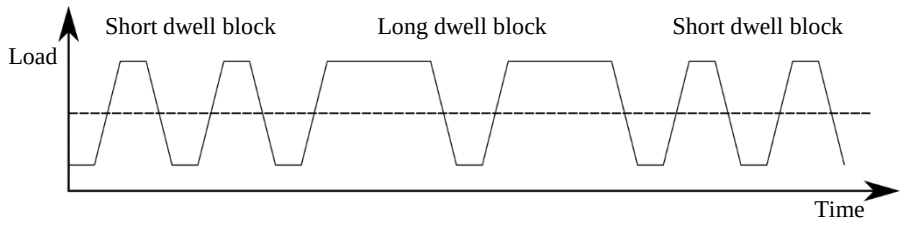

Figure 6.2: Loading waveform utilised for block tests.

6.2.3 Characterisation methods

The fracture surfaces were examined using a Wild M420 macroscope, an Alicona Infinite Focus microscope (IFM G4) and a JEOL JSM 6500 FEG-SEM at an acceleration voltage of 15kV. For the crack tip investigations, the interrupted test specimens were sectioned perpendicular to the crack front using a Mechatome T210 linear precision saw and a volume containing the crack was extracted as shown schematically in Figure 6.3a. The extracted sample was mounted in conductive bakelite and polished down to 0.02μm OPA. Investigation of the crack surface was performed on the JEOL FEG-SEM by both secondary electron (SEI) and backscattered electron imaging (BSE). An Oxford INCA energy dispersive X-ray (EDX) spectroscopy system retrofitted to the FEG-SEM was used for the chemical analysis of the crack oxides.

Microanalysis of the crack tip region was performed by extracting TEM thin foil samples by FIB milling in a Versa 3D dual beam system consisting of a focused gallium ion beam and a FEG SEM. The TEM samples were extracted parallel to the sample surface using a plan view method. Figure 6.3a and Figure 6.3b, show the TEM foil location and orientation relative to the SENB sample. Figure 6.3c to Figure 6.3e illustrate the TEM sample extraction procedure and location. Initially, the region of interest (ROI) around the crack tip was coated in–situ with a layer of platinum and two large trenches were milled on two of its sides (Figure 6.3c). Two more trenches were then milled on the remaining sides leaving a thin "neck" of material connecting the edge of the ROI with the surrounding alloy (Figure 6.3d). For the next step the sample was tilted at angle (to the FIB) sufficient to allow the beam to mill the internal side of one of the initial large trenches (milling under the ROI surface). Finally the sample was tilted and rotated to allow milling of the opposite trench side, creating a wedged specimen containing the ROI. Before commencing with the final milling a tungsten probe needle was welded on the edge of the ROI to hold it after being cut-off from the bulk (Figure 6.3e). Following polishing by milling, the TEM lamellas were examined

in a Talos F200X (STEM mode) equipped with 4 silicon drift detectors (SDD) for high resolution EDS analysis.

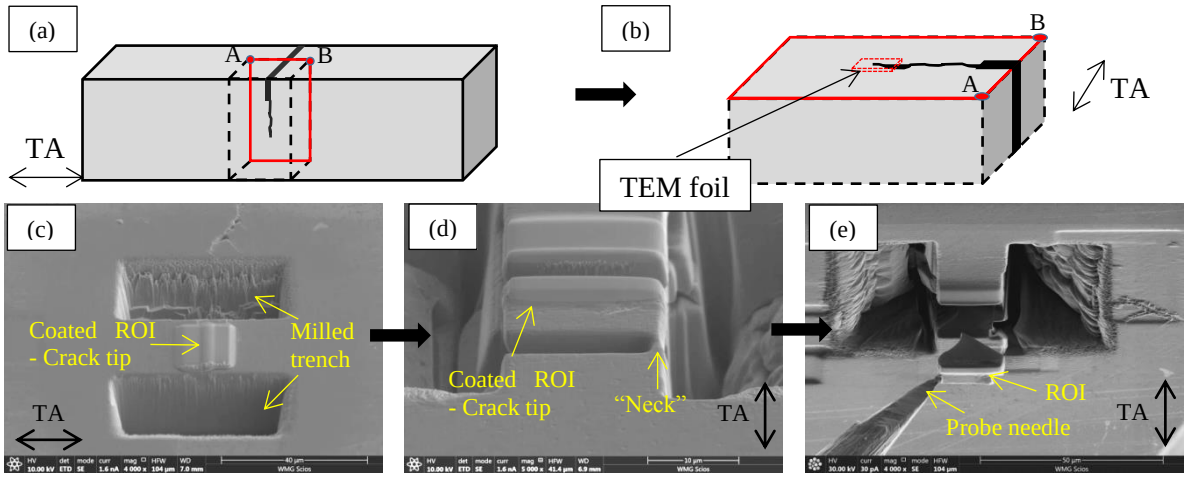

Figure 6.3: TEM sample location and extraction procedure, the tensile axis (TA) is included in all images: (a) shows a schematic of the interrupted test sample with the location of the ROI extracted around the crack region, (b) shows a schematic of the ROI and the location and orientation of the TEM foil sample and (c) – (e) shown SEM images of the preparation sequence and extraction of the foil with FIB milling.

6.3 Results

6.3.1 Fatigue crack growth in air and vacuum

Figure 6.4a compares the FCG rates of CMSX-4 at 450°C and 550°C in air and in a low oxygen environment, obtained using the baseline waveform 1-1-1-1 (0.25 Hz). Under these conditions, the FCG rates at 550°C seem to be unaffected by the environment. By comparing the results in either environment at 550°C with the results from the 450°C test the negative effect of temperature on the FCG rate resistance is also illustrated in Figure 6.4a.

Macroscopic overviews of the fracture surfaces for the three tests can be seen in Figure 6.4b to Figure 6.4d. The EDM notch, the pre-crack region (marked by a beach mark), the fatigue crack growth region and the final fracture can be easily distinguished and are indicated on Figure 6.4a. All tests produced, in general, smooth and flat fracture surfaces within the FCG region indicating a predominantly stage II propagation. The (001) "+" dendritic structure is more evident on the fracture surface produced in vacuum which has experienced less oxidation. Some degree of side faceting (crack growth occurring along {111} planes) was observed on all fracture surfaces but in vacuum and at 450°C side faceting was more pronounced.

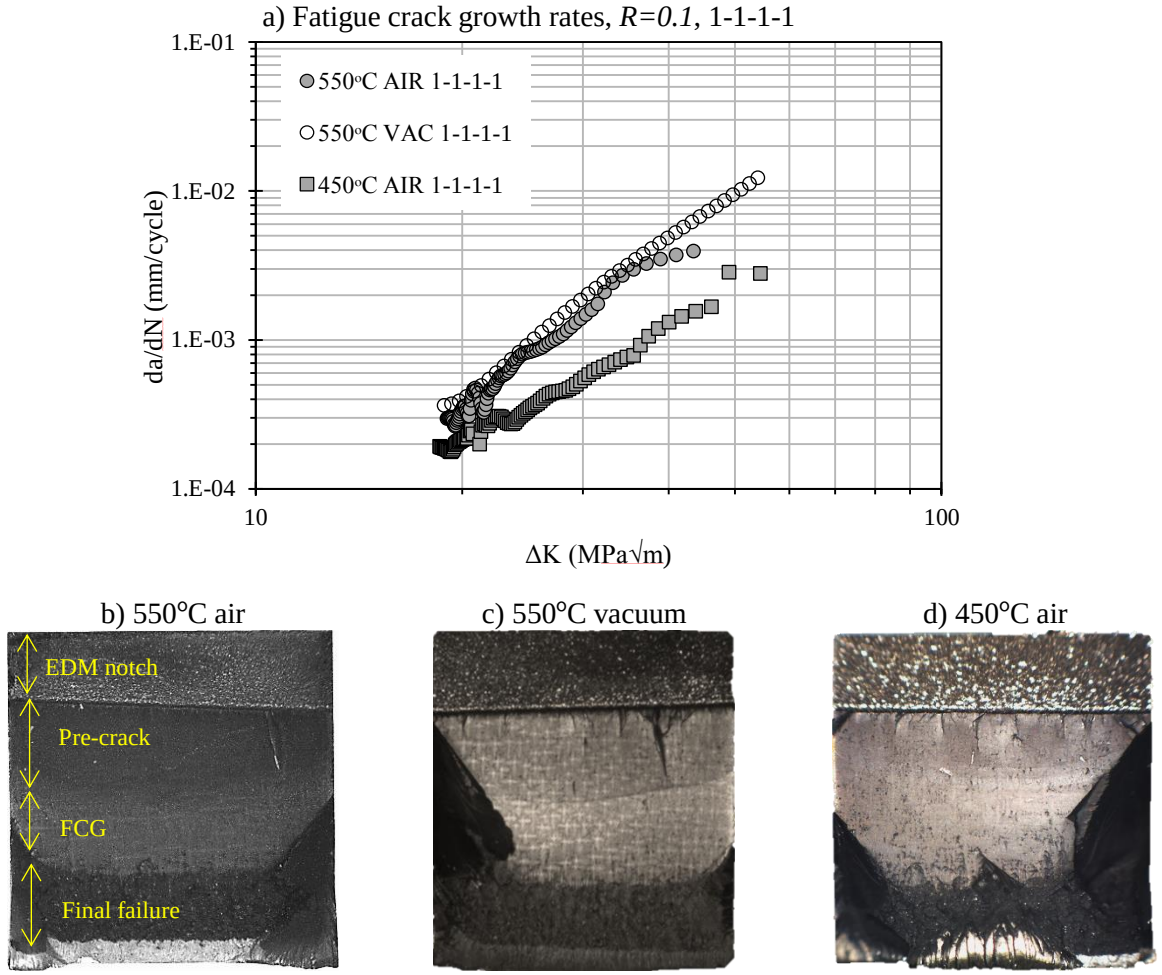

Figure 6.4: (a) Fatigue crack propagation rates in air and vacuum for CMSX-4 at 550ºC, (b) & (c) overviews of the fracture surfaces of the air and vacuum tests.

To further understand the mechanisms of fatigue crack propagation the fracture surfaces were examined under the SEM. Images of the fracture surfaces were taken at various levels of ΔK (I. low-mid Paris' regime, II. mid-high Paris' regime and III. just before failure) at a series of magnifications and the results are presented systematically in Figure 6.5 to Figure 6.7.

Effects of temperature (450°C vs. 550°C) on fracture mode

At all ΔK levels, the fracture surface of the 550°C test is generally more uniform and flat compared to the 450°C test. This might be attributed to the higher amount of oxidation which, even though it is evident on both fracture surfaces, is much more pronounced on the surface of the 550°C test. As a result, many of the microstructural features might have been masked post fracture. It would therefore be difficult to establish the exact propagation behaviour in the 550°C test, particularly at low and mid ΔK levels (Figure 6.5b-c and Figure 6.6b-c). In agreement with the results of section 4.3.2, preferential oxidation of the matrix was observed on the fracture surfaces of both air tests

(Figure 6.5b and d). At low ΔK, crack growth occurs macroscopically along the {100} plane for both temperatures as shown in Figure 6.5a and c. However, evidence of crystallographic slip was observed on the fracture surface of the 450°C test. PSBs appearing as white bands on the surface and γ' shearing by secondary cracks that appear to be oriented along the {111} planes are shown in Figure 6.5a and b.

At intermediate ΔK levels (30-35MPa), even though macroscopically the crack still advances along the {100} plane, the surfaces became increasingly blocky. Specifically, at 450°C the oxidised features shown in Figure 6.6b, resemble crack growth along {111} planes. Some γ' shearing can also be distinguished at 450°C (Figure 6.6b), indicating slip planarity. The equivalent region at 550°C had already developed a thick oxide which made the surface appear flat, even at high magnifications (Figure 6.6d). During the growth out portion of the test, regions formed at higher ΔK levels undergo progressively less oxidation and more surface features become evident. Interdendritic porosity observed on the fracture surface of the 450°C test was associated with a rougher propagation mechanism and with the promotion of {111} slip cracking (Figure 6.6a).

At high ΔK (40-45 MPa√m) (Figure 6.7), at both temperatures, the crack appeared to alternate between pairs of {111} planes as it propagated, but maintained the nominal $<0\bar{1}0>$ growth direction. At this stage the fracture surface of the 550°C (Figure 6.7c) resembled that of the 450°C at mid-ΔK (Figure 6.6b), where traces of slip along the {111} planes were projected on the surface by oxidation. This behaviour is more noticeable in the 450°C sample where oxidation effects were weaker. As expected, at such high ΔK levels, shearing across multiple γ' particles by slip bands was found to be particularly strong at 450°C as seen in Figure 6.7b.

In general, stage I crack growth was found to be promoted by the lower temperature and high stress intensity factor levels. Stage II crack growth appeared to be taking place at lower stress intensity factor levels at 550°C, even though the heavily oxidised surface does not allow conclusive fractographic observations

Effects of environment (oxidation) on the fracture mode at 550ºC

Despite the much lower oxygen partial pressure in the chamber during the "vacuum" test, oxidation was still observed on the fracture surface (Figure 6.5e). At low ΔK, the crack exhibited a Stage II behaviour and propagation was macroscopically along the {100} plane. The cuboidal steps formed on the fracture surface (Figure 6.5f) indicate that crack growth was confined within the γ channels. In addition, careful examination of the low ΔK region did not reveal any slip band cracking.

Transition to crack growth on the {111} plane appeared to occur earlier in vacuum at 550°C, as evidence of γ' shearing from {111} slip bands was found to take place even at intermediate ΔK levels (Figure 6.6f). Since the fracture surface of the air test was obscured by oxidation, this observation might not necessarily be linked to a change in the propagation mechanism. However, it is known that oxidation can homogenise slip, thus postponing any transition to crystallographic growth. This effect can also be seen in the larger side facet produced in vacuum conditions (Figure 6.4c) compared to the air test (Figure 6.4) at 550°C.

Increased shearing of the γ' particles was observed at higher ΔK levels as shown in Figure 6.6f. At that point the crack was evidently advancing by cutting multiple γ′ through alternating {111} planes. A sharper herring bone pattern compared to the air test resulting from the microscopic stage I propagation is visible in Figure 6.6e.

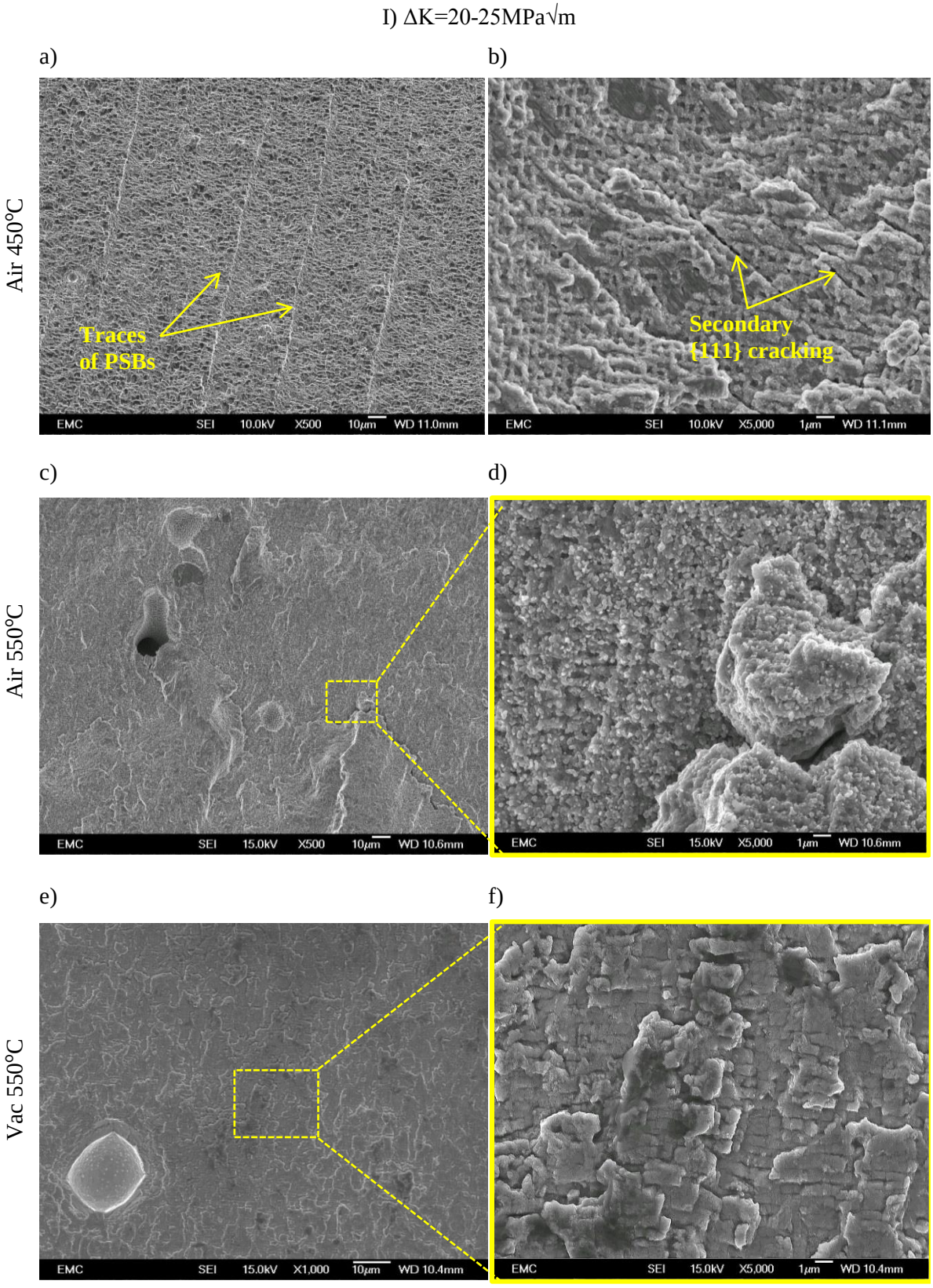

Figure 6.5: SEI micrographs of low ΔK regions on the fracture surface of CMSX-4 samples fatigued in: a-b) air at 450°C, b-c) air at 550°C and e-f) vacuum at 550°C.

II) ΔK=30-35MPa√m

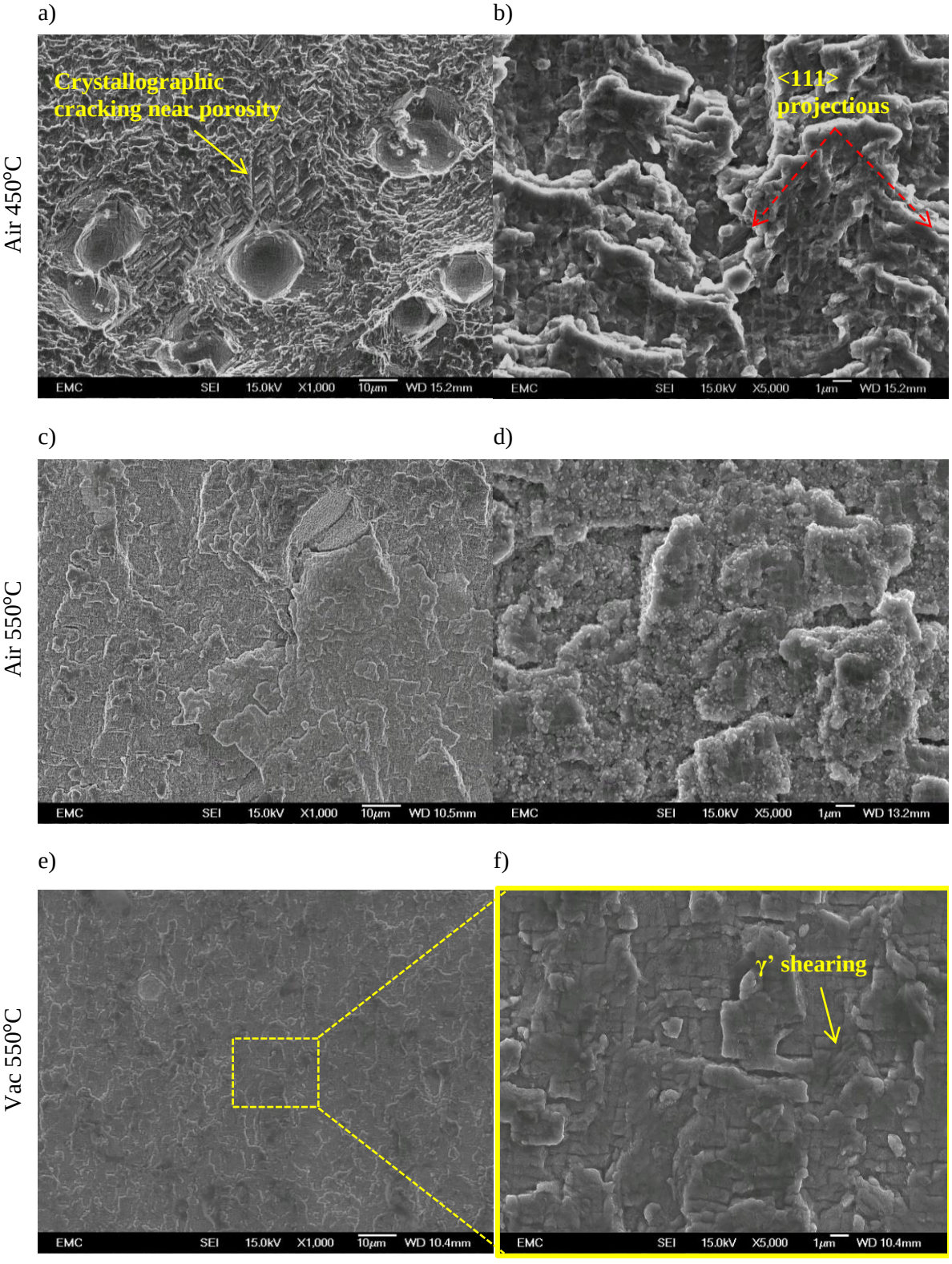

Figure 6.6: SEI micrographs of intermediate ΔK regions on the fracture surface of CMSX-4 samples fatigued in: a-b) air at 450°C, b-c) air at 550°C and e-f) vacuum at 550°C.

III) ΔK=40-45MPa√m

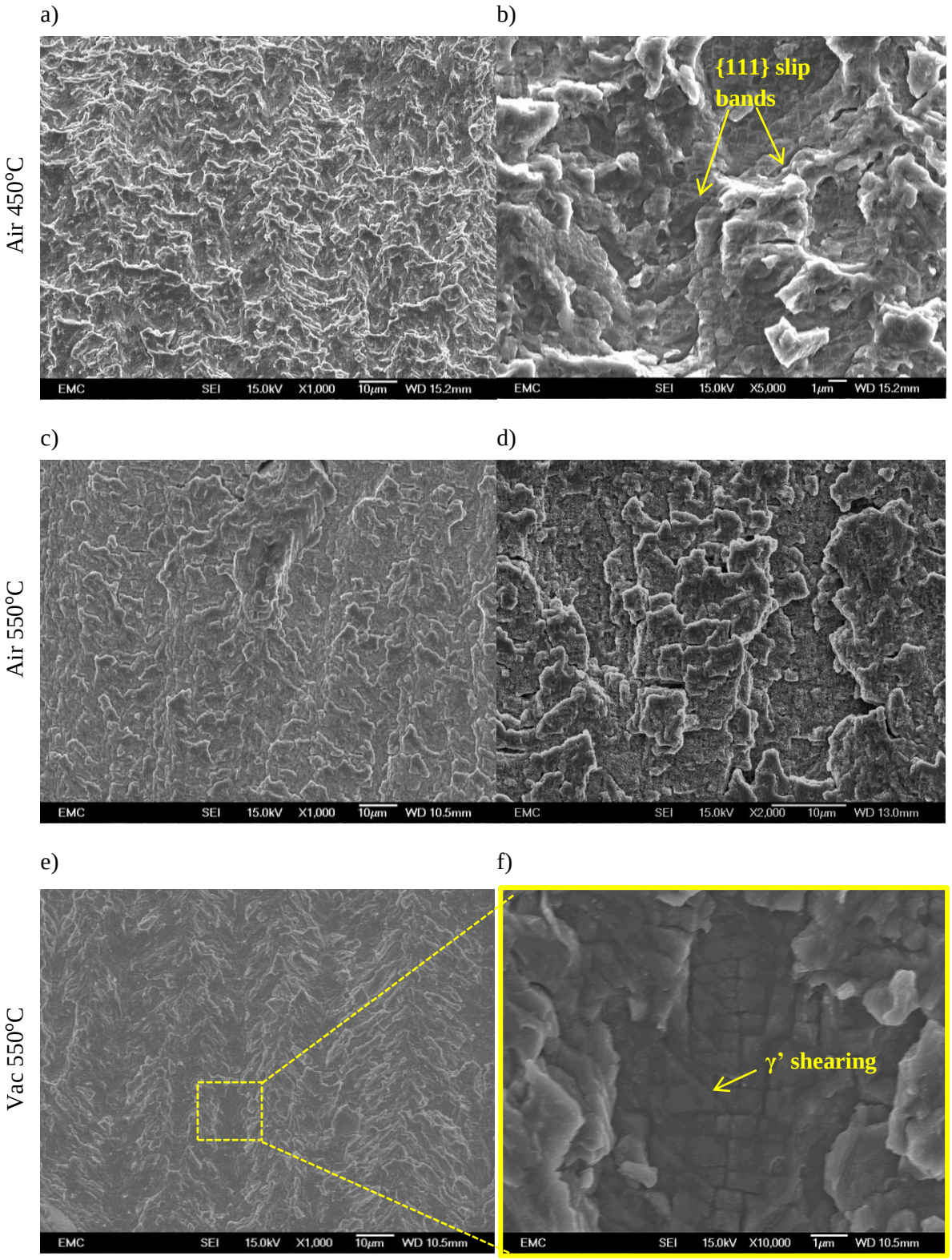

Figure 6.7: SEI micrographs of high ΔK regions on the fracture surface of CMSX-4 samples fatigued in: a-b) air at 450°C, b-c) air at 550°C and e-f) vacuum at 550°C.

6.3.2 Effects of frequency on fatigue crack propagation (constant ΔK)

The effects of frequency on the FCG are shown on the crack length against time plot obtained from the frequency scan test (constant ΔK=20MPa√m) and presented in Figure 6.8. The discontinuities of the plot represent the transition growth data which were discarded to ensure that only the stable growth of each frequency regime was further analysed (although these type of transition data are later analysed in more detail in the block tests). A topological surface map of the fracture surface created with the built in 3D Image-Field feature of the Alicona microscope is included in Figure 6.8 to illustrate the distinct markings (beach marks) formed due to changes in the propagation mechanism with alternating frequency.

The fatigue crack growth rates derived from the different waveform regions are shown in Figure 6.9 on the basis of (a) cycles ($\frac{da}{dN}$) and (b) of time ($\frac{da}{dt}$) against frequency. In both plots the FCG data can be fitted by two straight lines represented by a power law where the exponent is the slope of the line on the log-log plot. In Figure 6.9a the FCG rate increases with decreasing frequency with a slope of -1.04 for frequencies lower than 0.043Hz (corresponding to 1-20-1-1 waveform). In this region FCG rates are mainly time dependent and dwell time controls crack propagation rates. This is also evident in Figure 6.9b where the time required to grow the crack by a specific length appears to become constant at the lowest frequencies. On the other hand, at frequencies higher than 0.043Hz the slope of the curve in Figure 6.9a approaches 0, indicating a cycle dependent FCG.

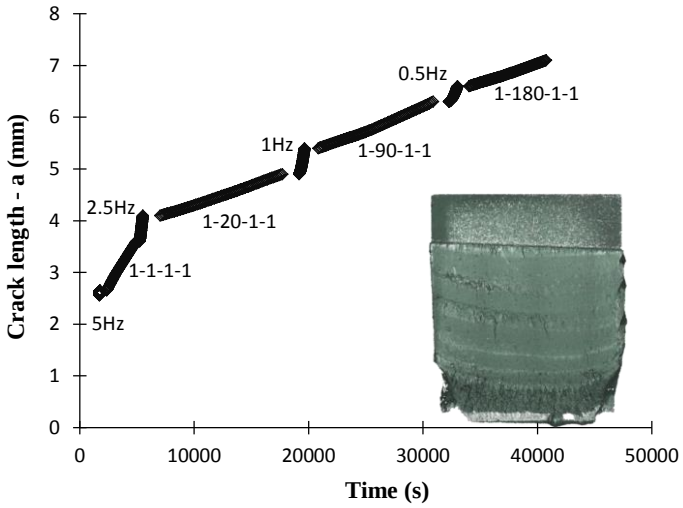

Figure 6.8: Fatigue crack length against time of CMSX-4 under constant ΔK at 550°C alternating between high and low frequencies.

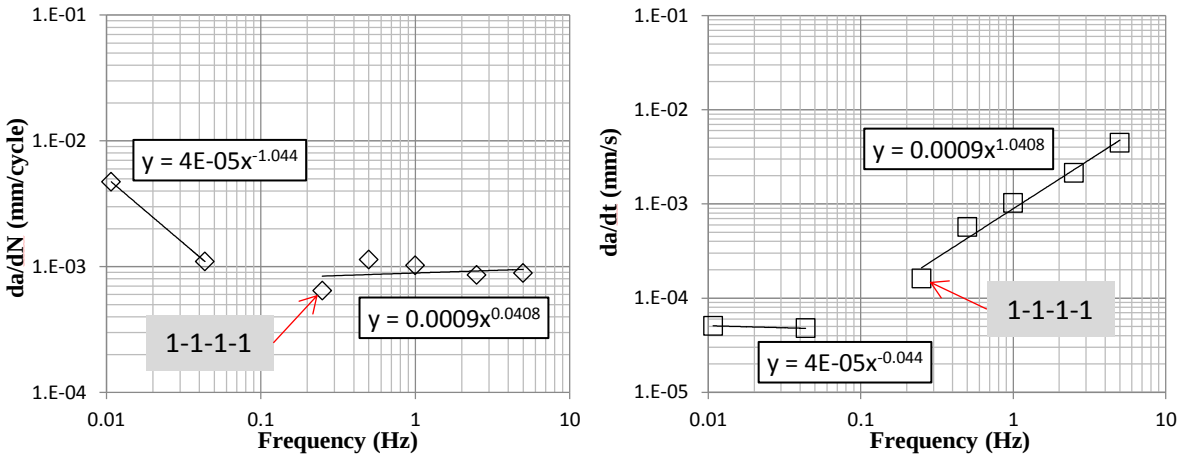

Figure 6.9: Effect of frequency on the crack growth rate of CMSX-4 at 550°C (at a constant $\Delta K \sim 20 MPa\sqrt{m}$) on the basis of: a) cycles and b) time

The fracture surface of the frequency scan sample was examined in the SEM to identify the propagation mode associated with each frequency. Figure 6.10(a), shows an overview of the fracture surface created by stitching four SEM images together. Similar to the topological map of Figure 6.8, the effects of alternating frequency on the fracture mode are illustrated by distinct bands that formed on the fracture surface.

Figure 6.10(b)-(h), show high magnification images of the different frequency areas arranged in order from the highest to the lowest frequency. At the higher frequency regions, the fracture surface appears smooth and flat but progressively becomes more blocky and ratcheted as the frequency decreases. To quantify this, the Alicona microscope was used to analyse the different regions in terms of their roughness. The results are presented in Figure 6.11 and show that both the average surface roughness (*Sa*) and the root mean square roughness (*Sq*) parameters considered here decrease with increasing frequency. At this stage, it is important to note that fracture surfaces corresponding to frequencies tested earlier in the experiment had been exposed (post cracking) to high temperatures for longer and that some of their features might have been masked by oxidation (for the testing sequence refer to Figure 6.8).

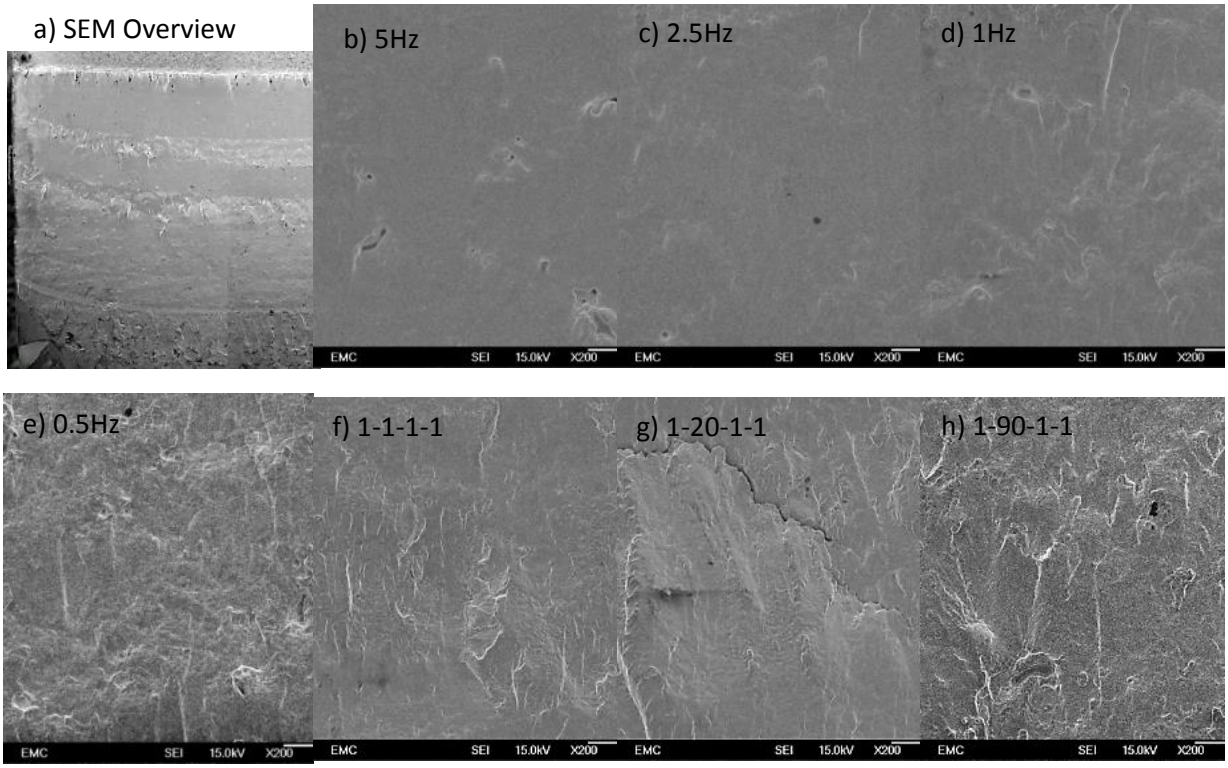

Figure 6.10: SEM fractography the CMSX-4 sample tested under constant ΔK at 550°C with alternating frequencies: (a) stitched images showing the entire fracture surface, (b)-(h) higher magnification images of regions formed under different frequencies in a descending order.

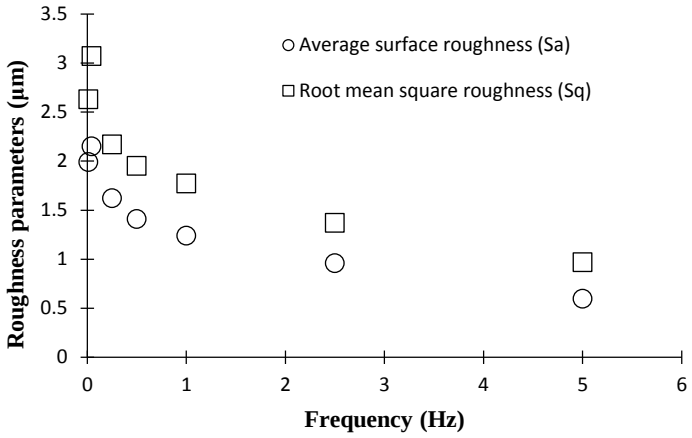

Figure 6.11: Roughness (S_a and S_q) values obtained from the various frequency regions from the fracture surface of the CMSX-4 sample tested under constant ΔK=20MPa√m on the frequency scan test sample.

6.3.3 Fatigue crack growth with alternating frequency (block loading)

The results from the frequency scan test indicated that time or mixed mode dependent fatigue crack growth would take place if a trapezoidal loading waveform with dwells longer than 20s is imposed at 550°C. Therefore, the long dwell times of 90s, 180s and 300s were selected for use in the block tests. The results from a total of five tests are shown in Figure 6.12. Two tests with a long dwell block of 300s were conducted with the transition (from short to long dwell block) taking place at mid and high ΔKs (Figure 6.12a). A third test was conducted with a long dwell block of 180s and the transition took place at mid ΔKs (Figure 6.12b). In a similar manner, a fourth test with a long dwell block of 90s and the transitions taking place at intermediate ΔKs is shown in Figure 6.12c. Finally, a single specimen was used to examine a block of 300s dwells at low ΔKs and a block of 180s at high ΔKs. The crack growth results of this tests were therefore split into two and are shown in Figure 6.12a and Figure 6.12b for the 300s block (green data) and the 180s block (grey data) respectively. The long dwell blocks are labelled and the 1-1-1-1 trendline from the test of Figure 6.4 was added for comparison to all figures. Table 6.1 shows the details of the tests conducted and the figure number the results are displayed on.

Sample ID	Long dwell block			No. of transitions between blocks	Figure displayed
	low	mid	high		
1	-	300	-	2	Figure 6.12a
2	-	-	300	1	Figure 6.12a
3	-	180	-	1	Figure 6.12b
4	-	90	-	2	Figure 6.12c
5	300	-	180	2	Figure 6.12a and b

Table 6.1: Test matrix summarising the block tests.

The crack growth results obtained during the long dwell blocks are generally associated with a significant amount of scatter as can be seen from Figure 6.12. In almost all cases, the FCG rates are observed to decrease during the long dwell block (low frequency, time-dependent) part of the test. This is in contrast with the trend observed in the frequency scan test (at a constant ΔK of 20 MPa √m), where longer dwells corresponded to higher rates of da/dN. An exception to this is seen in the FCG rates (grey data) shown in Figure 6.12b. At higher ΔK levels (>27MPa√m), during the 1-180-1-1 block of the test, the FCG is shown to have a step increase. It is important to note that the entire growth rate data obtained from this sample (sample 5) were noticeably higher than the baseline. This is also evident from the green data of Figure 6.12 which were derived from the same sample during propagation at low ΔKs. This is possibly attributed to the different (overall) propagation mechanism. All other samples have shown a macroscopic stage II propagation, while significant stage I type growth was observed in Sample 5, particularly during the formation of extensive side facets. To illustrate this, the fracture surface of sample 5 is compared with that of sample 2 (yellow data on Figure 6.12) on Figure 6.13.

Figure 6.12b also includes results obtained using sample 3, where the transition from the short dwell block to the long, 180s dwell block, took place at an intermediate ΔK range. Interestingly, the FCG rate, which initially seems to decrease when the block changes from short (1s dwells) to long (180s dwells) at ΔK=24MPa√m, can be presumed to increase when the ΔK approaches 30MPa√m.

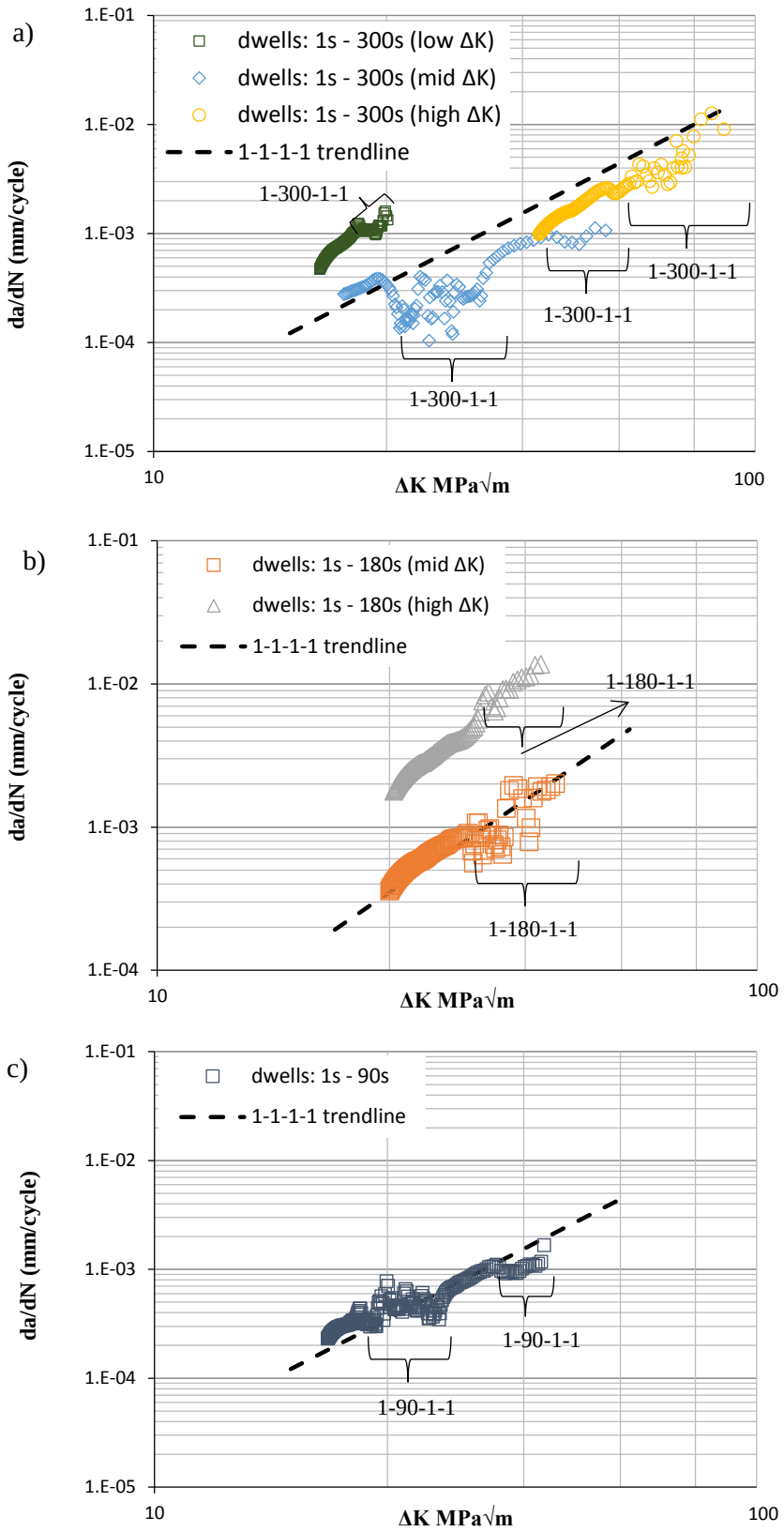

Figure 6.12: Fatigue crack growth rates from alternating dwell tests on CMSX-4 at 550°C: a) tests at low, mid and high ΔKs with 1s and 300s dwells, b) tests at mid and high ΔKs with 1s and 180s dwells and c) tests at low, mid and high ΔKs alternating 1s and 90s.

a)  b) 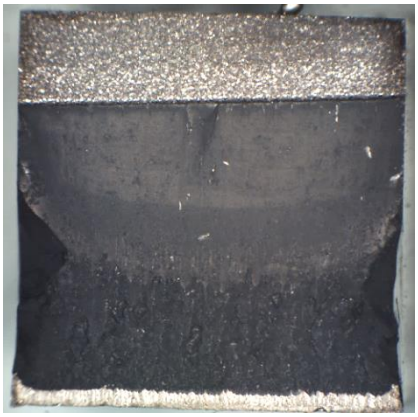

Figure 6.13: Fracture surface overviews of: a) sample 5 and b) sample 2

6.3.4 Crack tip characterisation

The two fatigue cracks formed under a 12h sustained load at 550°C are shown in the SEM BSE images of Figure 6.14a &b. Crack tip 1, was held at $K_{1_{opening}} = 34MPa\sqrt{m}$ and propagated for 15μm while crack tip 1was held at $K_{2_{opening}} = 28.5MPa\sqrt{m}$ and propagated for 7μm during the 12h hold. Both crack tips have a complex morphology with multiple branches emanating from the main body. Evidence of oxidised γ'along the branches of both tips are observed, but no indications of an oxide-induced damage zone are seen ahead of them. The complexity of the propagation mechanism can be seen in Figure 6.14c & d from the high magnification STEM high angle annular dark field (HAADF) images of the TEM specimens extracted from the crack tips of both samples.

Figure 6.15 shows high magnification BF and HAADF images of the three branches of "crack tip-1", shown in Figure 6.14c, accompanied by EDX element maps. From these high magnification images, it is apparent here that the crack propagates both near the γ/γ'interface and by shearing the γ' particles. Branch I, clearly shows that the oxidised tip propagates parallel and near the interface for the most part before it deflects, by approximately 45° degrees from the loading axis. Branch II, which itself branches out in two sub-tips, shows similar behaviour. Its top sub-tip seems to be propagating along the γ channel while its bottom half penetrates an oxidised γ' particle. Branch III, shown in Figure 6.14c, appears to be generally moving along the γ/γ' interface but its tip (Figure 6.15c) is seen arrested within a γ' particle. Co and Ni – rich oxides forming on the surfaces of all three branches are observed to bridge the crack near the tip. Just below these external oxides, a Cr-rich oxide forms a thin band. Internally, within a Ni-depleted zone, Ti and Al – rich oxides form finger-like protrusions which penetrate the substrate ahead and around the crack tip. The penetration depth of the oxide for crack tip 1 ranges between 50-150nm. The STEM EDX maps of crack tip 2 are illustrated in Figure 6.16. This is a less complex crack tip with only two branches propagating at approximately 45° to each other. The oxide layer sequence and the penetration

depths at the tips of the two branches are similar to “crack tip-1”. The edges of the tips are less defined compared to “crack tip-1” and the crack appears more open.

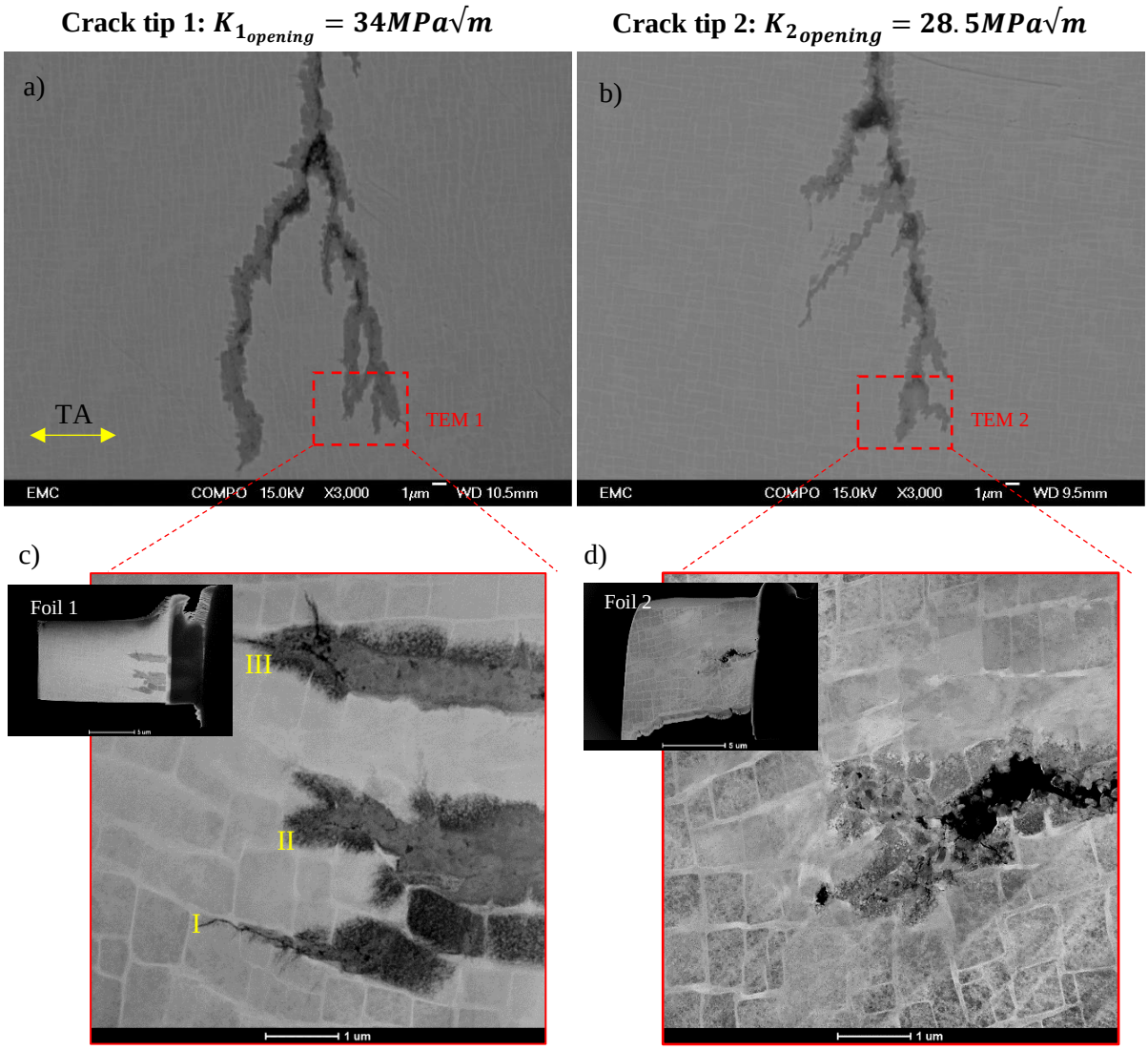

Figure 6.14: a) & b) SEM BSE images of the crack tips formed under sustained load for 12h at 550°C. The loading axis is shown in yellow and the location of the TEM foils is shown by the red rectangles, c) & d) HAADF STEM images of the crack tips with the individual branches marked as I, II and III.

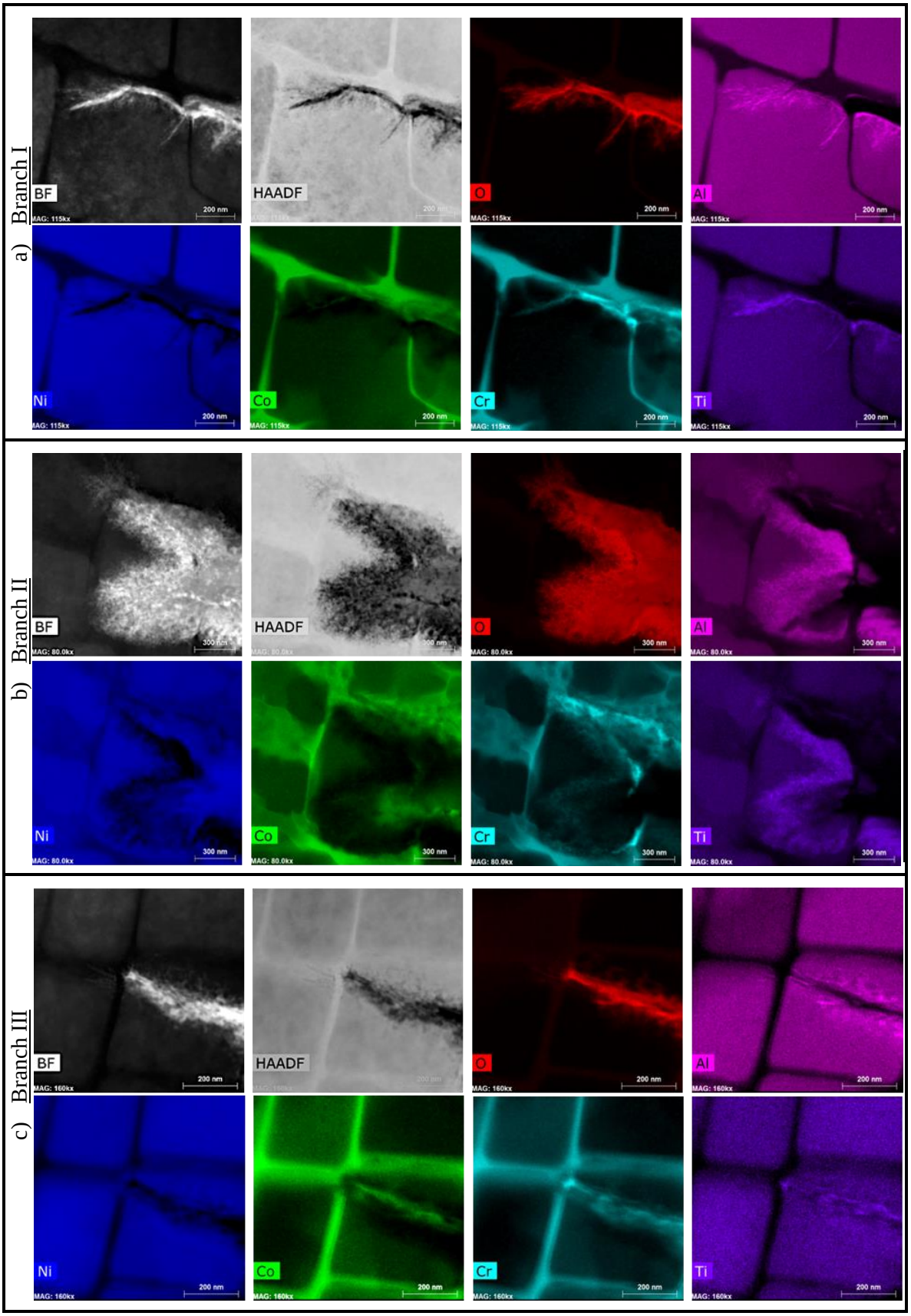

Figure 6.15: STEM-EDX maps of "crack tip-1" branches formed at constant load ($K_{1_{opening}} = 34MPa\sqrt{m}$) for 12h at 550°C.

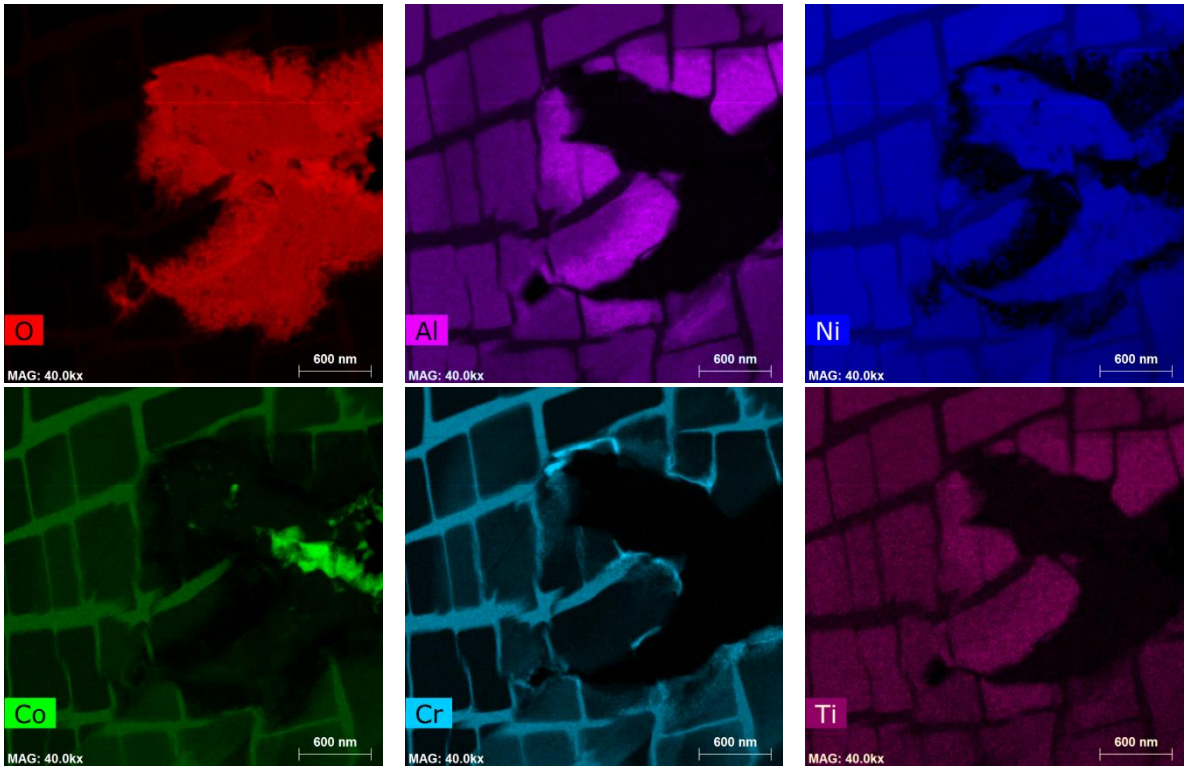

Figure 6.16: STEM-EDX maps of "crack tip 2" formed at constant load ($K_{1_{opening}} = 28.5MPa\sqrt{m}$) for 12h at 550°C.

6.4 Discussion

6.4.1 Effects of temperature and environment on the fatigue crack growth behaviour

At low to intermediate ΔK levels, crack growth in both 450°C and 550°C in air and 550°C in vacuum, takes place macroscopically along the {100} plane with an overall stage II mode. Stage II growth at elevated temperatures is generally attributed to thermally activated deformation processes such as dislocation climb or cross slip [85,101]. In addition, planar slip bands, which contribute to Stage I crack growth, can be suppressed by oxidation which then leads to homogenisation of the slip process, making Stage II behaviour more favourable [215]. Such processes have been generally observed during fatigue at higher temperatures in similar systems e.g. [100,101,216]. Even though the fracture surface of the 550°C test was obscured by oxidation and thus fractography could not yield conclusive results, similar processes could be presumed to be active here as well. This is because oxidation and other thermally activated processes, not only depend on temperature but also depend on time, and the 0.25Hz frequency used in this study is much lower than those used in the aforementioned research. As noted by Leverant and Gell [101], another condition for Stage I to occur is that the crack must form along the slip band faster than the time needed for dislocation recovery out of the bands themselves. This suggests that, even at lower

temperatures, given that the frequency is low enough, there could be enough time for the dislocations to diffuse out of the planar bands before the crack manages to grow along them; therefore promoting Stage II propagation.

Despite the macroscopic Stage II appearance, evidence of γ' cutting have been found on the fracture surfaces of the 450°C test in air and 550°C test in vacuum, suggesting a more complex propagation mechanism. Fundamentally, the critical resolved shear stress in FCC single crystals is much lower along the {111} planes [143] and thus deformation is easier than on the {100} planes. In addition, it is well established that the coherent γ' precipitates can be more easily sheared at low temperatures (peak strength of γ' is seen at approximately 700ºC) [217]. Therefore, it is possible for the fracture surfaces to contain evidence of sheared precipitates by {111} type slip bands at these temperatures. Notably, γ' shearing was only observed at intermediate and high ΔKs in the 550°C test in vacuum, whereas slip bands were found on the fracture surface of the 450°C test even at low ΔK levels. This is an indication that 550°C is sufficiently high to activate homogenisation of slip, if the crack growth rate (and CTOD) is low enough.

At high ΔK levels, near fracture, the fatigue crack growth became purely cycle dependent (propagation along alternating {111} planes) for both temperatures and environments. This type of propagation can be explained by the alternating shear model proposed by Neumann [218]. The model suggests that when a crack is propagating along the primary slip plane, the slip system ahead of the crack tip work hardens due to dislocation accumulation, shifting the crack tip to a plane where a softer slip system operates. Thus the crack frequently changes the growth direction from one slip system to another to essentially follow the path of least resistance.

Extensive slip-band cracking with faceted <111> crack growth can also take place locally in the vicinity of porosity, where complex local stress states may be expected to occur. Similar observations were seen on the fatigued surfaces of CMSX-4 samples at 650ºC under a 1-1-1-1 waveform [98]. The authors noted that porosity had promoted transition to alternating slip band cracking by providing local stress concentrations. Planar slip can be therefore promoted around defects of a certain size at ΔK levels lower than the ones required to produce extended slip band cracking across the whole sample. This behaviour is of particular interest when the interdendritic regions are considered where porosity is mainly concentrated.

The FCG rates at 550°C in air and vacuum were very similar. This is suggesting that oxidation has negligible effects on the fatigue performance at these temperatures and frequencies (strain rates). Testing conducted on CMSX-4 at a similar temperature (650ºC) by M. Joyce et al. [98] showed faster FCG rates in vacuum compared to air. The faster crack growth rates seen in vacuum were attributed to the homogenising effect of oxidation on slip which not only suppressed faster Stage I crack growth but possibly increased oxidation-induced closure. Henderson and Martin [216]

reported similar behaviour in another SX Ni-based superalloy (SRR-99), also at 650°C. Fractographic analysis conducted in both of these studies showed that the crack path followed the γ/γ' interface at low to mid ΔK levels. However, contrary to this study, the fracture surfaces of the samples tested by M. Joyce et al. [98] showed less stage I growth particularly when comparing side facet formation (refer to Figure 6.4). A previous study on U720 single crystal [219], has shown that Stage I type crack growth is fundamentally more rapid than stage II under the same applied stress levels (given that closure effects are accounted for). Hence, the interaction between the faster Stage I crack growth and oxidation induced retardation mechanisms would be expected to be competing in this study.

6.4.2 Mixed time/cycled fatigue crack growth dependence

The results of Figure 6.9 indicate that a dwell of 20s or longer (f < 0.043Hz) is sufficient to activate time-dependent damage processes. Comparing with the results of Figure 6.4, where the FCG rates in vacuum and air obtained with 1-1-1-1 waveform (f = 0.25Hz) were very similar, it can be deduced that (at ΔK=20MPa√m) a transition frequency between 0.25-0.04Hz exists where environmental damage will contribute to the overall growth rate.

To investigate the nature of the propagation mechanism in air further, a section was taken perpendicular to the fracture surface of the 550°C test (Figure 6.4c) and secondary cracks were examined under the SEM in the plain polished and etched conditions as shown in Figure 6.17. Observations confirm that the crack predominantly propagates through the γ/γ' interface, although some precipitate cutting is occasionally observed (Figure 6.17a). This indicates that a mechanism other than pure crystallographic or faceted crack growth (characteristic of cycle dependent damage) is taking place during 1-1-1-1 loading (0.25Hz). Depending on the ΔK level [220] (and R-ratio [221]), the transition between cycle and time dependent fatigue shifts. In agreement with previous studies [220,222] this transition spans over a range of frequencies where synergistic mechanical-environmental damage takes place. It is therefore possible that frequencies lower than 0.25Hz promote mixed time/cycle dependent damage. Pure time dependent crack growth would then require even longer dwells (at 550°C).

Assuming a mixed time/cycle dependence regime, at lower ΔK levels, where FCG rates are slower, thermally activated processes and oxidation induced closure might be significantly affecting the effective driving force. At higher ΔKs, the time allowed for O_2 diffusion at the near tip surfaces before the crack propagates further is potentially inadequate for the oxide to thicken enough and cause bridging of the surfaces. The mechanism of fatigue crack propagation was found to change significantly under the effect of oxidation when the loading frequency is changed. The exponential increase in the measured roughness parameters (Figure 6.11) indicates that prolonged tensile

stresses (lower frequencies) in the presence of O_2 create a more complex crack front. This could be linked to an increased amount of bificurations and branching resulting from stress/strain assisted oxygen diffusion ahead of the crack tip and localised damage. Recent work that examined arrested cracks in a polycrystalline Ni-based superalloy in air and vacuum employed micro X-ray CT to quantitatively analyse the amount of branching/secondary cracks near the crack tip region [163]. Their results revealed that oxidising environments promote more micro cracks and bificurations at the vicinity of the crack tip.

The complexity of the mechanisms operating during fatigue at 550°C was also illustrated from the results obtained by the block tests of Figure 6.12. According to the frequency scan test results, alternating between a cycle dependent regime (1-1-1-1) and a time or mixed dependent regime (1-90,180,300-1-1) the FCG rates should increase. In addition, according to the results of [117,214] the embrittling effects of oxidation should be evident and a damage zone ahead of the crack tip would be expected to promote higher FCG rates at least within its extent. Instead, FCG rates are found to decrease for the majority of the tests at all ΔK levels. Oxide induced crack closure is expected to be more dominant at lower ΔK levels because of the smaller crack tip opening displacements (CTOD) during a fatigue cycle. Given sufficient time, the thickness of the fracture surface oxide layer can become comparable in size to the CTOD resulting in unexpected face contact and reduction in the observed ΔK. This is evident from the SEM-EDX maps of Figure 6.18 obtained at the wake of the crack from an interrupted block test (1s and 300s blocks). The fracture surfaces were formed at a ΔK=21MPa√m and lie within the 300s dwell block of the test. It is clear that the oxides formed are in contact at a number of points but at the same time it should be taken into account that the crack surfaces have been exposed to high temperature post cracking for the duration of the test (approx. 15h). Assuming pure mode I loading the CTOD can be expressed as [223]:

$$\delta = \frac{{K_I}^2}{\sigma_y E m} \qquad (6.1)$$

,where m is a constant and equals to 1 for plane stress and 2 for plane strain conditions. K_I , for the specific crack length equals to 23.3MPa√m. The yield stress (σ_y) and Young's modulus (E) along the <001> direction at 550°C are taken from in house testing as 900MPa and 120GPa respectively and the resulting CTOD was found to be 2.5μm. The results of section 4.3.1 showed that the rate at which oxidation builds up on the surface of CMSX-4 at 550°C can be described by:

$$X^{6.2} = 3.44 \times 10^{-5} \times t \qquad (6.2)$$

,where X is the thickness (μm) of the oxide scale building on a surface (under isothermal conditions) and t is the exposure time in hours. Taking $t=0.08h$ (for 300s dwell) the oxide scale thickness (X) on each fracture surface is calculated to be 0.126μm, giving a total thickness (accounting for both surfaces) of ~0.25μm. This indicates that, for a 300s dwell, the crack tip would be filled with oxides within 10 cycles, which could explain the reduction in FCG rates observed during the long dwell blocks. In fact, according to the results of section 4.3.6, the plastic strains at the vicinity of the crack would enhance the oxide growth rate resulting in a much faster filling of the crack.

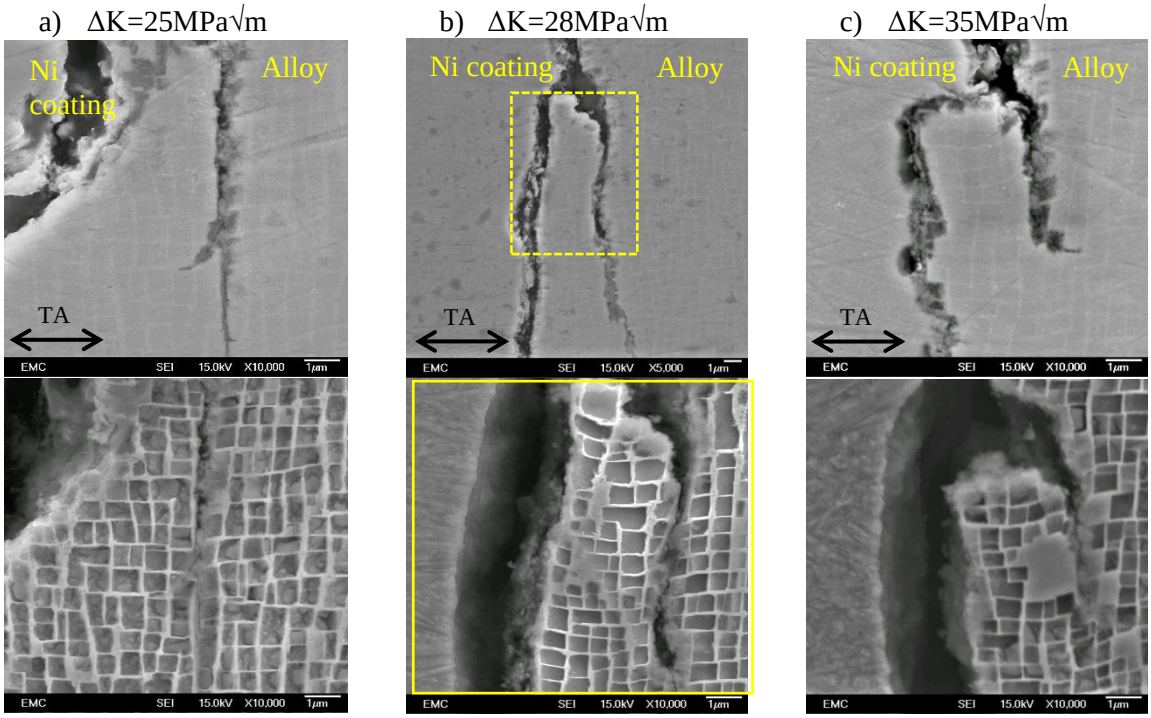

Figure 6.17: Secondary cracks, formed at different ΔK levels, penetrating the fracture surface of CMSX-4 fatigued at 550°C.

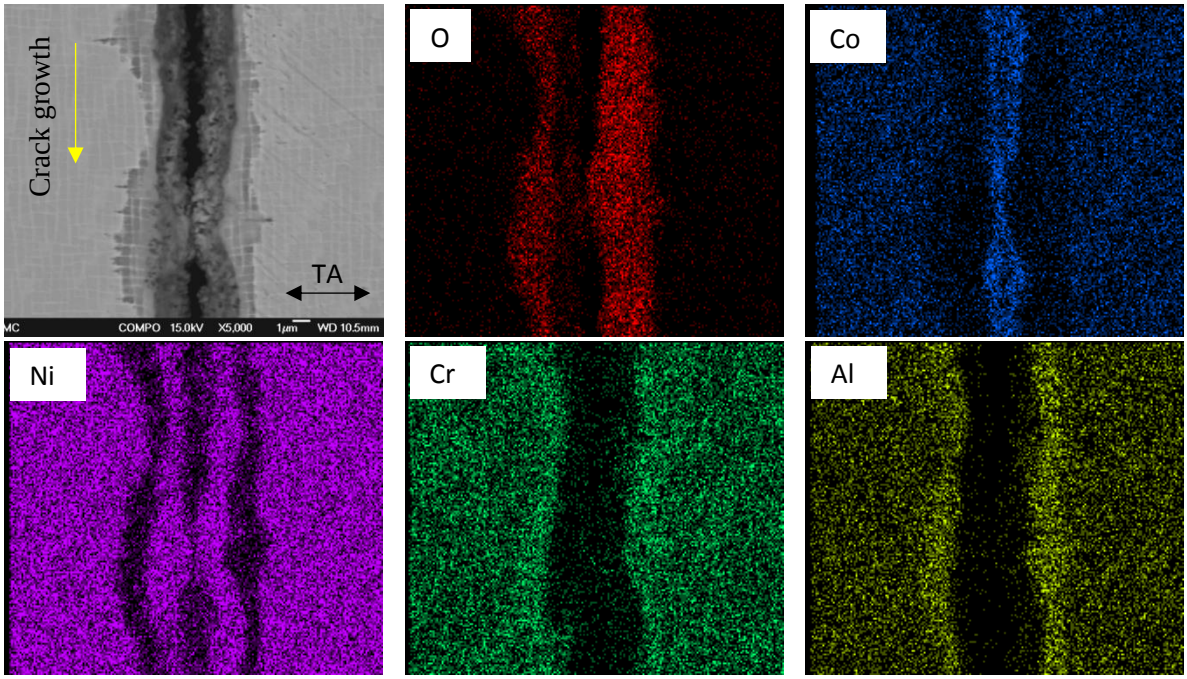

Figure 6.18: EDX mapping of the oxides formed on the crack surfaces at ΔK=21MPa

6.4.3 Damage ahead of a crack tip during dwell fatigue

The effects of long dwells and oxidation on the damage at a fatigue crack tip have been investigated by holding pre-cracked samples at a sustained load for 12h. According to the STEM-EDS results of Figure 6.15 and Figure 6.16, the oxide layering sequence at the crack tip, beginning from the innermost oxide, was Al→Ti→Cr→Ni→Co rich oxides. Interestingly, the results of Section 4.3.5, on isothermal oxidation of CMSX-4 at 550°C, did not show evidence of Cr or Co oxides forming even after 640h of exposure, which is significantly longer than the crack tip exposure during 1 cycle. However, evidence of Co-rich oxide forming externally was observed in the sustained load oxidation testing reported in Section 4.3.6. The thermodynamic driving force for the oxidation of Co is similar in magnitude to that of Ni at 550°C (see Ellingham diagram of Figure 2.12). The fact that it is only observed on strained surfaces implies that the rate of formation (kinetics) is the controlling factor and it is this that is affected by the stress state.

Contrary to polycrystalline Ni-based superalloys, where oxidation can readily attack grain boundaries and contribute to higher FCG rates [161,224], the effects of environmental damage in equivalent single crystal alloys can be twofold. Depending on temperature, load ratio and frequency, two opposing mechanisms can influence the crack growth: (i) decrease of the FCG rate resulting from a reduction in the effective ΔK (or of the crack opening threshold) arising from oxide induced closure taking place near the tip and at the wake of the crack [98,123,128]; (ii) increase in the FCG rate by time dependent embrittlement ahead of the crack tip due to increased O_2 diffusion promoted by prolonged stresses at high temperature [116,117,225].

Based on the findings of this work and the associated literature, two possible damage mechanisms are proposed to be acting on the crack tip during fatigue and oxidation interactions. The first mechanism involves propagation of the crack by failure of an embrittled volume ahead of the crack tip. The effects of such a mechanism would be realised at a microscopic level and it's extent would be analogous to the size of a microstructural feature that is susceptible to oxidation. The second mechanism involves damage at the nanoscale by decohesion at an interface. Such a mechanism is generally encountered in intergranular failure in polycrystalline alloys and it is termed as dynamic embrittlement. An equivalent mechanism could also be active during high temperature fatigue in single crystal superalloys, with the damage taking place at the γ/γ' interface. The two postulated mechanisms are schematically illustrated in Figure 6.19.

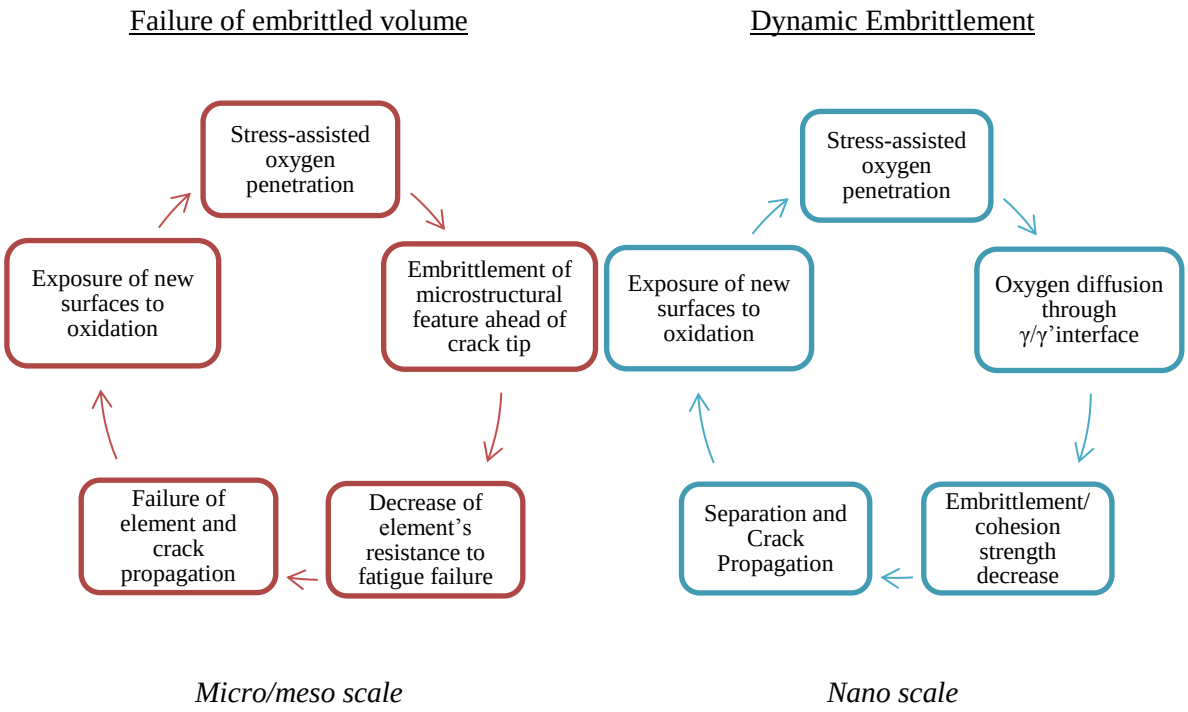

Figure 6.19: Postulate fatigue crack propagation mechanisms during oxidation fatigue damage in SX Ni-based superalloys.

The high magnification SEM and STEM images of Figure 6.14 and the STEM-EDS maps of Figure 6.15 - Figure 6.16 did not indicate extensive damage and oxide penetration was confined to within only a few tens of nm ahead of the crack. It is recognised though that propagation through a potentially damaged volume ahead of the crack tip might have taken place during unloading when retrieving the sample from the testing machine, even though there was no noticeable increase in the PD reading.

Naturally the absence of grain boundaries in single crystal superalloys makes them more resistant to time dependent damage mechanisms (e.g. creep, dynamic embrittlement). As anticipated at these

temperatures, after careful examination of the TEM samples of Figure 6.14 - Figure 6.16, no indication of creep effects on the microstructure, such as rafting of the γ' and/or expansion of the γ channels [226], were found. Nevertheless the difference in the lattice parameters of the γ and γ' phases represent a source of additional strain in the microstructure. The magnitude of this strain can be substantially increased in the case of exposure to high temperatures because of the difference in thermal expansion coefficients between the two phases. During the sustained load period in dwell fatigue conditions, the applied tensile load will further exaggerate the γ' tensile stresses and reduce the γ channel compressive stress parallel to the loading axis. Because of the Poisson effect, the opposite will take place in the direction perpendicular to the loading axis i.e. the γ' interface tensile stresses are reduced and the γ channel compressive stresses will increase. If the loads are high enough, plastic deformation would take place first in the horizontal channels since the compressive stress in vertical channels will oppose deformation. As a result, an increased number of dislocations would accumulate in the horizontal γ/γ' interface, perpendicular to the tensile axis (parallel to the crack growth direction) [195,227]. An illustration of this process is shown in the schematic of Figure 6.20.

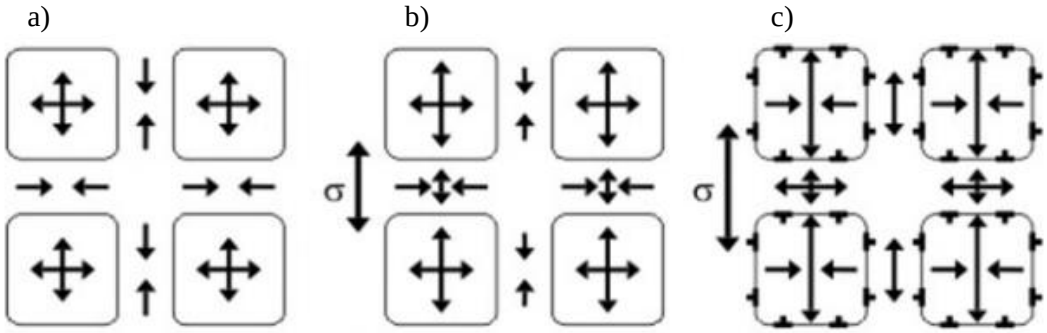

Figure 6.20: Schematic showing the stresses acting on the γ/γ'microstructure due to a) initial misfit, b) after application of an external load and c) after larger external stresses and small plastic deformation (after [228])

Single crystal nickel based superalloys have been designed to achieve large negative misfit (-0.2 to -0.8%) at service temperatures (1000°C) [229]. Large misfits form denser interfacial dislocations networks in order to relieve the misfit stress and act as effective barriers to further gliding dislocations from entering and shearing the γ' [230]. However, the larger amounts of line defects (dislocations) concentrated around the γ/γ' interface could act as low resistance paths for oxygen ingress. As shown in the study of Karabela et al. [231] the extent of oxygen induced damage at a fatigue crack tip depends on oxygen concentration/oxygen partial pressure and the stress state. Higher concentrations of oxygen and larger strains were associated with increased damage. In addition, other studies [125,232], by employing first principle density functional calculations,

found that oxygen preferentially segregates at the γ/γ' (Ni/Ni_3Al) interface and results in a reduction of the cleavage energy (energy required to separate the crystal structure).

Since the temperatures of 450°C and 550°C investigated here are much lower than 1000°C, it is expected that the misfit strains are also lower, resulting in a lower number of dislocations at the γ/γ'interface. However, it is well established that at higher temperatures the damage mechanism of creep prevails [109,233], during which, the large negative misfits promote particle coalescence and the formation of rafts normal to the tensile loading direction that form a plate-like structure on the transverse face [234]. This microstructural change opposes glide of dislocations through the γ channels [108] and thus alters the concentration of dislocation defects around the previously cuboidal γ'. Therefore a form of dynamic embrittlement, driven by a faster, short circuit diffusion of oxygen through dislocation defects along the γ/γ' interface, might be more detrimental at intermediate temperatures.

The occasional shearing of the γ' particles is generally observed to take place at an angle of approximately 45° to the loading axis, indicating that slip along the favourable {111} planes is not completely suppressed at these temperatures. This suggests that at 550°C a combination of planar slip damage and time dependent (oxidation) damage act simultaneously at the crack tip. Evidence of dislocations shearing the γ' particles ahead of the crack tip (Figure 6.21) indicate that the deformation micro-mechanism is similar to that at room temperature, where dislocations glide in the γ matrix and shear the γ' particles. Nevertheless, the crack tips of Figure 6.14 - Figure 6.16 and the secondary cracks of Figure 6.17, were found to propagate predominantly near the γ/γ' interface suggesting that oxidation influences propagation through a more macroscopic mechanism that could be explained by the form of dynamic embrittlement.

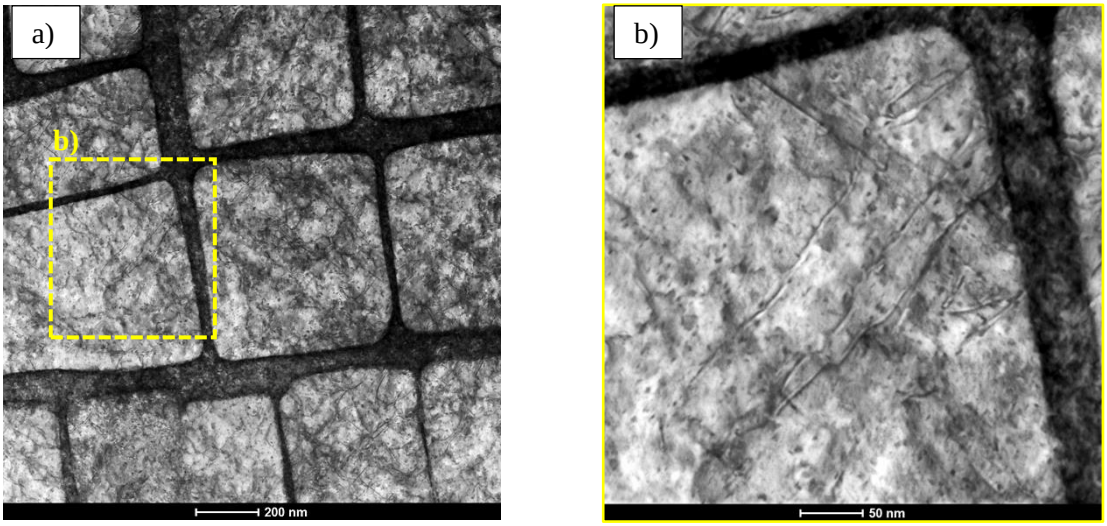

Figure 6.21: Dislocations propagating along a γ' particle located 3.5μm ahead of "crack tip 2".

6.5 Summary

The effects of oxidation during dwell fatigue on the long crack propagation of CMSX-4 at 450°C and 550°C were investigated in this chapter. Based on the aforementioned results and discussion, the following conclusions can be made:

1. The macroscopic fatigue crack propagation of CMSX-4 at 450°C and 550°C in both air and vacuum occurred in the nominal growth direction producing a Stage II - like fracture surface. At low ΔK levels, slip band cracking and γ'cutting was only evident at 450°C. At 550°C in both air and vacuum the crack propagated along the γ/γ′ interface. A characteristic herring bone pattern was formed on the fracture surfaces at high ΔK levels indicating a transition to extended slip band cracking. This transition took place earlier at 450°C.
2. Fatigue testing in vacuum and at 450°C resulted in the early formation of large side facets that extended all the way to fracture, contributing to the overall growth. In general, stage I crack growth was promoted by the lower temperature and lower oxygen partial pressures as well as the plane stress state at the specimen sides. Stage II crack growth took place at lower stress intensity factor levels and higher temperatures.
3. The FCG rate of CMSX-4 at 550°C is similar in air and vacuum. The fundamentally more rapid increased Stage I propagation in vacuum and the oxidation induced crack closure in air offset the overall effect of any oxidation induced damage mechanisms on crack growth rate.
4. Fatigue crack propagation with longer dwells results in rougher fracture surfaces indicating a more complex crack front. Examination of fatigue cracks that formed under sustained load for 12h (simulating a long dwell) had a complex morphology with multiple branches emanating from the main body forming a number of tips.
5. The crack propagation rates in single crystals are affected by the crack history particularly due to the formation of large facets. The fundamentally faster Stage I and the roughness induced closure results to less predictable FCG rates and significant sample to sample variability.
6. A layered oxide structure is formed at the crack tip of CMSX-4 during dwell fatigue at 550°C. This consists of an outer Co and Ni-rich oxide and an inner dominantly Al-rich oxide with Cr and Ti-rich oxides also being present. Even though this sequence is in good agreement with thermodynamic predictions, isothermal oxidation of unstressed samples did not form external Co – rich oxides indicating that the plastic strain acting at the crack tip alters the kinetics of the oxide species.

7. The micro-mechanism of fatigue crack propagation at intermediate temperatures is a complex process with several competing mechanisms acting on the crack tip simultaneously. Crystallographic slip damage by γ' shearing is still active at these temperatures but at the same time thermally activate processes that promote propagation through the γ channels also take place. In addition, the effects of oxidation are two-fold. Even though the temperature is not high enough to cause embrittlement of a microstructural element ahead of the crack tip, finger like protrusions were found to penetrate the material ahead of the crack tip. The kinetics of such a mechanism are accentuated by the plastic strains at the crack tip, which given enough time can promote cleavage fracture at the γ/γ' interface. The rate of oxide formation on the crack tip surfaces is high enough to form thick oxides that bridge the CTO and reduce the effective driving force.

Chapter 7 General discussion

7.1 Lifing implications – Life assessment roadmap

It has become apparent from the experimental work presented in Chapters 4 – 6 that the physical mechanisms and fatigue crack growth processes operating at intermediate temperatures in Ni-based turbine blade materials, are numerous and can act either competitively or cooperatively.

According to the results of Chapter 6, frequencies lower than 0.25Hz would promote a mixed time/cycle dependent crack growth at a ΔK of 20MPa and temperature of 550ºC. Previous work [220], has shown that the transition frequency at which time dependent processes, such as oxidation, become important can be generally described as a function of ΔK, R – ratio and temperature (i.e. Equation 8.1). It is important therefore to map this transition according to these parameters in order to be able to identify the operating regime and the underlying damage mechanisms. An example of a mechanism map for U720Li Ni-based superalloy showing the dependence of the transition frequency on the ΔK is shown in Figure 7.1.

$$f_{transition} = F(\Delta K, T, R) \qquad (8.1)$$

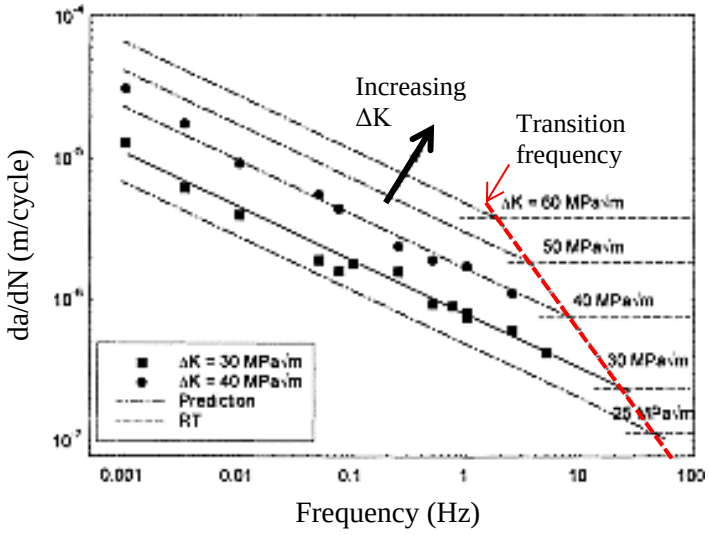

Figure 7.1: Mechanism map for U720Li showing the dependance of the transition frequency on the ΔK level (plot adapted from [220]).

Given that the FCP damage has a mixed time and cycle dependence, oxidation and fatigue can be presumed to act synergistically at the crack tip contributing to the damage. Based on the results of this work and the review of the literature, generally three possible interaction scenarios can take place. Firstly, adsorption of oxygen into the slipped surfaces at the crack tip can block returning dislocations during unloading and inhibit re-joining of the surfaces. A physics – based approach to slip irreversibility and its influence on fatigue crack propagation threshold was recently investigated for the Ni-based superalloy KM4 [119]. The basis of this model is derived from consideration of dislocation-based processes with the main source of irreversibility being the egress of dislocations from free surfaces. These were investigated by detailed TEM and AFM measurements on a number of specimens tested in compression at a range of temperatures. The result of the model is a dimensionless parameter ($f = \varphi^2$) intended to describe the net slip irreversibility during a loading cycle in grains connected to a free surface (as such it is also suitable for single crystals). Crack tips can also be considered as free surfaces where dislocations dissipate to form slip lines. With increasing slip irreversibility the net plastic deformation per cycle also increases and in turn increases fatigue crack growth rates. Although this model is claimed to be successful in capturing temperature effects (by quantifying slip homogenisation through slip line spacing measurements) it does not seem to include the effect of oxygen adsorption on the slip lines. Nevertheless, slip irreversibility was shown to be a fundamental parameter that contributes to damage and could be incorporated in lifing models. This route has not been investigated in this work and it is therefore a matter of future consideration.

Secondly, depending on the ΔK level, oxidation can either contribute to damage or reduce the effective ΔK by inducing closure. Although a definite transitional value of ΔK has not been achieved at the temperature of investigation in this study, the results of Section 6.3.2 and Section 6.3.3 indicate its existence. Its existence and value however appear to depend on the frequency or dwell time employed and clearly further testing is required to validate this. Whether oxidation crack closure will take place can be examined by comparing the CTOD with the thickness of the oxides forming on the cracked surfaces. The thickness of the oxide can be calculated using Equation 4.1 with the external oxidation constants of Table 4.3. In the case that crack closure does take place the fatigue crack propagation equations (Paris Law type) should be modified to include the effective ΔK. At ΔK levels higher than the transition value, where the effects of oxidation become detrimental to the FCP, depending on the temperature, the mechanism of dynamic embrittlement (cleavage of the γ/γ' interface) or failure of an embrittled feature ahead of the crack tip will take place. For the intermediate temperatures (and frequencies) considered here, oxidation damage was not found to extend enough or to be comparable with any microstructural feature so as to indicate a "failure of an embrittled volume" type of mechanism. On the other hand, evidence of

propagation along the γ/γ’ interface and separation of the two phases were found, indicating a dynamic embrittlement type of mechanism acting at the nano-scale.

The above discussion is summarised in the proposed road map of Figure 7.2. The boxes filled with red colour illustrate the issues that have been investigated experimentally in this work. The boxes outlined with red colour illustrate the issues that have been indicated but not explicitly investigated while the black and white boxes represent matters that have been raised or discussed only based on the available literature.

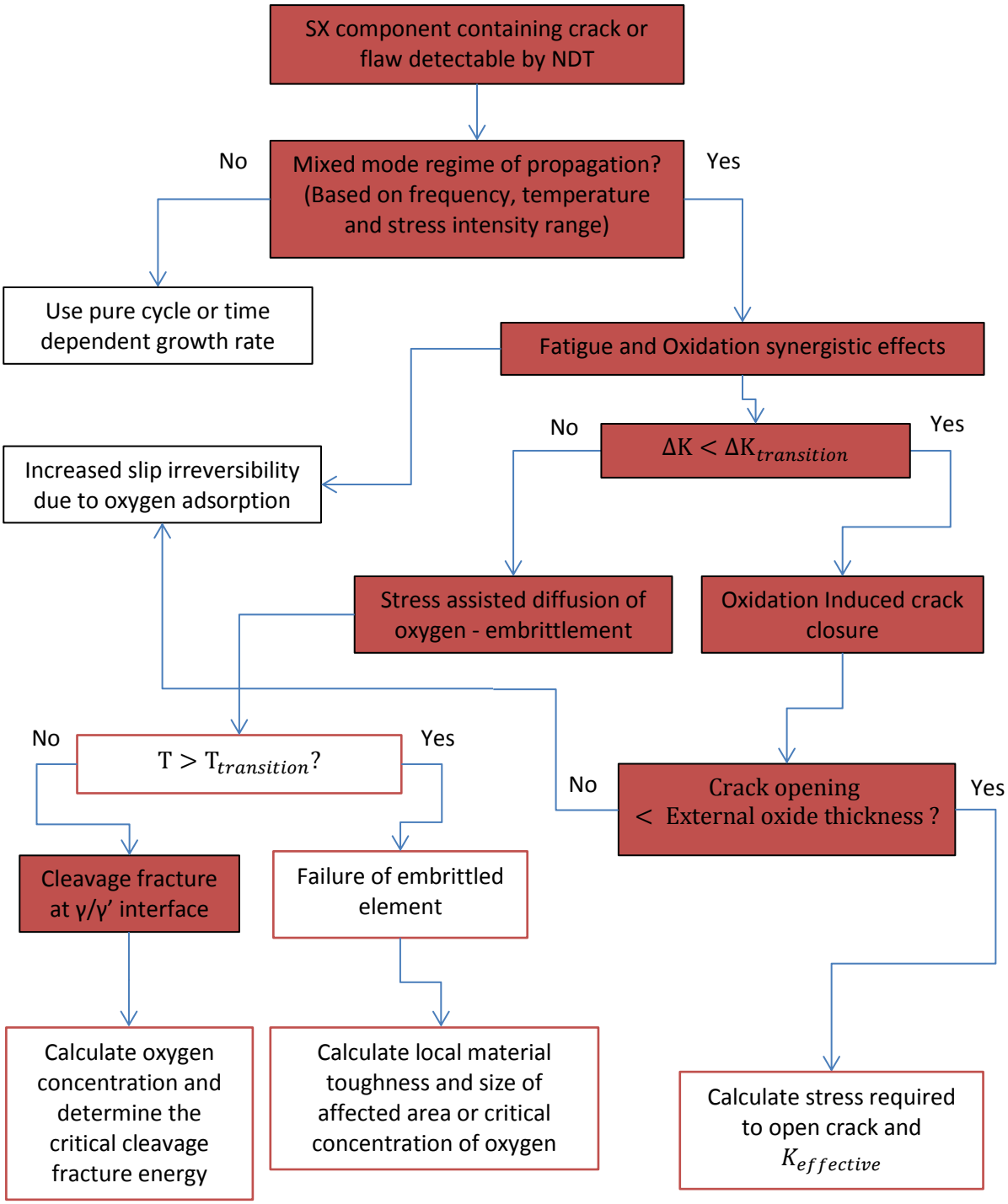

Figure 7.2: Proposed roadmap to inform current life assessment procedures and assist the development of future life assessment procedures of single crystal Ni-based superalloy turbine blade materials.

Chapter 8 Conclusions

Single crystal Ni-based superalloys are extensively used for the manufacturing of turbine blades components for use in the power generation industry. There is a drive towards reducing the conservatism in the life assessment procedures currently in place, to optimise maintenance intervals and avoid costly outages. However the complexity and the synergies between the damage processes that take place during operation make this an ongoing problem. To date there has been little focus on the combined effects of failure processes at moderate temperatures. This work has aimed to address these issues by experimentally investigating the damage micro-mechanisms that synergistically take place during fatigue – oxidation conditions in typical turbine blade materials.

The materials investigated in this study were the single crystalline Ni-based superalloys CMSX-4 and MD-2. Particular focus has been given to CMSX-4 as it is of most immediate interest to the industrial partners. Both CMSX-4 and MD-2 exhibit the typical, cuboidal γ/γ' microstructure with similar volume fraction of γ' (>70%). Interdendritic porosity is a common casting defect in both alloy microstructures and was found to be (0.205%) in CMSX-4 and (0.12%) in MD-2. The reduced amount of porosity observed in MD-2 was attributed to the physical presence of interdendritic carbides which also congregate within the interdendritic areas and have a volume fraction of (0.2%).

Isothermal oxidation tests were conducted on samples of both alloys at 450°C and 550°C. The slower reaction kinetics observed in MD-2 were attributed to the higher amounts of Cr which also promote the formation of internal Al-oxides. The overall isothermal oxidation mechanism at intermediate temperatures that can describe the behaviour of either alloy can be outlined as follows. First, the clean alloy surface comes into contact with oxygen and oxide clusters begin to form. Due to the high concentration of Ni, the γ matrix begins to form porous NiO surface protrusions. At the same time, a transition alumina forms over the γ' phase and internally within a Ni depleted zone. Since the scale is not yet protective, oxygen anions continue to diffuse into the alloy preferentially through the γ/γ' interface. Then, oxygen comes in contact with the γ' phase which contains higher levels of Al (which in thermodynamic terms is expected to oxidise preferentially). This then leads to the preferential oxidation of the γ' particles internally while the γ matrix remains relatively unaffected.

The presence of interdendritic (Ta, W) carbides in MD-2 was found to be detrimental to surface integrity during prolonged exposure. Isothermal oxidation of (Ta, W) carbides occurs readily in MD-2 at 550°C and form surface eruptions causing oxide decohesion. As a result of volume expansion due to high temperatures and in conjunction with the different thermal expansion coefficient of the substrate, significant plastic deformation and cracking takes place subsurface in the vicinity of the carbide. Such processes can contribute towards fatigue crack initiation by promoting stress concentrations and exposing substrate material to high temperatures.

In service conditions, turbine blade material experiences the combined effects of oxidation and stress. To examine this interaction, sustained load tests were conducted on CMSX-4 samples at 550°C. The external tensile loads resulted in thicker oxide scales (bulging morphology) with deeper oxidation affected zones when the associated strains caused plastic deformation. This is likely to be the result of increased dislocation densities near the surface and slip band formation that provided additional routes for oxygen penetration and diffusion of species.

The fatigue lives of notched CMSX-4 components at 450°C and 550°C are greater in air than in vacuum. At these temperatures oxidation does not degrade the surface of the material enough to cause initiation, rather it acts as a retardation mechanism to surface initiation processes by plugging porosity and interfering with the resulting strain levels. Pre-oxidised (stressed) samples exhibit even longer fatigue lives due to the increased amounts of oxidation promoted by the aforementioned mechanism. However, these processes are only confined within a range of intermediate temperatures and are particularly influential at the lower strain ranges.

The size and location of pores relative to the surface of the sample produced significant scatter in the fatigue lives obtained. This scatter is more evident in the case of notch geometries as the smaller strained volume increases the effect of localised sampling of the defect population. As stated earlier, plastic strains induced by the notch geometry substantially affects the oxidation rate (which is also a controlling factor for subsurface initiation). Porosity and the subsequent increased scatter are therefore inherent features of the service condition and need to be considered in lifing approaches.

Fatigue crack propagation at lower temperatures and lower oxygen partial pressures (as well as in the plane stress state at the specimen sides), generally promote a Stage I crack growth which is intrinsically faster than Stage II. The formation of large side facets during macroscopic Stage I growth (and the crack history in general) result in less predictable FCG rates and significant sample to sample variability. Stage II crack growth is promoted by lower ΔK levels and higher temperatures.

During dwell fatigue crack propagation at intermediate temperatures several competing mechanisms contribute synergistically to damage. Cracks forming under long dwell fatigue conditions have a complex morphology and form several sub-branches that result in rougher fracture surfaces. Crystallographic slip damage by γ' shearing is still active at these moderate temperatures but at the same time thermally activated processes that promote propagation through the γ channels also take place. In addition, the effects of oxidation are two-fold. Even though the temperature is not high enough to cause embrittlement of a microstructural element ahead of the crack tip, finger like intrusions were found to penetrate the material ahead of the crack tip. The kinetics of such a mechanism are accentuated by the plastic strains at the crack tip, which given enough time can promote cleavage fracture at the γ/γ' interface. The rate of oxide formation on the crack tip surfaces is high enough to form thick oxides that bridge the crack tip opening and reduce the effective driving force.

Chapter 9 Future work

9.1 Additional mechanical testing

The results of the frequency scan test (Figure 6.8 and Figure 6.9) and block tests (Figure 6.12) of Chapter 6 were contradictory. Even though these finding were discussed in detail, it is suggested that additional frequency scan tests at higher ΔK levels (e.g. 30MPa√m and 40 MPa√m) would help identify the parameters that affect the damage mechanism and cause transitions between fracture modes.

In addition, long dwell fatigue tests with hold times that promote time dependent processes should be carried out in both air and vacuum. This will not only allow for quantification of the oxidation damage per cycle but will also elucidate the extent of the beneficial effects of oxidation on the FCG rate. It should be noted that, during this work several attempts have been made to conduct such experiments. However, servo-hydraulic machines struggle to maintain waveforms that include prolonged hold times followed by steep ramps such as the trapezoidal waveform used here (i.e. 1s-300s - 1s -1s). In all of these tests, as time progressed, the actuator applying the load became less responsive, resulting in repeated overloads and more severe dwell instability. It is therefore suggested that such tests should be conducted on electromechanical systems.

9.2 Thermal cyclic oxidation

The isothermal oxidation behaviour of CMSX-4 and MD-2 was investigated in Chapter 4. However, data obtained from isothermal exposures only tell part of the story since under gas turbine service conditions, the components are subjected to thermal cycling. With the help of a project student, during this work nine additional samples were used for thermal cyclic oxidation. Testing was conducted on samples identical to the ones used for isothermal exposures (section 4.2.2) by operating at heat cycles of varying duration and dwell reaching a peak temperature of 550°C. Table 9.1 shows the details of the oxidation testing undergone by each sample in terms of number of cycles, time at peak temperature and total duration of exposure. Similarly to the isothermal samples, these samples were left to cool for 10-15min before being placed into a desiccator until they were replaced in the furnace for the subsequent cycle. Scale thickness

evaluation, spallation data and surface EDS analysis has already been completed but additional experimental work is required to provide meaningful results.

Sample No.	Dwell (hrs)	Number of cycles	Total time (hrs)
1	4	10	40
2	4	20	80
3	4	30	120
4	8	5	40
5	8	10	80
6	8	15	120
7	16	5	80
8	16	10	160
9	16	20	320

Table 9.1: Test summary of samples which have undergone thermal cyclic oxidation

9.3 Sustained load oxidation

Preliminary results and discussion on the effects of externally applied loads on oxidation have been presented in section 4.3.6 above. Additional analysis of the results, especially in terms of quantification is planned. EDX analysis within the elastically deformed regions will be conducted to investigate potential modification in the nature of the scale induced by the externally applied tensile loads. Image analysis will be employed to provide quantitative thickness measurements and statistical information on pits.

Additional testing to investigate the synergistic effects of load and exposure is currently ongoing. A sample has already been exposed for 160h (Figure 9.1) under the same loading conditions as the 70h test but the results have not been analysed yet.

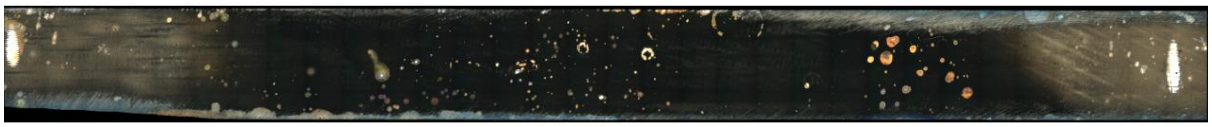

Figure 9.1: Optical microscopy imaging of the top (tensile) surface of a CMSX-4 sample oxidised under a bending load for 160h at 550ºC

In multicomponent systems such as the ones investigated here oxidation processes are complex and using the conventional and available characterisation techniques to understand these mechanisms is

very challenging. Thermodynamic calculations used in section 4.4.3, were found to be a powerful tool that can provide insight into the sequence of oxides forming and the consequences on the stability of the phases in the superalloy substrate. One of the limitations in the calculations of this work was that only the stable oxide phases were simulated. The possibility of further thermodynamic simulations that consider the oxide layer sequence in the transient and stable oxidation regimes separately should be examined as the results would be more applicable to dwell fatigue conditions. In a similar manner, incorporation of the effects of externally applied loads on the oxidation behaviour at various temperatures should provide more service relevant data.

9.4 Defect characterisation and effects on local stress strain distribution

The importance of incorporating defect data into life prediction models for nickel based single crystal superalloys was recently recognised by Remy et al. [117] who developed a unified model that uses pore statistics to assess micro-crack growth. The effect was incorporated into the model by assuming that pores can be treated as circular cracks of equivalent area. However, geometrical characteristics for the porosity were obtained through 2D metallographic sections from a single crystal rod. In order to fully comprehend porosity effects in engineering components such quantification, ideally, needs to include 3 dimensional analyses as well as understanding of the geometrical changes under an applied stimulus with time. X-Ray CT is a quantification technique that seems to provide these advantages and has been previously used to address this in Al or other light alloys [235–238].

The results of section 3.3.1 showed that micro X-Ray CT can be successfully employed to characterise porosity and carbide distributions in SX Ni-based superalloy systems. The downside of this technique is that in order to optimise resolution the sample size should be minimised. This is to allow sufficient amount of X-Rays to propagate through the material and provide adequate contrast with minimal noise.

It was shown in Chapter 6 that high temperature air tests initiate fatigue cracks predominantly from subsurface porosity. It is therefore desirable to be able to systematically characterise such subsurface defects and identify detrimental characteristics. Specifically, it would be beneficial to understand how porosity geometries, orientation and location affects stress concentrations that eventually lead to the initiation of cracks.

As shown in section 5.3.3, initiating pores can be easily identified post-fracture using an SEM. With this in mind, a methodology was developed with which the 3D morphology of the initiating pore can be reconstructed and analysed. The procedure involves four major steps as illustrated in

Figure 9.2. The first step involves use of the Alicona MeX software which allows the conversion of SEM stereoscopic images into a full 3D data set. To produce the 3D topology map the software requires three stereo images of the initiating feature. The three images should be captured by tilting the stage eucentrically at -5°, 0° and +5° and maintaining the same working distance and magnification. In the MeX software the images are superimposed and a 3D dataset is generated. An example of a topological map obtain using this method is shown in Figure 9.3 for the initiating pore of Figure 5.11b described in section 5.3.3. In the example of Figure 9.3 the 3D topology maps of both fracture surfaces are shown. The (x,y,z) coordinates of all points on the 3D surface were then exported and processed in Matlab to create a stack of binary 2D slices. A second Matlab script converted the 2D slices into an extruded volume which was saved as .raw file for processing in Avizo. A semi-automated process was then followed consisting of manual selection of the pore edges (on all three planes) and allowing the software to detect the edges of the next few slices. The pore segmentation process is shown in Figure 9.4. The selection was saved as a separate .raw file (consisting of 2D slices of the half pore itself). Following this, the two half pore volumes (segmented from the two fracture surfaces) were combined in VgStudio and fused into a single .raw file. Using ImageJ, the pore volume was concatenated with white images to create a solid block of volume that contained the pore. The solid volume and the pore surface were then meshed in ScanIP and the results are shown in Figure 9.5. The meshed volume is shown on the two planes that correspond to the fractured pore on each of the fracture surfaces of the sample.

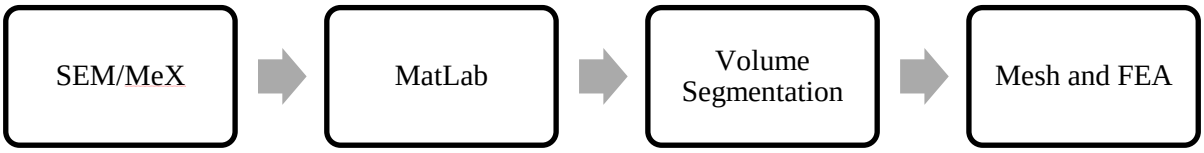

Figure 9.2: Summrised procedure for extracting and analyising porosity information from fracture surfaces.

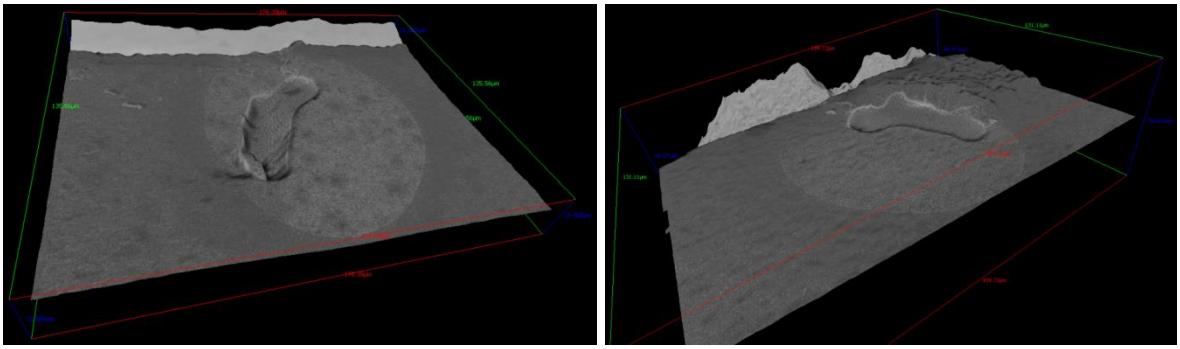

Figure 9.3: 3D topology map of the initiaitng pore shown in Figure 5.11b, created using the MeX software in conjuction with the SEM.

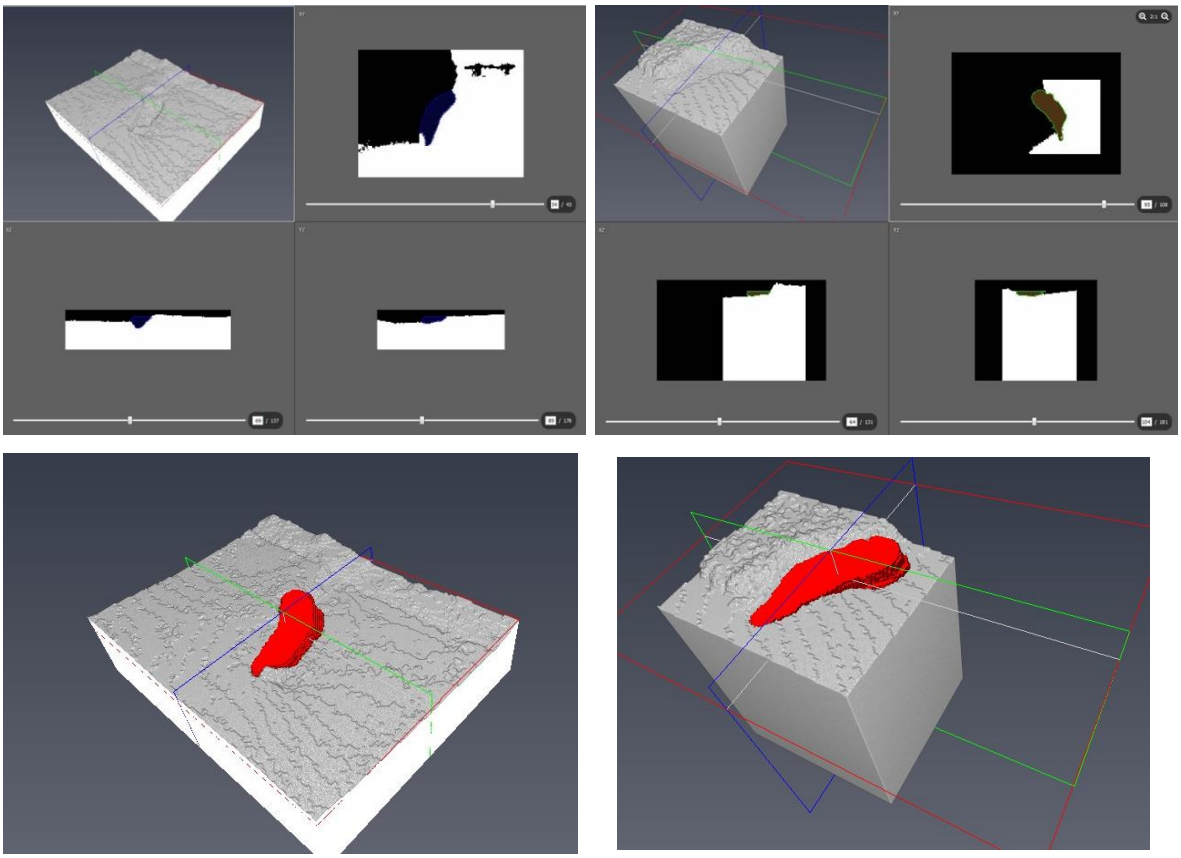

Figure 9.4: Pore volume segmentation from the two fracture surfaces of a fatigued sample using the Avizo software.

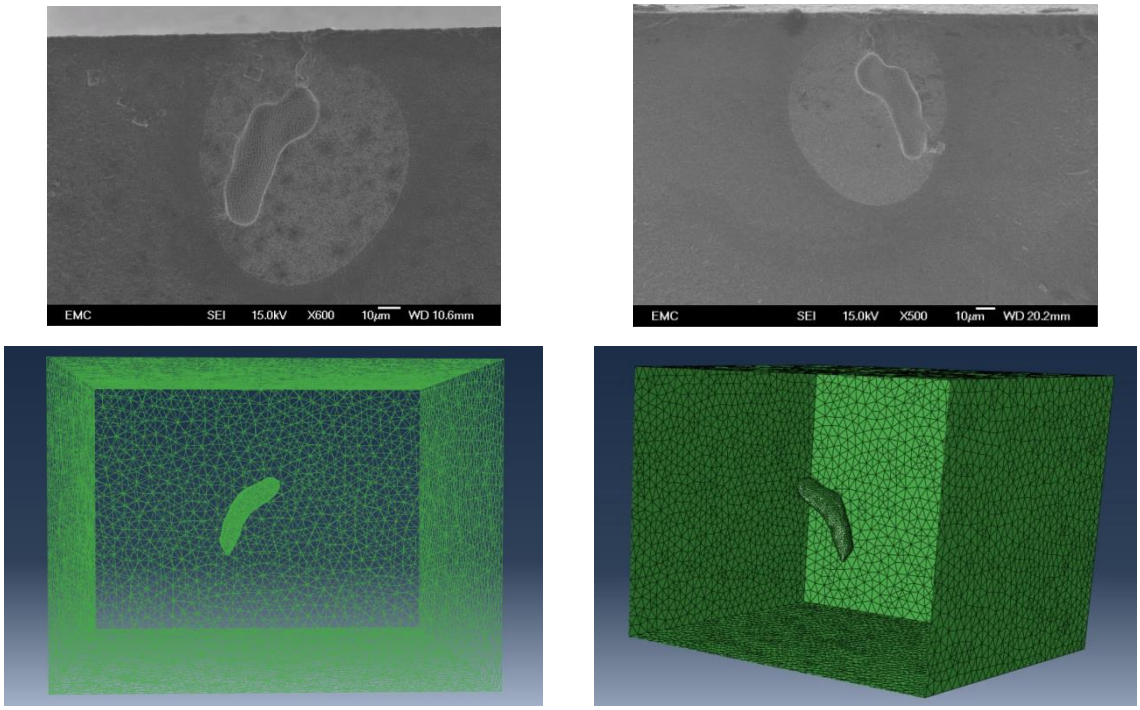

Figure 9.5: Meshed segmented porosity shown against the equivalent SEM images.

Appendix A – MatLab script for oxide thickness measurements

```
clear all

% Add scale 1px = ?um

scale=0.019047619047619;


I=imread('FILENAME.tif');

[height, width]=size(I);

table=zeros(width,2);

count=0;


for j=1:width

count=0;

for i=1:height

   if I(i,j)==0

   count=count+1;

   end

end

table(j,1)=j*scale;

table(j,2)=count*scale;

end


mean=mean(table(:,2));

sd=std(table(:,2));

area=sum(table(:,2))*scale;
```

Appendix B – DCPD & Noise Removal

Measurement of the crack growth rate during the experimental work was achieved using the Direct Current Potential Drop (DCPD) method. This technique has been used extensively for many years and it is validated by ASTM as an appropriate method to characterise the propagation of defects in metals [239]. The principle behind this method is that a constant current is passed through the specimen with the aid of two electrodes while a second pair, overlapping the crack, is used to measure the potential difference. An additional set of probes (reference probes) were spot welded away from the notch at the far left and right ends of the specimen. Readings from the reference probes were used to normalise the PD trace (by dividing the notch PD with the reference PD), in order to minimise problems associated with thermo-electrical effects, lack of stability in supplying current and changes of temperature [239]. As the crack propagates in the material less conductive medium is left therefore the electrical resistance increases and in turn the potential difference between the two sides of the crack rises. The signal is then fed to a computer which generates the results in the form of a plot of potential difference against time. By monitoring the change in potential difference (V) and comparing it against a reference value (Vo) it can be converted to crack length to width ratio (a/W) measurements with the use of a calibration function. The method provides a continuous and non-destructive crack length measurement but at the same time it may lead to underestimations of the actual crack length, especially at high temperatures. This is because at any given time the potential difference detected may also be influenced by time-depended deformation (creep), structural changes and oxide scale formation along the cracked faces. As a consequence, the specimen geometry, the testing environment, the material properties as well as the integrity of the test set up need to be accounted for in order to obtain an accurate crack length measurement [240], [241].

As mentioned earlier, the raw voltage data were converted to $\frac{a}{w}$ through the following function.

$$\left(\frac{a}{W}\right) = A\left(\frac{V}{V_O}\right)^3 + B\left(\frac{V}{V_O}\right)^2 + C\left(\frac{V}{V_O}\right) + D$$

The values of coefficients A, B, C and D are dependent on the geometry of the sample and were taken from a previous calibration undertaken at the University of Southampton on a geometrically similar sample. The initial and final $\frac{a}{w}$ values obtained were then compared against measured $\frac{a}{w}$ values (obtained by physically measuring the fracture surface under a microscope) and through the means of linear interpolation a calibrated $\frac{a}{w}$ value was obtained at each point. At this stage a graph

of $\frac{a}{w_{calibrated}}$ vs. $\frac{V}{V_O}$ was plotted and a 3rd order polynomial was fitted to it. The equation of the polynomial gave the new, calibrated values for the A, B, C and D coefficients which were then used to recalculate $\frac{a}{w}$ and hence the crack length.

The simplest method to calculate the crack growth rate ($\frac{da}{dN}$) and the stress intensity factor range (ΔK) is the secant method. Using this method $\frac{da}{dN}$ was obtained by computing the slope between two adjacent crack lengths and elapsed cycles as illustrated below.

$$\frac{da(j)_{avg.}}{dN} = \frac{a_j - a_{j-1}}{N_j - N_{j-1}}$$

For the calculation of the corresponding ΔK values the average crack length over the increment of crack extension were required by the method to be used. Therefore, average $\frac{a}{w}$ values were used in the equation below to calculate the stress intensity factor function (Y) as given by the British Standards for SENB specimens [213].

$$Y = \frac{6 \times (\frac{a}{w})^{\frac{1}{2}}}{[(1 + 2\frac{a}{w}) \times (1 - \frac{a}{w})^{\frac{3}{2}}]} \times \left\{1.99 - (\frac{a}{w})(1 - \frac{a}{w}) \times \left[2.15 - 3.93\left(\frac{a}{w}\right) + 2.7\left(\frac{a}{w}\right)^2\right]\right\}$$

The stress intensity factor (K) was then calculated using the relationship below.

$$\Delta K = \frac{\Delta P}{B \times W^{1/2}} \times Y \times 10^{1.5}$$

However, the increased amount of noise in the $\frac{V}{V_O}$ vs. time data resulted in erroneous crack growth rate results. Hence a number of noise reduction approaches, applied to the original $\frac{V}{V_O}$ vs. time data were compared. The three noise reduction methods were:

1. The running average of a sampling proportion of 0.1 - 0.3 was obtained for the $\frac{V}{V_O}$ vs. time data.
2. The Loess smoothing function was applied to all the data using sampling proportions of 0.1 - 0.3 and typically a second degree polynomial.
3. The data were divided into segments of equal size and the Loess smoothing function was applied to each one with a second degree polynomial but different sampling proportion.

The secant method was applied to the smoothed data produce by each technique and the resulting $\frac{da}{dN}$ vs ΔK were plotted and compared.

Appendix C – Chamber flush with N_2

In order to achieve a lower oxygen partial pressure within the vacuum chamber the process shown below was followed:

1) Chamber evacuation with rotor pump

Vacuum achieved $\approx 50mbar$

2) Chamber filled with Nitrogen

Total pressure in chamber rises to 1000mbar

∴ *Total pressure* = $P_{air} + P_{N_2\,in}$ =1000mbar

$P_{N_2\,in} = 1000 - 50 = 950mbar$

(P_{air} = 50mbar)

$Ratio(\frac{P_{N_2\,in}}{P_{air}}) = 19$

4) Chamber re-evacuation

Total pressure drops to $50mbar$

Assuming that the air pressure and the Nitrogen partial pressure will be reduced by the above ratio and no leakage takes place:

Final $P_{air} \approx \frac{1}{20} \times 50$

5) Repeat steps 1 – 4

The ratio of N_2 to air is calculated at the end of each cycle and the new P_{air} is calculated based on this value assuming perfect mixing.

When all cycles are completed the oxygen partial pressure is taken as 20% of the P_{air}

References

[1] M. Yuri, J. Masada, K. Tsukagoshi, E. Ito, S. Hada, Development of 1600°C-Class High-efficiency Gas Turbine for Power Generation Applying J-Type Technology, Mitsubishi Heavy Ind. Tech. Rev. 50 (2013).

[2] R.C. Reed., The superalloys : fundamentals and applications, Cambridge University Press, 2007.

[3] H.E. Evans, Stress effects in high temperature oxidation of metals, Int. Mater. Rev. 40 (1995) 1–40.

[4] Department of Energy and Climate Change, Government announces plans to close coal power stations by 2025 - GOV.UK, (2015). https://www.gov.uk/government/news/government-announces-plans-to-close-coal-power-stations-by-2025.

[5] S. Suresh, Fatigue of Materials, 2nd ed., Cambridge University Press, 1998.

[6] D. Kopeliovichi, Fatigue (Substances & Technology), (2014). http://www.substech.com/dokuwiki/doku.php?id=fatigue (accessed December 2, 2015).

[7] A.A. Griffith, The Phenomena of Rupture and Flow in Solids, Philos. Trans. R. Soc. A Math. Phys. Eng. Sci. 221 (1921) 163–198. doi:10.1098/rsta.1921.0006.

[8] E. Orowan, Fundamentals of brittle behaviour of metals, in: W.M. Murray (Ed.), Fatigue Fract. Met., 1952: pp. 139–167.

[9] M. Miller, Fatigue Life Prediction of Nickel Base Superalloys, University of Southampton, 2007.

[10] A. Borgoltz, W.J. Devenport, Fracture Toughness Testing (ESM Laboratory Course Notes), (2015). http://www.dept.aoe.vt.edu/~aborgolt/aoe3054/manual/expt5/.

[11] U. Krupp, Fatigue Crack Propagation in Metals and Alloys, (2007).

[12] B. Matej, Cyclic deformation and fatigue of metals, 1993.

[13] T. Broom, R.K. Ham, The Hardening and Softening of Metals by Cyclic Stressing, Proc. R. Soc. Lond. A. Math. Phys. Sci. 242 (n.d.) 166–179. doi:10.2307/100302.

[14] T.S. Srivatsan, Fatigue of Materials II: Advances and Emergence in Understandng, John Wiley & Sons, Inc., New Jersey, 2012.

[15] C.A. Yablinsky, K.M. Flores, M.J. Mills, J.C. Williams, J. Rigney, Fatigue behaviour in monocrystalline Ni-based superalloys for blade applications, Superalloys 2008. (2008) 535–540.

[16] M.H. El Haddad, N.E. Dowling, T.H. Topper, K.N. Smith, J integral applications for short fatigue cracks at notches, Int. J. Fract. 16 (1980) 15–30. doi:10.1007/BF00042383.

[17] D. Taylor, Fatigue of short cracks: the limitations of fracture mechanics, in: Behav. Short Fatigue Cracks, London, 1986: pp. 479–490.

[18] R.M.J. Kemp, Fatigue crack closure - A review, 1990.

[19] C.T. Sims, The superalloys, New York, 1972.

[20] P.Y. Hou, Shreir's Corrosion, in: Shreir's Corros., Elsevier, 2010: pp. 195–239. doi:10.1016/B978-044452787-5.00013-5.

[21] P. Kofstad, High temperature oxidationof metals, John Wiley & Sons, Inc., 1966.

[22] A. Sato, Y.L. Chiu, R.C. Reed, Oxidation of nickel-based single-crystal superalloys for industrial gas turbine applications, Acta Mater. 59 (2011) 225–240. doi:10.1016/j.actamat.2010.09.027.

[23] A. Akhtar, S. Hegde, R.C. Reed, The oxidation of single-crystal nickel-based superalloys, Jom. 58 (2006) 37–42. doi:10.1007/s11837-006-0066-0.

[24] The Ellingham diagram - DoITPoMS, (n.d.). http://www.doitpoms.ac.uk/tlplib/ellingham_diagrams/ellingham.php (accessed September 17, 2014).

[25] A. Oropesa, G.L. Drew, M.C. Hardy, A.J. Leggett, J.R. Nicholls, N.J. Simms, Effects of oxidation and hot corrosion in a nickel disc alloy, Superalloys 2004 (Tenth Int. Symp. (2008) 609–618.

[26] K. Kawagishi, H. Harada, A. Sato, A. Sato, T. Kobayashi, The oxidation properties of fourth generation single-crystal nickel-based superalloys, JOM. 58 (2006) 43–46. doi:10.1007/s11837-006-0067-z.

[27] M. Gobel, A. Rahmel, M. Sehiitzet, The Isothermal-Oxidation Behavior of Several Nickel-Base Single-Crystal Superalloys with and Without Coatings, Oxid. Met. 39 (1993) 231–261.

[28] N. Birks, G.H. Meier, F.S. Pettit, Introduction to the High Temperature Oxidation of Metals | Materials Science | Cambridge University Press, 2009.

[29] J. Stringer, The Importance of Short-Circuit and Related Transport Processes in High-Temperature Oxidation, in: M.S. Seltzer, R.I. Jaffee (Eds.), Defects Transp. Oxides, Springer US, Boston, MA, 1974: pp. 495–517. doi:10.1007/978-1-4615-8723-1.

[30] H.E. Evans, G.P. Mitchell, R.C. Lobb, D.R.J. Owen, A Numerical Analysis of Oxide Spallation, Proc. Math. Phys. Sci. 440 (1993) 1–22.

[31] D.L. Douglass, Exfoliation and the Mechanical Behavior of Scales, (1971).

[32] C.M. Younes, G.C. Allen, J.A. Nicholson, High temperature oxidation behaviour of single crystal superalloys RR3000 and CMSX-4, Corros. Eng. Sci. Technol. 42 (2007) 80–88. doi:10.1179/174327807X159925.

[33] D. Young, High Temperature Oxidation and Corrosion of Metals, 1st ed., 2008.

[34] C.T. Sims, A History of superalloy metallurgy for superalloy metallurgists, New York, 1984.

[35] R. Bowman, Superalloys: A Primer and History, Miner. Met. Mater. Soc. (2000). http://www.tms.org/meetings/specialty/superalloys2000/superalloyshistory.html (accessed June 27, 2014).

[36] M. Durante-Charre, The microstructure of the superalloys, Amsterdam, 1997.

[37] W. Liu, D. Tang, Effect of cooling rate after solution on microstructure and creep properties of single crystal superalloy DD3, Rare Met. 30 (2011) 396–400. doi:10.1007/s12598-011-0311-8.

[38] P.M. Sarosi, M.K. Miller, D. Isheim, M.J. Mills, The Effects of Cooling Rate on the Microstructure of a Commercial Ni-based Superalloy Using Atom Probe Tomography, Microsc. Microanal. 13 (2007).

[39] T.M. Pollock, S. Tin, Nickel-Based Superalloys for Advanced Turbine Engines: Chemistry, Microstructure and Properties, J. Propuls. Power. 22 (2006) 361–374. doi:10.2514/1.18239.

[40] E. Cadel, D. Lemarchand, S. Chambreland, D. Blavette, Atom probe tomography

investigation of the microstructure of superalloys N18, Acta Mater. 50 (2002) 957–966. doi:10.1016/S1359-6454(01)00395-0.

[41] G. Blaine, L. Hugo, H. Xiao, Superalloys : Alloying and Performance, ASM International, Ohio, 2010.

[42] D. Hull, D.J. Bacon, Introduction to Dislocations, 5th ed., Butterworth-Heinemann, 2011.

[43] M.R. Ahmadi, E. Povoden-Karadeniz, K.I. Öksüz, A. Falahati, E. Kozeschnik, A model for precipitation strengthening in multi-particle systems, Comput. Mater. Sci. 91 (2014) 173–186. doi:10.1016/j.commatsci.2014.04.025.

[44] F. Pyczak, B. Devrient, H. Mughrabi1, The effects of different alloying elements on the thermal expansion coeefficients, lattice constants and misfit of nickel-based superalloys investigated by X-ray diffraction, Superalloys 2004. (n.d.) 827–836.

[45] V. Arunachalam, T. Bhat Balakeishna, Strengthening mechanisms in alloys, Proceeding Indian Acad. Sci. - Eng. Sci. 3 (1980) 275–296.

[46] W.I. Mitchell, No Title, Z.Metallkd. 57 (1966) 586–589.

[47] T. Murakumo, T. Kobayashi, Y. Koizumi, Creep behaviour of Ni-base single crystal superalloys with various γ' volume fractions, Acta Mater. 40 (1992) 1–30.

[48] S. Takeuchi, E. Kuramoto, Temperature and orientation dependence of the yield stress in Ni{in3}Ga single crystals, Acta Metall. 21 (1973) 415–425. doi:10.1016/0001-6160(73)90198-3.

[49] V. Paidar, D.. Pope, V. Vitek, A theory of the anomalous yield behavior in L12 ordered alloys, Acta Metall. 32 (1984) 435–448. doi:10.1016/0001-6160(84)90117-2.

[50] J.M. Donachie, J.S. Donachie, Superalloys : A Technical Guide, 2nd ed., ASM International, Materials Park, OH, USA, 2002.

[51] K.Y. Cheng, C.Y. Jo, D.H. Kim, T. Jin, Z.Q. Hu, Influence of local chemical segregation on the γ′ directional coarsening behavior in single crystal superalloy CMSX-4, Mater. Charact. 60 (2009) 210–218. doi:10.1016/j.matchar.2008.09.002.

[52] R.A. Stevens, P.E.J. Flewitt, The effects of γ′ precipitate coarsening during isothermal aging and creep of the nickel-base superalloy IN-738, Mater. Sci. Eng. 37 (1979) 237–247. doi:10.1016/0025-5416(79)90157-5.

[53] S.R. Hegde, R.M. Kearsey, J. Beddoes, Design of solutionizing heat treatment for an experimental single crystal superalloy, Superalloys 2008. (2008) 301–310.

[54] G.L. Erickson, K. Harris, Single crystal alloy technology, US4643782 A, 1987.

[55] A. Szczotok, B. Chmiela, Effect of Heat Treatment on Chemical Segregation in CMSX-4 Nickel-Base Superalloy, J. Mater. Eng. Perform. (2013). doi:10.1007/s11665-013-0843-1.

[56] J. Watson, Materials Science and Technologies : Superalloys : Production, Properties and Applications, Nova Science, 2011.

[57] R. Schafrik, R. Sprague, Saga of Gas Turbine Materials, Part I, Adv. Mater. Process. (ASM Int. 162 (2004).

[58] R.J. Sidall, Comparison of the Attributes of VIM + ESR and VlM+VAR Alloy718, Miner. Met. Mater. Soc. (1991).

[59] D.K. Melgaard, R.L. Williamson, J.J. Beaman, Controlling remelting processes for superalloys and aerospace Ti alloys, JOM. 50 (1998) 13–17. doi:10.1007/s11837-998-0372-9.

[60] F.I. Versnyder, M.E. Shank, The development of columnar grain and single crystal high

temperature materials through directional solidification, Mater. Sci. Eng. 6 (1970) 213–247. doi:10.1016/0025-5416(70)90050-9.

[61] Turbine Blade Alloys, NASA. (2012). http://www.grc.nasa.gov/WWW/StructuresMaterials/AdvMet/research/turbine_blades.html (accessed July 2, 2014).

[62] P. Caron, T. Khan, Evolution of Ni-based superalloys for single crystal gas turbine blade applications, Aerosp. Sci. Technol. 3 (1999) 513–523. doi:10.1016/S1270-9638(99)00108-X.

[63] D. Blavette, P. Caron, T. Khan, An atom probe investigation of the role of rhenium additions in improving creep resistance of Ni-base superalloys, Scr. Metall. 20 (1986) 1395–1400. doi:10.1016/0036-9748(86)90103-1.

[64] A.F. Giamei, D.L. Anton, Rhenium additions to a Ni-base superalloy: Effects on microstructure, Metall. Trans. A. 16 (1985) 1997–2005. doi:10.1007/BF02662400.

[65] G.L. Erickson, A new, third-generation, single-crystal, casting superalloy, JOM. 47 (1995) 36–39. doi:10.1007/BF03221147.

[66] H. Guo, Y. Cui, H. Peng, S. Gong, Improved cyclic oxidation resistance of electron beam physical vapor deposited nano-oxide dispersed β-NiAl coatings for Hf-containing superalloy, Corros. Sci. 52 (2010) 1440–1446. doi:10.1016/j.corsci.2010.01.009.

[67] R. Darolia, D. Labrman, R. Field, Formation of topologically closed packed phases in nickel based single crystal superalloys, Superalloys. (1988) 255–264.

[68] Y. Koizumi, T. Kobayashi, T. Yokokawa, J. Zhang, M. Osawa, H. Harada, Y. Aoki, M. Arai, DEVELOPMENT OF NEXT-GENERATION NI-BASE SINGLE CRYSTAL SUPERALLOYS, Superalloys. (2004) 35–43.

[69] A. Sato, H. Harada, A.-C. Yeh, K. Kawagishi, T. Kobayashi, Y. Koizumi, T. Yokokawa, J. Zhang, A 5th generation SC superalloy with balanced high temperature properties and processabilty, Superalloys (TMS-The Miner. Met. Mater. Soc. (2008) 131–138.

[70] Y. Yuan, K. Kawagishi, Y. Koizumi, T. Kobayashi, T. Yokokawa, H. Harada, Creep deformation of a sixth generation Ni-base single crystal superalloy at 800°C, Mater. Sci. Eng. A. 608 (2014) 95–100. doi:10.1016/j.msea.2014.04.069.

[71] K. Kawagishi, A.-C. Yeh, T. Yokokawa, T. Kobayashi, Y. Koizumi, H. Harada, Development of an Oxidation-Resistant High-Strength Sixth-Generation Single-Crystal Superalloy TMS-238, in: E.S. Huron, R.C. Reed, M.C. Hardy, M.J. Mills, R.E. Montero, P.D. Portella, J. Telesman (Eds.), Superalloys 2012, John Wiley & Sons, Inc., Hoboken, NJ, USA, 2012. doi:10.1002/9781118516430.

[72] Johnson Matthey PMM, Market data tables, (n.d.). http://www.platinum.matthey.com/services/market-research/market-data-tables (accessed December 1, 2015).

[73] D. Konitzer, S. Duclos, T. Rockstroh, Materials for sustainable turbine engine development, MRS Bull. 37 (2012) 383.

[74] L. Anthony, Rhenium Market Overview • MMTA, (2012). http://www.mmta.co.uk/rhenium-market-overview (accessed December 1, 2015).

[75] R.M. Kearsey, J.C. Beddoes, K.M. Jaansalu, W.T. Thompson, P. Au, The Effects of Re, W and Ru on Microsegregation Behaviour in Single Crystal Superalloy Systems, Superalloys 2004 (Tenth Int. Symp. (2004) 801–810. doi:10.7449/2004/Superalloys_2004_801_810.

[76] D. Ma, U. Grafe, Microsegregation in directionally solidified dendritic-cellular structure of superalloy CMSX-4, Mater. Sci. Eng. A. (1999) 339–342.

[77] J. Safari, S. Nategh, On the heat treatment of Rene-80 nickel-base superalloy, J. Mater. Process. Technol. 176 (2006) 240–250. doi:10.1016/j.jmatprotec.2006.03.165.

[78] K.L. Gasko, G.M. Janowski, B.J. Pletka, The influence of γ-γ′ eutectic on the mechanical properties of conventionally cast MAR-M247, Mater. Sci. Eng. A. 104 (1988) 1–8. doi:10.1016/0025-5416(88)90400-4.

[79] B.C. Wilson, J.A. Hickman, G.E. Fuchs, The effect of solution heat treatment on a single-crystal Ni-based superalloy, JOM. 55 (2003) 35–40. doi:10.1007/s11837-003-0158-z.

[80] M. Gobel, A. Rahmel, M. Schiitze, The Cyclic-Oxidation Behavior of Several Nickel-Base Single-Crystal Superalloys Without and with Coatings, Oxid. Met. 41 (1994).

[81] R. Janakiraman, G.H. Meier, F.S. Pettit, The Effect of Water Vapor on the Oxidation of Alloys that Develop Alumina Scales for Protection, Metall. Trans. A. 30 (1999) 2905–2913.

[82] X. Lu, S. Tian, X. Yu, C. Wang, Oxidation behavior of a single-crystal Ni-base superalloy in air at 900 and 1050 °C, Rare Met. 30 (2011) 439–442. doi:10.1007/s12598-011-0320-7.

[83] M.H. Li, X.F. Sun, J.G. Li, Z.Y. Zhang, T. Jin, H.R. Guan, Z.Q. Hu, Oxidation Behavior of a Single-Crystal Ni-Base Superalloy in Air . I : At 800 and 900 ° C, 59 (2003) 591–605.

[84] F.H. Yuan, E.H. Han, C.Y. Jo, T.F. Li, Z.Q. Hu, The Effect of Crystallographic Orientation on the Oxidation Behavior of a Single-Crystal Nickel-base Superalloy, Oxid. Met. 60 (2003) 211–224.

[85] M. Gell, D.J. Duquette, The Effects of Environment on the Elevated Temperature Fatigue Behavior of Nickel-Base Superalloy Single Crystals, Metall. Trans. 3 (1972).

[86] J.E. Croll, G.R. Wallwork, The high-temperature oxidation of iron-chromium-nickel alloys containing 0 - 30% chromium, Oxid. Met. 4 (1972) 121–140. doi:10.1007/BF00613088.

[87] D. Wufeng, Z. Tietao, L. Heli, L. Shangping, L. Peiying, Effects of Hafnium and Yttirium on the Oxidation-Resistence of Ni3Al/CrMoB Alloy, Rare Met. Mater. Eng. 37 (2008) 1549–1554. doi:10.1016/S1875-5372(09)60041-2.

[88] H.E. Evans, M.P. Taylor, Creep relaxation and the spallation of oxide layers, Surf. Coat. Technol. 95 (1997) 27–33.

[89] C. Monier, C. Bertrand, J.-P. Dallas, M.-F. Trichet, M. Cornet, P. Veyssiere, Transmission electron microscopy analysis of the early stages of damage in a γ/γ′ nickel-based alloy under low cycle fatigue, Mater. Sci. Eng. A. 188 (1994) 133–139. doi:10.1016/0921-5093(94)90364-6.

[90] D.W. MacLachlan, D.M. Knowels, Fatigue behaviour and lifing of two single crystal superalloys, Fatigue Fract. Eng. Mater. Struct. 24 (2001) 503–521.

[91] P. Lukas, K. Obrtlik, L. Kunz, J. Cadek, Fatigue and Creep of superalloy single crystal CMSX-4, Kov. Mater. 36 (1998) 205–212.

[92] T.P. Gabb, R.V. Miner, J. Gayda, The tensile and fatigue deformation structures in a single crystal Ni-base superalloy, Scr. Metall. 20 (1986) 513–518. doi:10.1016/0036-9748(86)90245-0.

[93] U. Glatzel, M. Feller-Kniepmeier, Microstructure and dislocation configurations in fatigued [001] specimens of the nickel-based superalloy CMSX-6, Scr. Metall. Mater. 25 (1991) 1845–1850. doi:10.1016/0956-716X(91)90315-R.

[94] C.M. Whan, C.M.F. Rae, Parsons 2003, engineering issues in turbine machinery, power plant and renewables:, in: Proc. Sixth Int. Charles Parsons Turbine Conf. 16-18, Maney, London, 2003: pp. 789–801.

[95] C.M. Charles, G.A. Drew, S. Bagnall, C.M.F. Rae, Dislocation Deformation Mechanisms

during Fatigue of the Nickel-Based Superalloy CMSX-4, in: Mater. Sci. Forum, 2007: pp. 1211–1218.

[96] H.U. Hong, B.G. Choi, I.S. Kim, Y.S. Yoo, C.Y. Jo, Characterization of deformation mechanisms during low cycle fatigue of a single crystal nickel-based superalloy, (2011) 5245–5251. doi:10.1007/s10853-011-5462-3.

[97] M.D. Miller, P.A.S. Reed, M.R. Joyce, M.B. Henderson, J.W. Brooks, I. Wilcock, X. Wu, Effect of environment on notch fatigue behaviour in CMSX 4, Mater. Sci. Technol. 23 (2007) 1439–1445. doi:10.1179/174328407X213198.

[98] M.R. Joyce, X. Wu, P. a. S. Reed, The effect of environment and orientation on fatigue crack growth behaviour of CMSX-4 nickel base single crystal at 650 °C, Mater. Lett. 58 (2004) 99–103. doi:10.1016/S0167-577X(03)00423-3.

[99] F. Schubert, P.J. Ennis, T. Rieck, The Growth of Small Cracks in the Single Crystal Superalloy CMSX-4 at 750 and 1000°C, in: Superalloys 2008, Juelich, 2008.

[100] A. Sengupta, S.K. Putatunda, M. Balogh, Fatigue Crack Growth Behavior of a New Single Crystal Nickel-Based Superalloy (CMSX-4) at 650C, (1994) 540–550.

[101] G.R. Leverant, M. Gell, The influence of temperature and cyclic frequency on the fatigue fracture of cube oriented nickel-base superalloy single crystals, Metall. Trans. A. 6 (1975) 367–371. doi:10.1007/BF02667291.

[102] S. Muller, J. Rosier, C. Sommer, W. Hartnagel, The Influence of Load Ratio , Temperature , Orientation and Hold Time on the Fatigue Crack Growth of CMSX-4, in: Superalloys 2000, 2000: pp. 347–356.

[103] G. Onofrio, G.. Osinkolu, M. Marchioni, Fatigue crack growth of UDIMET 720 Li superalloy at elevated temperature, Int. J. Fatigue. 23 (2001) 887–895. doi:10.1016/S0142-1123(01)00053-6.

[104] A. Sengupta, S.K. Putatunda, Kinetics of γ' precipitation and its influence on fatigue crack growth behavior of a new single-crystal nickel- based superalloy (cmsx-4g) at room temperature, J. Mater. Eng. Perform. 2 (1993) 57–68. doi:10.1007/BF02649675.

[105] W. Schneider, J. Hammer, H. Mughrabi, Creep deformation and rupture behaviour of the monocrystalline superalloy CMSX4 - A comparison with the alloys SRR 99., Superalloys 1992. 26 (1992).

[106] V. Sass, U. Glatzel, M. Feller-Kniepmeier, Anisotropic creep properties of the nickel-base superalloy CMSX-4, Acta Mater. 44 (1996) 1967–1977. doi:10.1016/1359-6454(95)00315-0.

[107] N. Matan, D.C. Cox, P. Carter, M.A. Rist, C.M.F. Rae, R.C. Reed, Creep of CMSX-4 superalloy single crystals: effects of misorientation and temperature, Acta Mater. 47 (1999) 1549–1563. doi:10.1016/S1359-6454(99)00029-4.

[108] R.. Reed, N. Matan, D.. Cox, M.. Rist, C.M.. Rae, Creep of CMSX-4 superalloy single crystals: effects of rafting at high temperature, Acta Mater. 47 (1999) 3367–3381. doi:10.1016/S1359-6454(99)00217-7.

[109] C.M.F. Rae, M.A. Rist, D.C. Cox, R.C. Reed, N. Matan, On the primary creep of CMSX-4 superalloy single crystals, Metall. Mater. Trans. A. 31 (2000) 2219–2228. doi:10.1007/s11661-000-0139-6.

[110] H.J. Penkalla, F. Schubert, Dislocation Mechanisms Controlling the Deformation of CMSX-4 Single Crystals, in: ECCC Creep Conf., 2005.

[111] M.P. Miller, D.L. McDowell, R.L.T. Oehmke, A Creep-Fatigue-Oxidation Microcrack Propagation Model for Thermomechanical Fatigue, J. Eng. Mater. Technol. 114 (1992) 282.

doi:10.1115/1.2904174.

[112] M. Dedekind, L. Harris, Evaluation of premature failure of a gas turbine component, Int. J. Press. Vessel. Pip. 66 (1996) 59–76.

[113] J. Reuchet, L. Remy, Fatigue oxidation interaction in a superalloy—application to life prediction in high temperature low cycle fatigue, Metall. Trans. A. 14 (1983) 141–149. doi:10.1007/BF02643747.

[114] P.R. Wei, Z. Huang, Influence of dwell time on fatigue crack growth in nickel-base superalloys, Mater. Sci. Eng. A. 336 (2002) 209–214. doi:10.1016/S0921-5093(01)01957-8.

[115] E. Fleury, L. Rémy, Low cycle fatigue damage in nickel-base superalloy single crystals at elevated temperature, Mater. Sci. Eng. A. 167 (1993) 23–30. doi:10.1016/0921-5093(93)90332-9.

[116] L. Remy, A. Alam, N. Haddar, A. Koster, N. Marchal, Growth of small cracks and prediction of lifetime in high-temperature alloys, Mater. Sci. Eng. A. 468–470 (2007) 40–50. doi:10.1016/J.MSEA.2006.08.133.

[117] L. Rémy, M. Geuffrard, A. Alam, A. Köster, E. Fleury, Effects of microstructure in high temperature fatigue: Lifetime to crack initiation of a single crystal superalloy in high temperature low cycle fatigue, Int. J. Fatigue. 57 (2013) 37–49. doi:10.1016/j.ijfatigue.2012.10.013.

[118] P.J. Cotterill, J.E. King, Role of oxides in fatigue crack propagation, Mater. Sci. Technol. 6 (1990) 19–31.

[119] A. Shyam, W.W. Milligan, A model for slip irreversibility, and its effect on the fatigue crack propagation threshold in a nickel-base superalloy, Acta Mater. 53 (2005) 835–844. doi:10.1016/j.actamat.2004.10.036.

[120] F. Rezai-Aria, L. Remy, An oxidation fatigue interaction damage model for thermal fatigue crack growth, Eng. Fract. Mech. 34 (1989) 283–294. doi:10.1016/0013-7944(89)90143-4.

[121] A. Karabela, L.G. Zhao, J. Tong, N.J. Simms, J.R. Nicholls, M.C. Hardy, Effects of cyclic stress and temperature on oxidation damage of a nickel-based superalloy, Mater. Sci. Eng. A. 528 (2011) 6194–6202. doi:10.1016/j.msea.2011.04.029.

[122] N. Marchal, S. Flouriot, S. Forest, L. Remy, Crack-tip stress–strain fields in single crystal nickel-base superalloys at high temperature under cyclic loading, Comput. Mater. Sci. 37 (2006) 42–50. doi:10.1016/j.commatsci.2005.12.014.

[123] J.M. Martínez-Esnaola, A. Martín-Meizoso, E.E. Affeldt, A. Bennett, M. Fuentes, High temperature fatigue in single crystal superalloys, Fatigue Fract. Eng. Mater. Struct. 20 (1997) 771–788.

[124] Q. Ding, Z. Shen, S. Xiang, H. Tian, J. Li, Z. Zhang, In-situ environmental TEM study of γ′-γ phase transformation induced by oxidation in a nickel-based single crystal superalloy, J. Alloys Compd. 651 (2015) 255–258. doi:10.1016/j.jallcom.2015.07.017.

[125] S. Sanyal, U. V. Waghmare, P.R. Subramanian, M.F.X. Gigliotti, First-principles understanding of environmental embrittlement of the Ni/Ni3Al interface, Scr. Mater. 63 (2010) 391–394. doi:10.1016/j.scriptamat.2010.04.033.

[126] I.M. Edmonds, H.E. Evans, C.N. Jones, R.W. Broomfield, Intermediate Temperature Internal Oxidation in Fourth Generation Ru-bearing Single-Crystal Nickel-base Superalloys, Oxid. Met. 69 (2008) 95–108. doi:10.1007/s11085-007-9085-7.

[127] I.M. Edmonds, H.E. Evans, C.N. Jones, The Role of the γ′ Precipitate Dispersion in Forming a Protective Scale on Ni-Based Superalloys at 750 °C, Oxid. Met. 73 (2009) 193–206. doi:10.1007/s11085-009-9173-y.

[128] Y. Kiyak, B. Fedelich, T. May, A. Pfennig, Simulation of crack growth under low cycle fatigue at high temperature in a single crystal superalloy, Eng. Fract. Mech. 75 (2008) 2418–2443. doi:10.1016/j.engfracmech.2007.08.002.

[129] M.M. Nagl, W.T. Evans, D.J. Hall, S.R.J. Saunders, An in situ investigation of the tensile failure of oxide scales, Oxid. Met. 42 (1994) 431–449. doi:10.1007/BF01046759.

[130] C. Bruns, M. Schütze, Investigation of the Mechanical Properties of Oxide Scales on Nickel and TiAl, Oxid. Met. 55 (2001) 35–68. doi:10.1023/A:1010321108212.

[131] M. Schutze, Mechanical properties of oxide scales, Oxid. Met. 44 (1995) 29–61. doi:10.1007/BF01046722.

[132] G.R. Anstis, P. Chantikul, B.R. Lawn, D.B. Marshall, A Critical Evaluation of Indentation Techniques for Measuring Fracture Toughness: I, Direct Crack Measurements, J. Am. Ceram. Soc. 64 (1981) 533–538. doi:10.1111/j.1151-2916.1981.tb10320.x.

[133] P. Chantikul, G.R. Anstis, B.R. Lawn, D.B. Marshall, A Critical Evaluation of Indentation Techniques for Measuring Fracture Toughness: II, Strength Method, J. Am. Ceram. Soc. 64 (1981) 539–543. doi:10.1111/j.1151-2916.1981.tb10321.x.

[134] G.D. Quinn, R.C. Bradt, On the Vickers Indentation Fracture Toughness Test, J. Am. Ceram. Soc. 90 (2007) 673–680. doi:10.1111/j.1551-2916.2006.01482.x.

[135] J.L. Bouvard, F. Gallerneau, P. Paulmier, J.L. Chaboche, A phenomenological model to predict the crack growth in single crystal superalloys at high temperature, Int. J. Fatigue. 38 (2012) 130–143.

[136] C.M. Corporation, CMSX-4, (n.d.). http://www.c-mgroup.com/spec_sheets/CMSX_4.htm (accessed July 10, 2014).

[137] J.R. Mihalisin, J. Corrigan, G.M. Gratti, R.G. Vogt, Casting of single crystal superalloy articles with reduced eutectic scale and grain recrystallization, 2002.

[138] E.R. Cutler, A.J. Wasson, G.E. Fuchs, Effect of minor alloying additions on the carbide morphology in a single crystal Ni-base superalloy, Scr. Mater. 58 (2008) 146–149. doi:10.1016/j.scriptamat.2007.09.050.

[139] G.L. Ding, S.N. Tewari, Dendritic morphologies of directionally solidified single crystals along different crystallographic orientations, 236 (2002) 420–428.

[140] U. Hemmersmeier, M. Feller-Kniepmeier, Element distribution in the macro- and microstructure of nickel base superalloy CMSX-4, Mater. Sci. Eng. A. 248 (1998) 87–97. doi:10.1016/S0921-5093(98)00516-4.

[141] E.C. Caldwell, F.J. Fela, G.E. Fuchs, The segregation of elements in high-refractory-content single-crystal nickel-based superalloys, JOM. 56 (2004) 44–48. doi:10.1007/s11837-004-0200-9.

[142] A.J. Wasson, G.E. Fuchs, The Effect of Carbide Morphologies on Elevated Temperature Tensile and Fatigue Behavior of a Modified Single Crystal Ni-Base Superalloy, in: Superalloys 2008, 2008: pp. 489–497.

[143] A. Sengupta, S.K. Putatunda, L. Bartosiewicz, J. Hangas, P.J. Nailos, M. Peputapeck, F.E. Alberts, Tensile behavior of a new single-crystal nickel-based superalloy (CMSX-4) at room and elevated temperatures, J. Mater. Eng. Perform. 3 (1994) 73–81. doi:10.1007/BF02654502.

[144] L. Wang, Y. Liu, X. Song, J. Jin, B. Zhang, Tensile Deformation Behavior of a Nickel-base Superalloy under Dynamic Loads, in: 13th Int. Conf. Fract., 2013: pp. 16–21.

[145] X. Zhang, T. Jin, N.R. Zhao, Z.H. Wang, X.F. Sun, H.R. Guan, Z.Q. Hu, Effect of strain

rate on the tensile behavior of a single crystal nickel-base superalloy, Mater. Sci. Eng. A. 492 (2008) 364–369. doi:10.1016/j.msea.2008.03.040.

[146] X. Zhang, P.R. Stoddart, J.D. Comins, A.G. Every, High-temperature elastic properties of a nickel-based superalloy studied by surface Brillouin scattering, J. Phys. Condens. Matter. 13 (2001) 2281–2294. doi:10.1088/0953-8984/13/10/320.

[147] D. Siebörger, H. Knake, U. Glatzel, Temperature dependence of the elastic moduli of the nickel-base superalloy CMSX-4 and its isolated phases, Mater. Sci. Eng. A. 298 (2001) 26–33. doi:10.1016/S0921-5093(00)01318-6.

[148] N. Tsuno, S. Shimabayashi, K. Kakehi, C.M.F. Rae, R.C. Reed, Tension/compression assymetry and yield and creep strengths of Ni-based superalloys, in: Superalloys 2008, 2008: pp. 433–442.

[149] M. Segersäll, J.J. Moverare, Crystallographic Orientation Influence on the Serrated Yielding Behavior of a Single-Crystal Superalloy, Materials (Basel). 6 (2013) 437–444.

[150] K.L. Bhagi, V. Ratogi, P. Gupta, A Brief Review on Failure of Turbine Blades, in: Proc. STME-2013 Smart Technol. Mech. Eng., Delhi, 2013.

[151] M.R. Khajavi, M.H. Shariat, Failure of first stage gas turbine blades, Eng. Fail. Anal. 11 (2004) 589–597. doi:10.1016/j.engfailanal.2003.08.010.

[152] C.U. Hardwicke, Y.-C. Lau, Advances in Thermal Spray Coatings for Gas Turbines and Energy Generation: A Review, J. Therm. Spray Technol. 22 (2013) 564–576. doi:10.1007/s11666-013-9904-0.

[153] V. Postolenko, Failure Mechanisms of Thermal Barrier Coatings for High Temperature Gas Turbine Components under Cyclic Thermal Loading, RWTH Aachen University, 2008.

[154] B.J. Foss, M.C. Hardy, D.J. Child, D.S. McPhail, B.A. Shollock, Oxidation of a Commercial Nickel-Based Superalloy under Static Loading, JOM. 66 (2014) 2516–2524. doi:10.1007/s11837-014-1196-4.

[155] C. Mathieu, S. Toesca, Effects of mode-I stresses on the oxidation and failure mechanisms of Ni-20Cr and Ni-15Cr-8Fe alloys in sulfur dioxide, Oxid. Met. 39 (1993) 155–165. doi:10.1007/BF00665609.

[156] E. Chateau, L. Rémy, Oxidation-assisted creep damage in a wrought nickel-based superalloy: Experiments and modelling, Mater. Sci. Eng. A. 527 (2010) 1655–1664. doi:10.1016/j.msea.2009.10.054.

[157] B.R. Barnard, P.K. Liaw, R.A. Buchanan, D.L. Klarstrom, Affects of applied stresses on the isothermal and cyclic high-temperature oxidation behavior of superalloys, Mater. Sci. Eng. A. 527 (2010) 3813–3821. doi:10.1016/j.msea.2010.03.050.

[158] S. Cruchley, H.Y. Li, H.E. Evans, P. Bowen, D.J. Child, M.C. Hardy, The role of oxidation damage in fatigue crack initiation of an advanced Ni-based superalloy, Int. J. Fatigue. 81 (2015) 265–274. doi:10.1016/j.ijfatigue.2015.08.016.

[159] R. Jiang, S. Everitt, N. Gao, K. Soady, J.W. Brooks, P.A.S. Reed, Influence of oxidation on fatigue crack initiation and propagation in turbine disc alloy N18, Int. J. Fatigue. 75 (2015) 89–99. doi:10.1016/j.ijfatigue.2015.02.007.

[160] T. Connolley, M.J. Starink, P.A.S. Reed, Effect of oxidation on high temperature fatigue crack initiation and short crack growth in Inconel 718, Superalloys 2000. 5 (2000) 435–444.

[161] R. Jiang, P.A.S. Reed, Critical assessment: oxygen-assisted fatigue crack propagation in turbine disc superalloys, Mater. Sci. Technol. 32 (2016) 401–406. doi:10.1080/02670836.2016.1148227.

[162] S. Everitt, R. Jiang, N. Gao, M.J. Starink, J.W. Brooks, P.A.S. Reed, Comparison of fatigue crack propagation behaviour in two gas turbine disc alloys under creep–fatigue conditions: evaluating microstructure, environment and temperature effects, Mater. Sci. Technol. 29 (2013) 781–787. doi:10.1179/1743284713Y.0000000229.

[163] R. Jiang, D.J. Bull, D. Proprentner, B. Shollock, P.A.S. Reed, Effects of oxygen-related damage on dwell-fatigue crack propagation in a P/M Ni-based superalloy: From 2D to 3D assessment, Int. J. Fatigue. 99 (2017) 175–186. doi:10.1016/j.ijfatigue.2017.03.003.

[164] I.M. Edmonds, H.E. Evans, C.N. Jones, The Role of the γ' Precipitate Dispersion in Forming a protective a Protective Scale on Ni-Based Superalloys at 750C.pdf, Oxid. Met. (2010).

[165] M.A. Khan, S. Sundarrajan, S. Natarajan, P. Parameswaran, E. Mohandas, Oxidation and Hot Corrosion Behavior of Nickel-Based Superalloy for Gas Turbine Applications, Mater. Manuf. Process. 29 (2014) 832–839. doi:10.1080/10426914.2014.901530.

[166] D.J. Gardinger, Developments in Raman spectroscopy and applications to oxidation studies, Microsc. Oxid. (1993).

[167] D.M. Lipkin, D.R. Clarke, M. Hollatz, M. Bobeth, W. Pompe, Stress development in alumina scales formed upon oxidation of (111) NiAl single crystals, Corros. Sci. 39 (1997) 231–242. doi:10.1016/S0010-938X(97)83344-6.

[168] E. Schumann, C. Sarioglu, J.R. Blachere, F.S. Pettit, G.H. Meier, High-Temperature Stress Measurements During the Oxidation of NiAl, Oxid. Met. 53 (2000) 259–272. doi:10.1023/A:1004585003083.

[169] J.H. Chen, P.M. Rogers, J.A. Little, Oxidation behavior of several chromia-forming commercial nickel-base superalloys, Oxid. Met. 47 (1997) 381–410. doi:10.1007/BF02134783.

[170] I.A. Kvernes, P. Kofstad, The oxidation behavior of some Ni-Cr-Al alloys at high temperatures, Metall. Trans. 3 (1972) 1511–1519. doi:10.1007/BF02643040.

[171] N. Hussain, K.A. Shahid, I.H. Khan, S. Rahman, Oxidation of high-temperature alloys (superalloys) at elevated temperatures in air: I, Oxid. Met. 41 (1994) 251–269. doi:10.1007/BF01080783.

[172] N.F. Mott, The theory of the formation of protective oxide films on metals, II, Trans. Faraday Soc. 35 (1940) 472. doi:10.1039/tf9403500472.

[173] Z. Liu, W. Gao, Oxidation Behavior of Cast Ni3Al Alloys and Microcrystalline Ni3Al + 5% Cr Coatings with and without Y Doping, Oxid. Met. 556 (2001) 481–504.

[174] G. Zeng, M. Li, J. Han, X. He, W. Li, Oxidation kinetics of microcrystalline Ni-11.5Cr-4.5Co-0.5Al superalloy sheet fabricated by Electron Beam Physical Vapor Deposition at 800°C, Mater. Lett. 62 (2007) 289–292. doi:10.1016/j.matlet.2007.05.036.

[175] Z.D. Xiang, S.R. Rose, P.K. Datta, Low-temperature formation and oxidation resistance of nickel aluminide/nickel hybrid coatings on alloy steels, Scr. Mater. 59 (2008) 99–102. doi:10.1016/j.scriptamat.2008.02.034.

[176] R.L. Amaro, S.D. Antolovich, R.W. Neu, P.M. Singh, High temperature oxidation and γ′ depletion in the single-crystal superalloy PWA 1484, Mater. High Temp. 33 (2016) 476–488. doi:10.1080/09603409.2016.1180276.

[177] U. Krupp, R. Orosz, H.J. Christ, U. Buschmann, W. Wiechert, Internal Nitridation during Creep Loading of Polycrystalline Ni-Base Superalloys, Mater. Sci. Forum. 461–464 (2004) 37–44. doi:10.4028/www.scientific.net/MSF.461-464.37.

[178] J. Unnam, R.N. Shenoy, R.K. Clark, Oxidation of commercial purity titanium, Oxid. Met.

26 (1986) 231–252. doi:10.1007/BF00659186.

[179] R. Haugsrud, On the high-temperature oxidation of nickel, Corros. Sci. 45 (2003) 211–235. doi:10.1016/S0010-938X(02)00085-9.

[180] S. Cruchley, H.E. Evans, M.P. Taylor, M.C. Hardy, S. Stekovic, Chromia layer growth on a Ni-based superalloy: Sub-parabolic kinetics and the role of titanium, Corros. Sci. 75 (2013) 58–66. doi:10.1016/j.corsci.2013.05.016.

[181] M.S.A. Karunaratne, D.C. Cox, P. Carter, R.C. Reed., Modelling of the microsegregation in CMSX-4 superalloy and its homogenisation during heat treatment, Superalloys 2000. (2000) 263–272.

[182] É.I. Golovko, L.F. Ochkas, M.S. Koval'chenko, A.F. Nikityuk, Oxidation of tantalum carbide alloys, Sov. Powder Metall. Met. Ceram. 15 (n.d.) 777–780. doi:10.1007/bf00796196.

[183] Royal Society of Chemistry, ChemSpider | Search and share chemistry, (2015). http://www.chemspider.com/.

[184] WebElements, (n.d.). doi:10.1103/PhysRevLett.112.172501.

[185] S.A. Humphry-Baker, W.E. Lee, Tungsten carbide is more oxidation resistant than tungsten when processed to full density, Scr. Mater. 116 (2016) 67–70. doi:10.1016/j.scriptamat.2016.01.007.

[186] H.L. Lukas, S.G. Fries, B. Sundman, Computational thermodynamics : The CALPHAD method, Cambridge University Press, 2007.

[187] S. James, R. GIbala, Structure of Transient Oxides Formed on NiCrAI Alloys, Metall. Trans. A. 14 (1983) 2143–2161.

[188] P. Souza Santos, H.S. Santos, S.P. Toledo, Standard Transition Aluminas. Electron Microscopy Studies, Mater. Res. 3 (2000) 104–114.

[189] G.C. Wood, B. Chattopadhyay, Transient oxidation of Ni-base alloys, Corros. Sci. 10 (1970) 471–480. doi:10.1016/S0010-938X(70)80032-4.

[190] H.M. Hindam, W.W. Smeltzer, Growth and Microstructure of α - Al2O 3 on Ni-Al Alloys: Internal Precipitation and Transition to External Scale, J. Electrochem. Soc. 127 (1980) 1622–1630.

[191] J. Zygmuntowicz, P. Wiecińska, A. Miazga, K. Konopka, Characterization of composites containing NiAl2O4 spinel phase from Al2O3/NiO and Al2O3/Ni systems, J. Therm. Anal. Calorim. 125 (2016) 1079–1086. doi:10.1007/s10973-016-5357-2.

[192] J. Doychak, M. Ruhle, TEM studies of oxidized NiAl and Ni3Al cross sections, Oxid. Met. 31 (1989) 431–452. doi:10.1007/BF00666466.

[193] R. Peraldi, D. Monceau, S. Jean, B. Pieraggi, High temperature oxidation of high purity nickel: oxide scale morphology and growth kinetics, Mater. High Temp. 20 (2003) 649–655. doi:10.1179/mht.2003.073.

[194] Q. Ding, Z. Shen, S. Xiang, H. Tian, J. Li, Z. Zhang, In-situ environmental TEM study of γ′-γ phase transformation induced by oxidation in a nickel-based single crystal superalloy, J. Alloys Compd. 651 (2015) 255–258. doi:10.1016/j.jallcom.2015.07.017.

[195] H. Long, H. Wei, Y. Liu, S. Mao, J. Zhang, S. Xiang, Y. Chen, W. Gui, Q. Li, Z. Zhang, X. Han, Effect of lattice misfit on the evolution of the dislocation structure in Ni-based single crystal superalloys during thermal exposure, Acta Mater. 120 (2016) 95–107. doi:10.1016/j.actamat.2016.08.035.

[196] G. Calvarin-Amiri, R. Molins, A.M. Huntz, Effect of the Application of a Mechanical Load

on the Oxide-Layer Microstructure and on the Oxidation Mechanism of Ni–20Cr Foils, Oxid. Met. 53 (2000) 399–426. doi:10.1023/A:1004553623556.

[197] A.M. Limarga, D.S. Wilkinson, Modeling the interaction between creep deformation and scale growth process, Acta Mater. (2007) 189–201.

[198] A.M. Limarga, D.S. Wilkinson, Creep-driven nitride scale growth in γ-TiAl, Acta Mater. 55 (2007) 251–260.

[199] G. Moulin, P. Arevalo, A. Salleo, Influence of external mechanical loadings (creep, fatigue) on oxygen diffusion during nickel oxidation, Oxid. Met. 45 (1996) 153–181. doi:10.1007/BF01046824.

[200] A. Defrense, L. Remy, Fatigue behaviour of CMSX 2 superalloy [001] single crystals at high temperature. I. Low cycle fatigue of notched specimens, Mater. Sci. Eng. A. A129 (1990) 45–53.

[201] A.J. Wasson, G.E. Fuchs, The Effect of Carbide Morphologies on Elevated Temperature Tensile and Fatigue Behavior of a Modified Single Crystal Ni-Base Superalloy, Superalloys 2008. (2008) 489–497.

[202] A.P. Gordon, R.W. Neu, D.L. Mcdowell, Effect of pre-exposure on crack initiation life of a directionally solidified Ni-base superalloy, Int. J. Fatigue. 31 (2008) 393–401. doi:10.1016/j.ijfatigue.2008.07.009.

[203] D.P. DeLuca, C. Annis, Fatigue in Single Crystal Nickel Superalloys, 1993.

[204] D. Leidermark, J. Moverare, K. Simonsson, S. Sjöström, A combined critical plane and critical distance approach for predicting fatigue crack initiation in notched single-crystal superalloy components, Int. J. Fatigue. 33 (2011) 1351–1359. doi:10.1016/j.ijfatigue.2011.05.009.

[205] R. V. Miner, T.P. Gabb, J. Gayda, K.J. Hemker, Orientation and temperature dependence of some mechanical properties of the single-crystal nickel-base superalloy René N4: Part III. Tension-compression anisotropy, Metall. Trans. A. 17 (1986) 507–512. doi:10.1007/BF02643957.

[206] R. Jiang, Study of Fatigue Crack Initiation and Propagation Mechanisms in an Advanced Ni - based Superalloy : Effects of Microstructures and Oxidation, Univeristy of Southampton, 2015.

[207] H.U. Hong, B.G. Choi, I.S. Kim, Y.S. Yoo, C.Y. Jo, Characterization of deformation mechanisms during low cycle fatigue of a single crystal nickel-based superalloy, J. Mater. Sci. 46 (2011) 5245–5251. doi:10.1007/s10853-011-5462-3.

[208] R. Ohtani, N. Tada, M. Shibata, S. Taniyama, High temperature fatigue of the nickel-base single-crystal superalloy CMSX-10, Doi.org. 24 (2001) 867–876. doi:10.1046/j.1460-2695.2001.00451.x.

[209] P. Lukás, L. Kunz, Cyclic slip localisation and fatigue crack initiation in fcc single crystals, Mater. Sci. Eng. A. 314 (2001) 75–80. doi:10.1016/S0921-5093(00)01941-9.

[210] V. Brien, B. Decamps, Low cycle fatigue of a nickel based superalloy at high temperature: deformation microstructures, Mater. Sci. Eng. A. 316 (2001) 18–31. doi:10.1016/S0921-5093(01)01235-7.

[211] A. Pineau, S.D. Antolovich, High temperature fatigue of nickel-base superalloys – A review with special emphasis on deformation modes and oxidation, Eng. Fail. Anal. 16 (2009) 2668–2697. doi:10.1016/j.engfailanal.2009.01.010.

[212] W.W. Milligan, S.D. Antolovich, Yielding and deformation behavior of the single crystal superalloy PWA 1480, Metall. Trans. A. 18 (1987) 85–95. doi:10.1007/BF02646225.

[213] BS ISO 120108:2012 Metallic materials — Fatigue testing — Fatigue crack growth method, in: London, 2012.

[214] D. Gustafsson, J.J. Moverare, S. Johansson, K. Simonsson, M. Hörnqvist, T. Månsson, S. Sjöström, Influence of high temperature hold times on the fatigue crack propagation in Inconel 718, Int. J. Fatigue. 33 (2011) 1461–1469. doi:10.1016/j.ijfatigue.2011.05.011.

[215] P.A.S. Reed, Fatigue crack growth mechanisms in superalloys : overview, Mater. Sci. Technol. 25 (2009). doi:10.1179/174328408X361463.

[216] M.B. Henderson, J.W. Martin, Influence of precipitate morphology on the high temperature fatigue properties of SRR99, Acta Metall. Mater. 43 (1995) 4035–4043. doi:10.1016/0956-7151(95)00113-A.

[217] P.H. Thornton, R.G. Davies, T.L. Johnston, The temperature dependence of the flow stress of the γ′ phase based upon Ni3Al, Metall. Trans. 1 (1970) 207–218. doi:10.1007/BF02819263.

[218] P. Neumann, Coarse slip model of fatigue, Acta Metall. 17 (1969) 1219–1225. doi:10.1016/0001-6160(69)90099-6.

[219] P.A.S. Reed, I. Sinclair, X.D. Wu, Fatigue crack path prediction in UDIMET 720 nickel-based alloy single crystals, Metall. Mater. Trans. A. 31 (2000) 109–123. doi:10.1007/s11661-000-0058-6.

[220] J. Tong, J. Byrne, Effects of frequency on fatigue crack growth at elevated temperature, Fatigue Fract. Eng. Mater. Struct. 22 (1999) 185–193. doi:10.1046/j.1460-2695.1999.00160.x.

[221] P.K. Wright, M. Jain, D. Cameron, High Cycle Fatigue in Single Crystal Superalloy: Time dependence at Elevated Temperatures, Superalloys. 666 (2004).

[222] T. Weerasooriya, Effect of frequency on fatigue crack growth rate of Inconel 718 at high temperatures, Dayton, Ohio, 1987.

[223] X.-K. Zhu, J.A. Joyce, Review of fracture toughness (G, K, J, CTOD, CTOA) testing and standardization, Eng. Fract. Mech. 85 (2012) 1–46. doi:10.1016/j.engfracmech.2012.02.001.

[224] C.K. Sudbrack, S.L. Draper, T.T. Gorman, J. Telesman, T.P. Gabb, D.R. Hull, Oxidation and the effects of high temperature exposures on notched fatigue life of an advanced powder metallurgy disk superalloy, Superalloys 2012. (2012) 863–872.

[225] J.L. Bouvard, F. Gallerneau, P. Paulmier, J.L. Chaboche, A phenomenological model to predict the crack growth in single crystal superalloys at high temperature, Int. J. Fatigue. 38 (2012) 130–143. doi:10.1016/j.ijfatigue.2011.12.011.

[226] J.L. Bouvard, J.L. Chaboche, F. Feyel, F. Gallerneau, A cohesive zone model for fatigue and creep–fatigue crack growth in single crystal superalloys, Int. J. Fatigue. 31 (2009) 868–879. doi:10.1016/j.ijfatigue.2008.11.002.

[227] A. Ma, D. Dye, R.C. Reed, A model for the creep deformation behaviour of single-crystal superalloy CMSX-4, Acta Mater. 56 (2008) 1657–1670. doi:10.1016/j.actamat.2007.11.031.

[228] S. Reichstein, S. Kraft, H. Mughrabi, Sequence of distinct microyielding stages of the monocrystalline nickel-base superalloy CMSX-6 at high temperatures, Int. J. Mater. Res. 100 (2009) 494–499. doi:10.3139/146.110061.

[229] G. Brunetti, A. Settefrati, A. Hazotte, S. Denis, J.-J. Fundenberger, A. Tidu, E. Bouzy, Determination of γ-γ' lattice misfit in a single-crystal nickel-based superalloy using convergent beam electron diffraction aided by finite element calculations, Micron. 43 (2012) 396–406. doi:10.1016/j.micron.2011.10.009.

[230] J.X. Zhang, J.C. Wang, H. Harada, Y. Koizumi, The effect of lattice misfit on the dislocation motion in superalloys during high-temperature low-stress creep, (2005). doi:10.1016/j.actamat.2005.06.013.

[231] A. Karabela, L.G. Zhao, B. Lin, J. Tong, M.C. Hardy, Oxygen diffusion and crack growth for a nickel-based superalloy under fatigue-oxidation conditions, Mater. Sci. Eng. A. 567 (2013) 46–57. doi:10.1016/j.msea.2012.12.088.

[232] S. Sanyal, U. V Waghmare, T. Hanlon, E.L. Hall, P. Subramanian, M.F.X. Gigliotti, Interfaces in Ni-based Superalloys and Implications for Mechanical Behavior and Environmental Embrittlement: A First-principles Study, (2012).

[233] D.W. Maclachlan, D.M. Knowles, Creep-Behavior Modeling of the Single-Crystal Superalloy CMSX-4, Metall. Mater. Trans. A. 31A (2000).

[234] F.R.N. Nabarro, Rafting in Superalloys, Metall. Mater. Trans. A. 27A (1996).

[235] G. Nicoletto, R. Konečná, S. Fintova, Characterization of microshrinkage casting defects of Al–Si alloys by X-ray computed tomography and metallography, Int. J. Fatigue. 41 (2012) 39–46. doi:10.1016/j.ijfatigue.2012.01.006.

[236] P. Li, P.D. Lee, T.C. Lindley, D.M. Maijer, G.R. Davis, J.C. Elliott, X-ray Microtomographic Characterisation of Porosity and its Influence on Fatigue Crack Growth, Adv. Eng. Mater. 8 (2006) 476–479. doi:10.1002/adem.200600051.

[237] E. Padilla, V. Jakkali, L. Jiang, N. Chawla, Quantifying the effect of porosity on the evolution of deformation and damage in Sn-based solder joints by X-ray microtomography and microstructure-based finite element modeling, Acta Mater. 60 (2012) 4017–4026. doi:10.1016/j.actamat.2012.03.048.

[238] E. Maire, P.J. Withers, Quantitative X-ray tomography, Int. Mater. Rev. 59 (2014) 1–43. doi:10.1179/1743280413Y.0000000023.

[239] ASTM E647 - 13e1 Standard Test Method for Measurement of Fatigue Crack Growth Rates, n.d.

[240] B.L. Freeman, G.J. Neate, The measurement of crack lenght during elecated temperatures using the d.c potential drop method, in: C.J. Beevers (Ed.), Meas. Crack Length Shape Dur. Fract. Fatigue, Engineering Materials Advisory Services, 1980: pp. 435–459.

[241] C.J. Beevers, Halliday, The d.c potential drop method for crack lenght measurements, in: C.J. Beevers (Ed.), Meas. Crack Length Shape Dur. Fract. Fatigue, Engineering Materials Advisory Services, 1980: pp. 85–112.